acoustic Bragg diffraction

SHORT COURSE

IEEE Short Courses provide expert instruction plus member service

Choose the plan that best fills your capabilities and matches your needs

1. Full-Service Plan
The IEEE Continuing Education Department staff does practically all the arrangements. The sponsoring unit arranges for location, luncheons and refreshments; audio visuals and operator; local promotion of supplied pieces; registration on site. IEEE handles advance registrations.

2. Instructor and Course Notes Plan
Under this plan the sponsoring unit handles most of the arrangements, but has a chance to produce greater funds for the unit.

3. EAB and University/ Section Plan
Similar to Full Service Plan but with variations subject to discussion.
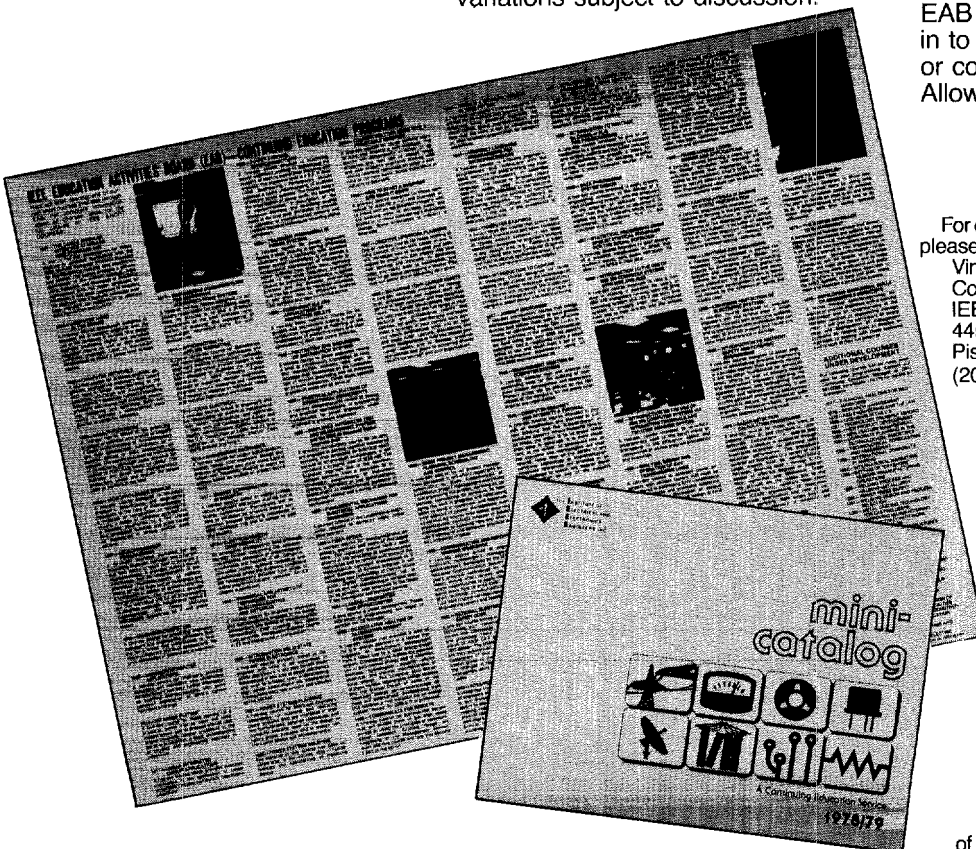
4. IEEE Society/ Group Plan
Similar to Section-sponsored plan, but "split" of fees differs.

5. Conference Plan
Arrangements for a course or courses during a major conference.

6. On-Premises Courses
EAB courses can be brought right in to your own company, institute, or college, for on-site training. Allow 30–60 days for scheduling.

For complete information, including costs, please contact:
Vincent J. Giardina, Manager
Continuing Education
IEEE
445 Hoes Lane
Piscataway, New Jersey 08854
(201) 981-0060
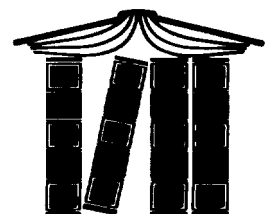
A Continuing Education Service of the IEEE Educational Activities Board.

PROCEEDINGS OF THE IEEE

contents

JANUARY

contents continued

COVER   A design based on acoustic Bragg diffraction of a beam of light by a sound wave. Both downshifting and upshifting are shown. See the special collection of papers beginning on page 48 for coverage of the general subject of acousto-optic signal processing.

Contributed Papers

The PROCEEDINGS OF THE IEEE welcomes for consideration 1) contributed tutorial-review papers in all areas of electrical engineering, and 2) contributed research papers on subjects of broad interest to IEEE members. The prospective author of a tutorial-review paper is encouraged to submit an advance proposal giving an outline of the proposed coverage and a brief explanation of why the subject is of current importance and of his relation to the subject.

JANUARY

PROCEEDINGS^{OF THE}IEEE ◆

Scanning the Issue

Understanding Monomode Optical Fibers, *Snyder,* page 6— Optical fibers are of great interest today since they will be a transmission medium of great importance tomorrow. Accordingly, it is highly desirable to be able to explain light propagation on such fibers using the simplest physical concepts possible so that both students and those engineers and scientists not directly involved can better appreciate the subject. Light propagation through multimode fibers, i.e. fibers of comparatively large diameter compared to wavelength, can be studied by classical geometric optics. *Monomode* fibers, however, are the most likely candidates for long-distance high-capacity communication, and these have comparatively small diameters, so small that geometric optics provides an inaccurate description of propagation along them. For such small-diameter fibers, Maxwell's equations must be solved, and this involves numerical methods, even for simple idealized fibers.

This paper offers a new approach that greatly facilitates the description of monomode fibers. Simple analytical forms are derived, using physical arguments, for the fields, propagation constant, and other parameters necessary to describe the fundamental mode on fibers of practical interest. A clearer understanding is possible from the resulting expressions, without recourse to graphical or numerical-methods.

Hill Shading and the Reflectance Map, *Horn,* page 14—*Disegno e rilievo,* creating the effect of relief in a flat image, was a subject much studied by artists of the Renaissance period. Shading, a style of painting using variation of gray tone over a surface to achieve the effect of a third dimension, was one of the primary tools in their arsenal. Thus developed *chiaroscuro,* the art of light and shade, clear and dark. Such well-known artists as Rembrandt van Rjin brought these techniques home with them from Italy.

The same methods were first used by Leonardo da Vinci in the portrayal of geological forms. Shaded maps, developed later primarily in Switzerland, give one an immediate "feel" for the shape of the surface of the earth—an appreciation which is not directly available from a contour map. Not many maps are shaded, since few cartographers have acquired the artistic skills required for land-form portrayal. Suggestions have been made over a period of two centuries to simplify and automate this process.

In this paper, various proposed methods are compared and contrasted using a graphic representation for the dependence of gray tone on surface orientation, the reflectance map. A bridge is built between cartography and computer graphics by means of this tool.

The reflectance map is also useful in understanding vision, since it captures the constraints available to the human visual system when confronted with the task of recovering the three-dimensional shape of an object from a two dimensional image.

SPECIAL SECTION ON ACOUSTO-OPTIC SIGNAL PROCESSING

The basic concepts for processing signals optically were developed in the late 1940's in terms of linear filtering theory. A coherently illuminated optical system displays the Fourier transform of a two-dimensional signal as a physical light distribution that can be measured to produce an estimate of the spectral content of the signal. Alternatively, the spectrum can be modified so that the optical system produces, after a second Fourier transform operation, a filtered version of the input signal. Operations such as spectral analysis, correlation or convolution are performed in parallel at a rate limited only by the characteristics of the input and output devices. Significant improvements in the performance of real-time processing systems were gained in the 1970's when devices such as acousto-optic cells and photodetector arrays were developed to the level necessary to implement practical systems.

Three papers in this issue describe the acousto-optic devices used to convert a wide-band electrical signal to an optical signal and the photodetector devices used to convert the processed optical signal to an electrical signal. The other papers show how processing algorithms can be implemented by various one- and two-dimensional system architectures. Electronic preprocessing and postprocessing are generally used to achieve the desired result; since these functions are similar to those that would be used if the computations were done electronically, they are not covered in this issue.

A broader set of optical processing techniques such as those used for pattern recognition, nondestructive testing, numerical calculation, reconstruction of tomographic data, image deconvolution or radar signal processing were covered in the Special Issue on Optical Computing in January 1977. Other applica-

tions of acousto-optic devices such as those used for ultrasonic imaging, Bragg-diffraction imaging, acousto-optic metrology, laser modulation and scanning were covered in a Special Issue on Acoustic Imaging in April 1979. Readers may wish to read selected papers in these issues which complement those presented here.

In the first paper, Korpel traces the history of the interaction of light and sound, beginning with the predictions of Brillouin in 1922 and the studies of weak interactions by Raman and Nath. Later, the analogies between strong interactions and X-ray diffraction as analyzed by Bragg became apparent; since strong interaction is generally desired to achieve high efficiency, acousto-optic cells are often called Bragg cells. Korpel reviews the fundamental relationships between the sonic wave, produced by an applied voltage, and the optical signal which it modulates. He also relates the physical parameters of the cell to important operational parameters such as the bandwidth W and the processing time T, and shows how a basic device can be used as a modulator, a beam deflector or a delay line.

Young and Yao describe the design and fabrication of acousto-optic cells based on a specification of their operating parameters. To achieve a high diffraction efficiency, a broad bandwidth and a long processing time requires careful matching of the momentum vectors of the optical and sonic waves. These considerations, in turn, impact the design of the transducers that convert electrical power to acoustic power. Several design examples are given for modulators and deflectors using different acousto-optic materials. Bandwidths up to 1 GHz and processing times up to 40 μs are achievable with the TW products generally in the 1000–2000 range for one-dimensional cells.

Rhodes focuses on the computational architectures and techniques useful for implementing algorithms such as convolution, correlation, and ambiguity function generation. He introduces the concepts necessary to use an acousto-optic cell with either incoherent or coherent light sources and explains how the inherent phase modulation produced by the cell can be rendered visible. Since the response of a photodetector is proportional to the light intensity, Rhodes reviews several interferometric or heterodyning techniques to recover both the amplitude and phase of a light distribution for those applications where such information is important. He further shows that a processing algorithm may be implemented either in a space-plane, which is equivalent to time-domain processing, or in the Fourier plane, which does not have a physical counterpart in electronics. The first optical processing systems used a space-integrating architecture in which the TW product is limited by the processing time of the cell. Rhodes describes some time-integrating architectures in which the processing time, and therefore the TW product, can be extended significantly to produce more correlation gain or frequency resolution. Another method for increasing the TW product is to use two acousto-optic cells, typically in orthogonal directions, to fully realize the two-dimensional processing capability of the optical system. A natural application of the two-cell approach is ambiguity function generation in which the Doppler and time delay of a received signal are displayed in orthogonal directions at the output of the system. The TW products of such systems are of the order of 10^6 for space-integrating architectures and even higher for time-integrating architectures.

Turpin concentrates on spectrum analysis and related topics. He starts with one-dimensional, space-integrating architectures and proceeds through to time-integrating and two-dimensional architectures. A hybrid architecture that is both time- and space-integrating is applied to the development of a radiometer bank for detecting signals where the noise power exceeds the signal power. Time-integrating and two-dimensional approaches are also used to provide frequency resolution finer than that achievable from the processing time of the Bragg cell. Turpin shows that the algorithm implemented by the two-dimensional spectrum analyzer can be related to the fast Fourier transform algorithm; the analogy is helpful in providing additional insights into optical processing techniques. An important recent development, called the triple product processor, is also described by Turpin. Due to its flexibility, many processing algorithms can be implemented using this architecture. As an example, Turpin describes how this processor can generate the ambiguity function; his description is based on spectrum analysis concepts whereas Rhodes' is derived from correlation concepts. Both viewpoints are valid and result in similar system architectures.

In a contributed paper, Kellman, Shaver, and Murray describe in greater detail the performance of a time-integrating channelized receiver. They establish the tradeoff between noncoherent processing gain and dynamic range, and show how digital postprocessing can be used to improve the performance of the system. Experimental results are included that agree with the predicted performance.

Photodetection techniques and devices also play an important role in signal processing applications. Early experimentors in real-time signal processing used a TV camera as the detection device. Although one- and two-dimensional solid-state photodetector arrays are now incorporated into operational systems, the driving force behind the development of these self-scanned arrays relate to imaging applications that do not require the wide dynamic range, linearity, geometric precision or readout flexibility desired for signal processing application. In the final paper, Borsuk describes recent efforts to develop photodetector arrays that are more responsive to the requirements established by optical signal processing. He reviews the basic device physics as it limits device performance and considers the effects due to packaging elements into a linear or an area array suitable for signal processing. He concludes by discussing the impact that advanced microelectronics technologies such as VLSI and GaAs could have on the development of improved devices. At the moment, the overall performance of the optical signal processing tends to be limited by the performance of the photodetection device, but significant and rapid progress is becoming evident.

As shown in the papers, the number of complex multiplies per second of the optical systems is typically greater than 10^9 for processing real-time, wide-bandwidth (100–500 MHz) analog or digital signals. As the device performance parameters increase, so too will the number of multiplies per second; this feature, along with the ability to readily implement certain processing algorithms, is the chief attraction of optical processing. Another attraction of optical processing is reliability. There are usually only three active elements in the processing architecture: a light source, a small number of solid-state acousto-optic devices and a photodetector array. The computational power of an optical system containing these three active elements exceeds that of some large, special-purpose

digital computers for which reliability and availability becomes an important operational factor.

The papers in this issue cover signal processing techniques using bulk-wave acousto-optic devices. Currently there is considerable research work to integrate surface acoustic wave technology with that of solid-state lasers and photodetector arrays. The objective is to develop subsystems in which the laser, lenses, interaction medium and photodetectors are integrated on a common substrate. Since the optimum substrate material is different for each active device, current efforts are directed toward developing hybrid subsystems in which the laser and photodetector array are butt-joined to the substrate containing the necessary surface acoustic wave device and lenses. Although some of the flexibility for implementing two-dimensional processing is lost, these new developments may result in very compact subsystems.

It is my hope that these papers will introduce the readership to some of the signal processing operations that are being performed optically and will stimulate thinking as to new processing algorithms that can be implemented optically. Some optical systems have been developed because an algorithm could be performed better, in some technical sense, than with existing techniques and with better reliability. In other instances, optics provided the first practical method for implementing a processing operation.

I thank the authors for their papers and the reviewers for their comments and suggestions for improving the overall quality of this issue. I also acknowledge the encouragement of Professor Glen Wade, who invited me to be the Guest Editor for this issue, and the assistance of Managing Editor Reed Crone.

ANTHONY VANDERLUGT
Guest Editor
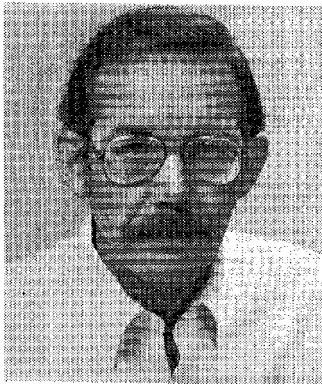
Anthony VanderLugt *(M'66) received the B.S.E.E. and M.S.E.E. degrees from the University of Michigan, Ann Arbor, in 1959 and 1962, and the Ph.D. degree from the University of Reading, Reading, England, in 1969.*

He was a member of the research staff at the Institute of Science and Technology at the University of Michigan from 1959 to 1969 where he worked on optical spatial filtering techniques, Fourier optics and applications of holography. In 1969 he joined the Harris Corporation as Director of Research at the ElectroOptics Center in Ann Arbor, MI. From 1973 to 1979 he managed research and development groups at the Government Systems Division of Harris in Melbourne, FL. In 1979 he joined the Advanced Technology Department where his major area of interest is optical signal processing.

Dr. VanderLugt is a Fellow of the Optical Society of America and a member of Sigma Xi, the Society of Photographic Instrumentation Engineers, Tau Beta Pi and Eta Kappa Nu. He was the American Editor of Optica Acta *from 1970 to 1974 and a member of the Advisory Board from 1974 to 1979.*

6

Understanding Monomode Optical Fibers

ALLAN W. SNYDER

Abstract—Because optical fibers that propagate one mode only are now the most likely candidate for future long-distance high-capacity communication, there is great interest in their light transmission characteristics. Standard descriptions of such fibers are rather unattractive both to students and to the physically minded scientist from several viewpoints, but mostly because numerical methods are always required at some stage in the analysis even if only to solve a transcendental eigenvalue equation. We reduce these restrictions by deriving simple analytical forms for the fields, propagation constant, and other parameters necessary to describe the fundamental mode on graded refractive index profiles. From these fully analytical expressions, we have a clearer understanding of propagation without recourse to numerical methods. Thus the theory of monomode fibers is now more accessible to undergraduates at elementary levels.

I. INTRODUCTION

OPTICAL FIBERS that propagate one mode only, the fundamental or HE_{11} mode, are the most promising transmission medium for future long-distance high-capacity communication [1], [2]. Accordingly, there are compelling reasons to study the characteristics of mode propagation on such fibers. However, there are features inherent to the solution of Maxwell's equations that make this task rather unattractive both to students and to the physically inclined scientist. Firstly, the step refractive index (or piecewise uniform) profile is the only profile of any practical interest for which Maxwell's equations can be solved exactly and the fields are algebraically complicated, involving Bessel functions, for fibers of circular cross section [3]-[5]. Secondly, and most importantly, even when a solution is possible, the physics is always obscured by having to solve a transcendental (eigenvalue) equation. In this sense, there are no fully analytical solutions for describing propagation on optical fibers. The purpose of this paper is to reduce these undesirable features by presenting an approximate analysis of propagation on fibers of practical interest that leads to simple analytical forms and no transcendental equations. From these simple expressions, we have a clearer understanding of light transmission on monomode fibers without recourse to graphical or numerical methods.

Our plan is to first derive the equation that governs propagation of the fundamental mode by using physical arguments. We then solve this equation for optical fibers with specific refractive index profiles and discuss the physics of propagation.

II. FUNDAMENTAL MODES OF WEAKLY GUIDING FIBERS

The electric and magnetic vector fields, E and H, for modes of a fiber with a circularly symmetric cross section can be

The author is with the Institute of Advanced Studies, Department of Applied Mathematics, Australian National University, Canberra, Australia.

(a)

Radial Distance

(b)
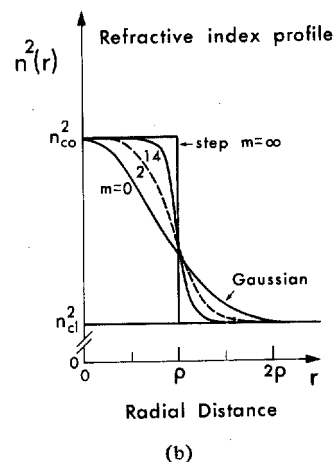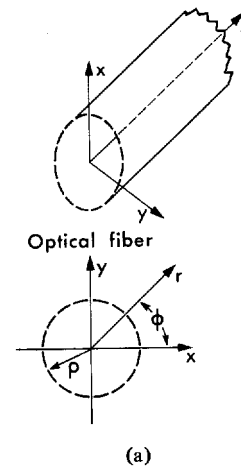
Fig. 1. (a) An optical fiber of circular cross section. (b) The class of refractive index profiles considered in this paper. The m notation in (b) is defined by (9) and (18) as discussed in Section VII.

expressed as [4]

$$E(r, \phi, z) = e(r, \phi) \exp(-i\beta z)$$

$$H(r, \phi, z) = h(r, \phi) \exp(-i\beta z) \tag{1}$$

where an $\exp(i\omega t)$ time dependence is implicit; β is the modal propagation constant, r and ϕ are the polar coordinates in the fiber cross section while z is the distance along the axis of the fiber as shown in Fig. 1(a). In general E and H are found by solving Maxwell's equations. However, because fibers used for optical communication are weakly guiding, i.e., they have refractive index profiles $n(r)$, where the variation between the maximum and minimum value of $n(r)$ is small, typically less than 1 percent, it turns out that E and H are approximate solutions of the *scalar* wave equation. This can be appreciated by the following arguments [5]-[9].

The propagation constant β of the fundamental mode must lie somewhere between two extremes given by the value of β for a z-directed plane wave propagating in an infinite medium of refractive index equal to the maximum or minimum values of the fiber profile $n(r)$. If we define these maximum and minimum values of $n(r)$ as

$$n_{c0} = \text{maximum refractive index of } n(r) \quad (2a)$$
$$n_{c1} = \text{minimum refractive index of } n(r) \quad (2b)$$

then β is bounded by

$$(2\pi n_{c1}/\lambda) < \beta < (2\pi n_{c0}/\lambda) \quad (3)$$

where λ is the wavelength in vacuum. Because fibers for optical communication are weakly guiding, i.e., $n_{c0} \cong n_{c1}$, it follows from (3) that $\beta \cong 2\pi n/\lambda$ which is the propagation constant of a z-directed plane wave in an unbounded medium of refractive index $n_{c1} \lesssim n \lesssim n_{c0}$.

Accordingly, the fundamental mode of an optical fiber must be nearly a transverse electromagnetic (TEM) wave, the simplest example being a wave polarized uniformly in one direction only.[1] Taking this direction of polarization to be x, the fields of the optical fiber are given by

$$E_x = \psi e^{-i\beta z}$$
$$H_y = (\epsilon/\mu)^{1/2} E_x \quad (4)$$

while the other field components E_y, E_z, H_x, and H_z are negligible, ψ specifies the spatial variation in the plane perpendicular to the fiber axis, μ is the permeability of the medium, $\epsilon = \epsilon_0 n^2$, where $n \cong n_{c0} \cong n_{c1}$ and ϵ_0 is the dielectric constant of vacuum.

Because $n_{c0} \cong n_{c1}$, the fields are only weakly influenced by the polarization properties of the fiber structure [5], [9]. If this is not obvious, then recall that plane wave reflection from a dielectric interface is nearly insensitive to the polarization of the incident wave when the two dielectrics are similar. Accordingly, the spatial dependence, ψ, of the fields must be insensitive to polarization effects so that ψ is a solution of the scalar wave equation, i.e.,

$$\left\{ \frac{\partial^2}{\partial r^2} + \frac{1}{r} \frac{\partial}{\partial r} + k^2(r) \right\} \psi(r) = \beta^2 \psi(r) \quad (5)$$

where $k(r)$ is given as

$$k(r) = 2\pi n(r)/\lambda. \quad (6)$$

The solution of (5) corresponding to the fundamental mode is that with the largest β and with ψ independent of the polar angle ϕ. Although polarization effects are very small, they must be considered in determining β for HE_{11} modes of a noncircular fiber (Section IX).

In summary, the fundamental mode is approximately a transverse electromagnetic wave given by (4) with the spatial dependence $\psi(r)$ a solution of the scalar wave equation. If our arguments are difficult to follow, then the reader may prefer

[1] The fields of higher order modes are also nearly TEM but they are not uniformly polarized in one direction.

the derivation by formal perturbation methods [5], [9], [10].

III. GAUSSIAN APPROXIMATION FOR FIELDS OF THE FUNDAMENTAL MODE

Our main objective is to find a good approximation for the field $\psi(r)$ and the propagation constant β of the fundamental mode on fibers with refractive index profiles, $n(r)$, like those of Fig. 1(b) where m is defined in Section VII. For such profiles, we know that $\psi(r)$ must be maximum at $r = 0$, decreasing to zero with increasing r. Furthermore, numerical solution of (5) for the step and power-law core profiles show that $\psi(r)$ is approximately Gaussian in appearance [11]–[15]. Accordingly we assume that the field of the HE_{11} mode has the form

$$\psi(r) \cong \exp\left[-\tfrac{1}{2}(r/r_0)^2 \right] \quad (7)$$

where r_0, the spot size, is determined by the following elementary, variational method [14]. If (7) is an accurate approximate solution of (5), then it can be used as a trial function in a stationary expression for the propagation constant, β, with the spot size found as the value of r_0 giving rise to the largest β [14], [16]. Recall that the fundamental mode is defined as that with the largest β. The stationary expression for β of (5) is (see *Additonal Note on (8)* at the end)

$$\beta^2 = \frac{\int_0^\infty \left\{ -\left(\frac{d\psi}{dr}\right)^2 + k^2(r)\psi^2 \right\} r \, dr}{\int_0^\infty r\psi^2 \, dr}. \quad (8)$$

Thus the procedure for finding the spot size r_0 is straightforward. We simply substitute the approximation of $\psi(r)$ given by (7) into (8) and then find r_0 as that value satisfying $(\partial \beta^2/\partial r_0) = 0$. The approximation for the propagation constant β is found by substituting r_0 into (8). Knowing r_0 and β, the field is fully specified by (4) and (7). It remains only to specify the refractive index profile $n(r)$ and perform the algebra discussed above. To this end we find it convenient to express $n(r)$ as

$$n^2(r) = n_{c1}^2 + s(r^2/\rho^2)\Delta^2 \quad (9)$$

where Δ, the refractive index difference parameter, is defined as

$$\Delta = (n_{c0}^2 - n_{c1}^2)^{1/2} \quad (10)$$

while $s(r^2/\rho^2)$ characterizes any profile shape ($s = 1$ at maximum) with ρ a scaling parameter. For the profiles of Fig. 1(b), $s = 1$ at $r = 0$ and $s = 0$ at $r = \infty$. Our definition of Δ differs from some authors, e.g., [7], but it is more convenient for this presentation.

IV. EXAMPLE 1: THE GAUSSIAN REFRACTIVE INDEX FIBER

We first consider the refractive index profile of Fig. 1(b) for which $s(r^2/\rho^2)$ is a Gaussian func-

tion of the form

$$s(r^2/\rho^2) = \exp\,[-(r/\rho)^2]. \qquad (11)$$

The Gaussian profile is unique because it has the same shape as the field intensity ψ^2 given by (7) but with ρ playing the role of r_0. Furthermore, it approximates those fibers for communication that undergo significant diffusion at the core-cladding interface during the manufacturing process. Most importantly however, the Gaussian profile provides us with a very simple model for understanding all aspects of propagation on monomode fibers and one where our approximate solution is highly accurate.

Substituting (7) and (11) into (8) leads to an expression for β in terms of r_0 given by

$$(\rho\beta)^2 = (\rho k_{c0})^2 - (\rho/r_0)^2 - V^2\{(\rho/r_0)^2 + 1\}^{-1} \qquad (12)$$

where $k_{c0} = 2\pi n_{c0}/\lambda$ and we have introduced the usual dimensionless fiber parameter V defined as

$$\boxed{V = 2\pi\rho\Delta/\lambda.} \qquad (13)$$

The spot size r_0 to be substituted into (7) and (12) is found by solving $(\partial\beta^2/\partial r_0) = 0$ leading to

$$r_0^2 = \rho^2/(V-1). \qquad (14)$$

This expression is physically meaningful only when $V \geqslant 1$ (r_0 positive) but we find below that this does not detract from (14) providing a comprehensive description of communication fibers. Substituting r_0 into (12) leads to an expression for β of the form

$$(\rho\beta)^2 = (\rho k_{c0})^2 - 2V + 1 \qquad (15)$$

which is restricted to $V \geqslant \frac{1}{2}$, since from (3) we know that $\beta \leqslant k_{c0}$.

The spot size and propagation constant fully specify the field of the fundamental mode and thus the light transmission properties of monomode fibers as we discuss below. The usefulness of the parameter V is evident from the fact that r_0/ρ, and hence $\psi(r)$, depend on V only.

Range of V for Single Moded Operation: When V is increased above a certain value other modes can propagate, e.g., this value is $V \cong 2.41$ for the step profile fiber of Fig. 1(b) [4] and $V \cong 2.59$ for the Gaussian profile fiber.[2] However, in practice fibers tend to be effectively single moded for larger values of V, say $V \leqslant 3$ for the step profile, because the higher order modes suffer radiation losses due to fiber imperfections [17].

From this discussion we can appreciate one reason why monomode fibers are weakly guiding. To be single moded, $V < 3$ for the profiles of Fig. 1(b), which from (13) restricts the physical dimensions of the fiber cross section to $\rho < 3\lambda/2\Delta$. Supposing that $\lambda \cong 1\,\mu m$, then we see that ρ is minute unless $\Delta \ll 1$. A small cross section has many disadvantages and is normally avoided in practice.

V. PHYSICS OF PROPAGATION ON THE GAUSSIAN PROFILE FIBER

Because we have simple analytical expressions for both the field and propagation constant of the HE_{11} mode of the

Gaussian profile fiber, we can derive simple expressions for all of the parameters that characterize propagation. For example, in Table I we give expressions for parameters of greatest interest. These parameters will be discussed in turn below.

A. Spatial Distribution of Light Intensity

The axial power density or intensity profile, $S(r)$ is shown in Table I to have the form $\exp\,\{-(r/\rho)^2(V-1)\}$, i.e., the intensity falls off exponentially with the square of the increasing distance from the fiber axis as shown in Fig. 2(a). This fall off is less rapid for smaller V values, so that the smaller the V, the smaller the fraction of total power flowing near the fiber axis. The effect is directly illustrated by calculating the fraction $\eta(r)$ of power within the region 0 to r as given in Table I and graphed in Fig. 2(b). It is clear that fibers of small V, say $V < 1.1$, transmit light which is spread over a large cross section compared with the case when $V > 2$. Because this is undesirable in practice, it explains why we are unconcerned by the restriction of (14) to $V > 1$.

B. Profile Dimension for Maximum Light Concentration

It is interesting to determine the refractive index profile dimension ρ for which the modal light intensity will be most densely concentrated near to the fiber axis, assuming a given Δ and wavelength of excitation. In other words, we ask what ρ gives the smallest spot size r_0. By differentiating (14) with respect to ρ, recalling from (13) that V is proportional to ρ, we find that the optimum ρ occurs when $V = 2$, i.e., $\rho = \lambda/\pi\Delta$. At $V = 2$, we also observe that $r_0 = \rho$ so that the intensity distribution, $S(r)$, exactly matches the shape of the refractive index profile $s(r^2/\rho^2) = \exp\,[-(r/\rho)^2]$.

This last result can also be appreciated in a qualitative fashion from elementary physics. Suppose we want to confine the light intensity to the profile shape $\exp\,[-(r/\rho)^2]$. Now we know that a light beam has an innate spread $\delta\theta$ in ray directions due to diffraction. Thus, if the Gaussian beam is to maintain its $\exp\,[-\frac{1}{2}(r/\rho)^2]$ field distribution as it propagates along the fiber, it is necessary that this $\delta\theta$ diffraction spread just equals the angle θ_c necessary for rays to be bound to the fiber, where both $\delta\theta$ and θ_c are inclined to the fiber axis. It is well known from geometric optics that light inclined at angles $\theta > \Delta/n_{c0}$, where Δ is given by (10), is lost by radiation (refraction), so we take $\theta_c = \Delta/n_{c0}$. The spread in ray directions $\delta\theta$ due to diffraction is determined by a two-dimensional Fourier transform of the field distribution, where the transform variables are r and $2\pi n\theta/\lambda$, with θ inclined to the fiber axis. This leads to $\exp\,[-2(\pi n\rho\theta/\lambda)^2]$ for the angular (θ) dependence of the transform of $\exp\,[-\frac{1}{2}(r/\rho)^2]$. Now we (arbitrarily) define the characteristic diffraction spread $\delta\theta$ as that value of θ for which the transform falls to e^{-2}, so that $\delta\theta = \lambda/2\pi n\rho$. Demanding that $\delta\theta = \Delta/n_{c0}$ to prevent radiation loss, is equivalent from (13) to demanding that $V = 2$. Obviously it is only fortuitous that this result is identical to that found above, since our arguments are qualitative. Nevertheless, the derivation does convey some insight into the physics of propagation on monomode fiber as a balance between the spread in ray directions due to diffraction on one hand and their containment by the refractive index gradient on the other hand.

C. Pulse Spreading

Because information is normally transmitted along optical fibers by pulses, i.e., by digital envelope modulation, we are interested in pulse distortion. Now a pulse of finite duration has a characteristic spread in frequencies as does any practical source so that the pulse spreads as it travels due to material dispersion because n depends on frequency, and also due to waveguide (intramodal) dispersion, because β

---

[2] The "exact" results reported in this paper for the smoothed out step profiles of Fig. 1(b) are determined by a numerical solution of (5).

TABLE I

PARAMETERS OF THE FUNDAMENTAL MODE

(Parameters of the fundamental mode expressed in terms of the spot size r_0 of the modal field as defined by (7) or by II.1 of Table II. Explicit expressions are given in Table II for both r_0 and β for the profiles considered in this paper. The expressions for V_g^{-1} and D are derived using II.4 and II.5 of Table II.)

z-directed power density	$S(r) = \frac{1}{2}E_x H_y^* = \frac{1}{2}(\epsilon/\mu)^{1/2} e^{-(r/r_o)^2}$
Total power	$P = 2\pi \int_0^r rS(r)\,dr = \frac{\pi}{2}\left(\frac{\epsilon}{\mu}\right)^{1/2} r_o^2$
Fraction of power within 0 to r	$\eta(r) = \dfrac{\int_0^r rS(r)\,dr}{\int_0^\infty rS(r)\,dr} = 1 - e^{-(r/r_o)^2}$
(Group velocity)$^{-1}$	$v_g^{-1} = \dfrac{d\beta}{d\omega} = \dfrac{\omega\mu\epsilon_{co}}{\beta}\left\{1 + \left(\dfrac{\Delta}{Vn_{co}}\right)^2 \left(\dfrac{\rho^2}{r_o^2} + y\right)\right\}$ $y = (\rho\beta)^2 - (\rho k_{co})^2$
Waveguide dispersion parameter	$D = \dfrac{1}{\rho\mu\epsilon_{cl}}\left(\dfrac{n_{co}}{\Delta}\right)^3 \dfrac{dv_g^{-1}}{d\omega} \cong \dfrac{1}{V^3}\left\{V\dfrac{d}{dV}\left(\dfrac{\rho}{r_o}\right)^2 - \left(\dfrac{\rho}{r_o}\right)^2\right\}$ (neglecting terms in Δ)

	Gaussian Profile	Step Profile	"Smoothed Out" Step Profile
$S(r)$ for V>1	$\frac{1}{2}\left(\frac{\epsilon}{\mu}\right)^{1/2} e^{-(r/\rho)^2(V-1)}$	$\frac{1}{2}\left(\frac{\epsilon}{\mu}\right)^{1/2} e^{-(r/\rho)^2 \ln V^2}$	$\frac{1}{2}\left(\frac{\epsilon}{\mu}\right)^{1/2} e^{-(r/\rho)^2(m+1)(V^{\frac{2}{m+2}}-1)}$
P for V>1	$\frac{\pi}{2}\left(\frac{\epsilon}{\mu}\right)^{1/2} \frac{\rho^2}{V-1}$	$\frac{\pi}{2}\left(\frac{\epsilon}{\mu}\right)^{1/2} \frac{\rho^2}{\ln V^2}$	$\frac{\pi}{2}\left(\frac{\epsilon}{\mu}\right)^{1/2} \rho^2/(m+1)(V^{\frac{2}{m+2}}-1)$
$\eta(r)$ for V>1	$1 - e^{-(r/\rho)^2(V-1)}$	$1 - e^{-(r/\rho)^2 \ln V^2}$ $= 1 - (1/V)^2, r=\rho$	$1 - e^{-(r/\rho)^2(m+1)(V^{\frac{2}{m+2}}-1)}$
v_g^{-1} for V>1	$\frac{\omega\mu\epsilon_{co}}{\beta}\left\{1 - \frac{1}{V}\left(\frac{\Delta}{n_{co}}\right)^2\right\}$	$\frac{\omega\mu\epsilon_{co}}{\beta}\left\{1 + \left(\frac{\Delta}{Vn_{co}}\right)^2\right\}$	$\frac{\omega\mu\epsilon_{co}}{\beta}\left\{1 - \left(\frac{\Delta}{n_{co}}\right)^2 \left(\frac{1}{V^2}\right)^{\left(\frac{m+1}{m+2}\right)}\right\}$
D for V>1	$1/V^3$	$2(1 - \ln V)/V^3$	$\frac{m+1}{V^3}\left\{1 - \left(\frac{m}{m+2}\right)V^{\frac{2}{m+2}}\right\}$
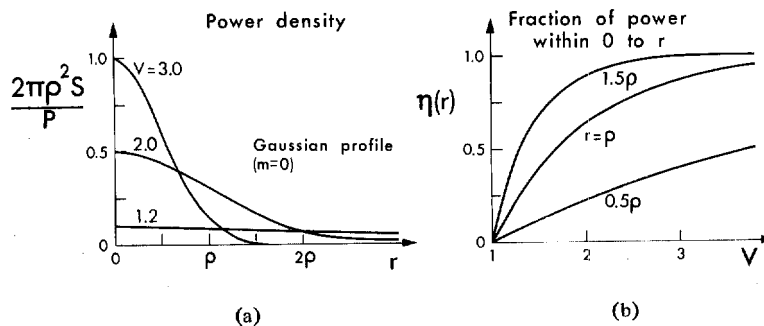
Fig. 2. (a) The normalized power density versus radial distance where S and P are defined on Table I. (b) The fraction of power flowing within the cross section 0 to r versus the dimensionless parameter V of (13) where η is defined on Table I. Both (a) and (b) are for the HE$_{11}$ mode of a Gaussian profile fiber. ρ is shown in Fig. 1(b).

has a nonlinear dependence on frequency. These two effects can combine in various ways depending on the nature of the material dispersion and normally cancel each other at some wavelength [18], [19]. Here we examine the influence of waveguide dispersion only.

The group velocity $v_g = d\omega/d\beta$ gives the average velocity of the pulse. The expression for v_g^{-1} in Table I is found by differentiating II.4 of Table II using II.5 to simplify. Pulse spread depends on the spread in the group velocity dv_g due to the spread in frequencies $d\omega$ associated with the pulse. In practice, however, it is common to quantify pulse distortion by the spread in the mode "transit time" or group delay [20], i.e., by a quantity proportional to $(dv_g/d\omega)^{-1}$. Differentiating v_g^{-1} in Table I, leads to an expression for pulse distortion that

TABLE II
FIELD OF THE FUNDAMENTAL MODE
(Outline of the procedure for finding the fields, i.e., spot size r_0 and propagation constant β, of the HE_{11} mode on fibers with a profile shape $s(r^2/\rho^2)$. Explicit results are given for the class of profiles depicted in Fig. 1(b).)

$E_x = e^{-\frac{1}{2}\left[\frac{r}{r_0}\right]^2} e^{i\beta z}$; $\qquad$ $H_y = (\epsilon/\mu)^{\frac{1}{2}} E_x$ with E_y, H_x, E_z and H_z negligible				II.1
$n^2(r/\rho) = n_{c1}^2 + s(r^2/\rho^2)\Delta^2$ $\Delta = \{n_{co}^2 - n_{c1}^2\}^{\frac{1}{2}}$				II.2 II.3
$(\rho\beta)^2 = (\rho k_{co})^2 - \left[\frac{\rho}{r_0}\right]^2 + V^2\left\{\int_0^\infty e^{-c_o x}\frac{ds(x)}{dx}\,dx + s(o) - 1\right\}$ where $k_{co} = 2\pi n_{co}/\lambda$ and $V = 2\pi\rho\Delta/\lambda$ with $x = (r/\rho)^2$ and $c_o = (\rho/r_0)^2$				II.4
$c_o = (\rho/r_0)^2$ is found by solving $1 = -V^2\int_0^\infty xe^{-c_o x}\frac{ds(x)}{dx}\,dx$				II.5
	Gaussian Profile	Step Profile	"Smoothed Out" Step Profile	
$s(r^2/\rho^2)$	$e^{-(r/\rho)^2}$	$\begin{array}{ll}1, & r < \rho \\ 0, & r > \rho\end{array}$	$\Gamma^{-1}(m+1)\int_a^\infty t^m e^{-t}\,dt$ $\qquad a = (m+1)r^2/\rho^2$	
$(\rho/r_0)^2$ for $V > 1$	$V - 1$	$\ln V^2$	$(m+1)(V^{\frac{2}{m+2}} - 1) \underset{m\to\infty}{\sim} \ln V^2 + \frac{(\ln V^2 - 2)\ln V^2}{2m}$	
$(\rho\beta)^2$ for $V > 1$	$(\rho k_{co})^2 - 2V + 1$	$(\rho k_{co})^2 - \ln V^2 - 1$	$(\rho k_{co})^2 - (m+2)V^{\frac{2}{m+2}} + (m+1)$ $\underset{m\to\infty}{\sim}(\rho k_{co})^2 - \ln V^2 - 1 - (\ln V^2)^2/2m$	

is proportional to $D\Delta^3$, where Δ is given by (10) and D is a dimensionless distortion parameter that depends on V only and is defined in Table I. The greater $|D|\Delta^3$, the greater the pulse spreading due to waveguide dispersion. Thus by *comparing fibers with the same V value*, we again see an advantage of the weakly guiding $\Delta \ll 1$ fiber. For the Gaussian profile fiber, we learn from Table I that $D = 1/V^3$ so that pulse spread depends on Δ^3/V^3.

D. Radiation Losses Due to Fiber Imperfections

In practice, optical fibers are imperfect so that light is attenuated as it propagates. The contribution of material absorption to the losses of communication fibers is small, the loss being dominated by radiation due to fiber jointing, bending and microbending [2]. Expressions are available elsewhere for jointing and microbending losses in terms of spot size [12], [21]-[23] so that, when taken with our expression for r_0, we have an analytical description of these losses. We can also derive an expression for the pure bending losses of the Gaussian profile fiber by substituting (7) into the expressions for radiation found by treating the bent fiber as an antenna [5], [24], [25]. This leads to an expression for the power attenuation coefficient α given by

$$\alpha = \rho^{-1}g\left(\frac{\rho}{R}, V\right)\exp\left[-\frac{2}{3}\left(\frac{\Delta}{n_{co}}\right)^2\frac{R}{\rho}\frac{(V-1)^3}{V^2}\right], \qquad V > 1$$

where R is the radius of curvature of the bend as measured from the fiber axis and g a function which is relatively unimportant compared to the exponential portion. Our reason for giving this expression is to illustrate that, for a fixed V, fibers with small Δ are highly susceptible to radiation losses. Thus the advantages in size and dispersion of weakly guiding fibers is in part offset by radiation losses due to fiber imperfections.

This completes our brief review of some physical aspects of propagation on the Gaussian profile, monomode fiber. However, we emphasize that simple, analytical expressions can be derived for most, if not all, parameters of interest for this fiber.

VI. EXAMPLE 2: THE STEP REFRACTIVE INDEX FIBER

Our second example is the step refractive index fiber shown in Fig. 1(b) and characterized by $s = 1$ for $r < \rho$ and $s = 0$ for $r > \rho$, where s is defined by (9). By following the identical procedure discussed in Section IV for the Gaussian profile fiber we find that

$$r_0^2 = \rho^2/\ln V^2$$

$$(\rho\beta)^2 = (\rho k_{co})^2 - \ln V^2 - 1 \qquad (17)$$

which leads to the other parameters shown in Table I, where $k_{co} = 2\pi n_{co}/\lambda$.

All of the general phenomena discussed in Section V above ... also to the step
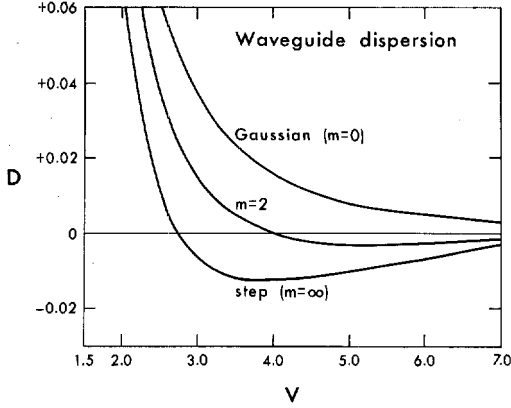
Fig. 3. The waveguide dispersion parameter D, which is a measure of the group delay or pulse spread in the absence of material dispersion, as is defined on Table I. m is shown in Fig. 1(b).

profile. However, the radius ρ for maximum confinement of light power is found from r_0 to occur when $V = e^{0.5} \cong 1.65$, corresponding to $r_0 = \rho = 1.65\lambda/2\pi\Delta$ compared to $V = 2$ with $r_0 = \rho = \lambda/\pi\Delta$ for the Gaussian profile. Accordingly, light of a given wavelength can be more highly confined by a step profile by the fact that r_0 for the step is 0.83 that of the Gaussian refractive index profile, assuming both profiles have the same Δ value of (10).

The step refractive index profile and the Gaussian profile differ significantly in their waveguide dispersion characteristics. The waveguide distortion parameter $D(V)$ for the step fiber equals $2(1 - \ln V)/V^3$ as shown in Table I. This function is compared to the Gaussian profile result in Fig. 3 where we note that the step profile has a V at which the waveguide dispersion is exactly zero.

VII. EXAMPLE 3: FIBERS WITH DIFFUSE CORE-CLADDING BOUNDARIES

The procedure we describe in Section III for finding the spot size is applicable to profiles of arbitrary shape so that, e.g., the fields of II.1 in Table II can represent any profile $n^2(r)$ as specified by II.2. Substituting this $n^2(r)$ into (8) and integrating by parts leads to an expression for β, in terms of the spot size, as given by II.4. The spot size is found by solving $(\partial\beta^2/\partial r_0) = 0$ or equivalently from II.5 of Table II. Thus Table II gives simple expressions for finding the spot size and β of arbitrary profile shapes. However, only special profiles will lead from II.5 to an analytical expression for spot size, e.g., the Gaussian profile fiber with $(ds(x)/dx) = e^{-x}$, with $x = (r^2/\rho^2)$ and the step profile fiber for which $(ds(x)/dx) = -\delta(x - 1)$ using the familiar Dirac delta function notation. Having analyzed both the step and the Gaussian profiles, it is of interest to study the characteristics of fibers with "smoothed out" step profiles intermediate between these two extreme cases. The step and Gaussian profile turn out to be extreme limits of the general class of profile shapes illustrated in Fig. 1(b) and defined by shape functions $s_m(x)$ of the form,

$$s_m(x) = \frac{1}{\Gamma(m+1)} \int_{(m+1)x}^{\infty} t^m e^{-t} \, dt \qquad (18)$$

where $x = (r/\rho)^2$ and Γ is the usual Gamma function and

$$\int_0^{\infty} rs_m \, dr = \rho^2/2.$$

For integer values of m, $\Gamma(m + 1) = m!$ and (18) becomes

$$s_m(r^2/\rho^2) = \exp\left[-(m+1)(r/\rho)^2\right] \sum_{i=0}^{m} \frac{(m+1)^i}{i!} \left(\frac{r}{\rho}\right)^{2i}.$$
$$(19)$$

We then see that $m = 0$ is the Gaussian profile while it can also be shown that $m = \infty$ is the step profile. Each profile has the same value.

The convenient property of these "smoothed out" step profiles is that $\partial s_m(x)/\partial x$ is a simple analytical expression as seen from (18). Substituting this into II.5 of Table II leads to an analytical expression for the spot size given by

$$r_0^2 = \rho^2/(m+1) \left\{ V^{2/(m+2)} - 1 \right\} \qquad (20)$$

which is valid for the continuum of values $m \geqslant 0$ and is identical to that of the Gaussian profile when $m = 0$ and the step profile when $m = \infty$, since $(x^\alpha - 1)/\alpha \rightarrow \ln x$ as $\alpha \rightarrow 0$. Substituting (20) into II.4 of Table II leads to the simple expression for β in Table II and the other parameters of Table I. As we mentioned in Section IV, the maximum V for single mode operation is about 2.41 for the step and 2.59 for the Gaussian so that the greater m, the closer the maximum value of V is to 2.41.

Because of our simple analytical expressions for the field, β and the other parameters of Tables I and II we can quantify the role of profile shape on propagation in monomode fibers without recourse to numerical methods. We consider waveguide distortion, since it is much more sensitive to profile shape than the other parameters discussed above. From the expression for waveguide dispersion D given in Table I, we see that there exists a value of V at which $D = 0$, occuring when $V = \{(m+2)/m\}^{(m+2)/2} \cong \exp(1 + 1/m)$ when m is large. Thus, the value of V for zero waveguide dispersion decreases from $V = \infty$ as $m \rightarrow 0$ to $V = e^1$ as $m \rightarrow \infty$. In Fig. 3 we compare D for the $m = 0$, 2 and ∞ profiles. It is clear that waveguide dispersion is highly sensitive to profile shape [26] for small values of m, say $m < 10$.

VIII. APPLICATION TO REFRACTIVE INDEX PROFILES OF MORE GENERAL SHAPE

While the procedure of this paper can be applied, at least formally, to profiles of arbitrary shape, we can obtain analytical expressions for a few special cases only. Accordingly, it is often useful to have a qualitative description of propagation. Such a description is suggested from the results of the smoothed out profiles, discussed in the last section. By comparing profiles with identical maximum height Δ and cross sectional area $2\pi \int_0^\infty rs(r) \, dr$, we have separated the dependence of modal parameters on profile shape from that of profile area. Our results show that spot size r_0 is comparatively insensitive to dramatic changes in profile shape, e.g., to within 4.6 percent, all profiles ($m = 0$ to ∞) have the same r_0 when $V = 3$. Furthermore, to within 3.5 percent, the lowest V for propagation of the second mode is $V = 2.5$ for all smoothed out profiles. These conclusions hold also for profiles of more general shape, including power law profiles and profiles with depressions about $r = 0$. Thus *profiles with the same maximum height, Δ and same area in cross section $2\pi \int_0^\infty rs(r) \, dr$ taking $s = 1$ at maximum, have approximately the same spot size and cutoff V for the second mode.* While it is possible to construct exceptions, most profiles of practical interest conform to the rule when operated near cutoff of the second mode. Suppose we are given a profile shape $s_0(r)$, with $s_0 = 1$ at maximum,

and a maximum refractive index difference Δ_0 defined by (2) and (10). Propagation of the HE_{11} mode on this fiber can then be modeled by one of the smoothed out step profiles characterized by Δ and ρ. Following our rule, we take $\Delta = \Delta_0$ and equate profile areas so that $\rho^2 = 2 \int_0^\infty r s_0(r) \, dr$. It is not critical which smoothed out profile we use as far as r_0 and the cutoff of the second mode are concerned. However, the waveguide dispersion parameter D varies significantly for the smaller m values ($m < 10$) of Fig. 1(b). Accordingly, we select a smoothed out profile which most nearly resembles the given profile. For example, if the given profile is step like with a dip near $r = 0$, then we use the step profile results listed in Tables I and II, $V \cong 2.41$ for cutoff of the second mode, where in all parameters ρ and Δ are defined as above. In this way we have a qualitative description of HE_{11} mode propagation for a more general class of profiles.

IX. PHILOSOPHY OF THE METHOD AND ITS EXTENSION TO NONCIRCULAR CROSS SECTIONS

By recognizing that (7) is an exact solution of (5) for a parabolic profile, i.e., for $s = 1 - (r/\rho)^2$, we appreciate the essence of the approximation presented in this paper—namely that the fields of the parabolic profile fiber can be "fit" to the fields of arbitrary profile fibers. The optimum fit is found from the stationary expression for β. Thus the approach can be generalized to fibers of noncircular cross section by fitting the HE_{11} fields of the noncircular parabolic profile fiber to the noncircular fiber of arbitrary refractive index grading. For example, the HE_{11} fields of fibers with elliptically deformed cross sections are approximated by

$$\psi(x, y) \cong \exp\left\{-\tfrac{1}{2}\left[(x/x_0)^2 + (y/y_0)^2\right]\right\} \qquad (21)$$

where the intensity distribution is now elliptical being characterized by lengths x_0 and y_0. This is the exact solution of the scalar wave equation for a parabolic profile $s = 1 - (x/\rho_x)^2 - (y/\rho_y)^2$ but, with the Cartesian form of (8), can be fit to arbitrary profiles $s(x^2/\rho_x^2, y^2/\rho_y^2)$. From the procedure of Section III we then derive two equations, each similar to II.5, for determining x_0 and y_0. The propagation of HE_{11} modes on noncircular waveguides is like that of plane waves in an anisotropic crystal in that the β's of the x- and y-polarized HE_{11} modes differ [9]. This behavior is not displayed by the scalar theory presented here but is accounted for by perturbation formulas once the solution for β and $\psi(x, y)$ of the scalar wave equation are known [5], [9].

In summary, we have used a powerful conceptual tool for finding the modes of optical fibers where the solution of the parabolic fiber is the building block from which the modes of arbitrary profile fibers are constructed.

X. ACCURACY OF THE APPROXIMATION

To appreciate the accuracy of the results presented here, we again note that (7) is an exact solution of (5) for the parabolic profile $s = 1 - (r/\rho)^2$. Thus the more the profile deviates from $1 - (r/\rho)^2$, the greater potential error. Now the Gaussian profile is significantly closer to $1 - (r/\rho)^2$ than is the step profile. Accordingly, the results for the Gaussian profile are significantly more accurate than those of the step profile. While this is true [14], we emphasize that the results for the step profile are themselves highly accurate but just not as accurate as those of the Gaussian profile. For example, the parameter $\eta(\rho)$ of Table I for the step profile is less than 1.2 percent in

error within the range of greatest practical interest, i.e., ($2 \leqslant V \leqslant 3$). Although the error in $\eta(\rho)$ increases as V decreases, even at $V = 1.25$ it is only 3.7 percent. The accuracy of β is even better, e.g., the dimensionless parameter $\rho\{k_{co}^2 - \beta^2\}^{1/2}$ is less than 1 percent in error within the range $2 \leqslant V \leqslant 3$. Obviously, the error depends on the parameter in question, e.g., while our approximation for β is highly accurate, its second derivative is susceptible to errors. Even so, the distortion parameter D which is proportional to $d^2(\rho\beta)/dV^2$ exhibits the correct qualitative features but the zero crossing in Fig. 3 is slightly in error, e.g., it should be $V = 3.01$ rather than 2.72 for $m = \infty$. On the other hand, the error[2] is less than 9.5 percent for D of the Gaussian profile when $V \geqslant 1.5$.

Field Far from Fiber Axis: The Gaussian approximation for $\psi(r)$ is deficient far from the axis, $r = 0$, where the exact fields of profiles with circular symmetry have a $K_0(wr)$ dependence rather than Gaussian, where K_0 is a modified Bessel function, $w = \{\beta^2 + (2\pi n_{c1}/\lambda)^2\}^{1/2}$ and $K_0(x) \sim (\pi/2x)^{1/2} e^{-x}$ for large x. The far (evanescent) field is usually of minor interest, but it is necessary to accurately evaluate evanescent coupling phenomena such as cross talk between fibers. We can use the results of the Gaussian approximation to generate an accurate expression for the far field. To do this we rearrange (5) by writing $k^2(r) = k_{c1}^2 + \{k^2(r) - k_{c1}^2\}$, leading to

$$\left\{\frac{\partial^2}{\partial r^2} + \left(\frac{1}{r}\right)\frac{\partial}{\partial r} - w^2\right\}\psi(r) = -\{k^2(r) - k_{c1}^2\}\psi(r)$$

$$(22)$$

with w defined as above. We then approximate $\psi(r)$ on the right-hand side by (7), because $k^2(r) - k_{c1}^2$ is significant only for small values of r when the Gaussian approximation is reasonable. The resulting equation is solved by standard Green's function methods [16], [27] leading, for example, to

$$\psi(r) \sim (V^2/V + 1) K_0\{(V - 1)r/\rho\} \exp\left[\tfrac{1}{2}(V - 1)^2/(V + 1)\right]$$

for the Gaussian profile (11). When $V = 2.5$, this result is less than 4 percent in error for $r > 1.5\rho$, taking modal power to be the same as in the Gaussian approximation (Table I).

Additional Note on (8): This result follows after multiplying (5) by $r\psi(r)$ and using the identity

$$r\psi\frac{\partial^2\psi}{\partial r^2} + \psi\frac{\partial\psi}{\partial r} = \frac{\partial}{\partial r}\left(r\psi\frac{\partial\psi}{\partial r}\right) - r\left(\frac{\partial\psi}{\partial r}\right)^2.$$

Then, by integrating from 0 to ∞, we obtain (8) plus another term $r\psi\partial\psi/\partial r$ evaluated at $r = 0$ and ∞. This term is zero because ψ is finite at $r = 0$ and decays to infinity exponentially fast.

REFERENCES

[1] M. Boerner and S. Maslowski, "Single-mode transmission systems for civil telecommunication," *Proc. Inst. Elec. Eng.*, vol. 123, pp. 627–632, June 1976.

[2] W. A. Gambling and H. Matsumura, "A comparison of single-mode and multimode fibres for long distance telecommunications," in *Fiber and Integrated Optics*, D. B. Ostrowsky, Ed. New York: Plenum, 1978, pp. 333–344.

[3] A. Hondros and P. Debye, "Electromagnetic waves in dielectric wires," *Ann. Phys.*, vol. 32, pp. 465–476, May 1910.

[4] D. Marcuse, *Light Transmission Optics*. New York: Van Nostrand Reinhold, 1972, ch. 8.

[5] A. W. Snyder and J. D. Love, *Optical Waveguide Theory*. London, England: Chapman and Hall, 1981, ch. 12, 13, and 30.

[6] A. W. Snyder, "Asymptotic expressions for eigenfunctions and eigenvalues of a dielectric or optical waveguide," *IEEE Trans. Microwave Theory Tech.*, vol. MTT-17, pp. 1130–1138, Dec. 1969.

[7] D. Gloge, "Weakly guiding fibers," *Appl. Optics*, vol. 10, pp. 2252–2258, Oct. 1971.

[8] J. A. Arnaud, "Transverse coupling in fiber optics. Part II: Coupling to mode sinks," *Bell Syst. Tech. J.*, vol. 53, pp. 675–696, Apr. 1974.

[9] A. W. Snyder and W. R. Young, "Modes of optical waveguides," *J. Opt. Soc. Amer.*, vol. 68, pp. 297–309, Mar. 1978.

[10] D. L. A. Tjaden, "First order corrections to weak-guidance approximations in fibre optics theory," *Philips J. Res.*, vol. 33, pp. 103–112, 1/2 1978.

[11] W. A. Gambling and H. Matsumura, "Simple characterization factor for practical single-mode fibres," *Electron. Lett.*, vol. 13, pp. 691–693, Nov. 1977.

[12] D. Marcuse, "Loss analysis of single-mode fiber splices," *Bell Syst. Tech. J.*, vol. 56, pp. 703–718, May 1977.

[13] ——, "Gaussian approximation of the fundamental modes of graded fibers," *J. Opt. Soc. Amer.*, vol. 68, pp. 103–109, Jan. 1978.

[14] A. W. Snyder and R. A. Sammut, "Fundamental (HE_{11}) modes of graded optical fibers," *J. Opt. Soc. Amer.*, vol. 69, pp. 1663–1671, Dec. 1979.

[15] A. W. Snyder, "Acuity of compound eyes: Physical limitations and design," *J. Comp. Physiol.*, vol. 116, pp. 161–182, Jan. 1977.

[16] J. Mathews and R. L. Walker, *Mathematical Methods of Physics*. New York: Benjamin, 1965, pp. 315–323; 261–262.

[17] W. A. Gambling, H. Matsumura, and C. M. Ragdale, "Zero mode dispersion in single-mode fibres," *Electron. Lett.*, vol. 14, pp. 618–620, Sept. 1978.

[18] F. Kapron, "Maximum information capacity of fibre optic waveguides," *Electron. Lett.*, vol. 13, pp. 96–97, Feb. 1977.

[19] W. A. Gambling, H. Matsumura and C. M. Ragdale, "Mode dispersion, material dispersion and profile dispersion in graded-index single-mode fibers," *IEE. MOA*, vol. 3, pp. 239–246, Nov. 1979.

[20] S. E. Miller and A. G. Chynoweth, *Optical Fiber Communications*. New York, Academic Press, 1979, ch. 4.

[21] W. A. Gambling, H. Matsumura, and C. M. Ragdale, "Joint loss in single-mode fibers," *Electron. Lett.*, vol. 14, pp. 491–493, July 1978.

[22] K. Peterman, "Fundamental mode microbending loss in graded-index and W-fibres," *Opt. Quantum Electron.*, vol. 9, pp. 167–175, Mar. 1977.

[23] C. Pask and R. A. Sammut, "Development in the theory of fibre optics," *Proc. IREE Aust.*, vol. 40, pp. 89–101, June 1979.

[24] A. W. Snyder, I. A. White, and J. D. Mitchell, "Radiation from bent optical waveguides," *Electron. Lett.*, vol. 11, pp. 275–277, July 1975.

[25] I. A. White, "Radiation from bends in optical waveguides: The volume current method," *IEE J. Microwave, Opt., Acoust.*, vol. 3, pp. 186–188, Sept. 1979.

[26] A. W. Snyder and R. A. Sammut, "Dispersion in graded single-mode fibers," *Electron. Lett.*, vol. 15, pp. 269–271, May 1979.

[27] P. M. Morse and H. Feshbach, *Methods of Theoretical Physics*. New York: McGraw-Hill, 1953, p. 804.

[28] R. S. Anderssen, F. de Hoog, and J. D. Love, "Modes of Gaussian profile optical fibres," *Opt. Quantum. Electron.* Submitted.

Hill Shading and the Reflectance Map

BERTHOLD K. P. HORN

Abstract—Shaded overlays for maps give the user an immediate appreciation for the surface topography since they appeal to an important visual depth cue. A brief review of the history of manual methods is followed by a discussion of a number of methods that have been proposed for the automatic generation of shaded overlays. These techniques are compared using the reflectance map as a common representation for the dependence of tone or gray level on the orientation of surface elements.

Fig. 1. Block diagram of a system for the generation of relief shading. The gray-value is calculated by applying the reflectance map to the gradient estimate obtained by sampling neighboring points in the digital terrain model.

I. INTRODUCTION

OF THE SEVERAL ways of depicting surface form on maps, hill shading has the most immediate appeal and provides for quick comprehension of the topography. In this sense, hill shading is complementary to the use of contours, which provide accurate terrain elevations but require careful scrutiny if one is to ascertain the surface form. Shaded maps are most important when the interpreter's time is limited, as in aviation, for users that are not trained cartographers, and for small scale maps, where contours degenerate into messy tangles of lines.

Why then do we not see more shaded maps? One reason is the expense of the present manual methods of production, which require skilled artists with good insight into cartography. Working from existing contour maps, ridge and stream lines extracted from such maps, and at times aided also by aerial photography, they wield airbrushes, in what is a slow, tedious, and imprecise operation. Different individuals called upon to create such images by manual methods will inevitably produce different results because of the inherent subjective judgment. The resulting differences in expression of the terrain characteristics of the same surface at the same scale provide a particular problem for a map series, where adjoining sheets should match in terms of hill-shading symbology. This justifies investigation of an objective system which makes the treatment of all terrain forms comparable and repeatable.

Attempts at automation began with the notion that the gray levels used in the shading should derive from a model of how light might be reflected from a surface. Ignoring shadowing and mutual illumination effects, it seems clear that the reflected intensity will be a function of the local surface inclination. The choice of a method for calculating the gray tone based on the orientation of each surface element has however been the subject of occasionally bitter controversy for almost two centuries. Much of the difficulty stems from a lack of a common representation that would allow comparison of methods which appear at first glance to be incomparable.

The recently developed reflectance map constitutes such a common denominator. It is a simple device developed originally for work in machine vision where one is interested in
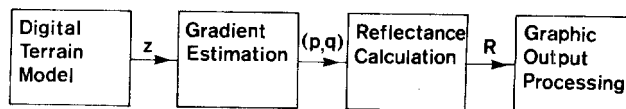
calculating surface shape from the gray levels in an image. This is clearly just the inverse of the problem of producing shaded pictures from a surface model. The reflectance map is a plot of apparent brightness versus two variables, namely the slope of the surface element in the west-to-east direction and the slope in the south-to-north direction. Producing a shaded overlay for a map then is simply a matter of calculating these two slopes for each surface element and looking up the appropriate gray level in the reflectance map (see Fig. 1). This is a very simple, local computation that can be carried out efficiently even on enormous databases. The resulting gray levels can then be fed to a graphic output device that will produce a continuous tone or halftone photographic transparency from the given stream of numbers.

What reflectance map is to be used? Careful comparison of more than a dozen proposed shading methods shows that some of the simplest provide a good impression of the shape of the surface. These experiments also show that the most commonly used assumptions about surface reflectance do not lead to the best results, while simple monotonic functions of the surface slope in the direction away from the assumed light source work admirably. What matters is the visual impression, not theoretical rules [1]. One goal of this paper is a review of various hill-shading methods that have been proposed in the past. Much can be learned from these efforts when they are evaluated in terms of the corresponding reflectance maps.

II. EARLY HISTORY OF HILL SHADING

Chiaroscuro, the technique of using light and shade in pictorial representation of three dimensional shapes, has been used by artists for many centuries. Leonardo da Vinci put it to good effect in his maps of Toscana, drawn in 1502 and 1503, that contained oblique shaded views of relief forms illuminated from the left [1]. Woodcuts of the area around Zürich in Switzerland drawn half a century later by Murer use shaded sideviews as well. Overhead views using relief shading appear for the first time in maps of the same area drawn a century after that by Gygers, but these then gave way to less desirable forms [1].

The choice of the representation for relief forms depend to a great extent on the available reproduction technology. Woodcuts and engraving methods lend themselves to linear forms, where brightness of an area in the reproduction is controlled by the spacing and width of darkened lines. Useful directional, textural effects can be generated by orienting these line frag-

ments, or hachures (Schraffuren), along lines of steepest descent. Crowding of such lines in steep areas may have given rise to notions of "steeper implies darker."

Lehmann proposed the first rigorous relationships [2], [3] between surface slopes and quantities measurable on the printed map. In 1799, when his method (Böschungsschraffen) was published anonymously, the techniques for measuring the surface accurately at a large enough number of points did not exist. Results of this first method of illustrating shape are in some ways analogous to those one might obtain by illuminating a model of the surface from above, an arrangement that gives rise to images that are difficult to interpret.

Partly as a result of this, an alternate form (Schattenschraffen) evolved [4]–[6], in which the line thickness is varied according to the orientation of the local surface patch with respect to a light source, usually assumed to be near the top left of the map when it is oriented properly for viewing. For maps with North at the top this corresponds to northwest. Surface patches sloping downward in that direction are portrayed with a light tone, while those sloping upward in that direction get a dark tone. Since flat areas have no lines of descent, they remain white. Aside from this defect, this method produces an image similar to one obtained by obliquely illuminating a diffusely reflecting model of the surface. Having flat areas appear white makes maps produced by this method a little difficult to interpret. They are nevertheless superior to those made by the earlier method, as evidenced for example by the "Dufourkarte" of Switzerland made between 1842 and 1864 using this approach [1]. These methods for portraying surface shape preceded the widespread use of contours [7], in part because the latter require detailed surface measurements that were not available before the advent of photogrammetry.

While lithography was invented by Alois Sneefelder in 1796, it found little application in cartography until around 1850. It permitted the production of multicolored maps, but more importantly, led to the use of halftones, destined to ultimately replace lines as a means of modulating the average reflectance in the printed map. W. H. Fox Talbot invented a photomechanical halftone process in 1852, but commercial success came only years after the patenting of the halftone screen by Frederick von Egloffstein in 1865, and the crossline screen of William A. Leggo in 1869.

Having access to these new reproduction schemes, Wiechel [8] developed shading methods (Schräglichtschummerung) to replace the use of hachures as described above. His fundamental paper, based in part on work by Burmester [9] on shaded pictures of *regular* surfaces, placed the field of hill-shading on a sound foundation. Wiechel discovered the error regarding flat surfaces, for example, and developed a graphic method for determining the gray value from contour interval and direction. Unfortunately, the means for controlled generation of halftones as a function of surface orientation did not then exist and his work was ignored for a long time.

III. HILL SHADING IN THIS CENTURY

Two methods based on lines, this time contours instead of lines of steepest descent, were explored by Kitirô Tanaka in the 1930's. His first method used the lines of intersection of the terrain surface with uniformly spaced, parallel, inclined planes [10], [11]. Tanaka's initiative gave rise to considerable discussion [12]–[19], partly in the form of an acrimonious debate [20]–[23]. His other method was based on portrayal of a terraced model of the terrain [24]–[26], an approach that

had been used previously, unguided by his careful analysis [27]–[29]. While line-based methods give rise to beautiful, easy to interpret maps, they cannot show the fine detail of surface topography possible with halftones and must be based on smoothed, generalized information such as contours. These lines also tend to interfere with others used to portray planimetric information.

A shaded overlay can also be produced by photographing an appropriately illuminated scaled model of the surface. If this model has a matte or diffusely reflecting surface, a map overlay of high quality will result provided attention is paid to the projection geometry. While this was an approach taken early on [27], it really only became practical in the 1950's with the introduction of milling machines that allow an operator to carve a model by tracing contours on an existing map [30]–[37]. This is still an expensive, slow process however, in part because of the manual work required to smooth out the resulting "terraced" model.

The Swiss school of cartography improved on earlier forms [28]–[30], [38], [39] and developed shading to a fine art, producing numerous outstanding maps in this time [40]–[48]. Imhof argues that automated methods, such as relief model photography, cannot produce results nearly as impressive, since the cartographer cannot easily influence the process [1]. The manual shading method is however slow and expensive, and consequently has not been used except for small areas and those of particular interest or military importance. One cannot expect, with significant areas of the world still not mapped at large scales, and the rising cost of labor, that shaded overlays produced this way will be used in many maps.

Yoéli [49]–[57] saw the potential of the digital computer in dealing with this dilemma. It is possible to implement Wiechel's method based on oblique illumination of a diffusely reflecting surface if terrain elevations can be read into a computer and suitable continuous tone output devices are available. Yoéli was hampered by the lack of such devices at that time. Blachut and Marsik tried to simplify the required calculations to the point where a computer might not even be required [58], [59]. Peucker helped popularize the whole idea of computer-based cartography [19], [60]–[62], and found a piecewise linear approximation to the equation for the brightness of a diffuse reflector that works well [61]. Many other interesting reports appeared during this time on the subject of hill-shading, too numerous to mention individually [63]–[70].

Brassel [71]–[74] took Imhof's admonitions seriously and tried to implement as much as had been formalized of the "Swiss manner." With the output devices available to him at that time it was not easy to judge whether the added complexity was worth the effort. All of these computer based methods require detailed digital terrain models. The storage capacity and techniques for handling this kind of information now exist [32], [75]–[81] as do the photographic output devices needed. There has been significant progress, too, in the automatic generation of digital terrain models directly from aerial photographs [81]–[87], partly as a byproduct of work on orthophoto generation [88]–[91]. More compact and appropriate representations for these terrain models are under investigation [92]–[95], as are alternate methods for relief portrayal such as block diagrams [96]–[102].

Considerable progress has been made recently in the computer graphics area in the portrayal of regular objects with simple surfaces [103]–[116]. Early models for the reflection of light from matte surfaces [117]–[120] are being elaborated, including some for the material on the lunar surface [121]–

[130]. In this context, work on models of the microstructure of surfaces is relevant [131]-[136]. In a recent effort in the machine vision area, a method was developed for portraying the dependence of brightness on surface orientation using the so-called reflectance map [137]-[141]. The reflectance map can be determined if the detailed geometric dependence of reflection from the surface [142], [143] and the distribution of light sources are known. Alternatively, it can be found empirically, or derived directly by analyzing the interaction of light rays with the surface microstructure.

As a result of the development of the reflectance map, the availability of detailed digital terrain data, small computers able to perform the simple calculations required, and geometrically accurate gray-level output devices, we may say that automatic hill shading has come of age.

IV. Digital Terrain Models

For many applications of cartographic data it is useful to have machine-readable surface representations. Such terrain models are used for example in the design of roads and in order to determine the region irradiated by a radio frequency antenna. Initially, digital terrain models were generated manually by interpolation from existing contour maps. This is a tedious error-prone process producing a digitized version of the surface represented by the contours, which in turn is a smoothed, generalized version of the real surface.

The contour information on topographic maps is produced by manual scanning of stereo pairs of aerial photographs. Today, fortunately, stereocomparators often come equipped with coordinate readouts that allow the extraction of information needed for the generation of digital terrain models [144]. Conveniently taken during orthophoto generation [88]-[91], the data tends to be accurate and detailed. Even more exciting is the prospect for machines that achieve stereo fusion without human help [81]-[87], since they will lead to the automatic production of digital terrain models. In the past such machines had difficulties dealing with uniform surfaces such as lakes, featureless surfaces, large slopes, and depth discontinuities, as well as broken surfaces, such as forest canopies. This is apparently still true when aerial photographs are used with disparities large enough to ensure high accuracy.

Various representations can be chosen for the surface elevation information. Series expansion, a weighted sum of mathematical functions such as polynomials, Gaussian hills or periodic functions may be used. These tend to be expensive to evaluate however and not accurate in approximating surfaces that have slope discontinuities. This is important for many types of terrain, at all but the largest scales. Perhaps the simplest surface representation is an array of elevations $\{z_{ij}\}$ based on a fixed grid, usually square. Determining the height at a particular point is simple and the interchange of terrain models between users is easy since the format is so trivial. One disadvantage of this kind of surface representation is the high redundancy in areas where the surface is relatively smooth. The illustrations in this paper are based on digital terrain models consisting of arrays of elevation values.

Methods that achieve considerable data compression by covering the surface with panels stretched between specially chosen points have been developed [92]-[95]. These exploit the fact that real geographical surfaces are not arbitrary sets of elevations but have definite structure and regularity. Such representations may

voluminous ones, if users can be persuaded to accept the greater programming complexities involved.

Digital terrain models may also be referred to as digital *elevation* models if they contain no information other than the elevation values.

V. The Reflectance Map

The human visual system has a remarkable ability to determine the distance to objects viewed, as well as their shape, using a variety of depth cues. One such cue is shading, the dependence of apparent brightness of a surface element on its orientation with respect to the light source(s) and the viewer. Without this particular depth cue we would be hard pressed to interpret pictures of smooth, opaque objects such as people, since other cues like stereo disparity and motion parallax are absent in a flat, still photograph. It can be shown that shading contains enough information to allow the observer to recover the shape. In fact, a computer program has been developed that can do this using a single digitized image [137].

Such work in the area of machine vision has led to a need to model the image-forming process more carefully [138]. The input to the visual sensing system is image irradiance, which is proportional to scene radiance (here loosely called apparent brightness) [140]. Scene radiance in turn can be related to the underlying geometric dependence of reflectance of the surface material and the distribution of light sources [142], [143]. Here we concentrate on the dependence of scene radiance on the orientation of the surface element. Shaded overlays for maps are interpreted by the viewer using the same mechanism normally employed to determine the shape of three-dimensional surfaces from the shading found in their images. Thus shaded overlays should be produced in a way that emulates the image-forming process, one in which brightness depends on surface orientation. This is why the reflectance map, which captures this dependence, is useful in this endeavor.

Consider a surface $z(x, y)$ viewed from a great distance above (see Fig. 2). Let the x-axis point to the east, the y-axis north, and the z-axis straight up. The orientation of a surface element can be specified simply by giving its slope p in the x (west-to-east) direction and its slope q in the y (south-to-north) direction. The slopes p and q are the components of the gradient vector, (p, q). The apparent brightness of a surface element $R(p, q)$ depends on its orientation, or equivalently, the local gradient. It is convenient to illustrate this dependence by plotting contours of constant apparent brightness on a graph with axes p and q. This reflectance map [138] provides a graphic illustration of the dependence of apparent brightness on surface orientation. The pq-plane, in which the reflectance map is drawn, is called the gradient space, because each point in it corresponds to a particular gradient.

Surface orientation has two degrees of freedom. We have chosen here to specify the orientation of a surface element by the two components of the gradient. Another useful way of specifying surface orientation is to find the intersection of the surface normal with the unit sphere. Each point on the surface of this Gaussian sphere again corresponds uniquely to a particular surface orientation. If the terrain is single-valued, with no overhangs, all surface normals will point more or less upwards and pierce the Gaussian sphere in a hemisphere lying above an equator corresponding to the horizontal plane. Gradient space happens to be the projection of this hemisphere from the center of the sphere onto a plane tangent at the upper
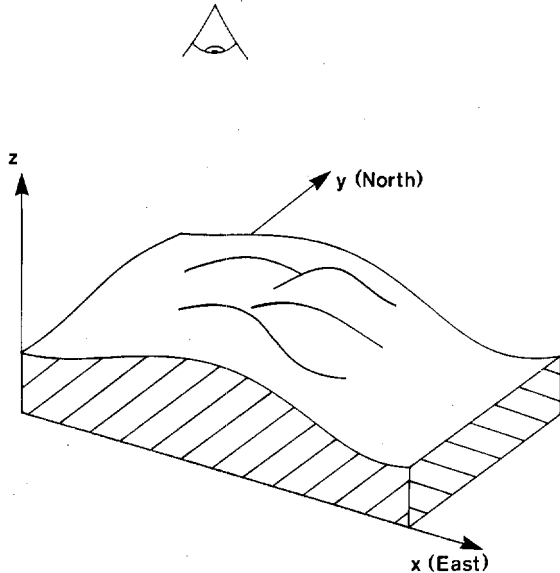
Fig. 2. Coordinate system and viewing geometry. The viewer is actually at a great distance above the terrain so that the projection is orthographic.

While we will not use this representation in the calculation of relief shading, it is helpful in understanding previous attempts at graphical portrayal of the dependence of apparent brightness on surface orientation. The first such method was developed by Wiechel more than a century ago [8]. His brilliant analysis appears to have been largely ignored partly because it depended on mathematical manipulations that may have been inaccessible to many of the intended users. Later, Kitirô Tanaka invented another method showing the variation of apparent brightness with surface gradient [10], [11], [24], [25]. This second precursor of the reflectance map also appears to have found little following.

VI. POSITION DEPENDENT EFFECTS

Since the reflectance map gives apparent brightness as a function of local surface gradient only, it does not take into account effects dependent on the *position* of the surface element. One such effect is illumination of one surface element by another. Fortunately this mutual illumination effect is small unless surface reflectance is quite high [138]. It is not known whether mutual illumination effects aid or hinder the perception of surface shape. They are difficult to calculate and so have not been emulated in work on hill-shading.

Another position dependent effect on apparent brightness is the blocking of light by one portion of the surface before it reaches another. Cast shadows can be calculated by determining which surface elements are not visible from the point of view of the light source [139]. Shadows cast by one complicated shape on another are hard to interpret however and apparently detract from the visual quality of shaded overlays [1], [35], [36]. They are thus rarely included.

Scattering of light by air molecules and aerosol particles changes the apparent brightness of a surface element viewed through the atmosphere. The brightness is shifted towards a background value equal to the brightness of an infinitely thick layer of air. The difference between the brightness and the background value decreases with the thickness of the gaseous layer through which the surface is viewed [145]. The resulting reduction in contrast as a function of distance is referred to as

aerial perspective and can be a useful depth cue, although there is no general agreement that it aids the perception of surface shape. It has been used at times by map-makers and can be modeled easily [1], [71], [73], [74]. The effect has not been added to any of the hill-shading schemes presented here in order to simplify comparisons.

VII. WHERE DO REFLECTANCE MAPS COME FROM?

A reflectance map may be based on experimental data. One can mount a sample of the surface in question on a goniometer stage and measure its apparent brightness from a fixed viewpoint under fixed lighting conditions while varying its orientation. Instead, one can take a picture of a test object of known shape and calculate the orientation of the corresponding surface element for each point in the image. The reflectance map is then obtained by reading off the measured brightness there.

Alternatively, one may use even more detailed information about light reflection from the surface. The bidirectional reflectance distribution function (BRDF) describes how bright a surface will appear viewed from one specified direction when illuminated from another specified direction [142], [143]. By integrating over the given light source distribution one can calculate the reflectance map from this information [140]. Crudely speaking, the reflectance map is like a "convolution" of the BRDF and the source-radiance distribution.

Most commonly, reflectance maps are based on phenomenological models, rather than physical reality. The so-called Lambertian surface, or perfect diffuser, for example, has the property that it appears equally bright from all viewing directions. It also reflects all light, absorbing none. It turns out that these two constraints are sufficient to determine uniquely the BRDF of such a surface, and from it the reflectance map, provided the positions of the light sources are also given. Some reflectance maps are based on mathematical models of the interaction of light with the surface. Such models tend to be either too complex to allow analytic solution or too simple to represent real surfaces effectively. Nevertheless some have come quite close to predicting the observed behavior of particular surfaces [134]–[136].

Here, new reflectance maps will be determined, based on proposed methods for producing shaded overlays for maps. Their derivation will not depend on an understanding of the image-formation process or the physics of light reflection. Instead, they will require an analysis of how the brightness of a point in the overlay depends on the gradient of the underlying geographical surface.

Which reflectance map should be used? The answer to this question must depend on the quality of the impression a viewer gets of the shape of the surface portrayed. Various methods for producing shaded overlays can be compared by evaluating sample products and classified according to the corresponding reflectance maps. It will become apparent that in this way general conclusions can be drawn about a new method just by inspecting its reflectance map.

VIII. NORMALIZATION OF GRAY TONE

A picture made by applying varying amounts of light absorbing substances, such as ink, to an opaque, diffusely reflecting material like paper, has a limited dynamic range. Reflectance is limited at the low end by the properties of the ink and at the high end by the paper, which will at most reflect all the light incident upon it, unless it fluoresces. The diffuse reflectance is thus always less than or equal to one. Similarly, if

absorbing substances are used on a transparent substrate, a limit applies, since transparency cannot be larger than one.

The problem of fitting a given image into the available dynamic range is fundamental to all methods of reproduction. A normalization is applied so that the maximum apparent brightness to be reproduced is represented by a reflectance of one (or whatever the maximum is for the paper being used). This scaling will have to be applied whenever relief shading is based on models of image-formation by light reflected from the terrain surface.

IX. Gradient Estimation

The apparent brightness of a surface element depends on its orientation with respect to the viewer and the light source. The orientation of the surface element is described fully by a surface normal, or equivalently by the gradient. The components of the gradient are the slopes p (in the west-to-east direction) and q (in the south-to-north direction). These slopes have to be estimated from the array of terrain elevations. It is convenient to use a short hand here for elevations in the neighborhood of a particular point (see Fig. 3). In the context of a single point at discrete coordinate (i, j), we will denote the elevation at that point by z_{00}, while elevations of the adjacent grid points to the west and east will be called z_{-0} and z_{+0}, respectively. Similarly, elevations at the points to the south and north will be denoted z_{0-} and z_{0+}.

The simplest estimates for the slope p might be

$$p_+ = (z_{+0} - z_{00})/\Delta x$$

and

$$p_- = (z_{00} - z_{-0})/\Delta x$$

where Δx is the grid interval in the west-to-east direction, expressed in the same units as the terrain elevations. These estimates are biased, actually estimating the slope half a grid interval to the right and left of the central point, respectively. Their average however, the central difference, is unbiased,

$$p_c = (z_{+0} - z_{-0})/2\,\Delta x.$$

Numerical analysis [146]-[149] teaches us that for certain classes of surfaces an even better estimate is obtained using a weighted average of three such central differences,

$$p_w = [(z_{++} + 2z_{+0} + z_{+-}) - (z_{-+} + 2z_{-0} + z_{--})]/8\Delta x.$$

Symmetrically, one can estimate the south-to-north slope,

$$q_w = [(z_{++} + 2z_{0+} + z_{-+}) - (z_{+-} + 2z_{0-} + z_{--})]/8\Delta y.$$

These expressions produce excellent estimates for the components of the gradient of the central point. The results depend on elevations in a 3 × 3 neighborhood, with individual elevation values weighted less than they are in the simpler expression for the central difference. This has the advantage that local errors in terrain elevation tend not to contribute as heavily to error in slope. At the same time, more calculations are required and three rows of the digital terrain model have to be available at one time.

Care has to be taken to avoid corruption of the slope estimates by quantization noise in the elevation values. Numerical problems due to the division of small integers may result when a terrain model is too finely interpolated, with limited vertical resolution. If it is necessary to generate many pixels in the output, it is better to interpolate the gray values produced by the shading algorithm corresponding to the

z_{-+}	z_{o+}	z_{++}
z_{-o}	z_{oo}	z_{+o}
z_{--}	z_{o-}	z_{+-}

Fig. 3. Short-hand notation for elevations of neighboring points.

X. Gradient Smoothing Effects

More complicated slope estimators than the ones described tend to introduce a *smoothing effect*, as can be seen by applying them near points of discontinuity in slope. To illustrate this more clearly, consider two horizontal smoothing operations H+ and H− that modify the terrain model as follows:

$$\text{H+: } z'_{00} = (z_{00} + z_{+0})/2$$

and

$$\text{H−: } z'_{00} = (z_{-0} + z_{00})/2.$$

It can now be seen that the central difference slope estimate p_c on the original terrain model, equals the biased estimate p_+ calculated from the terrain model smoothed using H−, or, equivalently, the biased estimate p_- calculated from the terrain model smoothed using H+. Next consider two vertical smoothing operation V+ and V− in which the terrain model is modified as follows:

$$\text{V+: } z'_{00} = (z_{00} + z_{0+})/2$$

and

$$\text{V−: } z'_{00} = (z_{0-} + z_{00})/2.$$

The complicated slope estimate p_w can be shown to produce the same result as the first difference p_+ calculated from a terrain model smoothed by applying H−, V+, and V−. Similarly the slope estimate q_w equals q_+ calculated from a terrain model smoothed by applying V−, H+, and H− (actually, since all of these operations are linear, their order can be arbitrarily rearranged). Perhaps any "smoothing" desired should be done as a separate editing operation, combined with the removal of "glitches" from the digital elevation model, rather than as part of the slope estimation. Also for terrain models of relatively limited size this smoothing may be undesirable. Some other slope estimators are simpler and introduce less smoothing. For example one can combine two biased estimates of the slope to get,

$$p_{1/2} = [(z_{++} + z_{+0}) - (z_{0+} + z_{00})]/2\Delta x$$

and symmetrically,

$$q_{1/2} = [(z_{++} + z_{0+}) - (z_{+0} + z_{00})]/2\Delta y.$$

Here the average gradient in the top-right quadrant (z_{00}, z_{+0}, z_{++}, z_{0+}) rather than at the central point is being estimated, using elevations in a 2 × 2 neighborhood only. For the graphic illustrations presented here, the expressions for $p_{1/2}$ and $q_{1/2}$ were used to estimate the gradient.

At this time some terrain models are still produced by hand and have rather limited size. Rather than smoothing the terrain, one may wish to increase apparent resolution by some means. This can be done quite effectively by combining biased slope estimates (see Fig. 4). For every point in the terrain model corresponding to the
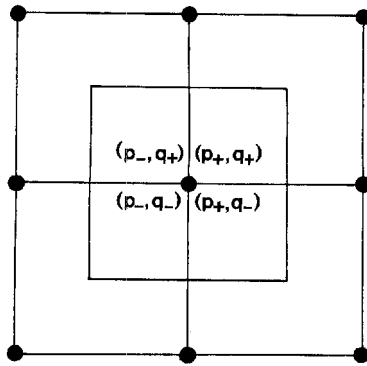
Fig. 4. Combinations of biased slope estimates can be used to plot four times as many gray-tones as there are elevations values in the terrain model. The limited amount of data in a small terrain model may be stretched this way to produce reasonably detailed hill-shading output.

four quadrants around it. Each is based on a different combination of the slope estimates (p_- or p_+) and (q_- or q_+) as appropriate for that quadrant. No miracles should be anticipated; this method cannot create information where there is none, but it can stretch what is available to its limits.

More complicated slope estimators than those discussed here do not seem called for, since the simple ones shown produce excellent results. Furthermore, estimators having wider support, while known to be more accurate for certain classes of functions such as polynomials, may perform worse on typical terrain with its discontinuities in slope along ridge and stream lines.

It has been cartographic practice to assume a light source in the northwest at a 45° elevation above the horizon. It is helpful in this case to introduce a rotated coordinate system as described in Appendix A.

XI. EXAGGERATION OF TERRAIN ELEVATIONS

Compared to objects of a size that allow for easy manipulation by a human observer, the surface of the earth is in many places, though not everywhere, rather flat. The range of slopes is often so small as to cause disappointment with correctly proportioned models, so that height is often exaggerated in physical models. Similarly, shading based on models of light reflection from a surface tends to have undesirably low contrast. Here too terrain elevations may be exaggerated for all but the most mountainous regions. This is equivalent to multiplication of the components of the gradient by a constant factor, and corresponds to a simple transformation of the reflectance map. For reflectance maps based on reflection of light originating from an assumed source, a similar effect can often be achieved by a decrease in the elevation of the source. For flat surfaces the source may be lowered to a mere 10° or 20° above the horizon, where normally it might be at 45°.

XII. PRODUCING SHADED OVERLAYS

The generation of shaded images from a digital terrain model using the reflectance map is straightforward (see Fig. 1). For each point in the terrain model the local gradient (p, q) is found. The reflectance map then provides the appropriate brightness $R(p, q)$, to be plotted on a suitable gray-level output device. All computations are local and can be accomplished in a single pass through the image.

To illustrate these ideas a simple program is shown (see Fig. 5) that does not incorporate any of the elaborations

```
procedure SHADING(N, M, DX, DY); integer N, M; real DX, DY;

  begin array Z[0:N,0:M], B[0:N—1,0:M—1];

    real procedure PE(I, J); integer I, J;
    PE := (Z[I,J] + Z[I—1,J] — Z[I,J—1] — Z[I—1,J—1]) / (2.0 × DX);

    real procedure QE(I, J); integer I, J;
    QE := (Z[I,J] + Z[I,J—1] — Z[I—1,J] — Z[I—1,J—1]) / (2.0 × DY);

    real procedure R(P, Q); real P, Q;
    RM := MAX(0.0, MIN(1.0, (1.0 + P — Q) / 2.0));

    <read terrain elevations into array Z> ·

    for J := 1 step 1 until M—1 do
      for I := 1 step 1 until N—1 do
        B[I—1,J—1] := RM(PE(I, J), QE(I, J));

    <write brightness values from array B>

  end
```

Fig. 5. Simple program to generate shaded output from a terrain model.

described later on. Two arrays are used, Z to store the terrain elevations and B to store the calculated brightness values. The latter has one row and one column fewer, since its entries correspond to points lying *between* those in the elevation array (the formulas for $p_{1/2}$ and $q_{1/2}$ are used). The spacing of the underlying grid is DX in the west-to-east direction and DY in the south-to-north direction. The procedures $PE(I, J)$ and $QE(I, J)$ estimate the slopes, while the procedure $RM(P, Q)$ calculates the corresponding brightness using a particularly simple reflectance map. The resulting values range from 0.0 (black) to 1.0 (white) and have to be scaled appropriately before they can be fed to a particular gray-level output device.

Typical terrain models are quite large and may exceed allowable array storage limits or even the address space of a computer. Fortunately only two (or three) rows of the terrain model are needed for the estimation of the local slopes. The program given can be easily modified to read the terrain model, and to write the calculated gray values, one line at a time. This makes it possible to deal with terrain models of essentially arbitrary size.

Next one should note that terrain models typically are stored using integer (fixed point) representation for elevations to achieve compactness and because elevations are only known with limited precision (an elevation may be given in meters as a 16-bit quantity for example). Similarly, gray values to be sent to a graphic output device are typically quantized to relatively few levels because of the limited ability of the human eye to discern small brightness differences and the limited ability of the device to accurately reproduce these (a typical output device may take values between 0 and 255). The calculations can thus be carried out largely in integer (fixed point) arithmetic and even a simple computer is adequate.

XIII. USE OF LOOKUP TABLES

Some of the formulas for reflectance maps discussed later on are quite elaborate and it would seem that a lot of computation is required to produce shaded output using them. Fortunately it is possible to make the amount of computation equally small in all cases by implementing the reflectance map as a lookup table, which is computed at the beginning.

Since elevations are quantized, so are the estimates of slope. It is therefore not necessary that one be able to determine the apparent brightness for all possible values of the gradient (p, q). Further, it is reasonable to place an upper limit on slope, so that only a finite number of possible values can occur (For example, if slopes between -1.55 and $+1.60$ are considered, in increments of 0.05, then there are only 64 possibilities for p and 64 for q, and a lookup table with 4096 entries can be used). A second justification for the use of a lookup table is the quantization of the gray values produced. It makes little sense to calculate the apparent brightness with very high precision only to coarsely quantize the result. A convenient rule of thumb is that the number of possible discrete values for each gradient component need not be more than the number of gray levels available from output device. The final choice of quantization must take into account both of the above considerations.

One can separate the estimation of slope from the calculation of gray value, and produce an intermediate file of coded surface gradient values. This file need not be larger than the original terrain model if the gradient is quantized properly (if p and q can each take on 64 values, each gradient can be encoded as a 12 bit value). The code in the lookup table can be based on ways of expression surface orientation other than in terms of components of the surface gradient. In any case, a file of surface orientation codes can be fed through a lookup table procedure to produce the final output. In this fashion different reflectance maps, encoded as different lookup tables, can be applied to a terrain model easily, with little more effort than reading and writing a file. The illustrations here were produced this way.

Many gray-level raster displays have a translation table between the image memory and the digital-to-analog converter driving the cathode ray tube intensity control. The quantized, packed reflectance map can be loaded into this lookup table, while the image memory is loaded with the coded slope matrix. This allows one to view the same terrain with a variety of assumed reflectance properties simply by reloading the translation table, which is small compared to the image memory.

XIV. TAXONOMY OF REFLECTANCE MAPS

Here we have discussed some of the issues one is likely to encounter when developing a program that produces shaded output. In the remainder of this paper we will analyze a number of proposed hill-shading methods in terms of their equivalent reflectance maps. Notational tools will be introduced as they are needed. Rather than proceed in strict historic order, we will discuss relief shading methods in the following groups:

1) rotationally symmetric reflectance maps—gray tone depends on slope only;
2) methods based on varying line spacing or thickness to modulate average reflectance;
3) ideal diffuse reflectance and various approximations thereto;
4) gray tone depends only on the slope of the surface in the direction away from the assumed light source;
5) methods depending on more elaborate models of diffuse reflectance from porous material, such as that covering the lunar surface;
6) models for gloss and lustrous reflection—smooth surface, extended source and rough surface, point source.

XV. AVERAGE REFLECTANCE OF EVENLY SPACED DARK LINES

Some early methods for hill shading achieve the desired control of gray tone by varying the spacing between printed lines. One advantage of this approach is the ease with which such information can be printed, since it is not necessary to first screen a continuous tone image. One disadvantage is the confusion created when the lines used for this purpose are layed on top of others portraying planimetric information. While the directional textural effects of the lines are important in conveying information about shape, we concentrate here on the average reflectance.

Consider inked lines with reflectance r_b covering an area of paper with reflectance r_w (see Fig. 6). The ratio of the area covered by ink to the area not covered is the same as the ratio of the width of the lines to the width of the uninked spaces. This in turn equals b/w, where b is the width of the inked line and w the width of the uninked space measured along any direction not parallel to the lines. If we ignore diffusion of light in the paper, then the average reflectance of the surface is

$$R = (w r_w + b r_b)/(w + b)$$

or

$$R = r_w - b(r_w - r_b)/(w + b).$$

If, for example, the paper reflects all the incident light, and the ink none, then $r_w = 1$ and $r_b = 0$, so that $R = 1 - b/(w + b)$.

XVI. SLOPE OF THE SURFACE IN AN ARBITRARY DIRECTION

In the calculation of gray value produced by some methods of hill shading it is necessary to know the slope of the surface in an arbitrary direction, given the slope p in the west-to-east direction and the slope q in the south-to-north direction. Note that p and q are the first partial derivatives of the elevation z with respect to x and y, respectively. Consider taking an infinitesimal step dx in the x direction and an infinitesimal step dy in the y direction. The change in elevation dz is given by

$$dz = p \, dx + q \, dy.$$

Along a contour line for example, the elevation is constant, so that for a small step $dx = a \, ds$ and $dy = b \, ds$, we can write:

$$(p, q) \cdot (a, b) \, ds = 0$$

where "$\cdot$" denotes the dot-product. The local direction of the contours, (a, b) is of course perpendicular to the local gradient (p, q).

Now consider taking a small step in an arbitrary direction (p_0, q_0) say. That is let $dx = p_0 \, ds$ and $dy = q_0 \, ds$. The length of the step, measured in the xy-plane is,

$$\sqrt{p_0^2 + q_0^2} \, ds.$$

While the change in elevation is,

$$dz = (p_0 p + q_0 q) \, ds.$$

Consequently the slope, change in elevation divided by length of the step, is

$$s = (p_0 p + q_0 q)/\sqrt{p_0^2 + q_0^2}.$$

If we let α be the angle between the vector (p_0, q_0) and the
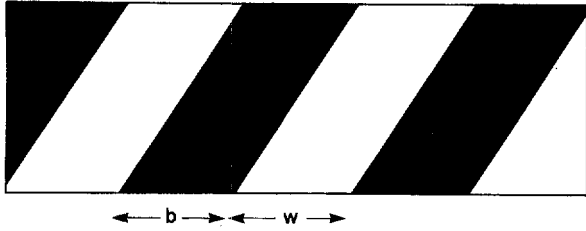
Fig. 6. Magnified portion of surface covered with lines. The average tone depends on the fractional area covered by the lines, as well as the reflectance of the paper and the ink.

x-axis, then, the above can also be written,

$$s = p \cos \alpha + q \sin \alpha.$$

The direction in the xy-plane in which the slope is maximal can be found by differentiating with respect to α. The direction of steepest ascent is (p, q) and the maximum slope equals $\sqrt{p^2 + q^2}$.

XVII. LEHMANN'S BÖSCHUNGSSCHRAFFEN (A)

One of the earliest methods for depicting surface shape using a form of shading is that of Lehmann [2], [3]. Illustrations based on *ad hoc* scales of increasing darkness as a function of slope ("Schwärzegradscalen") had been published before, but there was no systematic analysis of this approach until the appearance of an anonymous publication attributed to Lehmann. In his method, short lines in the direction of steepest descent, called hachures, are drawn with spacing and thickness specified by rules that ensure that the fractional area darkened is proportional to the angle of inclination of the surface θ. That is, steeper implies darker. The lines merge, producing a continuous black area, when θ exceeds some maximum value θ_0, typically $45°$ or $60°$. The slope of the surface equals the tangent of the angle of inclination or "dip." Using the expression for the slope in the direction of steepest ascent, we get,

$$\tan \theta = \sqrt{p^2 + q^2}.$$

Consequently, the average reflectance is,

$$R(p, q) = r_w - (r_w - r_b) \tan^{-1} \sqrt{p^2 + q^2}/\theta_0.$$

When the angle of inclination exceeds the maximum, the lines coalesce and $R(p, q) = r_b$. We can also write the above in another form,

$$R'(\theta, \phi) = r_w - (r_w - r_b)(\theta/\theta_0).$$

Here, ϕ, the azimuth of the direction of steepest descent, does not appear in the formula on the right, since apparent brightness in this case depends only on the magnitude of the slope. The direction *and* magnitude of the surface gradient can be found from a map prepared according to Lehmann's rules. The direction of steepest descent lies along the hachures, while the slope is directly related to the average tone that results from the width and spacing of these lines. In analyzing his method we have concentrated on calculating the average reflectance produced in the printed product. It should be pointed out that this method also gives rise to textural effects that will not be discussed.

Another interesting aspect of Lehmann's method is that the lines or hachures were drawn starting on one contour and ending on the next. This greatly contributed to the later development of the contour representation (Isohypsen) for terrain
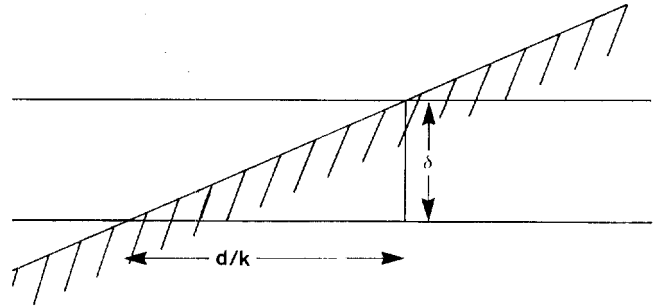
Fig. 7. Spacing between successive contour lines along a given direction on the topographic map.

surfaces, that was to ultimately replace most of these early attempts at portraying surface shape [7].

XVIII. CONTOUR DENSITY (B)

Another method is based on the observation that lines on a contour map are more crowded in steep areas and that this crowding leads to darkening of tone or average gray value. This side effect may be helpful in visually conveying information about the nature of the surface. In order to calculate the dependence of the average local reflectance on the gradient (p, q), we have to determine the spacing of contour lines on the map. We assume that the surface is locally smooth and can be approximated by a plane, at least on the scale of the spacing between contour lines (if this is not the case, aliasing, or undersampling problems occur in any case).

Consider a portion of the surface with slope s in some direction not parallel to the contour lines (see Fig. 7). Assume that the map scale is k and the vertical contour interval δ. Then it is clear that the spacing between contours on the map d can be obtained from the formula for slope,

$$s = \delta/(d/k).$$

If we take the cross section of the surface in the direction of steepest ascent, then $s = \sqrt{p^2 + q^2}$. As a result we can write,

$$d = k\delta/\sqrt{p^2 + q^2}.$$

On the map, $d = b + w$. That is, the spacing between contours is the sum of the width of the contour lines and the width of the blank spaces between them. The average reflectance then is,

$$R(p, q) = r_w - (b/k\delta)(r_w - r_b)\sqrt{p^2 + q^2}.$$

The result can also be expressed as,

$$R'(\theta, \phi) = r_w - (b/k\delta)(r_w - r_b) \tan \theta$$

where θ is the inclination of the surface. The above expressions only hold if w is not negative. When the slope is too steep, contour lines overlap, and the average reflectance is simply equal to r_b. In the special case that $r_w = 1$ and $r_b = 0$, the above simplifies to,

$$R(p, q) = 1 - (b/k\delta)\sqrt{p^2 + q^2}.$$

Typically $(b/k\delta)$ may equal 1 or $1/\sqrt{3}$.

XIX. DIFFUSE SURFACE UNDER VERTICAL ILLUMINATION (C)

The methods discussed so far produce tones that depend on the magnitude of the gradient only, not its direction. This is

similar to the effect one would obtain if a physical model of the terrain was illuminated vertically, with the light source placed near the viewer. An ideal diffusing surface has an apparent brightness that is proportional to the cosine of the incident angle i as discussed later. This is the angle between the direction of the incident rays and the local normal, which, in the case of vertical illumination, is just θ. Therefore,

$$R'(\theta, \phi) = \cos \theta$$

or

$$R(p, q) = 1/\sqrt{1 + p^2 + q^2}.$$

Instead of illumination from a point source, one may consider the effect of a distributed source. A uniform hemispherical source illuminating a diffusely reflecting surface leads to a result of the following form [140],

$$R'(\theta, \phi) = \cos^2 (\theta/2) = \tfrac{1}{2} + \tfrac{1}{2} \cos \theta$$

or

$$R(p, q) = (1 + 1/\sqrt{1 + p^2 + q^2})/2.$$

This reflectance map leads to flatter, even less interpretable pictures, since the range of reflectances has been halved and all reflectances have been shifted upwards by a half. In the derivation of the formula above, reflection from the surrounding terrain surface is ignored. If the terrain surface diffusely reflects a fraction ρ of the incident light, the constant term in the above expression is increased from $\tfrac{1}{2}$ to $(1 + \rho)/2$, while the coefficient of $\cos \theta$ decreased from $\tfrac{1}{2}$ to $(1 - \rho)/2$. It is at times suggested that a component of surface brightness due to distributed illumination from the sky be added to that resulting from oblique illumination. This however typically detracts from the shaded result, rather than improving it.

The methods discussed so far give rise to rotationally symmetric reflectance maps, that can be described adequately by a single cross-section, showing tone versus slope [1], [35], [36]. This representation has sometimes been misused for asymmetric reflectance maps, where it does *not* apply. Rotationally symmetric reflectance maps produce shaded images that are difficult to interpret. Moving the assumed light source away from the overhead position gives rise to better shaded map overlays, but forces us to introduce some new concepts.

XX. THE SURFACE NORMAL

The surface normal is a vector perpendicular to the local tangent plane. The direction of the surface normal n can be found by taking the cross-product of any two vectors parallel to lines locally tangent to the surface (as long as they are not parallel to each other). We can find two such vectors by remembering that the change in elevation when one takes a small step dx in the x-direction is just $dz = p \, dx$, while the change in elevation corresponding to a step dy in the y-direction is $dz = q \, dy$. The two vectors, $(1, 0, p) \, dx$ and $(0, 1, q) \, dy$, are, therefore, parallel to lines tangent to the surface and so their cross-product is a surface normal

$$n = (1, 0, p) \times (0, 1, q) = (-p, -q, 1).$$

Note that the gradient (p, q) is just the (negative) projection of this vector on the xy-plane. A unit surface normal N can be obtained by dividing the vector n by its magnitude $n = \sqrt{1 + p^2 + q^2}$.

While it is convenient to specify directions as vectors, it is at times helpful to use spherical coordinates instead. A direction
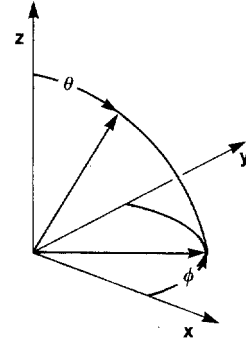
Fig. 8. Definition of the azimuth angle ϕ and the zenith angle θ. Here, azimuth is measured counter-clockwise from the x-axis in the xy-plane, while the zenith angle is measured from the z-axis.

can then be given as an azimuth angle ϕ measured anticlockwise from the x-axis, and a polar or zenith angle θ (see Fig. 8). (In navigation, the azimuth angle is usually measured clockwise from north, and the elevation angle is given instead of the zenith angle. These are just the complements of the angles used here.) The unit vector in the direction so defined equals,

$$N = (\cos \phi \sin \theta, \sin \phi \sin \theta, \cos \theta).$$

To find the azimuth and zenith angle of the surface normal we identify components of corresponding unit vectors. Then,

$$\sin \phi = -q/\sqrt{p^2 + q^2}$$

and

$$\cos \phi = -p/\sqrt{p^2 + q^2}$$

while

$$\sin \theta = \sqrt{p^2 + q^2}/\sqrt{1 + p^2 + q^2}$$

and

$$\cos \theta = 1/\sqrt{1 + p^2 + q^2}.$$

Conversely,

$$p = -\cos \phi \tan \theta$$

and

$$q = -\sin \phi \tan \theta.$$

We will find it convenient to use both vector and spherical coordinate notation to specify direction.

XXI. POSITION OF THE LIGHT SOURCE

The reflectance maps discussed so far are rotationally symmetric about the origin, only the magnitude of the gradient, not its direction affecting the resulting gray value. This corresponds to a situation where the light source is at the viewing position. Most hill-shading methods have the assumed light source in some other position, typically in the northwest, with a zenith angle of around 45° ($\theta_0 = 45^\circ$, $\phi_0 = 135^\circ$). The unit vector,

$$S = (\cos \phi_0 \sin \theta_0, \sin \phi_0 \sin \theta_0, \cos \theta_0)$$

points directly at the light source. A surface element will be illuminated maximally when the rays from the light source strike it perpendicularly, that is, when the surface normal points at the light source. By identifying components in the expression for the surface normal $n_0 = (-p_0, -q_0, 1)$ with those in the expression for the vector pointing at the source

one finds that the components of the gradient of such a surface element are,

$$p_0 = -\cos \phi_0 \tan \theta_0$$

and

$$q_0 = -\sin \phi_0 \tan \theta_0.$$

When the source is in the standard cartographic position, this means,

$$p_0 = 1/\sqrt{2}$$

and

$$q_0 = -1/\sqrt{2}.$$

This standard position for the assumed light source was probably chosen because we are used to viewing objects lighted from that direction [1]. When we look at nearby objects in front of us, our body blocks the light arriving from behind us. Further, when writing on a horizontal surface, many of use find our right hand blocking light coming from that direction. We thus often arrange for light sources to be to the left, in front of us. While we can certainly interpret shading in pictures where the light source is not in this standard position, there seems to be a larger possibility of depth reversal in that case, particularly if the object has a complex, unfamiliar shape.

Returning now to the specification of the position of the light source, we find two identities that will be helpful later.

$$\cos (\phi - \phi_0) = (p_0 p + q_0 q)/[\sqrt{p^2 + q^2} \sqrt{p_0^2 + q_0^2}]$$

$$p_0 p + q_0 q = \tan \theta \tan \theta_0 \cos (\phi - \phi_0).$$

It also follows that the slope of the surface in the direction (p_0, q_0) away from the light source is,

$$s = \tan \theta \cos (\phi - \phi_0).$$

XXII. TANAKA'S ORTHOGRAPHICAL RELIEF METHOD (D)

A method proposed by Kitirô Tanaka in 1930 [10], [11], involves drawing the lines of intersection of the surface with evenly spaced *inclined* planes. These planes are oriented so that their common normal points towards an equivalent light source (see Fig. 9). Thus slopes tilted away from this direction have contours spaced closely, giving rise to heavier shading than that on horizontal surfaces, while surfaces lying parallel to the inclined planes are lightest. As in Lehmann's method, some information may be conveyed by the directional texture of the contours. Here we concentrate on the average reflectance only.

A contour is the intersection of the terrain's surface $z = z(x, y)$ with a plane. The equation $z = z_0$ applies to a horizontal plane appropriate for ordinary contours. For "inclined contours" an inclined plane is used with an equation of the form

$$(-p_0, -q_0, 1) \cdot (x, y, z)/\sqrt{1 + p_0^2 + q_0^2} = z_0'.$$

The vector $(-p_0, -q_0, 1)$ is perpendicular to the inclined planes. Ordinary contours represent the locus of the solution of $z(x, y) = z_0$, while inclined contours are the loci of solutions of the equation,

$$[-p_0 x - q_0 y + z(x, y)]/\sqrt{1 + p_0^2 + q_0^2} = z_0'.$$

We can now apply our analysis of the contour density model to the modified surface $z'(x, y)$ defined by the left-hand side
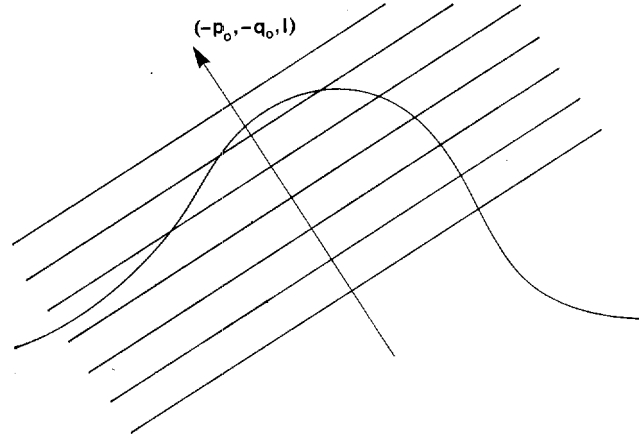
Fig. 9. Side-view of a hill cut by inclined planes. Viewed from above, the lines of intersection crowd together where the surface slopes away from the equivalent source. Conversely, there are no lines where the terrain surface is parallel to the inclined planes.

of this equation! All we need are the slopes of this new surface. Differentiating the above expression with respect to x and y, we get,

$$p' = (p - p_0)/\sqrt{1 + p_0^2 + q_0^2}$$

$$q' = (q - q_0)/\sqrt{1 + p_0^2 + q_0^2}.$$

Finally then,

$$R(p, q) = r_w - (b/k\delta)(r_w - r_b)\frac{\sqrt{(p - p_0)^2 + (q - q_0)^2}}{\sqrt{1 + p_0^2 + q_0^2}}.$$

We obtain the expression for contour density, derived earlier, when $p_0 = q_0 = 0$. Also, in the special case that $r_b = 0, r_w = 1$, $p_0 = 1/\sqrt{2}$, and $q_0 = -1/\sqrt{2}$,

$$R(p, q) = 1 - (b/k\delta)\sqrt{(p - 1/\sqrt{2})^2 + (q + 1/\sqrt{2})^2}/\sqrt{2}.$$

It is sometimes useful to express the apparent brightness as a function of the azimuth ϕ and zenith angle θ of the surface normal. If we let ϕ_0 be the azimuth and θ_0 the zenith angle of the normal to the inclined planes, then the formula can be rewritten as follows:

$$R'(\theta, \phi) = r_w - (b/k\delta)(r_w - r_b) \cos \theta_0$$
$$\cdot \sqrt{\tan^2 \theta - 2 \tan \theta \tan \theta_0 \cos (\phi - \phi_0) + \tan^2 \theta_0}.$$

When $\theta_0 = 45°$, $r_b = 0$ and $r_w = 1$, then, as Tanaka showed [10], [11],

$$R'(\theta, \phi) = 1 - (b/k\delta)\sqrt{1 - \sin 2\theta \cos (\phi - \phi_0)}/(\sqrt{2} \cos \theta).$$

How does one choose the parameter $(b/k\delta)$? Tanaka felt that the shading produced by his method should match that seen on a surface covered with an ideal material called a perfect diffuser. The apparent brightness of such a surface varies with the cosine of the incident angle, between the surface normal and a vector pointing at the light surface. He introduced a parameter called the line factor. It is the ratio of the width of the inked line b to the interval between inclined contours for a horizontal surface $k\delta/\sin \theta_0$. The line factor is just,

$$(b/k\delta)\sqrt{p_0^2 + q_0^2}/\sqrt{1 + p_0^2 + q_0^2}.$$

Tanaka proposed varying the line width b in order to produce shading that matches that seen on a perfect diffuser, but
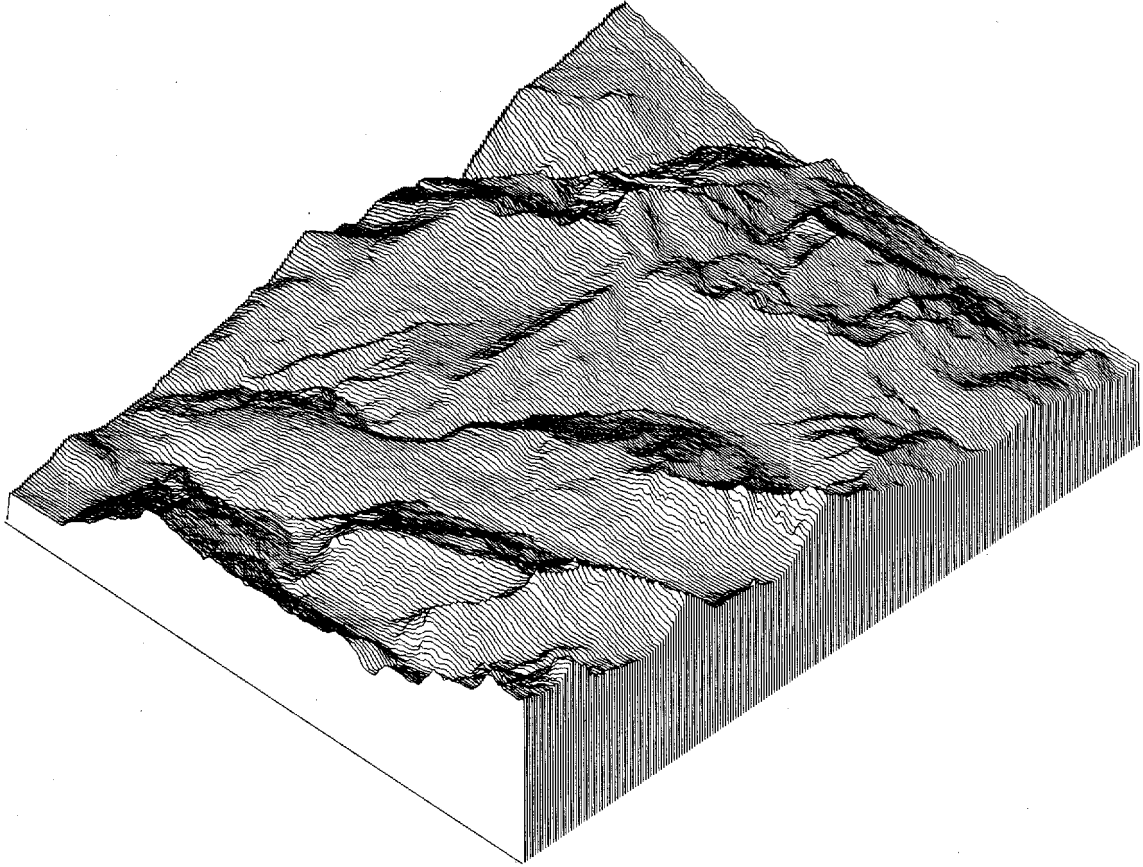
Fig. 10. "Block-diagram" representation of terrain surface. This is an isometric projection of a series of uniformly spaced vertical profiles of the surface viewed from the southeast. Note the shading effect due to the variation in line spacing.

realized the impracticality of this approach for all but polyhedral surfaces [10], [11]. Resigned to using a fixed line width, he chose to optimize the line factor by considering the brightness distribution on a spherical cap extending to 45° slope. With the source at 45° elevation, the least deviation from the brightness distribution one would see if the surface was a perfect diffuser is obtained when the line factor equals 0.3608. Consequently, $(b/k\delta) = 0.3608\sqrt{2}$. Finally then,

$$R(p, q) = 1 - 0.3608\sqrt{(p - 1/\sqrt{2})^2 + (q + 1/\sqrt{2})^2}.$$

It is unfortunate that this method later gave rise to some misunderstanding as well as a less rigorous hybridized form [15].

A common representation for relief form is the block diagram, an oblique view of a series of equally spaced vertical profiles [97]–[102]. The projection typically is orthographic, although at times a perspective projection is utilized. Surfaces not visible to the viewer are eliminated (see Fig. 10). Shading can of course be applied to oblique views as may be done in sophisticated flight simulators of the future. We concentrate here on map forms that provide for superposition of planimetric information however, and digress only to point out that part of the appeal of block diagrams lies in their implicit shading, due to the variation in the spacing of lines.

Following the discussion in the last section, it is clear that the equivalent light-source position is in the horizontal plane at right angles to the vertical cutting surfaces. The analysis just presented then applies directly. Things are a little more difficult if the result is to be expressed in terms of the coordi-

nate system of the surface rather than one oriented with respect to the viewer. Details may be found in Appendices B and C, where contour density shading and Tanaka's inclined contour method are shown to be special cases of this more general situation.

XXIII. WIECHEL'S CONTOUR-TERRACE MODEL   (E)

Imagine a three-dimensional model of the terrain built by stacking pieces of some material cut according to the shape of the contours on a topographic map [8]. If the thickness of the material is chosen correctly the model will be a scaled approximation of the terrain, looking a little like a tiered cake. Illuminating this construction with a distant point source will give rise to a form of shading since each contour "terrace" casts a shadow on the one beneath it (see Fig. 11). Wiechel [8] was the first to analyze the reflectance properties of such a surface. In order to calculate the average brightness of a portion of the model, when viewed from above, we must determine the width of the shadow relative to the width of the terrace.

The width of the shadow, measured perpendicular to the contours, varies, depending on the orientation of contours relative to the direction of the rays from the source. For example, when measured this way, the width is zero where the contour is locally parallel to the projection of the rays on the xy-plane. Measured in a vertical plane containing the light source however, the width of the shadow is constant, since the terrace has a fixed height (see Fig. 12). If the light source has
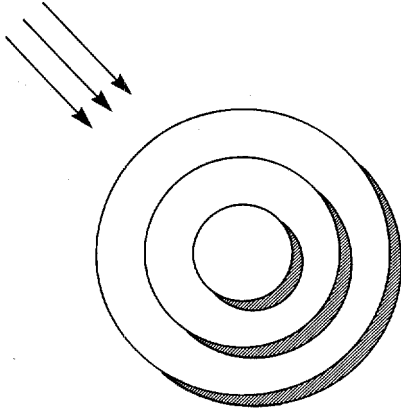
Fig. 11. Shadows cast in the contour terrace model. The width of the shadows, measured perpendicular to the contours, varies with the direction of the contours relative to the direction of the incident rays.
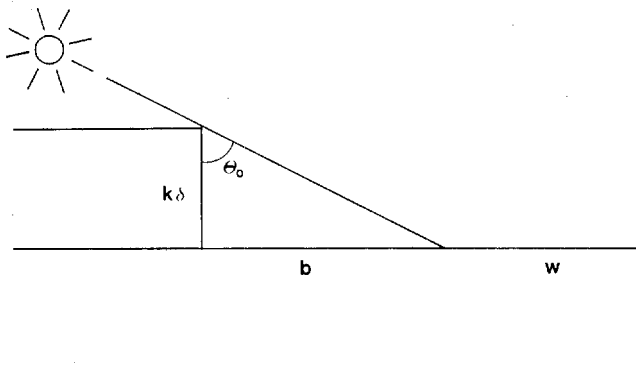
Fig. 12. Section of the contour terrace model in a vertical plane containing the light-source. The width of the shadow b measured in this plane is constant, while the width of the terrace $b + w$ depends on the slope of the surface in a direction parallel to the projection of the incident rays on the ground plane.

a zenith angle θ_0, the contour interval is δ, and the map scale k, then,

$$\tan \theta_0 = (b/k\delta)$$

but

$$\tan \theta_0 = \sqrt{p_0^2 + q_0^2}.$$

To calculate the average brightness we must know the width d of the terrace in the model, measured in the same vertical plane. The slope in this plane evidently is just

$$s = -k\delta/d.$$

We know that the slope of a surface in the direction (p_0, q_0) is,

$$s = (p_0 p + q_0 q)/\sqrt{p_0^2 + q_0^2}.$$

Solving for d from the last two equations and for b from the two before them, we get

$$b/d = -(p_0 p + q_0 q).$$

For example, when the local surface normal $(-p, -q, 1)$ is perpendicular to the direction to the source $(-p_0, -q_0, 1)$, their dot-product is zero and $b/d = 1$. The terrace is then covered exactly by the shadow. In the above expression both the con-

tour interval and the map scale have cancelled, as one might have predicted.

When $(p_0 p + q_0 q) < -1$, shadows coalesce and no further increase in b/d is possible. When, on the other hand, $(p_0 p + q_0 q) > 0$, the slope is facing *towards* the light source. This means that no shadow is cast. In this model, shading only occurs on slopes facing away from the source, while those facing towards it are all *uniformly* bright. This is certainly not what one would expect of a real surface and suggests that the contour-terrace model has some shortcomings. This is not surprising since apparent brightness depends on surface orientation, not height, and while the model represents height with reasonable accuracy it does a poor job of modeling surface orientation. Indeed the surface of the model is mostly horizontal, with some narrow strips of a vertical orientation. The latter are not even visible from above.

Wiechel noted that light would be reflected from these vertical surfaces onto the terraces [8]. The surface thus appears brighter, viewed from above, near vertical surfaces facing towards the light source. He made the simplifying assumption that reflection produces *uniformly* bright patches with the same shape as shadows that would be cast were a source to be placed opposite the actual light source. This is not a reasonable assumption unless the vertical surfaces are made of narrow mirror facets, each oriented perpendicular to the direction of the incident light! In this case, surfaces illuminated by reflection as well as by direct light have a brightness twice that of those illuminated only by direct light. This version of the model is fortunately simple enough to be amenable to analysis. First note that, if we assume the surface to be an ideal diffuser, then the brightness of horizontal surfaces that are neither shadowed nor illuminated by reflection equals the cosine of the zenith angle of the source. Therefore, let $r_b = 0$ and $r_w = \cos \theta_0$, where

$$\cos \theta_0 = 1/\sqrt{1 + p_0^2 + q_0^2}$$

and so

$$R(p, q) = (1 + p_0 p + q_0 q)/\sqrt{1 + p_0^2 + q_0^2}$$

or

$$R'(\theta, \phi) = [1 + \tan \theta \tan \theta_0 \cos (\phi - \phi_0)] \cos \theta_0.$$

When the source is in the standard position (northwest at 45°) this becomes,

$$R(p, q) = [1 + (p - q)/\sqrt{2}]/\sqrt{2}.$$

Note that here apparent brightness already becomes equal to one when the angle of inclination is about 30.36° towards the light source. This may be contrasted with the case of the ideal diffuser, to be discussed later, where it reaches one only for an inclination of 45°. Wiechel used this model as the second approximation to the ideal diffuser (the first will be discussed later) and expressed his result as [8]

$$(\cos i/\cos e)$$

where i is the incident angle, and e is the emittance angle, here equal to θ. These angles will play an important role in the discussion of more recent methods later on.

According to Raisz and Imhof [1], [27]–[29] terraced contour models were used in the late 1800's. An early example is an alpine excursion map published in 1865 that employed "contour shadows" [1]. The first attempts at photography of

obliquely illuminated surfaces also used terraced terrain models [27]. Wiechel probably was influenced by these early efforts when he chose to develop this method for hill shading.

XXIV. Wiechel's Helligkeitsmaassstab

Wiechel based his method for irregular surfaces on that developed earlier by Burmester for regular surfaces [9]. In order to make his approach practical he needed a graphical device for translating measurements of contour interval and direction of steepest descent into gray tones. The "Helligkeitsmaass-stab" (his spelling) is arranged so that these measurements can be transferred directly, and the correct tone determined from a series of isophotes, contours of constant brightness. Steep slopes, with small contour intervals correspond to points near the origin of this diagram, while those of gentle slope map into points further away.

His diagram therefore is a sort of inside-out reflectance map. The main difference is that radial distance from the origin in gradient space is proportional to $\tan \theta$, while it is proportional to $\cot \theta$ in this early precursor. This corresponds to a conformal mapping operation referred to as inversion with respect to the unit circle. Wiechel showed that his diagram corresponded to the image of an appropriate illuminated logarithmoid made of the desired material. The equation of this surface is $z = -\log \sqrt{x^2 + y^2}$. The reflectance map, by the way, can be thought of as the image of a paraboloid [138].

It is indeed unfortunate that Wiechel's construction was ignored. Wiechel developed two shading methods that did not require this two-dimensional diagram. In each case apparent brightness depended only on the slope of the surface in the direction away from the light source. This property manifests itself in the reflectance map in the form of parallel straight-line contours. The effect is less apparent in Wiechel's diagram, where isophotes become nested circles through the origin, with centers along the line in the direction of the light source.

XXV. Tanaka's Relief Contour Method   (F)

Kitirô Tanaka, in 1939, developed an ingenious method [24]–[26] for drawing the shadows one would see if one looked at a contour-terrace model. His method is based on the observation that the length of the shadow, measured in the direction of the incident rays, is constant. Using a pen with a wide nib one can trace the contours, while maintaining the orientation of the nib parallel to the direction of the incident rays (as in roundhand writing). Only those portions of the contours are traced that correspond to slopes facing away from the assumed light source. Tanaka used black ink on gray paper for reasons that will become apparent. If the reflectance of this paper is r_g then,

$$R(p, q) = r_g + (r_g - r_b)(p_0 p + q_0 q)$$

provided $(p_0 p + q_0 q) < 0$, otherwise $R(p, q) = r_g$.

Tanaka also came up with a way of modulating the average reflectance of the paper in areas that corresponded to slopes facing towards the source. His approach is somewhat analogous to taking the negative of a picture of the contour-terrace model obtained by illuminating it from the other side. Thus white "shadows" are cast in the opposite direction to the black shadows. These can be drawn with white ink on gray paper using the same method as before except that now the section of the contours that correspond to slopes facing towards the light source are traced. It is easy to see that the resulting average

reflectance will be,

$$R(p, q) = r_g - (r_g - r_w)(p_0 p + q_0 q)$$

where r_w is the reflectance of the white ink. When $(p_0 p + q_0 q) < 0$, no "shadows" appear and $R(p, q) = r_g$. Tanaka combined the two methods, tracing contours using both white and black ink. The corresponding reflectance map $R(p, q)$ equals one of the expressions above depending on whether the slope locally faces away from or towards the assumed source.

He apparently also experimented with nibs of different width for white and black ink. This corresponds to changing the elevation of the assumed sources. If the width of the nib is b, then the relationship is,

$$(b/k\delta) = \tan \theta_0 = \sqrt{p_0^2 + q_0^2}.$$

The results of this tedious manual method are most impressive [24]–[26]. One can write the above expressions in the alternate notation,

$$R'(\theta, \phi) = r_g + (r_g - r_b) \tan \theta \tan \theta_0 \cos(\phi - \phi_0),$$
$$\text{when } \cos(\phi - \phi_0) < 0$$

$$R'(\theta, \phi) = r_g - (r_g - r_w) \tan \theta \tan \theta_0 \cos(\phi - \phi_0),$$
$$\text{when } \cos(\phi - \phi_0) > 0.$$

Tanaka preferred a reflectance for the gray background halfway between that of the black ink and the white ink. Placing the light source in the standard position we get,

$$R(p, q) = [1 + (p - q)/\sqrt{2}]/2$$

or

$$R'(\theta, \phi) = [1 + \tan \theta \cos(\phi - \phi_0)]/2.$$

This result can also be expressed as, $(\cos i \cos g)/\cos e$, where g is the phase angle, here equal to θ_0. Note that except for scaling by $\cos g$, this is the same result as that obtained by Wiechel for his contour-terrace model. One effect of this scaling is that apparent brightness rises to one only when the angle of inclination is $45°$, on the other hand, horizontal surface now have a gray value of only 0.5.

XXVI. Tanaka's Hemispherical Brightness Distribution

Tanaka needed a way to display the dependence of tone on surface orientation to permit comparison of the results produced by his two methods and what would be seen if the surface modeled were an ideal diffuser. He chose an oblique view of the brightness distribution on a spherical cap extending to $45°$ inclination [10], [11], [24]–[26]. If the cap is increased until it is a hemisphere, one obtains something like the reflectance map. One difference is that radial distance from the origin in gradient space is proportional to $\tan \theta$, while here it is proportional to $\sin \theta$. Thus, while the reflectance map is a central projection of the Gaussian sphere onto a horizontal plane, this is a *parallel* projection. Put another way: we are dealing here with an image of a hemisphere, while the reflectance map is the image of a paraboloid.

Tanaka's oblique views of the distribution of brightness versus surface orientation do not provide the quantitative information available in a contour representation such as Wiechel's. His method is nevertheless very helpful and it is unfortunate that few seem to have paid any attention to it, judging by the continued use of inappropriate forms. It is

not uncommon for example to see the dependence of tone on surface orientation shown as a curve depending on one variable, slope, when it clearly depends on two, slope and the direction of steepest descent, or equivalently, the two components of the gradient.

XXVII. LAMBERTIAN SURFACES (G)

We now turn from graphical methods using variation in line spacing and line thickness to those utilizing continuous tone or halftone techniques. These are often based on a model of what the terrain would look like were it made of some ideal material, illuminated from a predetermined direction. The result differs from an aerial photograph, since no account is taken here of varying terrain cover, the light source is often placed in a position that is astronomically impossible, and the terrain model has been smoothed and generalized. Not being like an aerial photograph is an advantage, since aerial photographs, taken with the sun fairly high in the sky, often do not provide for easy (monocular) comprehension of surface topography.

The amount of light captured by a surface patch will depend on its inclination relative to the incident beam. As seen from the source the surface is foreshortened, its apparent (or projected) area equal to its true area multiplied by the cosine of the incident angle. Thus the irradiance is proportional to $\cos i$. Strangely, it is commonly assumed that the *radiance* (apparent brightness) of the surface patch is also proportional to $\cos i$. This is generally not the case since light may be reflected differently in different directions, as can be seen by considering a specularly reflecting material.

One can however postulate an *ideal* surface that reflects all light incident on it and appears equally bright from all viewing directions. Such a surface is called an ideal diffuser or Lambertian reflector and has the property that its radiance equals the irradiance divided by π [142], [143]. In this special case the radiance is proportional to the cosine of the incident angle. No real surface behaves exactly like this, although pressed powders of highly transparent materials like barium sulfate and magnesium carbonate come close. Matte white paint, opal glass, and rough white paper are somewhat worse approximations, as is snow [131]. Most proposed schemes for automatic hill-shading are based on models of brightness distribution on ideally diffusing surfaces [8], [10], [11], [49]–[57], [71], [73], [74], even though there is no evidence that perception of surface shape is optimized by this choice of reflectance model. As we will see, reflectance calculations based on this model are not particularly simple either.

The cosine of the incident angle can be found by considering the appropriate spherical triangle (see Fig. 13) formed by the local normal N, the direction towards the source S, and the vertical V. One then finds the following, as Wiechel already showed [8],

$$R'(\theta, \phi) = \cos\theta_0 \cos\theta + \sin\theta_0 \sin\theta \cos(\phi - \phi_0).$$

Alternatively one can simply take the dot-product of the unit vector N normal to the surface and the unit vector S pointing towards the source [138], [140]

$$\cos i = \frac{(-p, -q, 1)(-p_0, -q_0, 1)}{(\sqrt{1 + p^2 + q^2}\sqrt{1 + p_0^2 + q_0^2})}.$$

The reflectance map (normalized so that its maximum is one)
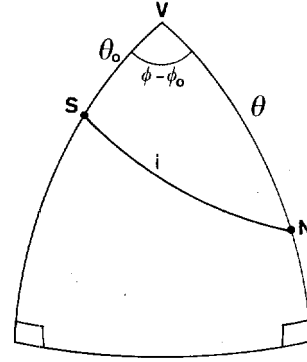
Fig. 13. Spherical triangle used in calculating the incident angle i from the azimuth and elevation of the light-source and the azimuth and elevation of the surface normal. The direction towards the viewer is V, the direction to the source is S, while the surface normal is N.

then is

$$R(p, q) = (1 + p_0 p + q_0 q)/(\sqrt{1 + p^2 + q^2}\sqrt{1 + p_0^2 + q_0^2}).$$

When $(1 + p_0 p + q_0 q) < 0$ the surface element is turned away from the source and is self-shadowed. In this case, $R(p, q) = 0$.

In the case of a point source of light at $45°$ zenith angle in the northwest, the reflectance map becomes

$$R(p, q) = [1 + (p - q)/\sqrt{2}]/[\sqrt{2}\sqrt{1 + p^2 + q^2}].$$

XXVIII. PEUCKER'S PIECEWISE LINEAR APPROXIMATION (H)

The computation of gray value using the equation for the cosine of the incident angle is complicated and slow because of the appearance of the square root. Peucker [61] experimented with a number of approximations that are easier to compute. He found that an adequate, piecewise linear approximation for slopes less than one, is

$$0.3441p - 0.5219q + 0.6599, \quad \text{for } p + q > 0$$

$$0.5129p - 0.3441q + 0.6599, \quad \text{for } p + q < 0$$

or

$$R(p, q) = 0.4285(p - q) - 0.0844|p + q| + 0.6599$$

where $|p + q|$ denotes the absolute value of $(p + q)$. The above approximation produces excellent shaded overlays, that in fact seem easier to interpret that those produced using the exact equation for a perfectly diffusing surface.

XXIX. BRASSEL'S ADJUSTMENT OF LIGHT SOURCE POSITION (I)

Perhaps the most outstanding examples of shaded maps come from Switzerland. Techniques for portraying the shape of the surface and integrating this information with planimetric detail have been perfected by a number of artists there [1], [40]–[47]. The results of automated methods as described here, cannot compete with the beauty of their products. Nevertheless, automated methods do provide a systematic, accurate way for generating shaded overlays. They will become of particular importance when good digital terrain models become easily available. Brassel attempted to incorporate as much as possible of the Swiss manner into his program [71]–[74]. He quickly realized two problems with methods based purely on Lambertian reflectance models.

The first effect is explained as follows. Surface elements sloping away from the source are dark, while those tilted

towards the source are brighter. Brightest are those that have the light rays falling perpendicularly on the surface. Surface elements sloped more steeply, however, become *darker* again. This lack of monotonicity of brightness with slope is apparently disturbing and reduces the ability of the observer to correctly interpret the shape. Brassel ameliorated this effect by reducing the elevation of the light source in regions where this problem occurred.

If the zenith angle of the source θ_0 is smaller than the zenith angle of the direction defined by the surface normal θ he moves the source to a new zenith angle θ_n that is a weighted average of θ_0 and θ. To be precise,

$$\theta_n = \max [\theta_0, \alpha\theta + (1 - \alpha)\theta_0]$$

where

$$\theta = \tan^{-1} \sqrt{p^2 + q^2}.$$

In his thesis [71], the weighting factor α was one, so that adjustment in elevation was complete. Curiously, this simple method has the effect of lowering the light source even for surface elements tilted *away* from the source, as long as the slope is large enough. The above method can also be expressed directly in terms of the components of the gradient. When $p^2 + q^2 > p_0^2 + q_0^2$,

$$p_n = p_0(\sqrt{p^2 + q^2} / \sqrt{p_0^2 + q_0^2})$$

and

$$q_n = q_0(\sqrt{p^2 + q^2} / \sqrt{p_0^2 + q_0^2})$$

where p_n and q_n are the components of the gradient of a surface element oriented to be maximally illuminated by the adjusted light source. If there are no further adjustments of source position, the reflectance map in the specified region becomes,

$$R(p, q) = \frac{1 + (p_0 p + q_0 q)(\sqrt{p^2 + q^2} / \sqrt{p_0^2 + q_0^2})}{(1 + p^2 + q^2)}.$$

XXX. Adjustment of the Azimuth of the Source

Next, Brassel observed that ridge and stream lines become indistinct when their direction was more or less aligned with a direction toward the source. Opposite faces of a mountain or valley may end up with similar gray values when the cosine of the incident angle is similar for the two, even though they have quite different surface orientations. Maximum contrast occurs when a linear feature lies at right angles to the direction of the incident light, and Brassel therefore moves the light source in azimuth towards the local direction of steepest ascent or descent (whichever is closer).

The amount of adjustment depends on two parameters (see Fig. 14). The maximum amount of adjustment is specified by w (55° for example), while the azimuth difference at which this maximum occurs is specified by g (80° for example). The details of the computation are not very important but are given here for completeness. First, the azimuth of the direction of steepest descent is computed using

$$\phi = \text{atan} (-q, -p)$$

where atan (y, x) is the direction of the line from the origin to the point (x, y) measured counterclockwise from the x-axis. Next, the difference between ϕ and the azimuth of the source ϕ_0 is reduced to the range $-\pi/2$ to $+\pi/2$ by adding or subtracting integer multiples of π. Let the result be $\Delta\phi$. The adjusted

azimuth of the source is then calculated as follows,

$$\phi_n = \phi_0 + w \text{ sign } (\Delta\phi) \min [|\Delta\phi|/g, (\pi/2 - |\Delta\phi|)/(\pi/2 - g)]$$

where sign $(\Delta\phi)$ is $+1$ when $\Delta\phi > 0$, and -1 when $\Delta\phi < 0$. Now one can calculate the gradient (p_n, q_n) of the maximally illuminated surface element, or instead, use Wiechel's formula to get the cosine of the incident angle directly,

$$R'(\theta, \phi) = \cos\theta_n \cos\theta + \sin\theta_n \sin\theta \cos (\phi - \phi_n).$$

Here it should be pointed out that in Brassel's scheme the gradient (p, q) used in the above formulas for adjusting the azimuth of the source is a *regional* value derived from ridge and stream lines in the area near a particular point. In this way the cartographer can influence the final appearance of the shaded overlay by altering these *manually* entered linear features. This method involves rather complicated global calculations that do not lend themselves to implementation in the straightforward way we have discussed. The apparent brightness of a surface element depends on both its orientation and some function of its surround.

A possible objection to this idea is that the distribution of light sources does not vary from place to place in a real imaging situation unless the sources are very close to the surface. It must be pointed out, however, that people seem to have little difficulty interpreting synthetic images where the assumed light source position varies. In fact, few notice such drastic changes in assumed light source position as are apparent in a recent map of the polar regions of Mars [150]. This may be related to the fact that our perception of shaded images does not give us a good appreciation for global differences in depth, instead giving us an excellent appreciation of local surface orientation patterns.

Whatever the merits of this argument, the above method can be modified to fit in with the notion of the reflectance map, as defined earlier, if one uses the *local* gradient (p, q) in the calculation of the adjusted source position. The illustration shown here uses this modified version. Note that in Brassel's scheme the adjustment in azimuth and zenith angle of the source are independent and can be carried out in either order.

Brassel also adjusted the apparent brightness according to the height of the terrain. This is a simple local computation that can be easily added to any of the basic methods presented here. It was not included here to simplify comparisons.

XXXI. Alternate Light Source Adjustment Method (J)

Brassel used a piecewise linear adjustment in azimuth. A similar effect can be achieved using a smoothly varying function like

$$\sin\delta\phi = (\beta/2) \sin 2(\phi - \phi_0) = \beta \sin (\phi - \phi_0) \cos (\phi - \phi_0).$$

That is,

$$\sin\delta\phi = \beta [(p_0 q - q_0 p) (p_0 p + q_0 q)]/[(p^2 + q^2) (p_0^2 + q_0^2)].$$

Adjusting the azimuth of the source by $\delta\phi$ leads to a new position specified by,

$$p_s = p_0 \cos\delta\phi - q_0 \sin\delta\phi$$

$$q_s = p_0 \sin\delta\phi + q_0 \cos\delta\phi.$$

Adjustment is complete for small angles when $\beta = 1$. The use of trigonometric functions is avoided in the above calculations,
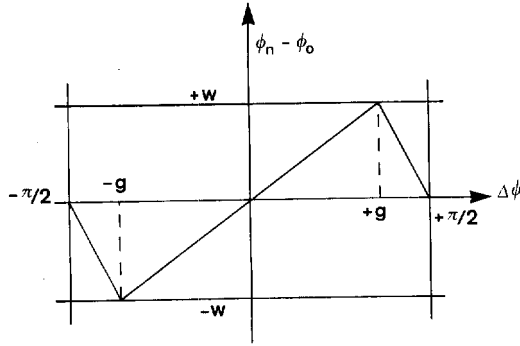
Fig. 14. Sawtooth function giving adjustment of azimuth of the light source as a function of the angle between "regional" ridge and valley directions and the direction of the light source in Brassel's scheme.

Fig. 15. Projection of the surface normal on a vertical plane containing the assumed light-source. The projected normal is perpendicular to the line in which the plane cuts the terrain surface.

since both the sine and the cosine of $\delta\phi$ can be computed without them.

Next we turn to the adjustment in the elevation of the source. To avoid the peculiar phenomena of the lowering of the source even for surface elements turned *away* from it, we adjust the elevation according to the projection of the surface normal on a plane containing the source. When $p_s p + q_s q > p_s^2 + q_s^2$,

$$p_n = p_s(p_s p + q_s q)/(p_s^2 + q_s^2)$$

$$q_n = q_s(p_s p + q_s q)/(p_s^2 + q_s^2).$$

In this region then the reflectance map becomes,

$$R(p,q) = \sqrt{1 + (p_s p + q_s q)^2/(p_s^2 + q_s^2)}/\sqrt{1 + p^2 + q^2}.$$

Otherwise it is calculated as before, that is, the cosine of the incident angle is

$$R(p,q) = (1 + p_n p + q_n q)/(\sqrt{1 + p^2 + q^2}\sqrt{1 + p_n^2 + p_n^2}).$$

The advantage of the above method of adjustment is that simple calculation in terms of the components of the gradient replace trigonometric equations in terms of azimuth and zenith angles.

XXXII. Wiechel's Projected Incident Angle (K)

The first serious analysis of an approach based on the shading seen on the surface of an obliquely illuminated matte object is that of Wiechel [8]. He started by assuming a perfectly diffusing surface and proposed connecting points of equal apparent brightness by isophotes. He correctly determined the brightness of a perfect diffuser as already mentioned. In order to make calculations less unwieldy he also suggested three approximations, the second of these being the contour-terrace model already discussed. His *first* method involved approximating the cosine of the incident angle i by the cosine of i', the projection of this angle onto a vertical plane lying parallel to the rays (see Fig. 15). By applying the analogue formulas to the lower spherical triangle (see Fig. 16) we get,

$$\sin i' \cos i = \cos i' \sin i \cos \chi.$$

Applying the analog formulas next to the whole triangle we get

$$\sin i \cos \chi = \cos \theta \sin \theta_0 - \sin \theta \cos \theta_0 \cos (\phi - \phi_0).$$

The second equation allows us to eliminate χ from the first
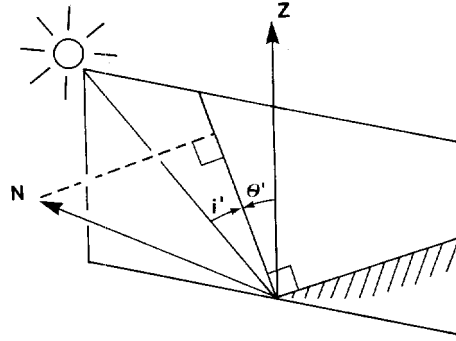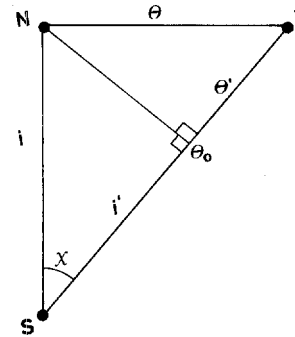
Fig. 16. Spherical triangles used to calculate the projected incident angle i' and the projected surface inclination θ'. The direction towards the viewer is V, the direction to the source is S, while the surface normal is N.

and obtain an expression for $\tan i'$. Using the identity $\cos i' = 1/\sqrt{1 + \tan^2 i'}$, we finally find,

$$R'(\theta, \phi) = \cos i/[\cos \theta \sqrt{1 + \tan^2 \theta \cos^2 (\phi - \phi_0)}]$$

where, using the cosine formula as before,

$$\cos i = \cos \theta \cos \theta_0 + \sin \theta \sin \theta_0 \cos (\phi - \phi_0).$$

Alternatively one can project the vector $n = (-p, -q, 1)$ onto the plane with normal $s = (q_0, -p_0, 0)$. The result will equal,

$$n' = n - (n \cdot s)s/s^2$$

where s is the magnitude of the vector s. This projected vector will be perpendicular to the line in which a vertical plane including the light source cuts the surface:

$$n' = [-p_0(p_0 p + q_0 q)/(p_0^2 + q_0^2),$$

$$-q_0(p_0 p + q_0 q)/(p_0^2 + q_0^2), 1].$$

Taking the dot-product of the projected vector and the vector pointing at the source, then dividing by their magnitudes we find,

$$R(p,q) = \frac{(1 + p_0 p + q_0 q)}{\sqrt{1 + p_0^2 + q_0^2}\sqrt{1 + (p_0 p + q_0 q)^2/(p_0^2 + q_0^2)}}.$$

This mathes the expression for perfectly diffuse reflection for values of (p, q) along the line from the origin to the source point (p_0, q_0). When the source is in the standard position the equation becomes

$$R(p,q) = [1 + (p - q)/\sqrt{2}]/[\sqrt{2}\sqrt{1 + (p - q)^2/2}].$$

While these equations are more complicated than the original equations for the cosine of the incident angle i, it must be pointed out that the angle i' can be estimated graphically by measuring the contour interval in a direction parallel to the incident light rays. The same is true of Wiechel's second approximation introduced earlier. This greatly simplifies the manual construction of shaded maps from contour maps, and makes it possible to use a simple one-dimensional scale for brightness instead of Wiechel's more elaborate "Helligkeits-maassstab". This property manifests itself in the reflectance map by the appearance of parallel straight line contours. It is also interesting to note that Wiechel's "approximations" produces results that seem better than those obtained using the equation for the perfect diffuser. Unfortunately, experimentation at his time was limited because of the lack of appropriate technology for systematically generating continuous tone patterns. Apparently no maps made by this method were ever published [1].

XXXIII. WIECHEL'S MODIFIED BRIGHTNESS (L)

Finally, Wiechel postulated a material that would *not* appear equally bright from all viewing directions, but instead had brightness varying as the cosine of the emittance angle. This was used in part to discuss the relationship between the contour-terrace model and the original surface, but also put forward as a third, "modified brightness" model that might be used in calculating gray tone. In this case brightness varies in proportion to $(\cos i \cos e)$. We can normalize his result here by dividing by the maximum of this product, $\cos^2 (g/2)$, where g is the so-called phase angle, here equal to θ_0. (The term phase angle stems from work on lunar photometry, where this angle equals the phase of the moon). Then,

$$R(p, q) = 2 (\cos i \cos e)/(1 + \cos g)$$

or

$$R(p, q) = \frac{2(1 + p_0 p + q_0 q)}{(1 + \sqrt{1 + p_0^2 + q_0^2})(1 + p^2 + q^2)}.$$

Incidentally, this function does not satisfy Helmholtz's reciprocity law [124], and therefore cannot correspond to the reflectance of any real surface illuminated by a point source.

XXXIV. MARSIK'S AUTOMATIC RELIEF SHADING (M)

Blachut and Marsik further modified Wiechel's approximation, partly as a result of their dissatisfaction with the fact that a horizontal surface does not appear white when a perfectly diffusing material is assumed [58], [59]. This may have stemmed in part from early conventions in map-making where horizontal surfaces were portrayed without hachures [4]–[6]. Marsik also aimed for simpler calculations and considered the slope in the direction towards the source. For some reason, he proposed making the *density* of the printed result equal to the tangent of the projected slope angle θ' (see Fig. 15). Density is the logarithm (base 10) of the reciprocal of the reflectance. Applying the analogue rule to the upper spherical triangle (see Fig. 16) one can show that,

$$0 = \cos \theta \sin \theta' - \sin \theta \cos \theta' \cos (\phi - \phi_0).$$

Thus

$$\tan \theta' = \tan \theta \cos (\phi - \phi_0),$$

$$R'(\theta, \phi) = 10^{\tan \theta \cos (\phi - \phi_0)}$$

Using the expression for the projected normal n' developed in the last section, or, remembering the expression for the slope in the direction (p_0, q_0), one can also show,

$$R(p, q) = 10^{(p_0 p + q_0 q)/\sqrt{p_0^2 + q_0^2}}.$$

When $p_0 p + q_0 q > 0$, $R(p, q) > 1$ and so all surfaces facing towards the light source are white. No information is available to the viewer regarding surface shape in these areas. If the assumed light source is in the standard position we get the simple formula,

$$R(p, q) = 10^{(p - q)/\sqrt{2}}.$$

Marsik also limited the density to a maximum of 0.7 to avoid interference with planimetric information on the map.

XXXV. LOMMEL–SEELIGER LAW (N)

Many surfaces have reflectance properties that differ greatly from those of an ideal diffuser. The photometry of rocky planets and satellites has intrigued astronomers for many years [121]–[130]. Several models have been proposed to explain the observed behavior. One of the earliest, developed by Lommel [119] and modified by Seeliger [120], is based on an analysis of primary scattering in a porous surface [126], [128]. Their model consists of a random distribution of similar particles suspended in a transparent medium and results in a reflectance function that is given here in its simplest form,

$$1/[1 + (\cos e/\cos i)]$$

unless $\cos i < 0$, when the surface is self shadowed. Here i is the incident angle, and e is the emittance angle, the angle between the local surface normal and the direction to the viewer, here equal to θ. The expression equals $1/(1 + \cos g)$ when $i = 0$, where g is the phase angle, here equal to θ_0. Using this value for normalization and remembering the expression for $\cos i$ one finds,

$$R'(\theta, \phi) = (1 + \cos \theta_0)/[1 + \cos \theta/(\cos \theta \cos \theta_0$$
$$+ \sin \theta \sin \theta_0 \cos (\phi - \phi_0))]$$

or

$$R(p, q) = \frac{[1 + 1/\sqrt{1 + p_0^2 + q_0^2}]}{[1 + \sqrt{1 + p_0^2 + q_0^2}/(1 + p_0 p + q_0 q)]}$$

unless $(1 + p_0 p + q_0 q) < 0$, when $R(p, q) = 0$. When the source is in the standard position,

$$R(p, q) = \frac{(1 + 1/\sqrt{2})[1 + (p - q)/\sqrt{2}]}{(1 + \sqrt{2}) + (p - q)/\sqrt{2}}$$

The Lommel–Seeliger law has been used in automated relief shading by Batson, Edwards, and Eliason [70].

Based on detailed measurements and modeling, Fesenkov [123], [127] and later Hapke [128]–[130] further improved the equations for the reflectance of the material in the *maria* of the moon. Hapke imagined the surface as an open porous network into which light can penetrate freely from any direction. His result has three components: the Lommel–Seeliger formula for reflection from a surface layer containing many scattering points of low reflectance, Schönberg's formula [122] for reflection from a Lambertian sphere and a complicated factor resulting from mutual obscuration of the particles. The results of such investigations are often expressed in terms of angles other than the ones introduced so far. The Lommel–

simplifies the problem of calculating the shape of the lunar surface from shading in a single image [137], [138], [151]. The angles needed, luminance longitude and luminance latitude, are defined in Appendix D.

XXXVI. Minnaert's Reflectance Function (O)

Minnaert discusses a large variety of models for the reflection of light from rough surfaces [126]. He also proposed a class of simple functions of the form,

$$\cos^{\kappa} i \, \cos^{\kappa-1} e$$

intended to fit observations of the radiance of lunar material while obeying the reciprocity law [124]. Here κ is a parameter to be chosen so that the best fit with experimental data is obtained. This parameter is meant to lie between zero and one, with the above expression becoming equal to that for the perfect diffuser when $\kappa = 1$. We can normalize this expression so it equals one when $i = 0$,

$$R(p, q) = \cos^{\kappa} i \, \cos^{\kappa-1} e/\cos^{\kappa-1} g$$

$$R(p, q) = [(1 + p_0 p + q_0 q)/(1 + p^2 + q^2)]^{\kappa}$$

$$\cdot (\sqrt{1 + p^2 + q^2}/\sqrt{1 + p_0^2 + q_0^2}).$$

XXXVII. Particularly Simple Reflectance Maps (P)

Several methods discussed here have reflectance depending only on the slope in the direction away from the assumed light source, leading to parallel straight line contours in the reflectance map. These include Wiechel's first and second "approximation," Tanaka's relief contour method, the "law" of Lommel and Seeliger, Minnaert's formula when $\kappa = \frac{1}{2}$, as well as Marsik's automatic relief shading. These methods are quite effective in producing overlays that are easy to interpret. One can construct more such reflectance maps, including some that are even easier to calculate. One possibility, for example, is,

$$R(p, q) = \frac{1}{2} + \frac{1}{2}(p' + a)/b$$

where

$$p' = (p_0 p + q_0 q)/\sqrt{p_0^2 + q_0^2}$$

is the slope in the direction away from the source. Values less than or equal to zero correspond to black, while values greater than or equal to one correspond to white. The parameters a and b allow one to chose the gray value for horizontal surfaces and the rapidity with which the gray values changes with surface inclination. The simple program shown earlier (see Fig. 5) uses this form with $a = 0$, $b = 1/\sqrt{2}$ and $p_0 = 1/\sqrt{2}$, $q_0 = -1/\sqrt{2}$.

A simple alternative, where all possible slopes are mapped into the range from zero to one is,

$$R(p, q) = \frac{1}{2} + \frac{1}{2}(p' + a)/\sqrt{b^2 + (p' + a)^2}.$$

This has the advantage that the reflectance does not saturate for any finite slope and all changes of inclination in the vertical plane including the source translate into changes in gray level.

Another way to achieve this effect is the following, somewhat reminiscent of Lehmann's approach,

$$R(p, q) = \frac{1}{2} + (1/\pi) \tan^{-1} [(\pi/2)(p' + a)/b].$$

These three formulas are given in a form where the rate at which the gray value changes with surface inclination is the same at $(p' + a) = 0$.
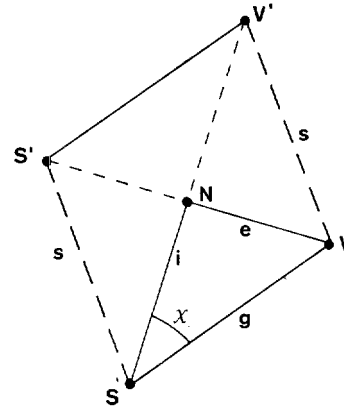
Fig. 17. Spherical triangles used to calculate the first off-specular angle s. It is the angle between S, the center of the source, and S', the direction from which light is specularly reflected towards the viewer. Equivalently, it is the angle between V, the direction of the viewer, and V', the direction in which light from the center of the source is specularly reflected.

XXVIII. Glossiness—The First Off-Specular Angle

Not all surfaces are matte. Some are perfectly specular or mirror-like. Since smooth, specularly reflecting surfaces form virtual images of the objects around them, patches of high brightness will appear when such a surface is illuminated by an extended source, like a fluorescent light fixture, or by light streaming in through a window. The size of the patches depends on the solid angle subtended by the source as well as the surface curvature, while the brightness distribution is that of the source.

To study reflection of an extended source in a specular surface, it is useful to introduce the "off-specular" angle s between the direction S to the center of the source and the direction S', of the point that is specularly reflected to the viewer (see Fig. 17). This, incidentally, is also the angle between the direction to the viewer V and the direction V' in which the rays from the center of the source are specularly reflected.

We assume a circularly symmetric source, with brightness $L(s)$ at eccentricity s. This is the brightness the viewer observes in the specularly reflecting surface. Calculating the first off-specular angle s is simple using the appropriate spherical triangles:

$$\cos s = \cos 2i \cos g - \sin 2i \sin g \cos \chi$$

$$\cos e = \cos i \cos g - \sin i \sin g \cos \chi.$$

Here, i is the incident angle, between the local normal and the direction to the source, $e = \theta$, is the emittance angle, between local normal and the direction to the viewer, while $g = \theta_0$ is the phase angle, between source and viewer. Eliminating χ from the two equations and expanding the sine and cosine of $2i$, one gets,

$$\cos s = 2 \cos i \cos e - \cos g.$$

Substituting expressions in p and q for $\cos i$, $\cos e$ and $\cos g$ one can rewrite this as,

$$\cos s = [2(1 + p_0 p + q_0 q)/(1 + p^2 + q^2) - 1]/\sqrt{1 + p_0^2 + q_0^2}.$$

This result can also be obtained simply by finding the direction S' from which a ray must come to be specularly reflected to the viewer V, by a surface element with normal N,

$$S' = 2(V \cdot N)N - V$$

where $V = (0, 0, 1)$. The off-specular angle is the angle between S' and the center of the source S so

$$\cos s = S \cdot S' = 2(S \cdot N)(V \cdot N) - (S \cdot V).$$

Note that the cosine of the first off-specular angle can be calculated easily, without using trigonometric functions. The contours of constant $\cos s$ turn out to be nested circles in gradient space, with centers lying on the line from the origin to the point (p_0, q_0). This can be seen by noting that the locus of the point S', for constant s, is a circle about the point S and that circles on the Gaussian sphere give rise to circles in gradient space when projected stereographically [138].

The cosine of the off-specular angle s equals one when conditions are right for specular reflection, that is, when $e = i$ and $g = i + e$. This can be seen by setting $e = i = g/2$ in the trigonometric expression for $\cos s$.

XXXIX. Bui-Tuong's Formula—Specular Surface, Extended Source (Q)

Having seen how to calculate the off-specular angle s, we can now make a reflectance map, by assigning the distribution of source brightness $L(s)$. This function should be nonnegative monotonically decreasing with s, and equal to one when $s = 0$. For ease of calculation one choice might be

$$L(s) = \cos^n (s/2) = [\tfrac{1}{2}(1 + \cos s)]^{n/2}$$

where n is a number that defines how compact the bright patch is (a useful value might be around 20). So far, we have developed the reflectance map for a specular surface and a circularly symmetric source. Many surfaces, such as glazed pottery or smooth plastic, have both glossy and diffuse components reflection. Specular reflection takes place at the smooth interface between two materials of different refractive index, while the matte component results from scattering of light that penetrates some distance into the surface layer.

We can combine these two components as follows

$$R(p, q) = [(1 - \alpha) + \alpha L(s)] \cos i / \cos (g/2)$$

where α determines how much of the incident light is reflected specularly. The expression is scaled so that its maximum is (approximately) equal to one. Here we have assumed the source, while distributed, is compact enough so that the diffuse reflection component can be approximated as $\cos i$. The above expression obeys the reciprocity law of Helmholtz [124] which applies to real surfaces illuminated by a point source. Bui-Tuong used a reflectance function similar to the one derived above in his computer graphics work [113]. He apparently tried to model reflection from a surface that is not perfectly smooth. This requires a *different* off-specular angle however, as will be seen in the next section.

XL. Luster—The Second Off-Specular Angle

Refulgency, gloss or shine can also appear when a point source is reflected in a surface that is not perfectly smooth. When a slightly uneven surface, of a material that gives rise to metallic or dielectric reflection, is illuminated by a point source, bright patches will be seen surrounding points where the local tangent plane is oriented correctly for specular reflection. The size of these patches will depend on the roughness of the surface and the surface curvature, while the distribution of brightness will depend to some extent on the texture of the microstructure of the surface.
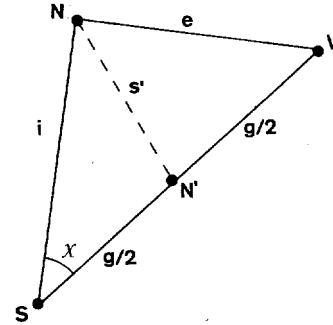
Fig. 18. Spherical triangles used to calculate the second off-specular angle s'. It is the angle between the actual surface normal N and a surface normal N' oriented to specularly reflect rays from the source towards the viewer.

In this case we will need to calculate the second off-specular angle s' between the local normal N and the normal N' oriented for specular reflection of rays from the source S towards the viewer V (see Fig. 18). By considering the appropriate spherical triangles one finds,

$$\cos s' = \cos i \cos (g/2) - \sin i \sin (g/2) \cos \chi$$

$$\cos e = \cos i \cos g - \sin i \sin g \cos \chi.$$

Eliminating χ from the two equations and expanding the sine and cosine of the phase angle g, one finds,

$$\cos s' = (\cos i + \cos e)/(2 \cos (g/2))$$

or

$$\cos s' = (\cos i + \cos e)/(\sqrt{2} \sqrt{1 + \cos g}).$$

This result can also be obtained by finding the vector N', normal to a surface element oriented to specularly reflect a ray from the source in the direction of the viewer V. That is,

$$N' = (S + V)/|S + V|.$$

The off-specular angle is the angle between the actual surface normal N, and this vector N'

$$\cos s' = N \cdot N' = [(S \cdot N) + (V \cdot N)]/\sqrt{2} \sqrt{1 + (S \cdot V)}.$$

The surface microstructure of an uneven surface can be modeled by many randomly disposed mirror-like facets, too small to be optically resolved, each turned a little from the average local surface orientation. One can define a distribution $P(s')$ describing what fraction of these microscopic facets are turned away from the average local normal by an angle s'. For ease of calculation one choice might be,

$$P(s') = \cos^n s'.$$

XLI. Blinn's Formula—Rough Surface, Point Source (R)

One can use the fact that a normal N' oriented for specular reflection of the point source towards the viewer, lies in the direction $(-p_1, -q_1, 1)$, where

$$p_1 = -\cos \phi_0 \tan (\theta_0/2)$$

and

$$q_1 = -\sin \phi_0 \tan (\theta_0/2).$$

We can also find N' by normalizing the vector $(S + V)$, so that

its third component equals 1:

$$p_1 = p_0/[1 + \sqrt{1 + p_0^2 + q_0^2}]$$
$$q_1 = q_0/[1 + \sqrt{1 + p_0^2 + q_0^2}].$$

A surface with gradient (p_1, q_1) is oriented just right to specularly reflect a ray from the source to the viewer. This can be seen by noting that when $p = p_1$ and $q = q_1$,

$$\cos i = \cos e = 1/\sqrt{1 + p_1^2 + q_1^2}$$

and

$$\cos g = 2/(1 + p_1^2 + q_1^2) - 1.$$

In any case,

$$\cos s' = (1 + p_1 p + q_1 q)/(\sqrt{1 + p^2 + q^2}\ \sqrt{1 + p_1^2 + q_1^2}).$$

Note that s' will tend to be (roughly) half of s when both angles are small. Combining matte components of surface reflection with those from the rough outer surface we get,

$$R(p, q) = [(1 - \alpha) + \alpha P(s')] \cos i/\cos (g/2).$$

The above reflectance map also obeys Helmholtz's reciprocity law and is normalized so that its maximum is (approximately) equal to one. Blinn and Newell give a similar reflectance function, claiming it was what Bui-Tuong had proposed [114]. The two are not the same however since the two off-specular angles are different; in fact, the contours of constant s' are nested ellipses in gradient space, while, as mentioned earlier, the contours of constant s are nested circles. Indeed, Bui-Tuong's model corresponds to reflection of an extended, rotationally symmetric source in a specular surface, while the model presented in this section applies to reflection of a point source in a rough surface.

XLII. BLINN AND NEWELL'S MODEL FOR SPECULAR SURFACES

One of the methods described by Blinn and Newell [114] assumes a perfectly specular surface in which the world surrounding the object is reflected. To make computations feasible, they imagine the surrounding objects at a distance great enough so that each part of the surround appears to lie in essentially the same direction from every point of the surface of the object. In this case one can imagine the brightness distribution of the surrounding objects projected onto the inside of a large sphere. The gray value used for a particular surface patch then is found by computing the direction S' from which a ray must come to be specularly reflected to the viewer V, by a patch with surface normal N. We have already seen that,

$$S' = 2(V \cdot N)N - V.$$

The appropriate gray value is then determined from the spherical distribution of brightness. In practice the sphere is mapped onto a plane by calculating the zenith angle, θ_0 and azimuth, ϕ_0 of S' [114]. The brightness distribution can be equally well specified in gradient space [138], since it is also a projection of the Gaussian sphere.

Surface models incorporating randomly dispersed mirror-like facets were first studied in the 1700's by Bouguer [118]. This type of microstructure has been investigated extensively since then, despite the difficulties of reasoning about the three-dimensional nature of reflection from such surfaces. Recently,

Torrance and Sparrow further elaborated on these models [134], [135] in order to match more closely experimental data showing maximum brightness for angles of reflection *larger* than the incident angle. They included in their considerations the effects of obstruction of the incident and emergent rays by facets near the one reflecting the ray. Blinn simplified and explained their calculations [115] and used them in producing shaded images of computer models of various objects. The overall result can be broken into a product of three terms, one dependent on the distribution of facet orientations, the second being the formula for Fresnel reflection from a flat dielectric surface, while the third is the geometric attenuation factor accounting for partial occlusion of one facet by another. We will not discuss these models in any more detail here.

Models for glossy or lustrous reflection have been used with great success in computer graphics to increase the impression of realism the viewer has when confronted with a synthetic picture of objects represented in the computer. Unfortunately, these methods do not seem to improve the presentation of surface shape for cartographic purposes.

XLIII. COLORED SHADING

It is often said that quantitative information about the surface cannot be obtained from relief shading [1]. Contour lines on the other hand do allow measurements of elevation and estimation of the gradient. Shading does provide *some* information about the gradient too, but cannot be used to determine both of its components locally, since only one measurement is available at each point. Since we can perceive the shape of objects portrayed by shaded pictures, it seems that these local constraints do lead to a *global* appreciation of shape, apparently based on our assumption that the surface is continuous and smooth.

If two shaded images, produced with the assumed light source in different positions, were available however, two measurements could be made at each point allowing one to determine the gradient *locally* [141]. It is inconvenient to work with two shaded overlays; fortunately though, they can be combined by printing them in different colors. In fact, yet another overlay can be added in a third color, but it adds no new information, since the two components of the gradient are already fully determined by the first two.

Colored shading corresponds to illumination by multiple sources, each of a different color. The exact color at each point in the printed result is uniquely related to the gradient at that point. Thus quantitative information *is* available in this new kind of map overlay. Further, ambiguities present in black and white presentations disappear. By positioning the light sources properly, one can avoid problems occasioned by the accidental alignment of ridge or stream lines with the direction of incident light. Thus the need for *ad hoc* adjustments of the azimuth of the assumed light source is removed.

Colored shading is easy to interpret in terms of surface shape and effective in portraying surface form. It is unlikely however that it will be widely used because of the added expense of printing and conflict with existing uses of color in cartography to distinguish various kinds of planimetric information. Amongst other things, color is now used to code height and surface cover. Further, yellow is used in ordinary shading for sun-facing slopes, while violet is used for shaded regions [152]. This is thought to simulate the increased sky illumination component in areas turned away from the sun.
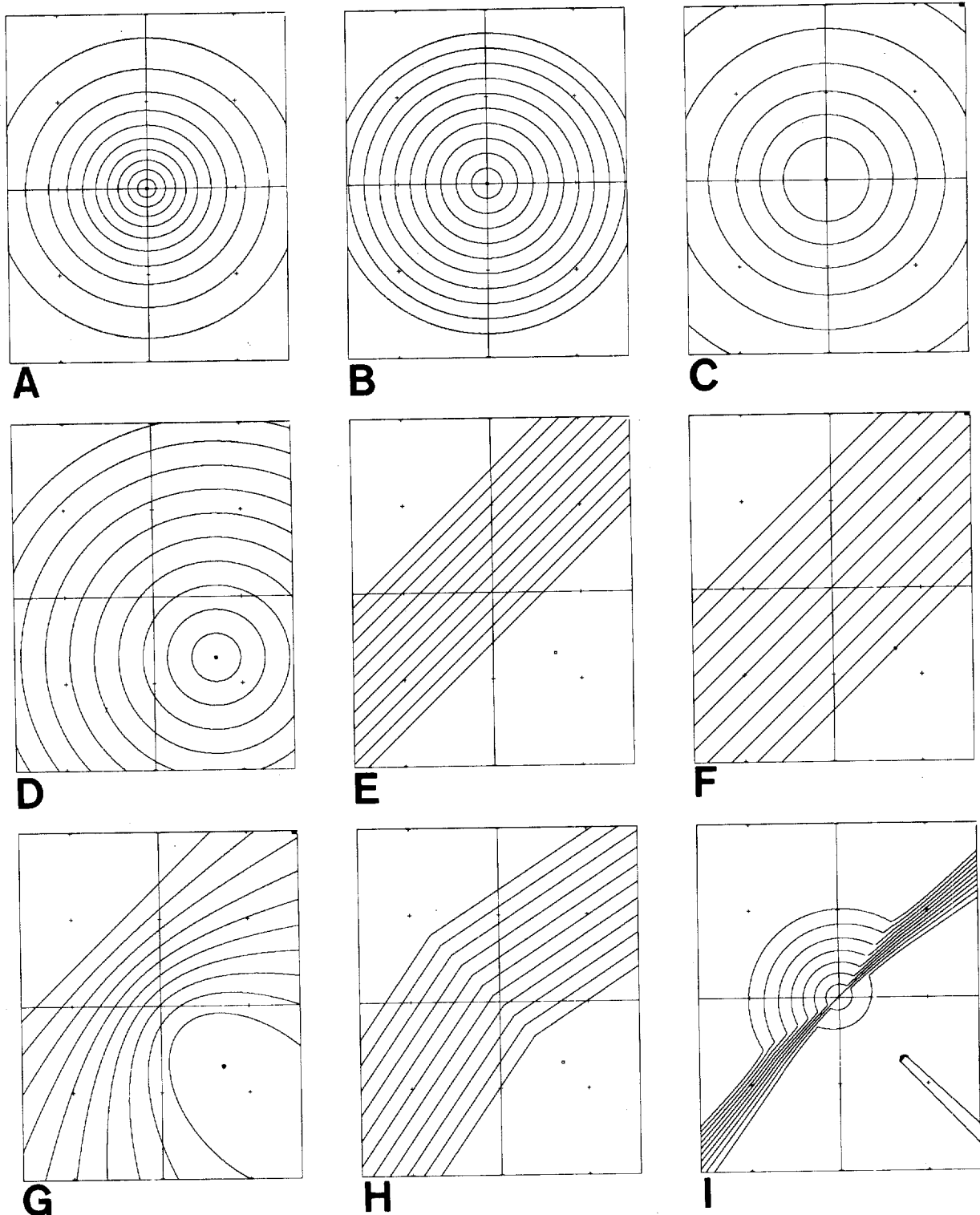
Fig. 19. Reflectance maps in the order in which they were introduced. The letter codes on subfigures match the letters found after the headings of corresponding sections of this paper. Small crosses mark points in gradient space where slope-components are integer multiples of 1. Where appropriate, a small square marks the gradient of a surface element that is perpendicular to the rays from the assumed light-source.

XLIV. Summary and Conclusions

After a brief review of the history of hill-shading an efficient method for providing shaded overlays was described. It depends on a lookup table containing sampled values of the reflectance map. Traditional, manual methods were explored in terms of their equivalent reflectance maps, as were phenomenological models used in the computer graphics community.

Methods that have been proposed for mechanizing the generation of relief shading were also treated. The automated method described here is very flexible, since it can use any reflectance map.

Eighteen of the reflectance maps described were plotted as contour diagrams (see Fig. 19). The letter under a subfigure corresponds to the letter appearing after the heading of the
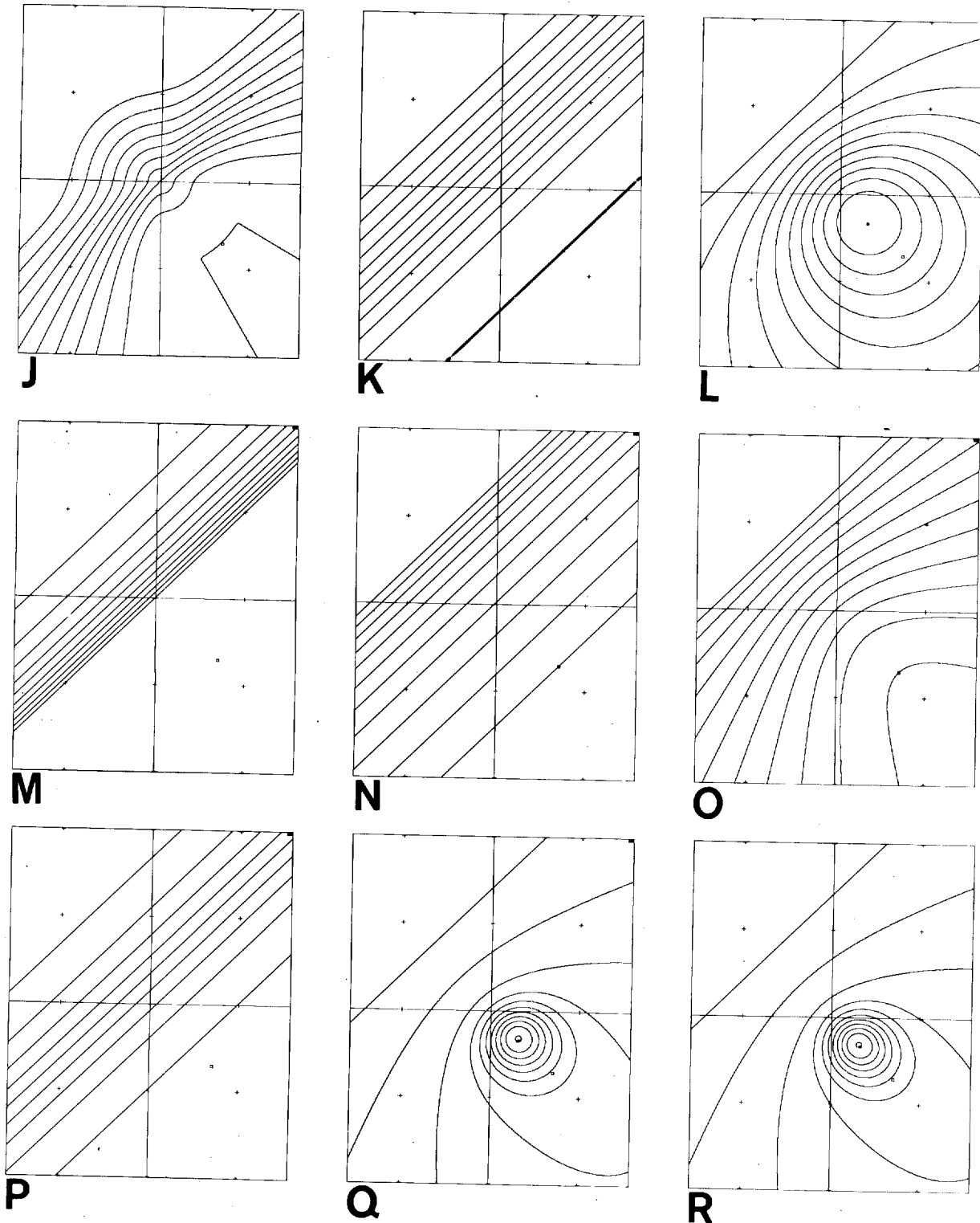
Fig. 19. (*Continued.*)

section in which the corresponding reflectance map is discussed. The first three (*A, B,* and *C*) are independent of the direction of the gradient, depending only on the slope. These give rise to rotationally symmetric diagrams. Six other diagrams (*E, F, K, M, N,* and *P*) show parallel straight lines. These correspond to reflectance maps which depend only on the slope in the direction away from the source. Reflectance maps for perfectly diffusing (*G*) and glossy (*Q* and *R*) surfaces are also included.

Shaded images of a mathematically defined surface were then created using these reflectance maps (see Fig. 20). Several of the subfigures give one a good appreciation for the shape of the object. Assumption of a perfectly diffusing surface (*G*) and Wiechel's modified brightness function (*L*) lead to good results, while the images corresponding to glossy surfaces (*Q* and *R*) are perhaps the most vivid.

The same set of reflectance maps was then used to make shaded images of a region in Switzerland for which a digital
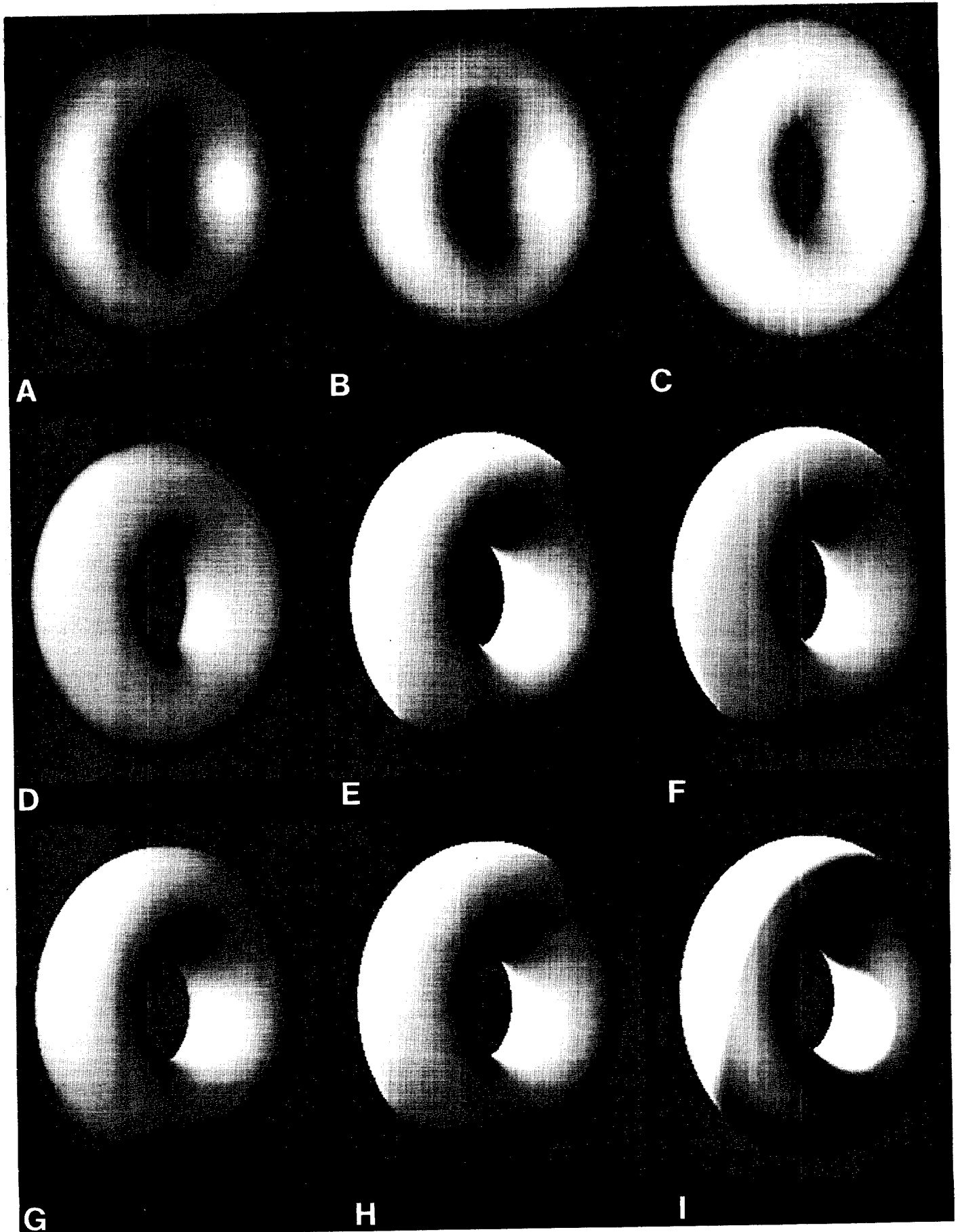
Fig. 20. Shaded images of a torus, based on geometry used in the previous figure.
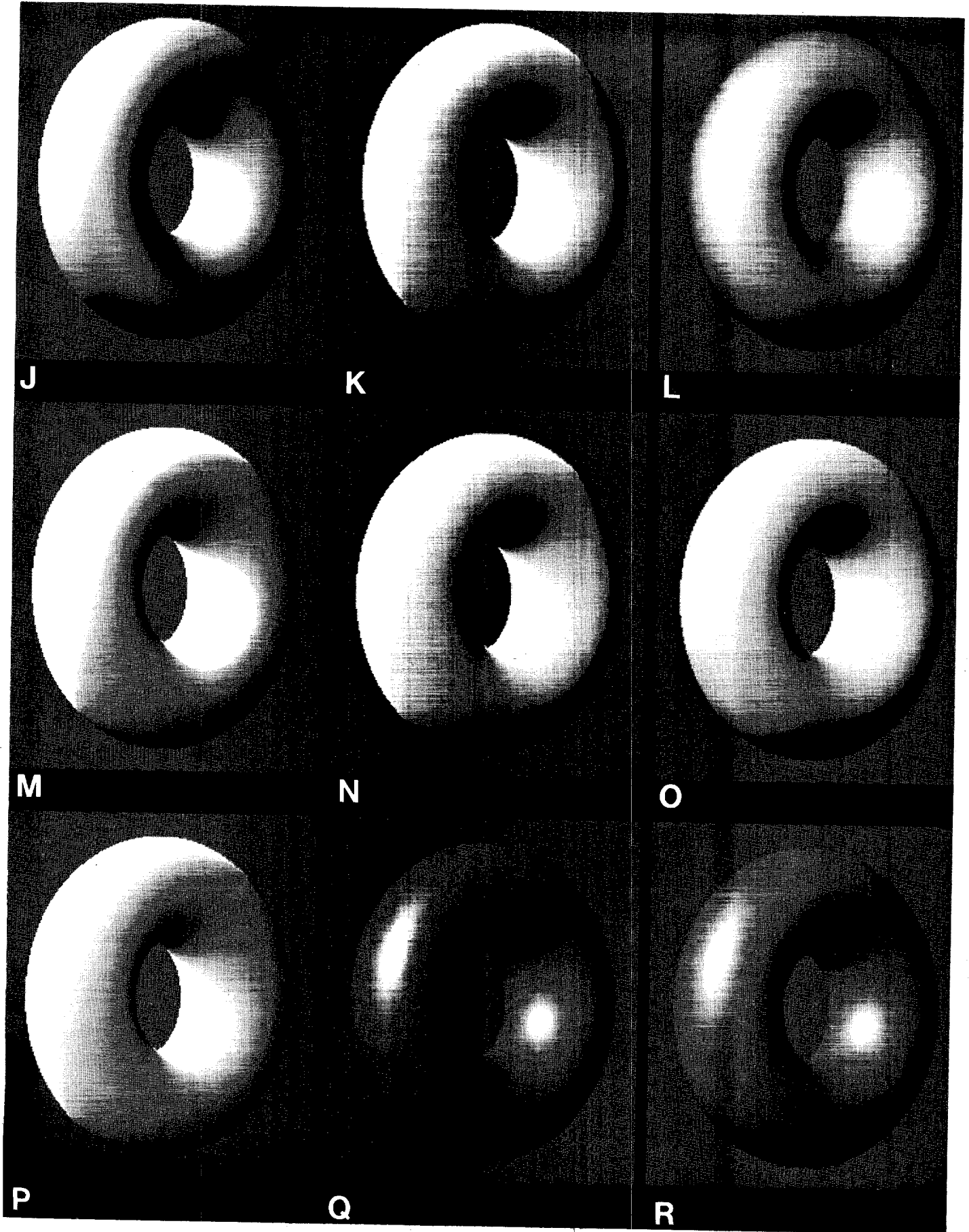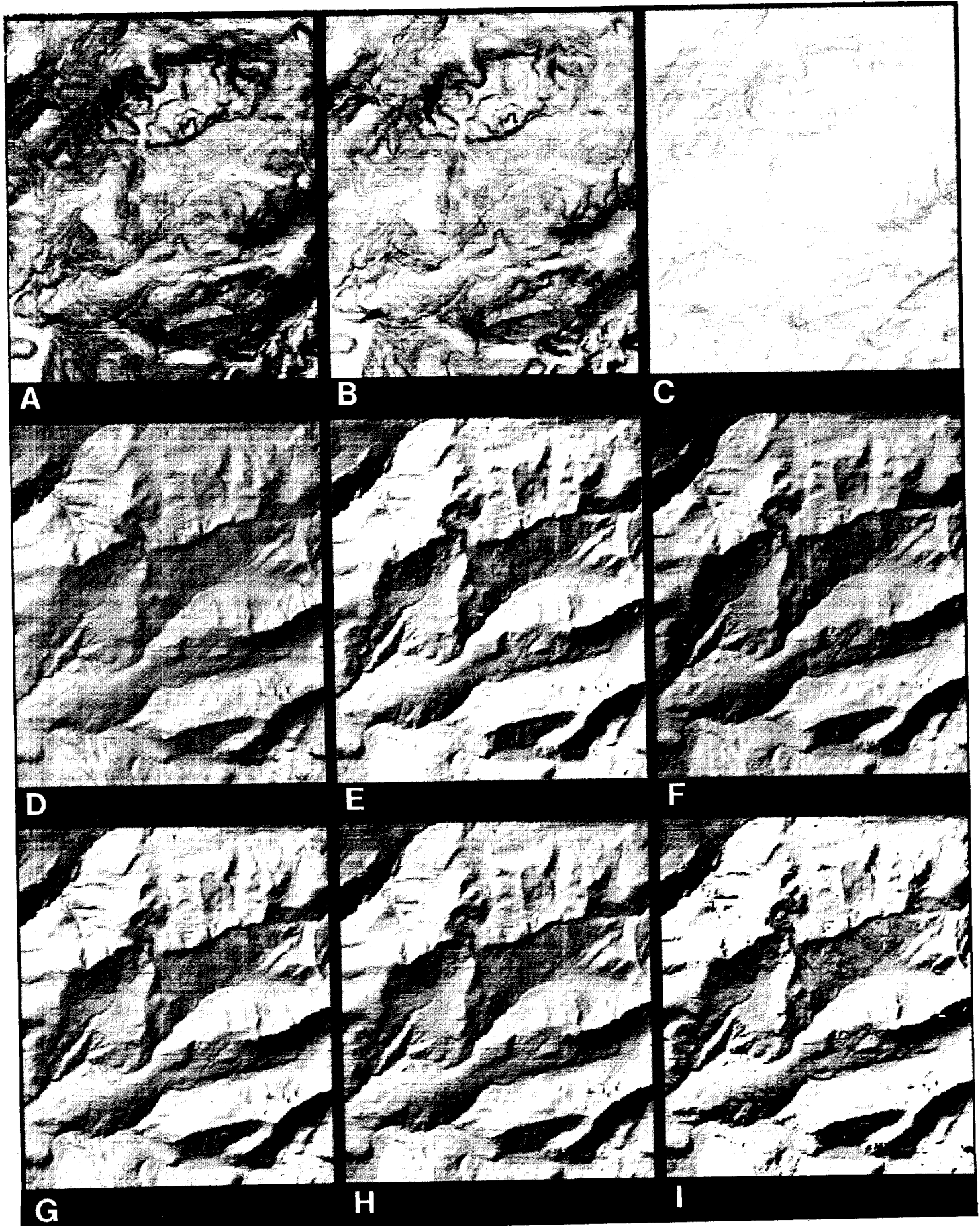
Fig. 21. Shaded images of a digital terrain model. The subfigures were made using the same reflectance maps as those used for the previous figure.

J

K

L

M

N

O

P

Q

R

Fig. 23. (Continued.)
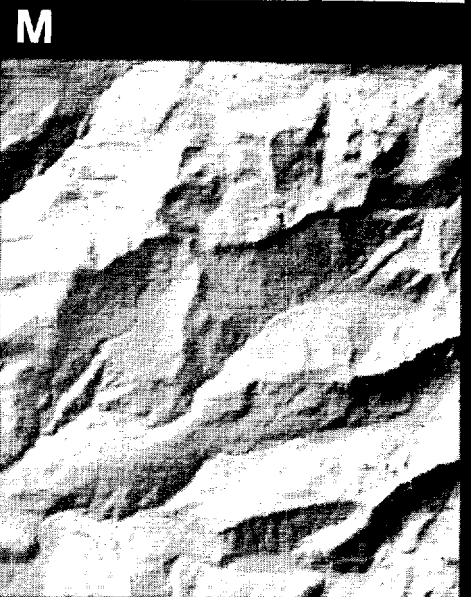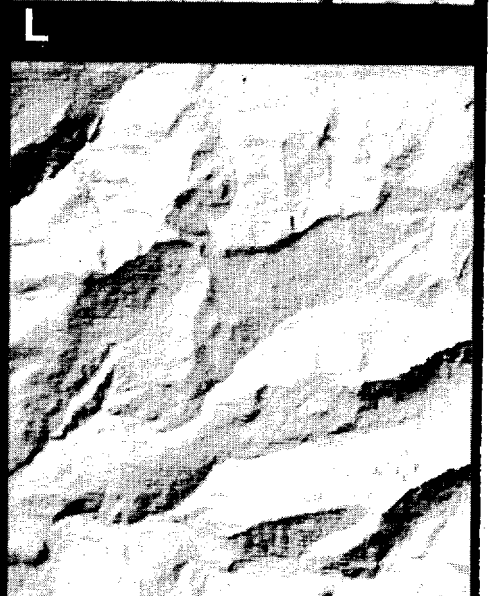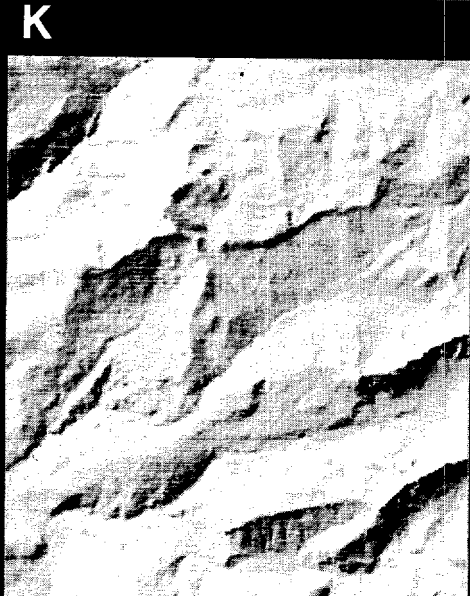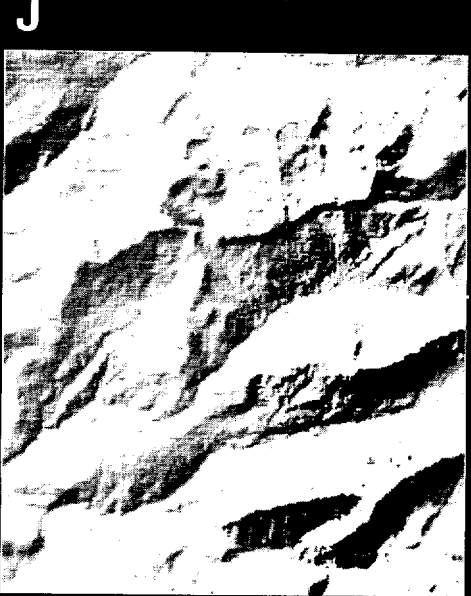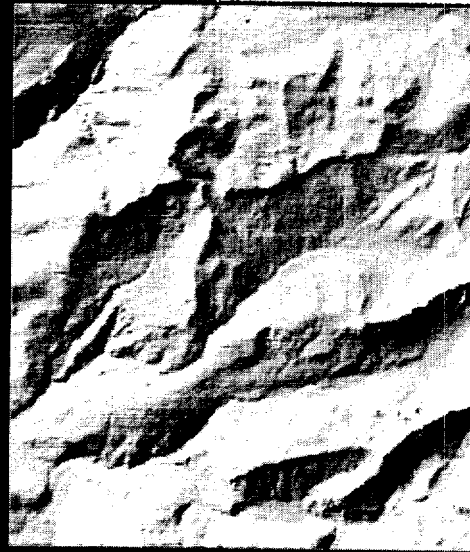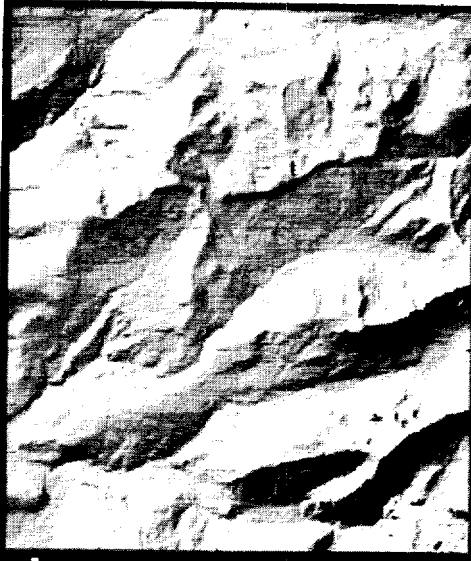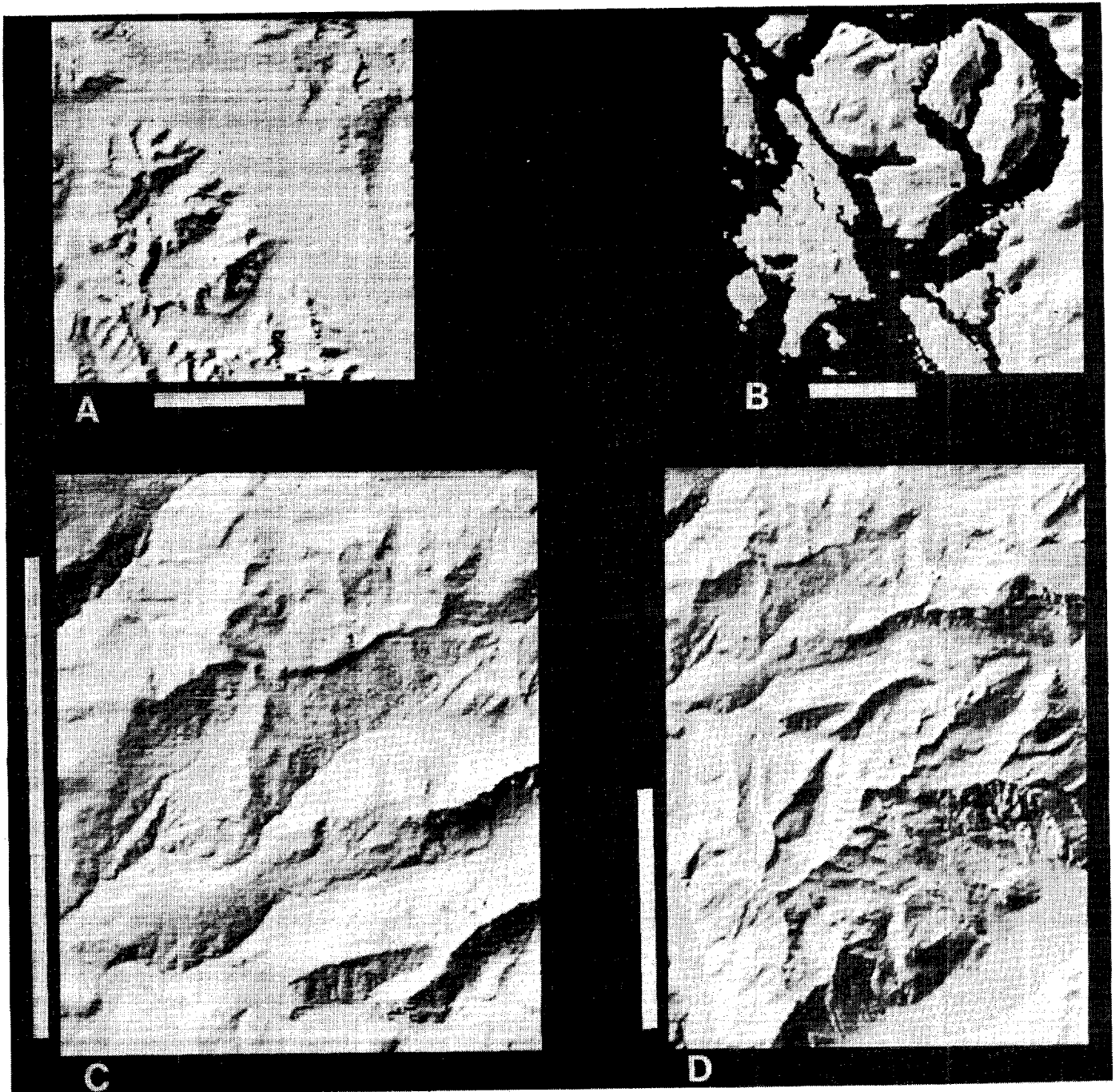
Fig. 22. Shaded images of several digital terrain models. A particularly simple reflectance map was used. The lines in the subfigures correspond to a length of 10 km on the surface. (a) Lake Louise, Alberta, Canada. (a) Gulf Islands, British Columbia. (c) Les Diablerets. Switzerland. (d) Dent de Morcles, Switzerland. (3) Mexico City, Mexico. (f) Jewell Ridge, Virginia. (g) White Tail Butte, Wyoming. (h) Tehacnapi Mountains, California. (i) Mount Index, Washington. (j) Mauritius, Indian Ocean.

terrain model was available (see Fig. 21). Some reflectance maps appear much better than others in conveying an immediate impression of surface shape. Rotationally symmetric reflectance maps (A, B, and C), corresponding to overhead illumination of the terrain, are not very good for example. Perfectly diffuse reflectance (G) is not optimal either. In fact, various approximations to the formula for a Lambertian reflector (H and K) seem to produce better results. Glossy reflectance components (Q and R), while very useful in the portrayal of regular objects, result in tones that are too dark to be useful in a map overlay. We may also not be used to seeing a geographi

Marsik's method (M), in which half of the surface is a featureless white, is clearly not very effective. Several of the other methods require careful scrutiny before conclusions about their adequacy can be made. Amongst the best are Wiechel's modified brightness method (L) and the modification of Brassel's method presented here (J). Several of the methods depending on the slope in the direction away from the light source appear to be quite adequate (F, K, N, and P). These are to be recommended unless there are good reasons to prefer one of the other methods.

Shaded images were created from several other digital terrain models (see Fig. 23) using one of these simple methods (P).
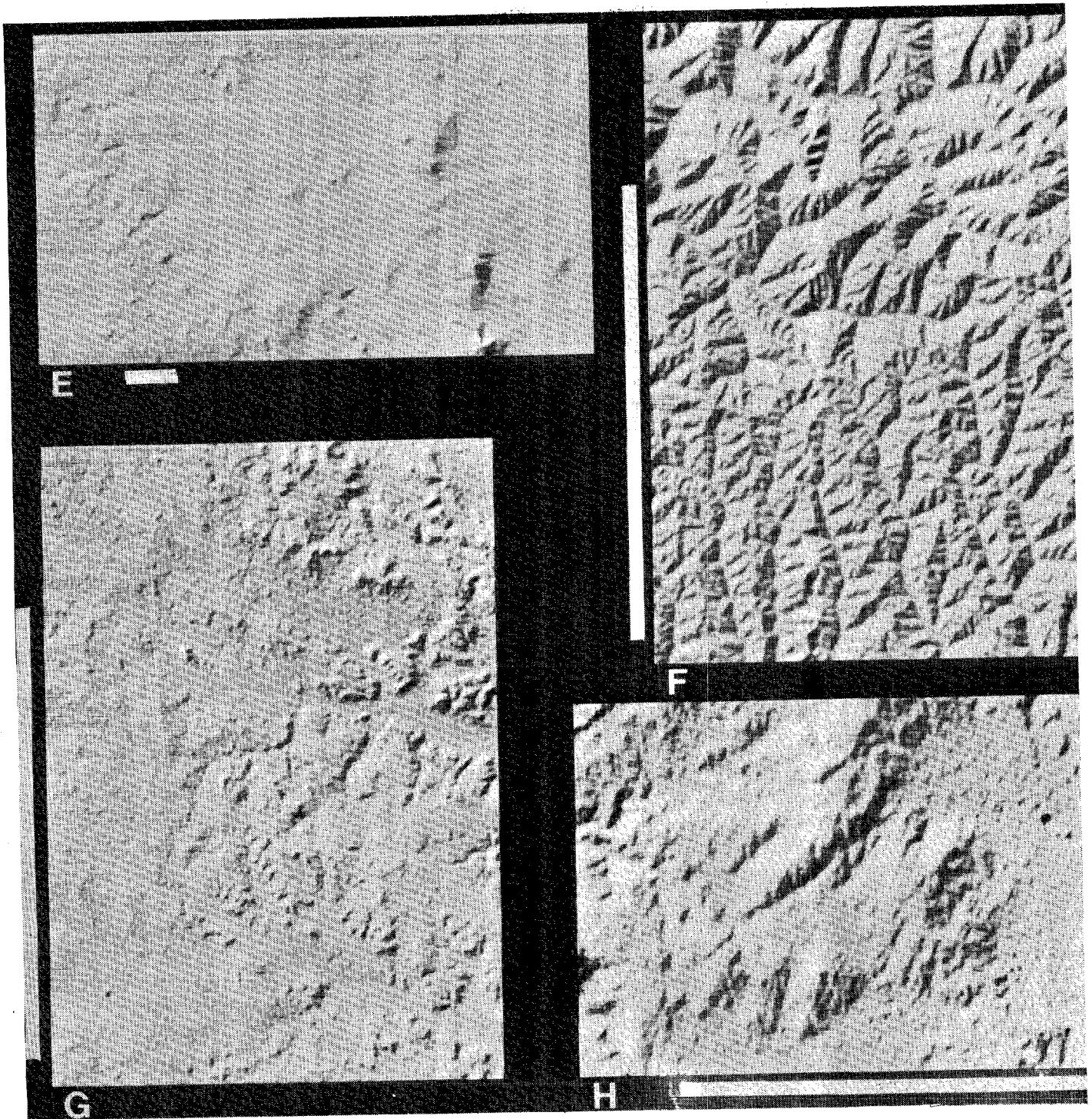
Fig. 22. (*Continued.*)

The terrain models differ widely in their quality, resolution and origin. They do show the utility of the methods described here in presenting the information in a digital terrain model to a human observer.

Shading is an important depth cue. The choice of reflectance map should not be based on some *ad hoc* model of surface behavior, experimental measurement of reflectance of some material, or formulas that happen to be easy to calculate. Instead, one should use a reflectance map that gives rise to an immediate, accurate perception of surface shape.

It is important to arrange for the range of gray tones in the shaded overlays to be limited so as to avoid obscuring plani-

metric detail [153]. This is an area that has not received much attention so far. Another important issue relates to the appropriate scale for shaded overlays. Shaded overlays are useful for large scale maps. For small scale maps it is necessary to generalize the surface to avoid the appearance of complex textures that may be difficult to interpret [1], [48], [73], [74], [154], [155]. This nonlinear process of removing small hills, ridges and valleys has not yet been satisfactorily automated.

An as yet unexplored possibility depends on finely sampled terrain elevations. This is the ability of shading to show fine detail. Contour maps have to be carefully generalized or smoothed to avoid showing confusing detail on a scale smaller
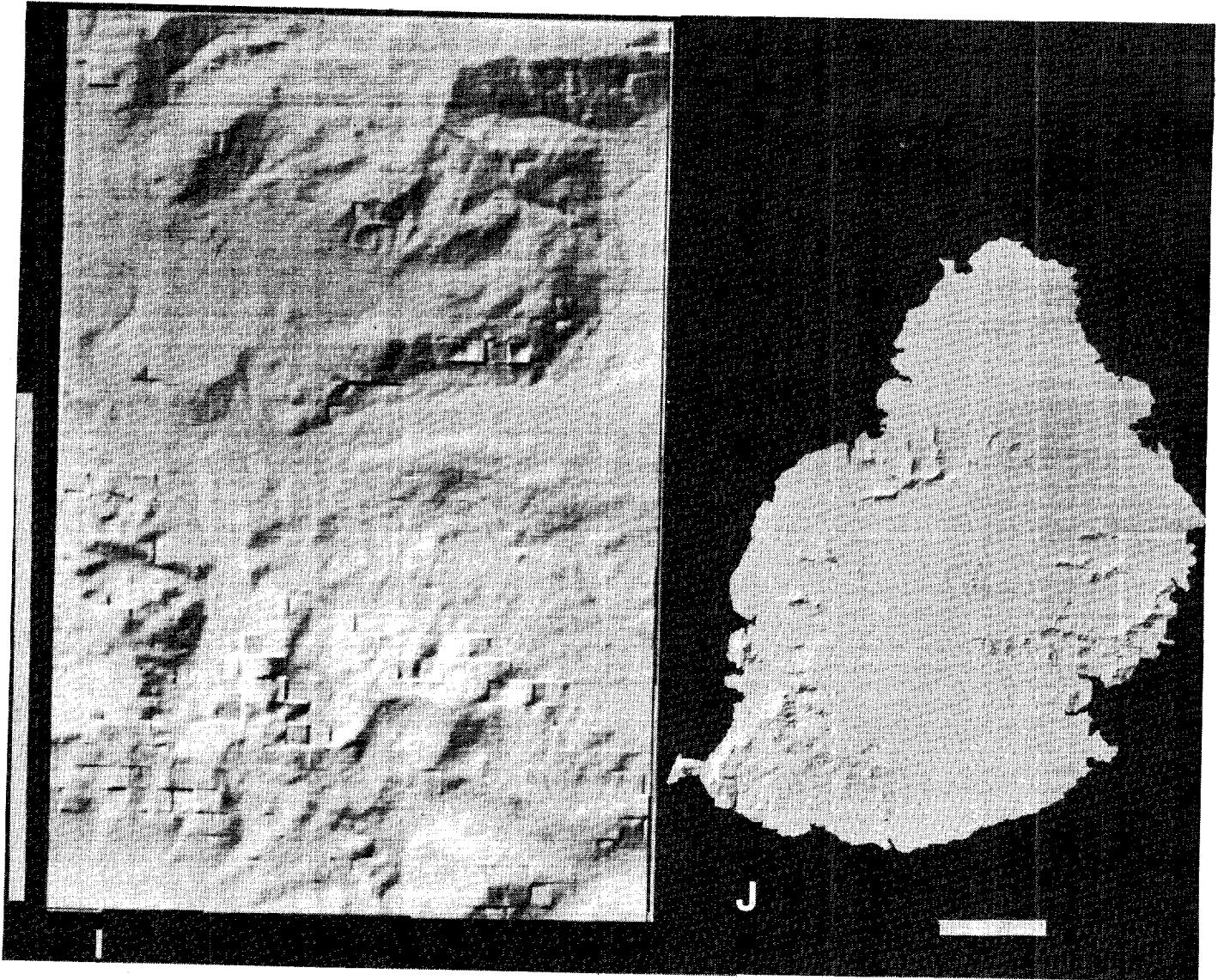
Fig. 22. (*Continued.*)

than the contour interval. This is not the case with shading, although historically the manually produced maps have always shown only quite coarse features. We do not yet know whether the textures produced by the shading method when working from really fine terrain models will be confusing, or of great value in identifying different types of terrain.

APPENDIX A
ROTATED GRADIENTS

It has been cartographic practice to assume a light source in the Northwest at a $45°$ elevation above the horizon. It is helpful in this case to introduce a rotated coordinate system (see Fig. 23) with

$$p' = (p - q)/\sqrt{2}$$

and

$$q' = (p + q)/\sqrt{2}.$$

If $\Delta x = \Delta y = \Delta$ say, then the slopes in the Northwest to Southeast and in the Southwest to Northeast direction, can be estimated particularly easily by combining the formulas for p_w
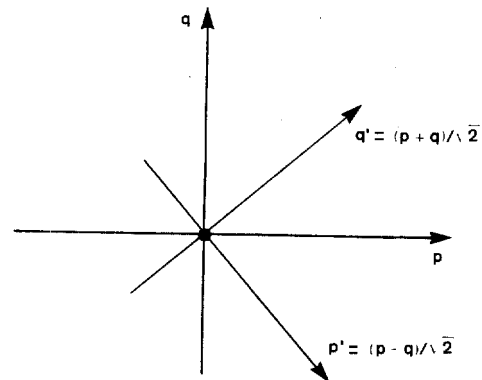
Fig. 23. Rotated coordinate system that may be convenient when the assumed light-source is in the northwest. The reflectance map is symmetrical about the p'-axis.

and q_w,

$$p'_w = [(z_{+0} + z_{+-} + z_{0-}) - (z_{-0} + z_{-+} + z_{0+})]/4\sqrt{2}\,\Delta$$

$$q'_w = [(z_{0+} + z_{++} + z_{+0}) - (z_{0-} + z_{--} + z_{-0})]/4\sqrt{2}\,\Delta.$$

If one wishes to estimate the slopes for the center of the top-right quadrant (in the unrotated coordinate system) rather than the central point one may combine the expressions for $p_{1/2}$ and $q_{1/2}$ to get the simple formulas,

$$p'_{1/2} = (z_{+0} - z_{0+})/\sqrt{2}\ \Delta$$

and

$$q'_{1/2} = (z_{++} - z_{00})/\sqrt{2}\ \Delta.$$

One advantage of the rotated coordinate system stems from the fact that models of surface reflectance considered here are symmetric with respect to a line pointing towards the source. That is, a surface element with slopes $p' = p'_0$ and $q' = q'_0$ say, has the same apparent brightness as one with slopes $p' = p'_0$ and $q' = -q'_0$. Thus a lookup table based on the rotated coordinate system can be smaller, since only that half of the table corresponding to $q' > 0$ need be stored.

So far we have assumed that the grid of the terrain model is aligned with the geographical coordinates. If instead the whole model is rotated anticlockwise by an angle θ, then slopes p'' and q'' can first be estimated from the model as described and then transformed as follows:

$$p = p'' \cos \theta - q'' \sin \theta$$

and

$$q = p'' \sin \theta + q'' \cos \theta.$$

Alternatively, the model can be resampled to produce a new version on a grid aligned with the axes.

APPENDIX B
SHADING APPARENT IN BLOCK DIAGRAMS

We can analyze the shading apparent in block diagrams by calculating the spacing between lines as a function of the surface orientation. Let a local surface normal be $n = (-p, -q, 1)$. A series of parallel planes, with common normal s, cuts the terrain surface. The intersections of these planes with the surface are viewed from a direction specified by the vector v. It is assumed that the viewer is at a great distance so that the profiles are projected orthographically along lines parallel to v (see Fig. 24).

The line of intersection of one of the cutting planes with the local tangent plane will be parallel to the vector $n \times s$, since the line lies in both planes and is therefore perpendicular to the normals, n and s. Now construct a plane through the line of intersection and the viewer. This plane, called the viewing plane, contains both $n \times s$ and v. The normal e of the viewing plane must therefore be perpendicular to both and can be defined as,

$$e = (n \times s) \times v$$

or

$$e = (n \cdot v)s - (s \cdot v)n.$$

If we let $p = (x, y, z)$, then the equation for the local tangent plane can be written,

$$n \cdot p = c_n$$

for some value of the constant c_n. Similarly, the equation of a particular cutting plane is,

$$s \cdot p = c_s.$$
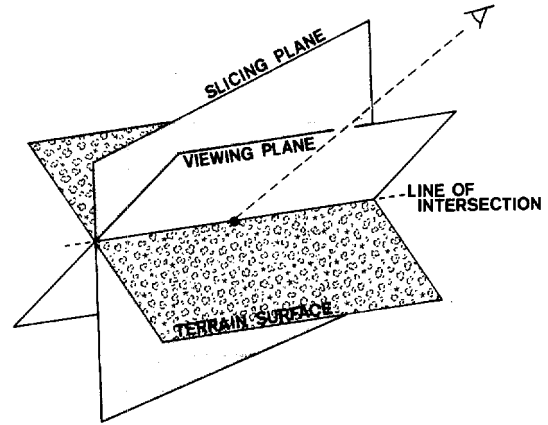
Fig. 24. The viewing plane contains the viewer and the line of intersection of the slicing plane with the terrain surface. Line spacing in the block diagram equals the spacing between successive viewing planes. The dotted line is parallel to the vector v.

Different values of c_s correspond to different cutting planes. The plane corresponding to the value $c_s + dc_s$ is separated from the plane corresponding to the value c_s by a distance dc_s/s, where s is the magnitude of the vector s. The equation for the viewing plane is just

$$e \cdot p = c_e.$$

Successive cutting planes will intersect the tangent plane in parallel lines. These give rise to parallel viewing planes corresponding to different values of the constant c_e. The spacing of these viewing planes is of interest, since it equals the spacing of the lines in the orthographic projection. The plane corresponding to the value $c_e + dc_e$ is separated from the plane corresponding to the value c_e by a distance of dc_e/e, where e is the magnitude of the vector e. In order to relate the spacing of lines in the block diagram to the spacing of the cutting planes we need to find the relationship between dc_e and dc_s.

A point p on the line of intersection lies in all three planes and therefore simultaneously satisfies the three equations given above for these planes. Expanding the last one of these, $e \cdot p = c_e$, we obtain,

$$(n \cdot v)(s \cdot p) - (s \cdot v)(n \cdot p) = c_e$$

or

$$(n \cdot v)c_s - (s \cdot v)c_n = c_e.$$

Here, c_n is fixed and so the relationship between changes in c_e and c_s is simply

$$dc_e = (n \cdot v)dc_s.$$

If the interval between cutting planes is δ and the map scale is k, then $dc_s/s = (k\delta)$. Consequently the spacing between lines in the block diagram dc_e/e is

$$d = k\delta (n \cdot v)(s/e)$$

where e is the magnitude of the vector $e = (n \cdot v)s - (s \cdot v)n$. Finally, we remember that

$$R(p, q) = r_w - (r_w - r_b)(b/d)$$

where b is the thickness of the lines. Thus

$$R(p, q) = r_w - (b/k\delta)(r_w - r_b)(e/s)(1/n \cdot v).$$

The view vector is tangent to the surface when $n \cdot v = 0$. When this dot product becomes negative, the surface is turned *away* from the viewer and should not be visible. Also note that $d = k\delta$, when $s \cdot v = 0$. One should therefore choose s and v so that they are not orthogonal, to avoid getting only evenly spaced parallel lines.

In the case of perspective projection, line density will increase with distance, and the resulting reflectance will be lowered because of a change in the effective scale factor k. If the projected profiles are plotted on a raster device, one has to also take into account the fact that the number of dots per unit line length is not constant. The dot density varies as max $[|\cos \theta|, |\sin \theta|]$, where θ is the angle between the line and the direction of the raster. This variation should be included if an accurate reflectance map is to be derived for output of this form.

APPENDIX C
ISOMETRIC VIEWS OF VERTICAL PROFILES

The transformation between the terrain coordinate system and that of an observer viewing the terrain obliquely can be found by multiplying a rotation matrix corresponding to rotation by θ_v about the x-axis with a matrix corresponding to rotation by $(\pi/2 + \phi_v)$ about the z-axis, where ϕ_v is the azimuth and θ_v is the zenith angle of the direction specified by the vector v. If the coordinates in the observer's system are x', y', and z', one finds,

$$x' = -\sin \phi_v x + \cos \phi_v y$$

$$y' = -\cos \phi_v \cos \theta_v x - \sin \phi_v \cos \theta_v y + \sin \theta_v z$$

$$z' = +\cos \phi_v \sin \theta_v x + \sin \phi_v \sin \theta_v y + \cos \theta_v z.$$

In the case of orthographic projection, the values of x' and y' are simply multiplied by the map scale k, to determine coordinates in the block diagram.

The general formula derived in Appendix B applies to all combinations of viewpoint and cutting plane orientation. It is interesting to look at a few special cases however. We can, for example, check our result for the contour interval in an ordinary contour map. Here $n = (-p, -q, 1)$, as always, and $s = (0, 0, 1)$, since we are considering the intersection of the surface with horizontal planes. Further, $v = (0, 0, 1)$ since the viewer is vertically above the surface. Here then $s = 1, n \cdot v = 1$, and $e = (p, q, 0)$. The line interval is, therefore,

$$d = (k\delta)/\sqrt{p^2 + q^2}.$$

The same reflectance map is obtained as before. Slightly more complicated is the case of Tanaka's inclined contours, where $s = (-p_0, -q_0, 1)$. Here, again, $n \cdot v = 1$, while,

$$e = (p - p_0, q - q_0, 0)$$

and

$$s = \sqrt{1 + p_0^2 + q_0^2}.$$

The line interval is, therefore,

$$d = (k\delta)[\sqrt{1 + p_0^2 + q_0^2}/\sqrt{(p - p_0)^2 + (q - q_0)^2}].$$

A result leading to the same reflectance map as the one derived before.

Finally, consider profiles running West to East, that is, $s = (0, 1, 0)$. The resulting traces may be viewed isometrically from the Southeast, a fairly common arrangement. Consult the
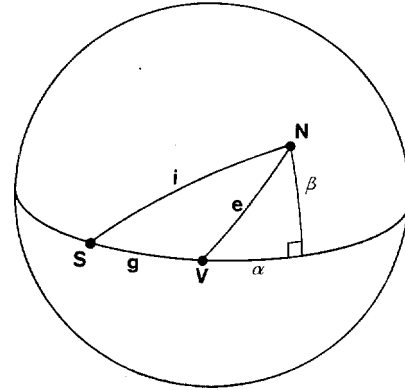
Fig. 25. Luminance longitude α and luminance latitude β of a surface element are defined as the longitude and latitude of a patch on a sphere with the same orientation. Longitude and latitude are measured relative to the luminance equator through the light source S and the viewer V.

diagram. Then $v = (1, -1, 1)$. Consequently, $n \cdot v = (1 - p + q)$ and $s \cdot v = -1$. Further, $e = (-p, 1 - p, 1)$ and hence,

$$d = (k\delta)(1 - p + q)/(\sqrt{2} \sqrt{1 - p + p^2}).$$

So, if $r_b = 0$ and $r_w = 1$,

$$R(p, q) = 1 - \sqrt{2} (b/k\delta) \sqrt{1 - p + p^2}/(1 - p + q).$$

Similarly, for profiles running South to North, $s = (1, 0, 0)$, and,

$$R(p, q) = 1 - \sqrt{2} (b/k\delta) \sqrt{1 + q + q^2}/(1 - p + q).$$

At times two orthogonal sets of slicing planes will be used, producing a mesh on the surface. The reflectance map corresponding to this case can be found by adding the last two formulas and subtracting one from the result.

APPENDIX D
LUMINANCE LONGITUDE AND LUMINANCE LATITUDE

A convention for specifying the orientation of the surface element relative to the direction of a light source and the viewer has become established in the work on planetary and lunar photometry. Imagine a sphere illuminated by a light source above the point S, viewed by an observer above the point V (see Fig. 25). These two points define a great circle which is called the luminance equator. Points on the sphere can be referenced using the longitude α measured from the point V along the equator, and the latitude β.

All possible surface orientations can be found on the sphere, and each surface orientation can be identified with some point N say. The luminance longitude and luminance latitude corresponding to a particular surface orientation are the longitude and latitude of N. It is not difficult to show that,

$$\cos e = \cos \beta \cos \alpha$$

and

$$\cos i = \cos \beta \cos (\alpha + g).$$

Conversely,

$$\tan \alpha = (\cos e \cos g - \cos i)/(\cos e \sin g)$$

and

$- 2IEG + E^2$]

45

where we have used the shorthand notation, $I = \cos i$, $E = \cos e$, and $G = \cos g$. These results can also be expressed in terms of the components of the gradient:

$$\tan \alpha = (p_0 p + q_0 q)/\sqrt{p_0^2 + q_0^2}.$$

So $\tan \alpha$ is simply the slope in the direction away from the source. Now,

$$1 + 2IEG - (I^2 + E^2 + G^2) = \frac{(q_0 p - p_0 q)^2}{[(1 + p^2 + q^2)(1 + p_0^2 + q_0^2)]}$$

$$I^2 - 2IEG + E^2 = \frac{[(p_0 p + q_0 q)^2 + (p_0^2 + q_0^2)]}{[(1 + p^2 + q^2)(1 + p_0^2 + q_0^2)]}$$

so,

$$\tan \beta = (q_0 p - p_0 q)/\sqrt{(p_0 p + q_0 q)^2 + (p_0^2 + q_0^2)}.$$

The Lommel–Seeliger law can be expressed in terms of luminance longitude and luminance latitude as,

$$\cos (\alpha + g)/[\cos \alpha + \cos (\alpha + g)]$$

and it is clear from this form that scene radiance is independent of luminance *latitude*.

ACKNOWLEDGMENT

REFERENCES

[1] E. Imhof, *Kartographische Geländedarstellung*. Berlin, Germany: W. de Gruyter & Co., 1965.

[2] J. G. Lehmann, *Darstellung einer neuen Theorie der Bezeichnung der schiefen Flächen im Grundriss oder der Situationzeichnung der Berge*. Leipzig, Germany, 1799.

[3] ——, *Die Lehre der Situations-Zeichnung oder Anweisung zum richtigen Erkennen und genauen Abbilden der Erd-Oberfläche in topographischen Charten und Situation-Planen*. Dresden, Germany: Arnoldische Buch- und Kunsthandlung, 1816.

[4] F. Chauvin, *Die Darstellung der Berge in Karten und Plänen, mit besonderer Rücksicht auf ihre Anwendbarkeit im Felde*. Berlin, Germany: Nauck'sche Buchhandlung, 1852.

[5] ——, *Das Bergzeichnen rationell entwickelt*. Berlin, Germany: Nauck'sche Buchhandlung, 1854.

[6] C. Vogel, "Die Terraindarstellung auf Landkarten mittels Schraffierung," *Petermanns Geogr. Mitt.*, vol. 39, p. 148, 1893.

[7] H. Bach, *Die Theorie der Bergzeichnung in Verbindung mit Geognosie*. Stuttgart, Germany, 1853.

[8] H. Wiechel, "Theorie und Darstellung der Beleuchtung von nicht gesetzmässig gebildeten Flächen mit Rücksicht auf die Bergzeichnung," *Civilingenieur*, vol. 24, pp. 335–364, 1878.

[9] L. Burmester, *Theorie und Darstellung gesetzmässig gestalteter Flächen*. Leipzig, Germany, 1875.

[10] Kitirô Tanaka, "A new method of topographical hill delineation," Memo. of the College of Engineering, Kyushu Imperial Univ., Fukuoka, Japan, vol. 5, no. 3, pp. 121–143, 1930.

[11] ——, "The orthographical relief method of representing hill features on a topographical map," *Geographical J.*, vol. 79, no. 3, pp. 213–219, Mar. 1932.

[12] H. StJ. L. Winterbotham, "Note on Professor Kitiro's method of orthographical relief," *Geographical J.*, vol. 80, pp. 518–520, 1932.

[13] P. Wilski, "Eine neue Japanische Darstellung der Höhen auf Landkarten," *Petermanns Geogr. Mitt.*, vol. 80, p. 359, 1934.

[14] Jadwiga Remiszewska, " Metoda cieć pochylych w kartograficznym obrazie urzeźbienia" (The method of inclined cut in the cartographic presentation of the form of the land), *Polish Geographical Rev.*, vol. 27, pp. 125–134, 1955.

[15] A. H. Robinson and N. J. W. Thrower, "A new method for terrain representation," *Geographical Rev.*, vol. 47, no. 4, pp. 507–520, Oct. 1957.

[16] A. H. Robinson, "The cartographic representation of the statistical surface," *Int. Yearbook of Cartography*, vol. 1, pp. 53–63, 1961.

[17] N. J. W. Thrower, "Extended uses of the method of orthogonal mapping of traces of parallel, inclined planes with a surface, especially terrain," *Int. Yearbook of Cartography*, vol. 3, pp. 26–28, 1963.

[18] C. M. King, *Techniques in Geomorphology*. New York: St. Martin's Press, 1966, pp. 255–256.

[19] T. K. Peucker, M. Tichenor, and W.-D. Rase, "Die Automatisierung der Methode der schrägen Schnittflächen," *Kartographische Nachrichten*, vol. 22, no. 4, pp. 143–148, 1972.

[20] T. M. Oberlander, "A critical appraisal of the inclined contour technique of surface representation," *Ann. Assoc. Amer. Geographers*, vol. 58, no. 4, pp. 802–813, 1968.

[21] A. H. Robinson, and R. D. Sale, *Elements of Cartography*, 3rd ed. New York: Wiley, 1969, pp. 189–196.

[22] A. H. Robinson, and N. J. W. Thrower, "On surface representation using traces of parallel inclined planes," *Ann. Assoc. Amer. Geographers*, vol. 59, no. 3. pp. 600–603, 1969.

[23] T. M. Oberlander, "Reply to Robinson–Thrower commentary," *Ann. Assoc. Amer. Geographers*, vol. 59, no. 3, pp. 603–605, 1969.

[24] Kitirô Tanaka, "The relief contour method of representing topography on maps," *Geographical Rev. Jap.*, vol. 15, nos. 9 & 10, pp. 655–671, 784–796 (Japanese) p. 797 (English abstract), 1939.

[25] ——, "The relief contour method of representing topography on maps," *Geographical Rev.*, vol. 40, no. 3, pp. 444–456, 1950.

[26] ——, "The relief contour method of representing topography on maps," *Surveying and Mapping*, vol. 11, p. 27, 1951.

[27] C. Köpcke, "Ueber Reliefs und Relief-Photogramme," *Civilingenieur*, vol. 31, 1885.

[28] Y. Pauliny, "Memoire über eine neue Situations Pläne- und Landkartendarstellungsmethode," *Streffen's Oesterreichischer Militärische Zeitschrift*, vol. 36, pg. 177, 1895.

[29] Erwin Raisz, *General Cartography*. New York and London, 1938.

[30] W. Pillewizer, "Geländedarstellung durch Reliefphotographie," *Kartographische Nachrichten*, vol. 7, p. 141, 1957.

[31] O. C. Stoessel, "Photomechanische Reliefschummerung," *Nachrichten aus dem Karten- und Vermessungswesen*, vol. 1, no. 10, pp. 53–55, 1959.

[32] A. A. Noma, and M. G. Misulia, "Programming topographic maps for automatic terrain model construction," *Surveying and Mapping*, vol. 19, no. 3, p. 335, Sept. 1959.

[33] H. R. Wilkerson, "Reliefschummerung durch Photographie von Geländemodellen," *Nachrichten aus dem Karten- und Vermessungswesen*, vol. 1, no. 10, pp. 60–62, 1959.

[34] H. Friedemann, "Von neuen Erfindungen: Anordnung und Verfahren zur Herstellung von Schummerungen für kartographische Zwecke," *Kartographische Nachrichten*, vol. 12, p. 150, 1962.

[35] P. Richarme, "L'estompage photographique," *Bulletin du comité francais de cartographie*, vol. 17, p. 188, 1963.

[36] P. Richarme, "The photographic hill shading of maps," *Surveying and Mapping*, vol. 23, no. 1, pp. 47–59, 1963.

[37] C. R. Gilman, "Photomechanical experiments in automated cartography," in *Proc. ASM Fall Meeting* (San Francisco, CA), 1971.

[38] H. G. Lyons, *The Representation of Reliefs on Maps*. Ministry of Finance, National Printing Department, Egypt, 1909.

[39] L. J. Harris, *Hill-shading for Relief-depiction in Topographical Maps*. London, 1959.

[40] E. Imhof, "Geländedarstellung in Karten grosser und mittlerer Massstäbe," *Vortrag Natf. Ges. Zürich*, January 1947.

[41] B. Carlberg, "Schweizer Manier und wirklichkeitsnahe Karte, Probleme der Farbgebung," *Kartographische Nachrichten*, vol. 4, pp. 8–14, 1954.

[42] G. Pöhlmann, "Heutige Methoden und Verfahren der Geländedarstellung," *Kartographische Nachrichten*, vol. 8, no. 3, pp. 71–78, 1958.

[43] H. Mietzner, "Die Schummerung unter Annahme einer naturgemässen Beleuchtung," *Kartographische Nachrichten*, vol. 9, no. 3, pp. 73–79, 1959.

[44] E. Imhof, "Probleme der Kartographischen Geländedarstellung," *Nachrichten aus dem Karten- und Vermessungswesen*, vol. 1, no. 10, p. 9–31, 1959.

[45] J. S. Keates, "Techniques of relief representation," *Surveying and Mapping*, vol. 21, no. 4, pp. 459–463, Dec. 1961.

[46] F. Hölzel, "Die Geländeschummerung in der Krise?" *Kartographische Nachrichten*, vol. 12, no. 1, pp. 17–21, Feb. 1962.

[47] E. Imhof, Ed., *International Yearbook of Cartography*. London, England: George Philip and Son, 1963.

[48] F. Hölzel, "Generalization problems in hill shading," *Nach-

richten aus dem Karten- und Vermessungswesen, vol. 5, no. 5, pp. 23–33, 1963.

[49] P. Yoéli, "Relief shading," *Surveying and Mapping*, vol. 19, p. 229, 1959.

[50] ——, "Analytische Schattierung," *Kartographische Nachrichten*, vol. 14, no. 4, pp. 142–148, 1965.

[51] ——, "Analytical hill shading," *Surveying and Mapping*, vol. 25, no. 4, pp. 573–579, Dec. 1965.

[52] ——, "Analytische Schattierung und Dichte," *Kartographische Nachrichten*, vol. 16, no. 1, pp. 17–23, 1966.

[53] ——, "Analytical hill shading and density," *Surveying and Mapping*, vol. 26, no. 2, pp. 253–259, June 1966.

[54] ——, "Die Mechanisierung der Analytischen Schattierung," *Kartographische Nachrichten*, vol. 16, no. 3, pp. 103–107, 1966.

[55] ——, "The mechanisation of analytical hill shading," *Cartographic J.*, vol. 4, no. 2, Dec. 1967.

[56] ——, "Die Richtung des Lichtes bei analytischer Schattierung," *Kartographische Nachrichten*, vol. 17, no. 2, pp. 37–44, 1967.

[57] ——, "An experimental electronic system for converting contours into hill-shaded relief," *International Yearbook of Cartography*, vol. 11, pp. 111–114, 1971.

[58] T. J. Blachut, Z. Marsik, and D. Makow, "Relief shading process," Canadian Patent No. 051-814, 1969.

[59] Z. Marsik, "Automatic Relief Shading," *Photogrammetrica*, vol. 27, no. 2, pp. 57–70, 1971.

[60] T. K. Peucker, "Computer cartography," Association of American Geographers, Washington, DC, Commission on College Geography, *Resource Paper No. 17*, pp. 41–54, 1972.

[61] T. K. Peucker and D. Cochrane, "Die Automation der Reliefdarstellung—Theorie und Praxis," *International Yearbook of Cartography*, vol. 14, pp. 128–139, 1974.

[62] T. K. Peucker, M. Tichenor, and W.-D. Rase, "The computer version of three relief representations," in *Display and Analysis of Spatial Data*, J. C. Davis, and M. McCullagh, Eds. New York: Wiley, 1974.

[63] M. Eckert, *Die Kartenwissenschaft: Forschung und Grundlagen zu einer Kartographie als Wissenschaft - Vol. 1*. Berlin, Germany: Walter de Gruyt, 1962.

[64] L. D. Carmichael, "Experiments in relief portrayal," *Cartographic J.*, vol. 1, pp. 11–17, 1964.

[65] M. Eckert, *Die Kartenwissenschaft: Forschung und Grundlagen zu einer Kartographie als Wissenschaft - Vol. 2*. Berlin, Germany: Walter de Gruyt, 1965.

[66] M. S. Monmonier, "The production of shaded maps on the digital computer," *Professional Cartographer*, vol. 17, no. 5, pp. 13–14, Sept. 1965.

[67] P. K. Koldayev, "Plastic colour and shadow relief representation," *Academy of Sciences of the USSR*, Council of Soviet Cartographers, Moscow, 1967.

[68] B. F. Sprunt, "Computer-generated halftone images from digital terrain models," M.Sc. dissertation, Dep. Mathematics, Univ. Southampton, Southampton, England. 1969.

[69] B. Anda, "Automatic hill-shading using an automatic flatbed drafting machine with a standard photohead," *ITC Journal* (Enschede, The Netherlands). no. 2, pp. 212–216, 1974.

[70] R. M. Batson, E. Edwards, and E. M. Eliason, "Computer generated relief images," *J. Res., U. S. Geological Survey*, vol. 3, no. 4, pp. 401–408, July–Aug. 1975.

[71] K. Brassel, *"Modelle und Versuche zur automatischen Schräglichtschattierung,"* Ph.D. dissertation, Geography Dep., Univ. Zurich, Klosters, Switzerland, 1973.

[72] ——, "Ein- und mehrfarbige Printerdarstellungen," *Kartographische Nachrichten*, no. 5, pp. 177–183, 1973.

[73] ——, "Ein Modell zur Automatischen Schräglichtschattierung," *International Yearbook of Cartography*, pp. 66–77, 1974.

[74] ——, "A Model for Automated Hill Shading," *Amer. Cartographer*, vol. 1, no. 1, pp. 15–27, Apr. 1974.

[75] W. Blascke, "Le Modele Digital M.I.T.," *Societe Francaise de Photogrammetrie*, Bull. 27, pp. 37–40, July 1967.

[76] B. W. Boehm, "Tabular representations of multi-variate functions—with applications to topographic modelling," in *ACM, 22nd National Conf. Proc.*, pp. 403–415, 1967.

[77] W. Aumen, "A new map form: Numbers," *International Yearbook of Cartography*, vol. 10, pp. 80–84, 1970.

[78] M. W. Grist, "Digital ground models: An account of recent research," *Photogrammetric Rec.*, vol. 70, no. 4, pp. 424–441, Oct. 1972.

[79] F. Silar, "Das digitale Geländemodell—Theorie und Praxis," *Vermessungstechnik*, vol. 20, no. 9, pp. 327–329, 1972.

[80] K. Torlegard, "Digital terrain models—General survey and Swedish experiences," *Bildmessung und Luftbildwesen*, vol. 40, no. 1, pp. 21–30, 1972.

[81] American Society of Photogrammetry, *Proc. Digital Terrain Models (DTM) Symp.* (St. Louis, MO, May 9–11, 1978).

[82] Wild Heerburg and Raytheon, "B8 Stereomat Automated Plotter," company sales literature, 1968.

[83] S. Bertram, "The UNIMACE and the automatic photomapper," *Photogrammetric Eng.*, vol. 35, pp. 569–576, 1969.

[84] R. H. Seymour and A. E. Whiteside, "A new computer-assisted stereocomparator," *Bendix Tech. J.*, pp. 1–5, Spring 1972.

[85] B. G. Crawley, "Gestalt contours," *Canadian Surveyor*, vol. 28, no. 3, pp. 237–246, Sept. 1974.

[86] Bendix Research Laboratories, "AS-11B-X automatic stereo mapper," RADC-TR-76-100, Rome Air Development Center, Griffiss A F B, N Y, Apr. 1976.

[87] D. J. Panton, "Digital stereo mapping," *Countermeasures*, p. 12, May 1976.

[88] W. Loscher, "Some aspects of orthophoto technology," *Photogrammetric Rec.*, vol. 6, no. 30, pp. 419–432, 1967.

[89] T. J. Blachut, "Further extension of the orthophoto technique," *Canadian Surveyor*, vol. 22, no. 1, pp. 206–220, 1968.

[90] T. J. Blachut and M. C. Van Wijk, "3-D information from orthophotos," *Photogrammetric Eng.*, pp. 365–376, April 1970.

[91] T. A. Hughes, A. R. Shope, and F. S. Baxter, "USGS automatic orthophoto system," *Photogrammetric Eng.*, vol. 37, pp. 1055–1062, 1971.

[92] A. Beyer, "Zur Erfassung flächen Geländes durch willkürlich verteilte Höhenpunkte," *Vermessungstechnik*, vol. 20, no. 6, pp. 204–207, 1972.

[93] T. K. Peucker and N. Chrisman, "Cartographic data structures," *American Cartographer*, vol. 2, no. 1, pp. 55–69, Apr. 1975.

[94] E. Keppel, "Approximating complex surfaces by triangulation of contour lines," *IBM J. Res. Develop.*, Jan. 1975.

[95] T. K. Peucker, R. J. Fowler, J. J. Little, and D. M. Mark, "Digital representation of three-dimensional surfaces by triangulated irregular networks (TIN)," Tech. Rep. 10 (Revised), Dep. Geography, Simon Fraser University, Barnaby, BC, Canada, 1976.

[96] A. K. Lobeck, *Block Diagrams*. New York: Wiley, 1924. Reprinted by Emerson-Trussell, Amherst, MA, 1958.

[97] M. Schuster, *Das Geographische und Geologische Blockbild*. Berlin, Germany: Akademie Verlag, 1954.

[98] D. A. Goosen, "Blockdiagrams," *ITC Information* (Delft, The Netherlands), no. 3, Spring 1962.

[99] G. F. Jenks and D. A. Brown, "Three-dimensional map construction," *Science*, vol. 154, no. 3750, pp. 857–864, 18 Nov. 1966.

[100] B. Kubert, J. Szabo, and S. Giulieri, "The perspective representation of functions of two variables," *J. A.C.M.*, vol. 15, no. 2, pp. 193–204, Apr. 1968.

[101] D. Douglas, "Viewblok: A computer program for constructing perspective view block diagrams," *Rev. Geographie de Montreal*, vol. 26, pp. 102–104, 1971.

[102] T. J. Wright, "A two-space solution to the hidden line problem for plotting functions of two variables," *IEEE Trans. Comput.*, vol. C-22, pp. 28–33, Jan. 1973.

[103] C. Wylie, G. Romney, and D. Evans, "Half-tone perspective drawings by computer, " in *Proc. Fall Joint Computer Conf.*, pp. 49–58, 1967.

[104] A. Appel, "Some Techniques for shaded machine rendering of solids," in *Proc. Spring Joint Computer Conf.*, pp. 37–45, 1968.

[105] J. E. Warnock, "A hidden-surface algorithm for computer generated half-tone pictures," TR 4-15, Dep. Computer Science, Univ. Utah, Salt Lake City, 1969.

[106] G. S. Watkins, "A real-time visible surface algorithm," Report UTEC-CSC-70-101, Dep. Computer Science, Univ. Utah, Salt Lake City, June 1970.

[107] W. J. Bouknight, "A procedure for generation of three-dimensional half toned computer graphics presentations," *Commun. A.C.M.*, vol. 13, no. 9, pp. 527–536, Sept. 1970.

[108] R. A. Goldstein and R. Nagel, "3-D visual simulation," *Simulation*, vol. 16, pp. 25–31, 1971.

[109] H. Gouraud, "Computer display of curved surfaces," *IEEE Trans. Comput.*, vol. C-20, pp. 623–629, June 1971.

[110] M. E. Newell, R. G. Newell, and T. L. Sancha, "A new approach to the shaded picture problem," in *Proc. ACM National Conf.* (Boston, MA), vol. 1, pp. 443–450, 1973.

[111] J. Staudhammer and D. J. Odgen "Computer graphics for half-tone three-dimensional object images," *Computers and Graphics*, vol. 1, no. 1, pp. 109–114, 1975.

[112] E. A. Catmull, "Computer display of curved surfaces," in *Proc. IEEE Conf. Computer Graphics, Pattern Recognition and Data Structures* (Los Angeles, CA, May 1975), IEEE Cat. No. 75CH0981-1C, pp. 11–17, 1975.

[113] Phong Bui-Tuong, "Illumination for computer-generated images," *Commun. A.C.M.*, vol. 18, no. 6, pp. 311–317, June 1975.

[114] J. F. Blinn and M. E. Newell, "Texture and reflection in computer generated images," *Commun. A.C.M.*, vol. 19, no. 10, pp. 542–547, Oct. 1976.

[115] J. F. Blinn, "Models of light reflection for computer synthesized pictures," in *SIGGRAPH '77, Proc. 4th Conf. Computer Graphics and Interactive Techniques*, A.C.M., pp. 192–198, 1977.

[116] ——, "A scan line algorithm for displaying parametrically de-

fined surfaces," in *SIGGRAPH '78, Proc. 5th Conf. on Computer Graphics and Interactive Techniques*, A.C.M., 1978.

[117] J. H. Lambert, *Photometria sive de mensura de gratibus luminis, colorum et umbrae*, Eberhard Klett, Augsburg, 1760. Translated by W. Engelman "Lambert's Photometrie," *Ostwald's Klassiker der exacten Wissenschaften*, no. 31-33, Leipzig, Germany, 1892.

[118] l'Abbé de Lacaille, *Traite d'optique sur la gradation de la lumière*, (Ouvrage posthume de M. Bouguer), L. F. Delatour, A Paris, 1760. Translated by W. E. K. Middleton, *Optical Treatise on the Gradation of Light*. Toronto, Ont., Canada: University of Toronto Press, 1961.

[119] E. Lommel, "Ueber Fluorescenz," *Ann. Phys.* (Leipzig, Germany), vol. 10, pp. 449-472, 1880.

[120] H. Seeliger, "Die Photometrie von diffus reflektierenden Flächen," *S. B. Bayer. Akad. Wiss.*, vol. 18, p. 20, 1888.

[121] A. Markov, "Les particularités dans le réflexion de la lumière par la surface de la lune," *Astronomische Nachrichten*, vol. 221, pp. 65-78, 1924.

[122] E. Schönberg, "Untersuchungen zur Theorie der Beleuchtung des Mondes auf Grund photometrischer Messungen," *Acta Soc. Sci. Fennicae*, vol. 50, pp. 1-70, 1925.

[123] V. G. Fesenkov, "Photometric investigations of the lunar surface," *Astronomicheskii Zhurnal*, vol. 5, pp. 219-234, 1929. Translated by Redstone Scientific Information Center. Apr. 1968.

[124] M. Minnaert, "The reciprocity principle in lunar photometry," *Astrophys. J.*, vol. 93, pp. 403-410, 1941.

[125] V. A. Fedoretz, "Photographic photometry of the lunar surface," *Publ. Kharkov Obs.*, vol. 2, pp. 49-172, 1952.

[126] M. Minnaert, "Photometry of the moon," in *Planets and Satellites*, G. P. Kuiper, and B. M. Middlehurst, Eds. Chicago, IL: Univ. Chicago Press, 1961, vol. 3, ch. 6, pp. 213-248.

[127] V. Fesenkov, "Photometry of the Moon," in *Physics and Astronomy of the Moon*, Z. Kopal, Ed. New York: Academic Press, 1962, pp. 99-130.

[128] B. W. Hapke, "A Theoretical Photometric Function for the Lunar Surface," *J. Geophys. Res.*, vol. 68, no. 15, pp. 4571-4586, Aug. 1963.

[129] B. Hapke and H. Van Horn, "Photometric studies of complex surfaces, with applications to the moon," *J. Geogphys. Res.*, vol. 68, no. 15, pp. 4545-4570, Aug. 1963.

[130] B. Hapke, "An improved theoretical lunar photometric function," *Astronomical J.*, vol. 71, no. 5, pp. 333-339, June 1966.

[131] W. E. Middleton and A. G. Mungall, "The luminous directional reflectance of snow," *J. Opt. Soc. Amer.*, vol. 42, no. 3, pp. 572-579, 1952.

[132] M. Planck, *The Theory of Heat Radiation*. New York: Dover, 1959.

[133] P. Beckmann and A. Spizzichnio, *The Scattering of Electromagnetic Waves from Rough Surfaces*. New York: Pergamon Press, 1963.

[134] K. E. Torrance, E. M. Sparrow, and R. C. Birkebak, "Polarization, directional distribution, and off-specular peak phenomena in light reflected from roughened surfaces," *J. Opt. Soc. Amer.*, vol. 56, no. 7, pp. 916-925, July 1966.

[135] K. E. Torrance and E. M. Sparrow, "Theory for off-specular reflection from roughened surfaces," *J. Opt. Soc. Amer.*, vol. 57, no. 9, pp. 1105-1114, Sept. 1967.

[136] T. S. Trowbridge and K. P. Reitz, "Average irregularity representation of a rough surface for ray reflection," *J. Opt. Soc. Amer.*, vol. 65, no. 5, pp. 531-536, May 1975.

[137] B. K. P. Horn, "Determining shape from shading," in *The Psychology of Computer Vision*, P. H. Winston, Ed. New York: McGraw-Hill, 1975, ch. 4.

[138] ——, "Understanding image intensities," *Artificial Intelligence*, vol. 8, no. 11, pp. 201-231, 1977.

[139] ——, and B. L. Bachman, "Using synthetic images to register real images with surface models," *Commun. A.C.M.*, vol. 21, no. 11, pp. 914-924, Nov. 1978.

[140] —— and R. W. Sjoberg, "Calculating the reflectance map," *Appl. Opt.*, vol. 18, no. 11, pp. 1770-1779, June 1979.

[141] R. J. Woodham, "Photometric stereo: A reflectance map technique for determining surface orientation from image intensity," *Image Understanding Systems and Industrial Applications*, in *Proc. S.P.I.E.*, Aug. 1978, vol. 155.

[142] F. E. Nicodemus, J. C. Richmond, and J. J. Hsia, I. W. Ginsberg, T. Limperis, "Geometrical considerations and nomenclature for reflectance," NBS Monograph 160, National Bureau of Standards, U.S. Dep. Commerce, Washington, DC, Oct. 1977.

[143] F. E. Nicodemus, Ed., "Self-Study manual on optical radiation measurements," NBS Technical Notes 910-1, 910-2, & 910-3, National Bureau of Standards, U.S. Dep. Commerce, Washington, DC, 1976, 1977, & 1978.

[144] H. C. Babcock, "Evaluation of a stereocompilation digitizer," in *Congress on Surveying and Mapping, 30th Annual Meeting*, 1970, pp. 338-347.

[145] E. J. McCartney, *Optics of the Atmosphere: Scattering by Molecules and Particles*. New York: Wiley, 1976.

[146] S. D. Conte and C. de Boor, *Elementary Numerical Analysis*, New York: McGraw-Hill, 1972.

[147] R. W. Hamming, *Numerical Methods for Scientists and Engineers*. New York: McGraw-Hill, 1962.

[148] R. D. Richtmeyer and K. W. Morton, *Difference Methods for Initial-Value Problems*. New York: Wiley, 1967, pp. 136-143.

[149] F. B. Hildebrand, *Introduction to Numerical Analysis*. New York: McGraw-Hill, 1956, 1974.

[150] P. M. Bridge and J. L. Inge, "Shaded relief of Mars," Atlas of Mars, MH 25 M IR, JPL Contract WO-8122, USGS, U.S. Dep. Interior, 1972.

[151] T. Rindfleisch, "Photometric method for lunar topography," *Photogrammetric Eng.*, vol. 32, pp. 262-276, 1966.

[152] W. Bantel, "Der Reproduktionsweg vom einfarbigen Relieforiginal zur mehrfarbigen Reliefkarte," *International Yearbook of Cartography*, vol. 13, pp. 134-136, 1973.

[153] A. DeLucis, "The effect of shaded relief terrain representation on map information accessibility," in *American Congress on Surveying and Mapping, 31st Annual Meeting* (Washington, DC), pp. 641-657, 1971.

[154] J. Neumann, "Begriffsgeschichte und Definition des Begriffes 'Kartographische Generalisierung'," *International Yearbook of Cartography*, vol. 13, pp. 59-67, 1973.

[155] F. Topfer, Ed. *Kartographische Generalisierung*. Gotha, Leipzig, Germany: Geographisch-Kartographische Anstalt, 1974.

Acousto-Optics—A Review of Fundamentals

ADRIANUS KORPEL, FELLOW, IEEE

Invited Paper

Abstract—The paper first reviews the historical development of acousto-optics and its applications. Following this, a heuristic explanation of acousto-optic effects is presented, with the emphasis on the plane wave model of interaction. Finally, there is a discussion of some basic configurations of relevance to signal processing.

I. INTRODUCTION

ACOUSTO-OPTICS deals with the interaction of sound and light. The existence of such an interaction was predicted by Brillouin [1] in 1922. Experimental verification followed in 1932, by Lucas and Biquard [2] in France, and Debye and Sears [3] in the U.S. Brillouin's original theory predicted a phenomenon closely analogous to X-ray diffraction in crystals. In the latter, the atomic planes cause multiple reflections of an incident electromagnetic plane wave. These reflections interfere constructively for certain critical angles of incidence, to cause enhanced overall reflection (also called diffraction or scattering). In acoustic diffraction, the role of the atomic planes is assumed by planes of compression and rarefaction, induced by ultrasonic waves with frequencies between 1 MHz and 2 GHz. As a result, similar diffraction effects occur as in crystals.

The similarity between atomic planes and sound wave fronts should, however, not be carried too far. For one thing, atomic planes are sharply defined in location and regular in structure. Sound waves, on the other hand, are essentially sinusoidal and, when limited in the transverse direction, spread as they propagate, thereby giving rise to very complex density distributions and wavefronts. To a first approximation however, the analogy is very useful.

The fact that the sound wavefronts move causes the diffracted light to be Doppler shifted. Brillouin predicted a basic Doppler shift equal to the sound frequency. This phenomenon of frequency shifting became of importance only in recent times and forms, in fact, the basis of heterodyning techniques in modern signal processing applications.

Long before such sophisticated techniques became practical through the invention of the laser, the application of acousto-optics as such to (parallel) signal processing had become evident, and experiments were already in progress using arc lamps and other conventional light sources. The pioneer in this field is probably Okolicsanyi who, in the early 1930's used acousto-optic techniques in the Scophony television projector [4]. In the course of this work Okolicsanyi made a thorough investigation of possible sound cell applications (for instance time compression) which he published in 1937 [5].

It was not until the early 1960's that the subject was taken up again when signal processors were investigated by Rosenthal [6], Liben [7], Slobodin [8] and Arm *et al.* [9]. By the end of the 1960's lasers were beginning to be used routinely which in turn led to the development of coherent heterodyne detection techniques by King *et al.* [10] and Whitman *et al.* [11]. Thus, almost 50 years after Brillouin's analysis, all the phenomena he predicted had been put to use.

During the past decade even more refined techniques of signal processing were developed, in particular ones involving crossed sound cells (two-dimensional processing) and time integration. A detailed discussion of this development is outside the scope of this introduction. The interested reader will find abundant information in a number of review articles [12]-[17], as well as in subsequent papers in this issue.

In what follows, the author will first give a brief, heuristic explanation of acousto-optic effects, emphasizing the plane wave interaction model but tracing, wherever practical, the connection with other, perhaps more familiar models. Next, some configurations that form the building blocks of most signal processors will be reviewed. This paper will be limited to the basic elements and avoid system details such as lens configurations, dynamic range considerations, intermodulation effects, etc. A discussion of such details is not appropriate for this brief review; they can best be learned from the papers that follow.

II. HEURISTIC THEORY

As pointed out in the Introduction, Brillouin's analysis of acousto-optic interactions predicted an effect, now called acoustic Bragg diffraction, similar to X-ray diffraction in crystals. The principle of acoustic Bragg diffraction is illustrated in Fig. 1 which shows a beam of light directed at a high frequency sound wave. At certain critical angles of incidence $\pm\alpha_B$, the incident beam generates a new one whose direction differs by $2\alpha_B$. The angle α_B is called the Bragg angle and is given by

$$\sin \alpha_B = \frac{\lambda}{2\Lambda} \tag{1}$$

where λ is the wavelength of light in the acoustic medium and Λ is the acoustic wavelength.

The value given by (1) refers to the angle observed inside the medium of sound propagation. Outside the medium, Snell's law changes the value of α_B to α_B'

$$\sin \alpha_B' = \frac{n\lambda}{\Lambda} = \frac{\lambda_v}{\Lambda} \tag{2}$$
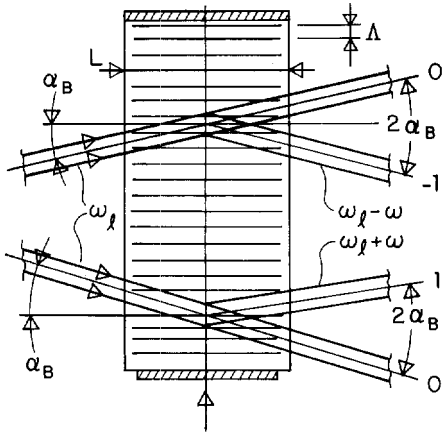
Fig. 1. Diffraction in the Bragg region showing downshifted (top) and upshifted (bottom) interaction.
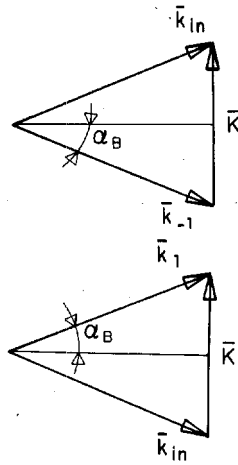
Fig. 2. Wave vector diagrams illustrating diffraction in the Bragg region for downshifted (top) and upshifted (bottom) interaction.

Fig. 3. Diffraction in the Debye–Sears region showing many generated orders.
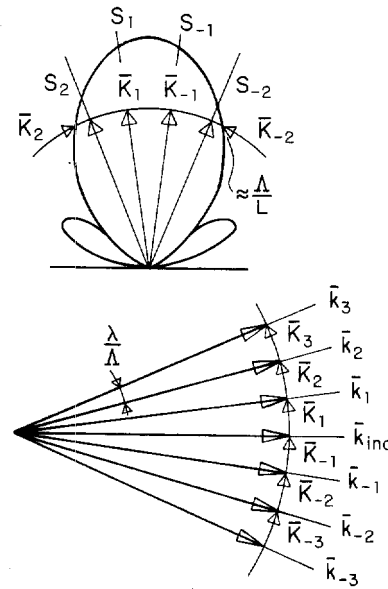
Fig. 4. Multiple scattering in the Debye–Sears region (bottom) made possible by the presence of many plane waves of sound in the radiation pattern of the transducer (top).

where λ_v denotes the vacuum wavelength. In the drawings, this refraction effect is not shown; for simplicity beams are shown propagating in the direction appropriate to the medium.

If the wavefronts of the sound move away from the incident light (Fig. 1, top), they also move away from the diffracted beam which is called the −1 order in this case. It is easily shown that this results in a negative Doppler shift, i.e., the diffracted light is downshifted in frequency by the sound frequency ω. The case of upshifted Bragg diffraction is also shown in Fig. 1 (bottom); the diffracted light is now called the +1 order.

The essential properties of Bragg diffraction can be explained in many different ways [18]–[22]. This author's preference lies with the model in which the interaction is thought of as a collision between photons and phonons. The momenta of the interacting particles are given by $\hbar \bar{k}$ and $\hbar \bar{K}$ for the photons and phonons respectively, where $\hbar = h/2\pi$, h is Planck's constant, $\bar{k}$ and $\bar{K}$ are the propagation vectors of light and sound. Conservation of momentum is then illustrated by the diagrams of Fig. 2, from which the Bragg angle conditions can be derived easily [18]

$$\sin \alpha_B = \tfrac{1}{2} K/k = \tfrac{1}{2} \lambda/\Lambda. \qquad (3)$$

Frequency up- or downshift follow from the same diagrams by considering energy conservation in terms of photon—and phonon energies $\hbar \omega_l$ and $\hbar \omega$.

Note that, classically, the diagrams of Fig. 2 represent phase synchronous interaction, a concept which was already implicit in Brillouin's early paper.

If the width of the transducer L is decreased, as in Fig. 3, the column of sound in the medium will look less and less like a plane wave. More accurately, the angular plane wave spectrum of the soundfield (i.e., the radiation pattern) broadens so as to make available additional plane waves of sound for a wider range of interaction. The basic idea is shown in Fig. 4. The first effect of shortening L is that the up-and-down-shifted orders $\bar{k}_1$ and $\bar{k}_{-1}$ are now both generated due to the simultaneous presence of soundwaves $\bar{K}_1$ and $\bar{K}_{-1}$ with amplitudes S_1 and S_{-1}. If L is decreased further, additional soundwaves $\bar{K}_2$ and $\bar{K}_{-2}$ appear, with amplitudes S_2 and S_{-2}, which interact with already scattered lightwaves $\bar{k}_1$ and $\bar{k}_{-1}$ to generate the second orders $\bar{k}_2$ and $\bar{k}_{-2}$. If we continue to decrease L, more and more orders are generated, as shown in Fig. 3. (Note that the nth order is shifted in frequency by an amount $n\omega$.) The extent to which this multiple scattering process can operate is determined by the ratio of the angular width Λ/L, of the sound radiation pattern to the separation λ/Λ between orders. Customarily a parameter Q, inversely proportional

to this ratio, is used [23]

$$Q = \frac{K^2 L}{k} = 2\pi \frac{\lambda L}{\Lambda^2} \, . \qquad (4)$$

Thus the condition for Bragg diffraction (the Bragg region) is stated as

$$Q \gg 1 \qquad (5)$$

while the opposite condition denotes the multiple scattering regime where many orders may be generated. This latter regime is called the Raman–Nath [24], Lucas–Biquard, or Debye–Sears region after early investigators.

Conventionally, Debye–Sears diffraction is analyzed by using a moving phase grating model as was first done by Raman and Nath [24]. This approach can be shown to lead to the same results as are obtained by using multiple scattering calculations [25], [26]. The amplitude of the diffracted orders is given by

$$A_n = (-j)^n E_{\text{inc}} J_n(kC|S|L/2). \qquad (6)$$

where E_{inc} is the amplitude of the incident light, $|S|$ represents the peak condensation or strain in the soundfield $S(x, t) = |S| \cos(\omega t - kx)$, and C is a material constant in terms of which the refractive index variation is given by

$$\Delta n(x, t) = \tfrac{1}{2} nCS(x, t). \qquad (7)$$

With (7) it is easily shown that (6) may also be written as

$$A_n = (-j)^n E_{\text{inc}} J_n(\widehat{\alpha}) \qquad (8)$$

where $\widehat{\alpha} = k_v \widehat{\Delta} nL$ denotes the peak phase shift of the light due to the peak refractive index variation $\widehat{\Delta} n$, and $k_v = 2\pi/\lambda_v$.

The constant C is related to the so called strain-optic coefficient p by

$$C = -n^2 p. \qquad (9)$$

More generally [18], n is a tensor and strictly speaking, equation (9) applies only to liquids.

Fig. 5 shows the dependence of the diffracted orders on $\widehat{\alpha}$, leaving out the $(-j)^n$ form. Quite often a modest sound pressure is used (weak interaction, $\widehat{\alpha} \ll 1$) and effectively only the +1 and −1 orders are generated. In that case (6) may be approximated by

$$A_o = E_{\text{inc}}$$
$$A_{\pm 1} = -jE_{\text{inc}} \cdot \tfrac{1}{4} kC|S|L. \qquad (10)$$

The situation in the Bragg region may be analyzed by using a model of two coupled modes, i.e., E_o and E_1 (or E_{-1}), as was first done by Van Cittert [27]. The results are given by

$$E_o = E_{\text{inc}} \cos(kC|S|L/4) = E_{\text{inc}} \cos\left(\frac{\widehat{\alpha}}{2}\right)$$

$$E_{\pm 1} = -jE_{\text{inc}} \sin(kC|S|L/4) = -jE_{\text{inc}} \sin\left(\frac{\widehat{\alpha}}{2}\right). \qquad (11)$$

This behavior is illustrated in Fig. 6. For weak interaction ($\widehat{\alpha} \ll 1$), the expressions (11) become identical to (10), with the understanding though, that only one order is effectively generated.

For maximum efficiency in Bragg diffraction it is necessary that $\widehat{\alpha} = \pi$. It is easily shown that the required acoustic intensity is given by

$$I_s = K_v/2M_2 L \qquad (12)$$
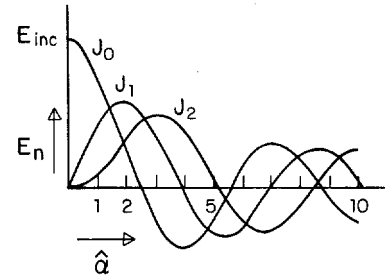
Fig. 5. Amplitude of diffracted orders versus peak phase shift $\widehat{\alpha}$ in the Debye–Sears region.
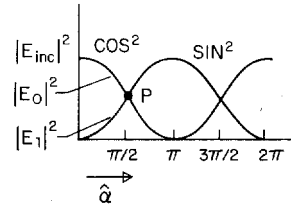
Fig. 6. Intensity of diffracted orders versus peak phase shift $\widehat{\alpha}$ in the Bragg region.

where M_2 is a figure of merit [18], [28] defined by the material properties of the acoustic medium

$$M_2 = n^6 p^2/\rho V^3. \qquad (13)$$

In (13), ρ represents the density of the medium and V the sound velocity. In practice, diffraction efficiencies range from $\simeq 95$ percent at 100 MHz to $\simeq 10$ percent at 2000 MHz.

III. APPLICATIONS

It will be clear immediately that a sound cell may be used to modulate light, either in the Raman–Nath mode or the Bragg mode. The latter is illustrated in Fig. 7 where the sinusoidal contour of the sound beam represents amplitude modulation of the carrier. It is readily recognized that the maximum modulation frequency f_m is reached when the modulation wavelength Λ_m equals the diameter d of the light beam

$$f_{m\,(\text{max})} = \frac{V}{d} = \frac{1}{\tau} \, . \qquad (14)$$

At this frequency, the effective modulation drops to zero. In (14), the parameter τ signifies the transit time of the sound through the light beam. To achieve a high f_m, the light beam is often focused into the cell, thus decreasing d and τ.

For a linear modulation transfer, the Bragg cell must be operated near a linear region of the light intensity versus sound/pressure curve, such as illustrated by point P in Fig. 6. Operation near the origin results in a linear relation between light amplitude and sound pressure.

Another application of Bragg diffraction is beam deflection. This is illustrated in Fig. 8, where the diffracted beam of light is shown in three successive positions, corresponding to sound frequencies f_1, f_2, and f_3. Because the relation between deflection angle and frequency sweep is linear,

$$\alpha_{\text{defl}} = \frac{\lambda}{V} f \qquad (15)$$

a simple frequency sweep is all that is needed to operate a beam deflector. In such a device the number of resolvable angles N is determined by the ratio of the range of deflection
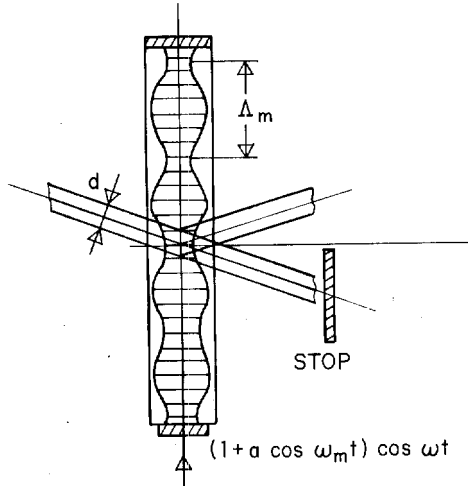
Fig. 7. Bragg diffraction sound cell used as modulator.
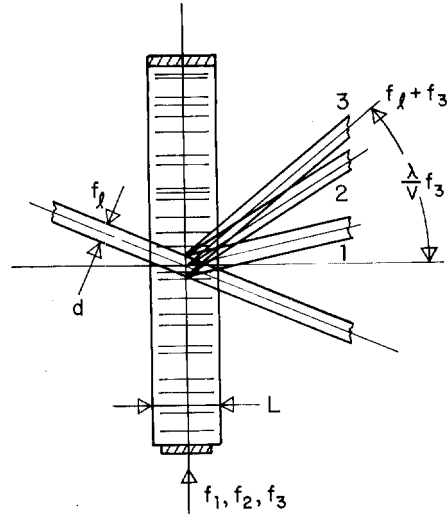
Fig. 8. Bragg diffraction sound cell used as beam deflector.

angles $\Delta\alpha_{defl}$ to the angular spread λ/d of the light beam

$$N = \frac{\Delta\alpha_{defl}}{\lambda/d} \qquad (16)$$

As $\Delta\alpha_{defl}$ is determined by the maximum frequency deviation Δf through (15)

$$\Delta\alpha_{defl} = \frac{\lambda}{V}\,\Delta f \qquad (17)$$

we may combine (16) and (17) to find

$$N = \frac{d}{V}\,\Delta f = \tau\Delta f. \qquad (18)$$

Note that, if the deflector is used to randomly access N positions by using N different frequencies within Δf, τ also connotes the access time of the system. Likewise, for general signal processing, the parameter $\tau\Delta f$ represents the cell's time–bandwidth product. Considerations of maximum optical aperture and finite acoustic loss limit this product at present to values of 1000–2000, with τ ranging from $1\,\mu s$ to $10\,\mu s$ and Δf from 10 MHz to 1 GHz.

The extent to which a beam deflector works satisfactorily over its entire range depends on whether a wide enough spectrum of plane waves is available in the radiation pattern of the transducer to satisfy the Bragg angle condition at all frequencies. The condition for this is given by

$$\frac{\Lambda_{nom}}{L} > \frac{1}{2}\,\frac{\lambda}{V}\,\Delta f$$

or

$$L < \frac{2\Lambda^2{}_{nom}}{\lambda} \cdot \frac{f_{nom}}{\Delta f} \qquad (19)$$

where Λ_{nom} and f_{nom} are the nominal sound wavelength and frequency respectively. Equation (19) indicates that for large Δf the interaction length L must be decreased. This, however, reduces the overall efficiency (see (12)), and also increases the strength of additional orders by moving out of the Bragg region (see (5)). Such difficulties may be circumvented by using a phased array transducer, designed in such a way that the frequency-dependent change in sound beam direction tracks the Bragg angle [29].
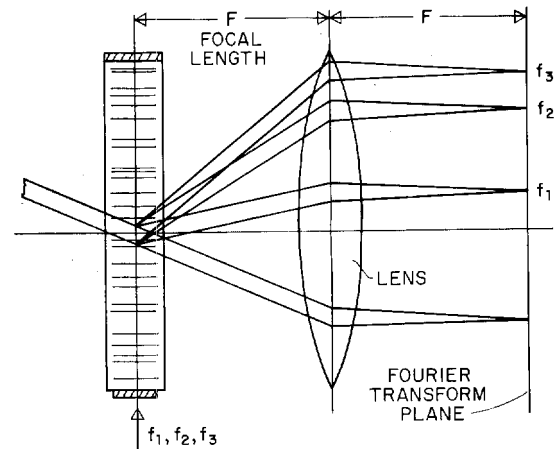
Fig. 9. Bragg diffraction sound cell used as spectrum analyzer.

One other aspect of the beam deflectors is of importance; it has to do with the rate of change df/dt of the instantaneous frequency in the soundcell. If this is large, a considerable frequency gradient (and hence deflection angle gradient) can appear across the light beam. At first glance it may be thought that this would impair the optical performance. It may be shown, however, that, for a linear frequency sweep, the effect is merely that of an additional positive or negative cylinder lens which moves up with the sound beam [30]. The focal length F of the lens is given by [18]

$$F = \frac{V^2}{\lambda}\left(\frac{df}{dt}\right)^{-1}. \qquad (20)$$

If, in Fig. 8, the frequencies f_1, f_2, f_3 are fed into the sound cell simultaneously rather than sequentially, the device acts as a spectrum analyzer. Each frequency generates a beam at a specific angle; if desired, a subsequent lens will focus these beams in its back focal plane as shown in Fig. 9. This plane will then display the frequency spectrum or Fourier transform of the sound signal. It is important to realize that this is indeed a "true" frequency spectrum and not just a display of brightness versus frequency. This comes about because each beam is actually shifted in frequency by the spectrum component that generated it; also, both its amplitude and phase
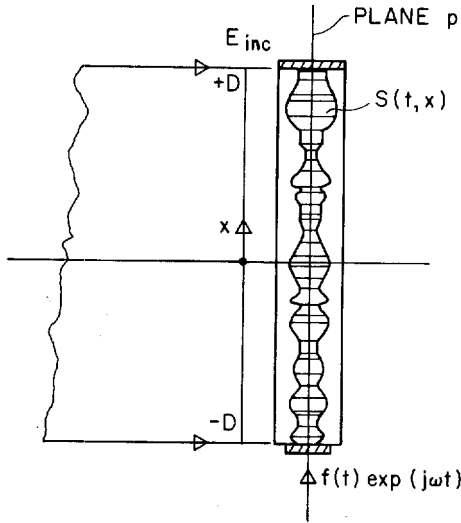
Fig. 10. Typical input configuration of an acousto-optic signal processing system.

are directly related to that component. Having available this "physical" Fourier transform makes it possible to perform complex filtering operations by optical heterodyning [11].

The spatial resolution in the Fourier transform plane corresponds to a frequency resolution $\delta f = 1/\tau$ as is to be expected from processing time considerations. Of late, efforts have been made to increase this limiting resolution by further electronic processing in the frequency plane [15]-[17]. One of the ways to achieve this is by means of an array of photodiodes subject to an optical local oscillator field of which the local frequency varies from diode to diode. Coincidence of local oscillator frequency and signal frequency at a particular diode location leads to a dc component in the heterodyne current through that diode, thereby causing an additional charge on its capacitance. The total charging time before sampling determines the signal averaging and hence the frequency resolution.

Quite frequently, signal processing is performed in an image plane of the soundcell, rather than in a Fourier transform plane. In such cases the signal processing operations are expressed by convolutions and correlations of a signal with reference fields or reference masks in an image plane [13], [14], rather than direct or conjugate multiplications through optical heterodyning or masking in the Fourier transform plane. Both techniques are of course equivalent [12]; the choice is mainly a matter of convenience.

A typical input system for image plane processing is shown in Fig. 10. The signal fed to the transducer is assumed to be modulated in both phase and amplitude, hence of the general form

$$\text{Re}\ \{f(t)\ \exp\ (j\omega t)\} \qquad (21)$$

where, for amplitude modulation, $f(t) = A(1 + a\ \cos\ \omega_m t)$ and, for phase modulation $f(t) = A\ \exp\ [j\phi(t)]$. The constant A is, in general, complex. If the origin of the coordinate system is located in the center of the cell, the sound field may be written:

$$S(t, x) = \text{Re}\left[s\left\{ t - \frac{(x + D)}{V} \right\} \exp j\{\omega t - K(x + D)\} \right] \qquad (22)$$

where $2D$ is the length of the sound cell and $s(t, -D) \propto f(t)$.
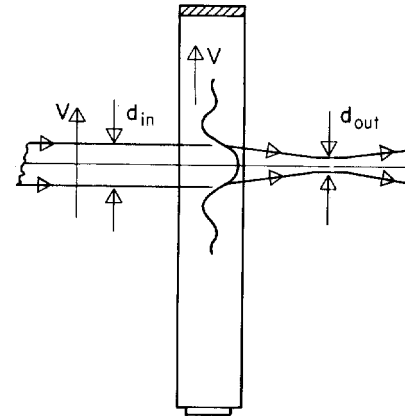
Fig. 11. Acousto-optic traveling lens, showing spot demagnification for increase of resolution.

Fig. 10 shows the light perpendicularly incident on the sound cell, as is appropriate for Raman–Nath interaction. Let E_{inc} be the amplitude of the incident light, referred to plane p through the center of the cell. For weak interaction, the exit light, also referred to plane p, may then be approximately written [12] (in complex notation)

$$E_{exit} \simeq E_{inc} +$$

$$-\frac{1}{4}\ jkCL \cdot E_{inc}\ s\left\{ t - \frac{(x + D)}{V} \right\}$$

$$\cdot \exp\ \{j(\omega_c + \omega)t - jK(x + D)\}$$

$$-\frac{1}{4}\ jkCL \cdot E_{inc}\ s^*\left\{ t - \frac{(x + D)}{V} \right\}$$

$$\cdot \exp\ \{j(\omega_c - \omega) + jK(x + D)\} \qquad (23)$$

where the asterisk denotes the complex conjugate. The second term in (23) gives rise to the plus first-order scattered light, the third term to the minus first order. This is most easily seen by taking s to be constant: the second term then describes the cross section of a light beam propagating in the direction $\alpha_{+1} \simeq K/k$, the third term refers to a beam in the direction $\alpha_{-1} \simeq -K/k$.

Note that the downshifted field is described by s^* rather than s; as either of the two fields may be used for further processing (the other one and the zeroth-order field can be removed by suitable stops in a focal plane), it is easily conjectured that both correlation (needing a conjugate term) and convolution may be achieved with suitable configurations.

For Fig. 10 to describe a Bragg diffraction configuration, the light must be incident at the appropriate Bragg angle. The exit light is then still described by (23) with the understanding that either the second or the third term be absent. Due to the frequent need for systems with large bandwidth and hence high carrier frequency, Bragg diffraction signal processing is more common (see (5)).

Early descriptions of acousto-optic signal processing often model the action of the sound cell, in qualitative terms, as carrying a moving replica of the electrical signal [5]. Modern accounts usually talk about parallel processing.

All of the applications described so far rely on diffraction effects. This requires that many wavelengths of sound are simultaneously present within the lightbeam. Where this condition is not satisfied, any possible effects are better analyzed on the basis of ray bending. Such refractive effects are often

useful in their own right. An example of some importance to various signal processing schemes is the so called traveling lens [31]. Fig. 11 shows the principle of operation. A high level pulse of sound is launched into an acoustic medium and the central part of it used to focus an incoming light beam of diameter d_{in} into a smaller diameter d_{out}. It is necessary that the incoming beam track the sound pulse, but that may conveniently be achieved by an acousto-optic beam deflector. Traveling lenses have been successfully operated to extend the resolution of beam deflectors by factors of 10 or more [32].

Many more details and applications of acousto-optics could be discussed such as polarization effects, birefringence, Bragg diffraction imaging, guided wave effects, etc. This short review has necessarily been limited to some fundamental aspects of immediate concern to signal processing. The interested reader will find excellent discussions of subjects neglected here, in the review articles cited in the text.

REFERENCES

[1] L. Brillouin, "Diffusion de la lumière et des rayons X par un corps transparent homogène," *Ann. Phys. (Paris)*, vol. 17, pp. 88–122, 1922.
[2] R. Lucas and P. Biquard, "Propriétés optiques des milieux solides et liquides soumis aux vibration élastiques ultra sonores," *J. Phys. Rad.*, vol. 3, pp. 464–477, 1932.
[3] P. Debye and F. W. Sears, "On the scattering of light by supersonic waves," *Proc. Nat. Acad. Sci.* (U.S.), vol. 18, pp. 409–414, June 1932.
[4] D. M. Robinson, "The supersonic light control and its application to television with special reference to the Scophony television receiver," *Proc. IRE*, vol. 27, pp. 483–486, Aug. 1939.
[5] F. Okolicsanyi, "The wave-slot, an optical television system," *Wireless Engineer*, vol. 14, pp. 527–536, Oct. 1937.
[6] A. H. Rosenthal, "Application of ultrasonic light modulation to signal recording, display, analysis and communication," *IRE Trans. Ultrason. Eng.*, vol. UE-8, pp. 1–5, Jan. 1961.
[7] W. Liben, "Some applications of an ultrasonic light modulator," *J. Acoust. Soc. Amer.*, vol. 34, pp. 860–861, June 1962.
[8] L. Slobodin, "Optical correlation technique," *Proc. IEEE*, vol. 51, p. 1782, Dec. 1963.
[9] M. Arm, L. Lambert, and I. Weissman, "Optical correlation technique for radar pulse compression," *Proc. IEEE*, vol. 52, p. 842, July 1964.
[10] M. King, W. R. Bennett, L. B. Lambert, and M. Arm, "Real time electro-optical signal processors with coherent detection," *Appl. Opt.*, vol. 6, pp. 1367–1375, Aug. 1967.
[11] R. Whitman, A. Korpel, and S. Lotsoff, "Application of acoustic Bragg diffraction to optical processing techniques," in *Proc.*

Symp. Modern Optics, pp. 243–255, 1967.
[12] A. Korpel, "Acousto-optic signal processing," in *Optical Information Processing*, Yu E. Nesterikhin and G. W. Stoke, Eds. New York: Plenum, 1976, ch. 10, pp. 171–194.
[13] R. A. Sprague, "A review of acousto-optic signal correlators," *Opt. Eng.*, vol. 16, pp. 467–474, Sept./Oct. 1977.
[14] L. N. Flores and D. L. Hecht, "Acousto-optic signal processors," in *SPIE Conf. Proc.*, vol. 118, pp. 182–192, 1977.
[15] P. Kellman, "Time integrating optical processors," in *SPIE Conf. Proc.*, vol. 185, pp. 130–139, 1978.
[16] T. M. Turpin, "Time integrating optical processors," in *SPIE Conf. Proc.*, vol. 154, pp. 196–203, 1978.
[17] T. R. Bader, "Acousto-optics spectrum analysis," *Appl. Opt.*, vol. 18, pp. 1668–1672, June 1979.
[18] A. Korpel, "Acousto-optics," in *Applied Solid State Science*, Vol. 3, R. Wolfe, Ed. New York: Academic Press, 1972, ch. 2, pp. 73–179.
[19] —, "Acousto-optics," in *Applied Optics and Optical Engineering*, Vol. VI, R. Kingslake and B. J. Thompson, Eds. New York: Academic Press, 1980, ch. 4, pp. 89–136.
[20] R. Adler, "Interaction between light and sound," *IEEE Spectrum*, vol. 4, pp. 42–53, May 1967.
[21] E. I. Gordon, "A review of acousto-optical deflection and modulation devices," *Proc. IEEE*, vol. 54, pp. 1391–1401, Oct. 1966.
[22] C. F. Quate, C. D. W. Wilkinson, and D. K. Winslow, "Interaction of light and microwave sound," *Proc. IEEE*, vol. 53, pp. 1604–1622, Oct. 1965.
[23] W. R. Klein and B. D. Cook, "Unified approach to ultrasonic light diffraction," *IEEE Trans. Sonics Ultrason.*, vol. SU-14, pp. 723–733, July 1967.
[24] C. V. Raman and N. S. Nagendra Nath, "The diffraction of light by high frequency sound waves," *Proc. Ind. Acad. Sci.*, vol. 2, pp. 406–420, 1935; vol. 3, pp. 75–84, 1936; vol. 3, pp. 119–125, 1936; vol. 3, pp. 459–465, 1936.
[25] A. Korpel, "Two-dimensional plane wave theory of strong acousto-optic interaction in isotropic media," *J. Opt. Soc. Amer.*, vol. 69, pp. 678–683, May 1979.
[26] A. Korpel and T. C. Poon, "An explicit formalism for acousto-optic multiple plane wave scattering," *J. Opt. Soc. Amer.*, vol. 70, pp. 817–820, July 1980.
[27] P. H. Van Cittert, "Zur Theorie der Lichtbeugung an Ultraschallwellen," *Physica IV*, pp. 590–594, July 1937.
[28] T. M. Smith and A. Korpel, "Measurement of light-sound interaction efficiencies in solids," *IEEE J. Quantum Electron.*, vol. QE-1, pp. 283–284, Sept. 1965.
[29] A. Korpel, R. Adler, P. Desmares, and W. Watson, "A television display using acoustic deflection and modulation of coherent light," *Appl. Opt.*, vol. 5, pp. 1667–1675, Oct. 1966; *Proc. IEEE*, vol. 54, pp. 1429–1437, Oct. 1960.
[30] J. S. Gerig and H. Montague, "A simple optical filter for chirp radar," *Proc. IEEE*, vol. 52, p. 1753, Dec. 1964.
[31] L. C. Foster, C. B. Crumley, and R. L. Cohoon, "A high resolution optical scanner using a traveling wave acoustic lens," *Appl. Opt.*, vol. 9, p. 2154, 1970.
[32] S. K. Yao, D. Weid, and R. M. Montgomery, "Guided acoustic wave traveling lens for high speed optical scanners," *Appl. Opt.*, vol. 18, pp. 446–453, Feb. 15, 1979.

Design Considerations for Acousto-Optic Devices

EDDIE H. YOUNG, JR., AND SHI-KAY YAO, SENIOR MEMBER, IEEE

Invited Paper

Abstract—The design and fabrication of wide-band bulk acousto-optic modulators (temporal modulation) and beam deflectors (spatial modulation) are described. Optimized device parameters can be obtained systematically for given specifications of the desired modulation bandwidth, throughput efficiency and number of resolvable elements. As the device operating frequency goes beyond a few hundred megahertz, the acoustic transducer response becomes sensitive to the intermediate metal layers between the piezoelectric transducer and the acousto-optic interaction medium. Transducer bandwidth and impedance matching can be optimized using computer modeling programs. Criteria for material selection based on performance requirements and propagation loss are presented. Practical considerations for the fabrication of high performance devices and specific device parameters are discussed.

INTRODUCTION

THE DIFFRACTION of light by acoustic waves in liquids and solids was first predicted by Brillouin in 1922 and was first observed ten years later by several experimenters [1], [2]. Since then, this phenomenon, often called Brillouin scattering, has been extensively studied both experimentally and theoretically [3]–[6]. At first, the experiments were used mainly to determine elastic constants and to study thermo-phonon distributions of various materials. Later, the effect was also used in constructing light modulators; the Scophony system for television projection is an early example of its application [7]. The invention of lasers as coherent light sources, the development of high-frequency acoustic transducers, and the development of materials having excellent acoustic and optical properties and large photoelastic constants [8]–[10] have generated intensive interest in the subject. Acousto-optic devices developed for the purpose of optical beam control, such as light modulators and deflectors [11]–[13], are widely used in various laser applications. Advanced optical systems utilizing acousto-optic devices for optical signal processing have been actively under development.

There are two important regimes for acousto-optic interactions: the Raman–Nath scattering, also known as the Debye-Sears effect, and the Bragg diffraction regime. Raman–Nath diffraction occurs at relatively low frequencies when the acoustic beam width along the optical propagation direction is small. In this regime the light enters the medium parallel to the acoustic wavefronts, and the diffracted light appears symmetrically on both sides of the primary beam at equally spaced angles.

The mth diffracted order is separated from the undiffracted light by an angle given by the relation

$$\theta_m \cong \pm \frac{m\lambda}{n\Lambda}; \qquad m = 1, 2, 3 \tag{1}$$

where λ is the optical wavelength, n is the index of refraction and Λ is the acoustic wavelength. Also, each of the diffracted orders are frequency shifted by an amount equal to $\pm m\omega_a$, where ω_a is the input acoustic frequency.

If, however, the acoustic column becomes sufficiently wide (with a long interaction length), the acousto-optic process enters the Bragg regime. In this case, the diffracted light will appear predominantly in a single order and its intensity will be maximum when the light is incident at the Bragg angle θ_B, where $\theta_B \cong \lambda/2n\Lambda$. For wide bandwidth acousto-optic devices, the Bragg diffraction regime is of prime interest for maximum performance.

The interaction of light with the acoustic waves is governed by several key parameters. One key parameter is defined as [4]

$$Q = \frac{2\pi}{n}\frac{\lambda L}{\Lambda^2} \tag{2}$$

where L is the interaction length of the acoustic wave column. For $Q < 1$, Raman–Nath diffraction dominates; when $Q > 7$, Bragg diffraction dominates and the output light wave can then be approximated by the first-order term whose relative light intensity is

$$\frac{I_1}{I_0} = \eta \, \text{sinc}^2 \, (\eta + (\Delta kL/2)^2)^{1/2} \tag{3}$$

where I_1 and I_0 represent the diffracted and the incident light intensity and Δk is the momentum mismatch of the incident light and acousto-optic propagation vectors. The parameter η is defined as

$$\eta = \frac{\pi^2}{2\lambda^2}\left(\frac{n^6 p^2}{\rho v^3}\right)\frac{L}{H}P_a \tag{4}$$

where p is the photoelastic coefficient, ρ is the mass density, v is the acoustic velocity, H is the height of the acoustic beam (as shown in Fig. 1), P_a is the acoustic power, and the quantity $(n^6 p^2/\rho v^3)$ is the acousto-optic figure of merit M_2.

If the argument of the sinc-function given in (3) is small, we have $I_1/I_0 = \eta$, so that η is the diffraction efficiency of the device. Equation (4), then, relates the diffraction efficiency to the physical and geometrical properties of the device, and to the amount of acoustic power within the device. All the
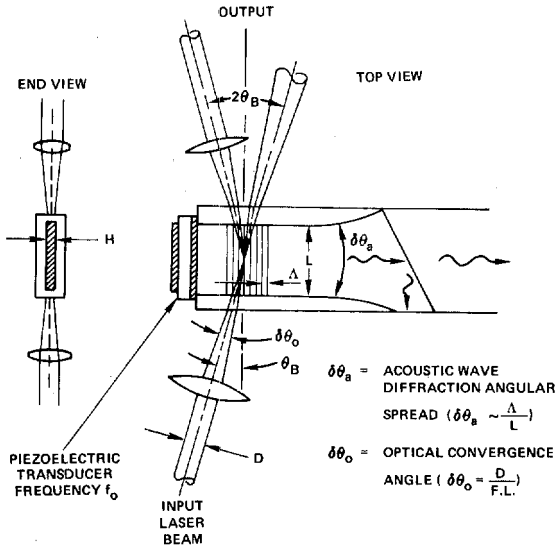
Fig. 1. Acousto-optic modulator configuration.

k in, k' in:	INCIDENT OPTICAL WAVE VECTORS
k out, k' out:	SCATTERED OPTICAL WAVE VECTORS
K_a K'_a:	ACOUSTIC WAVE VECTOR
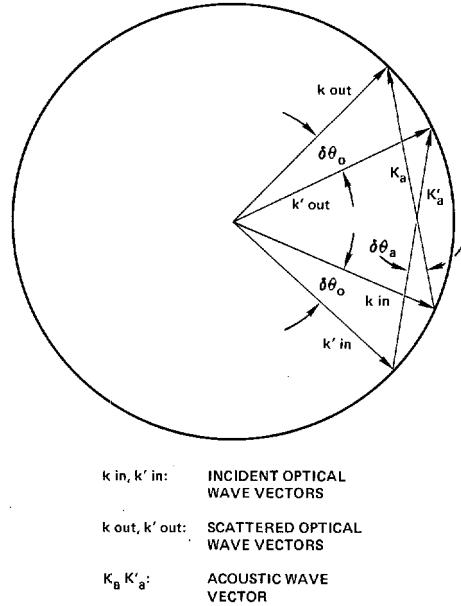
Fig. 2. Bragg diagram for acousto-optic modulation.

physical properties are given by the figure of merit M_2 of the interaction material; we see that a high index of refraction and a low velocity of propagation are desirable. The geometrical properties are given by the ratio of L/H; we noted previously that the parameter Q is also a function of the interaction length L. The importance of the other parameters will be developed later.

Generally, the parameter Δk cannot be assumed to be equal to zero or to remain constant for a given device configuration. A major part of acousto-optic device design analysis is aimed toward reducing the adverse effect of the finite Δk value on device performance to a tolerable level.

In this paper, relevant results of a study on the acousto-optic interaction process using the optical angular spectrum of the incident optical wavefront are presented briefly. Optimized modulator and deflector design procedures are thus obtained.

ACOUSTO-OPTIC MODULATION

To achieve wide bandwidth modulation of an optical beam with an acousto-optic modulator, the optical beam must be focused to a small beam width in the interaction region with the acoustic beam as shown in Fig. 1. A focused beam is needed because the rise time associated with the modulation bandwidth is proportional to the time required for the acoustic beam to travel across the optical beam. Thus as the acoustic transit time decreases, the rise time decreases and the corresponding bandwidth increases.

The use of a convergent light beam with the acousto-optic modulator, although providing a larger modulation bandwidth, imposes special requirements on the characteristics of the acoustic beam. The momentum conservation law for acousto-optic diffraction requires that the momentum vector k_{out} of the diffracted light beam is equal to the vector sum of the momentum vector k_{inc} of the incident light beam and the momentum vector k_a of the acoustic wave; i.e., the vector relation $k_{out} = k_{inc} + k_a$ holds. The incident light beam has a range of k_{inc} vectors of constant magnitude but distributed over an angular range $\delta\theta_0$ since the light beam is convergent. For the vector relation to be satisfied, the acoustic wave must have a corresponding range of angular directions $\delta\theta_a$. The condition for matching the angular spreads of the acoustic and optical
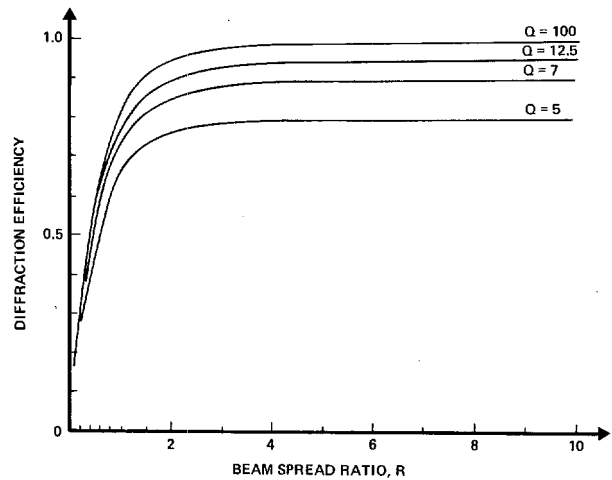
Fig. 3. Acousto-optic device diffraction efficiency as a function of R and Q.

beams is indicated in Fig. 2, which shows the Bragg diagram for the diffraction process. The range of the acoustic wave components is provided by the angular diffraction spread caused by the limited acoustic beam aperture. When $\delta\theta_a \ll \delta\theta_0$, momentum cannot be conserved for all optical wave components; this results in an elliptical output beam cross-section. On the other hand, if $\delta\theta_a \gg \delta\theta_0$, bandwidth is reduced. To minimize the amount of ellipticity in the diffracted beam, the beam spread ratio R, which is the ratio of the acoustic beam spread $\delta\theta_a$ to the optical beam spread $\delta\theta_0$, must be large, but not so large as to significantly reduce the bandwidth.

Numerical calculations show that the degree of ellipticity decreases rapidly as R increases. For R greater than 1.5, the major to minor axis ratio of the beam is less than 1.1 which is generally acceptable. If R is greater than 2.0, the bandwidth is reduced; therefore an acceptable range for R is $1.5 < R < 2.0$. Fig. 3 shows the diffraction efficiency of an acousto-optic modulator as a function of the parameters R and Q. We see that a second reason for choosing $1.5 < R < 2.0$ is that the

diffraction efficiency is then near its maximum value for all values of Q. Furthermore, there is little additional gain in diffraction efficiency for $Q > 7$.

The modulator frequency response will now be derived. Let $E(x)$ describe the laser beam amplitude profile at the center of the modulator where x is the acoustic wave propagation direction. The optical wavefront can be described by a collection of optical plane wave components given by [14]

$$E(x) = \int_{-\pi}^{\pi} A_f(\theta) \exp\left(j \frac{2\pi n}{\lambda}\right) (\sin \theta \cdot x) \, d\theta \qquad (5)$$

where $A_f(\theta)$ is the angular spectrum and θ is the angle of propagation for the plane wave component. By using Kirchhoff's formulation of Huygens' principle [14], the light amplitude diffracted by the acoustic field can be expressed. The result is that for a Gaussian input beam

$$|E(x)|^2 = I_0 \exp\left(-2x^2/w_0^2\right)$$

where w_0 is the $1/e^2$ radius of the laser beam, the output light intensity in response to a cosinusoidal RF input frequency can be represented as [15]

$$I(f) = \frac{I_0}{2} + I_0 \left[J_1\left(\frac{\alpha\pi}{2}\right) \exp\left(\frac{-\pi^2 f^2 \tau^2}{8}\right) \cos(2\pi ft) \right. $$
$$+ \sum_{n=1}^{\infty} (-1)^n J_{2n+1}\left(\frac{\alpha\pi}{2}\right) \exp\left[-(2n+1)^2 \frac{\pi^2 f^2 \tau^2}{8}\right] $$
$$\left. \cdot \cos\left\{(2n+1)\, 2\pi ft\right\} \right] \qquad (6)$$

where $\tau = 2w_0/v$ is the acoustic transit time required to pass through the optical $1/e^2$ beam waist, f is the modulation frequency and α is the modulation index.

The first-order Bessel function term in (6) represents the desired modulation. The modulation linearity is given by the Bessel function and the modulation frequency response is given by the exponential factor. The remaining terms represent the harmonics generated by the interaction. Fig. 4 shows the modulation frequency response of the acousto-optic interaction as a function of the product of the frequency and the transit time.

The frequency response falloff β, expressed in decibel, is defined as

$$\beta = 10 \log \left[\frac{I(f) - I_0/2}{I(o) - I_0/2} \right] \qquad (7)$$

which, by using (6), becomes

$$\beta = 10 \log \left[\exp\left(-\pi^2 f^2 \tau^2/8\right) \right]. \qquad (8)$$

The modulation bandwidth δf associated with a response falloff in decibel of β is simply the value of the modulation frequency f which satisfies (8):

$$\delta f = \frac{c}{\pi} \frac{\sqrt{\beta}}{\tau} \qquad (9)$$

where $c = \sqrt{0.8 \ln 10} \cong 1.4$. The optical beam waist can then be expressed as

$$w_0 = \frac{cv\sqrt{\beta}}{2\pi\delta f} \qquad (10)$$
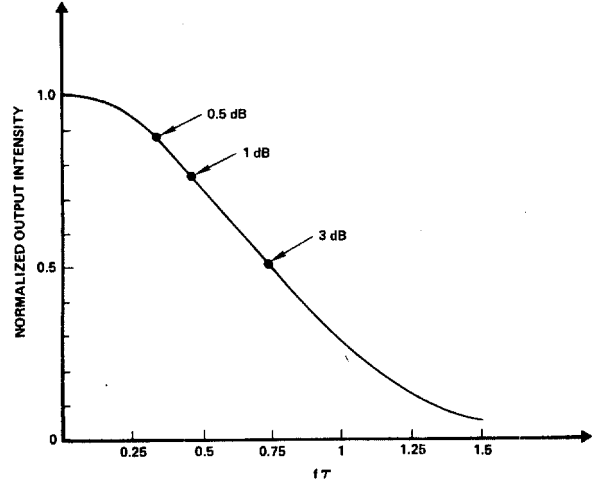
Fig. 4. Modulation frequency response for analog acousto-optic modulation.

which will be a useful relationship in later derivations. The optical risetime t_r for an acousto-optic modulator with a Gaussian input beam profile is given by [13]

$$t_r = \tau/1.5 \qquad (11)$$

where t_r is the 10–90 percent risetime. By combining (9) and (11), we find that the relationship between the modulation bandwidth and the rise time is

$$\delta f = \frac{0.29\sqrt{\beta}}{t_r}. \qquad (12)$$

It is important to note that δf is the analog modulation bandwidth; the RF bandwidth is twice δf because we retain the upper and lower sidebands about the carrier (or center) frequency.

For a desired modulation bandwidth δf, at β dB in rolloff, the R parameter can be expressed as

$$R = \frac{1.4\eta\sqrt{\beta v^2}}{4\delta f\lambda} \left(\frac{1}{f_0 L}\right) \qquad (13)$$

where f_0 is the carrier frequency. Likewise, the interaction parameter can be written as

$$Q = \frac{2\pi\lambda}{\eta v^2} L f_0^2. \qquad (14)$$

By selecting $R = 1.5$ and allowing δf and Q to be parameters, we show a family of curves in Fig. 5 in which we plotted the value of the center frequency f_0 as a function of the interaction length L. As an example, we show a family of curves for the Q values of 8, 10, and 12, and two curves for δf equal to 110 and 140 MHz. The key design consideration is to find the largest value of L where two curves intersect, because a large value of L results in smaller drive power requirements. Furthermore, a large value of L results in a lower value for f_0 which, in turn, results in less acoustic attenuation.

Suppose we consider the design of a modulator fabricated using a tellurium dioxide material whose parameters are shown in Fig. 5. If we want a 140-MHz bandwidth and a $Q = 12$, the largest value of L is approximately 220-μm as shown by the intersection of the curve for 140 MHz with the curve for $Q = 12$. The value of f_0 is 825 MHz; a lower value of f_0 could be obtained without sacrificing too much diffraction efficiency
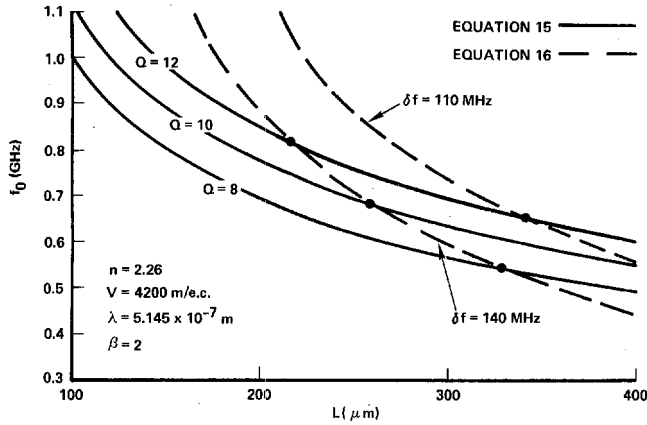
Fig. 5. Center frequency versus interaction length.

Fig. 6. Number of resolvable elements for a lead molybdate crystal.

by letting $Q = 8$. The interaction length is also longer, resulting in less acoustic drive power.

As a second example, suppose we want to design a high efficiency modulator with a 110-MHz bandwidth. We select $Q = 12$, and find that the interaction length is $L = 340$ microns and that the center frequency is $f_0 = 670$ MHz. This design procedure has been proven to be valuable in practice.

The final step is to determine the required acoustic drive power. The remaining parameter is the transducer height H, which is usually chosen to be 2 to 3 times the optical beam waist $(2W_0)$ expressed in (10). For a desired efficiency we can now calculate the acoustic drive power from (4).

ACOUSTO-OPTIC DEFLECTOR DESIGN

The acousto-optic interaction deflects the optical beam at prescribed positions as a linear function of the input acoustic frequency. The basic design equations and applications for acousto-optic beam deflectors in signal processing will be discussed. The key parameter for acousto-optic deflectors used in signal processors is the number of resolvable elements. The number of resolvable elements relates either to the number of resolvable frequencies in a Fourier transform plane or to the number of resolvable elements in an image plane.

The number N of resolvable elements can be determined by the ratio of the maximum deflection angle $\Delta\theta$ divided by the angular spread of the optical beam λ/D, where D is the diameter of the beam

$$N = \frac{\Delta\theta D}{\lambda}. \tag{15}$$

The above expression can be simplified by noting that

$$\Delta\theta = \lambda \Delta f/v \tag{16}$$

and, since $D/v = \tau$, we have that

$$N = \tau \Delta f \tag{17}$$

which is the product of the aperture processing time τ and the bandwidth Δf of the device. For high-performance devices, it is necessary to have N as large as possible; N is limited by geometric factors and acoustic attenuation. The first geometric factor is the maximum reasonable length D of the acousto-optic deflector. Therefore equation (17) can be expressed as

$$N \leqslant \frac{D}{2} \frac{1}{\Lambda_0} \tag{18}$$
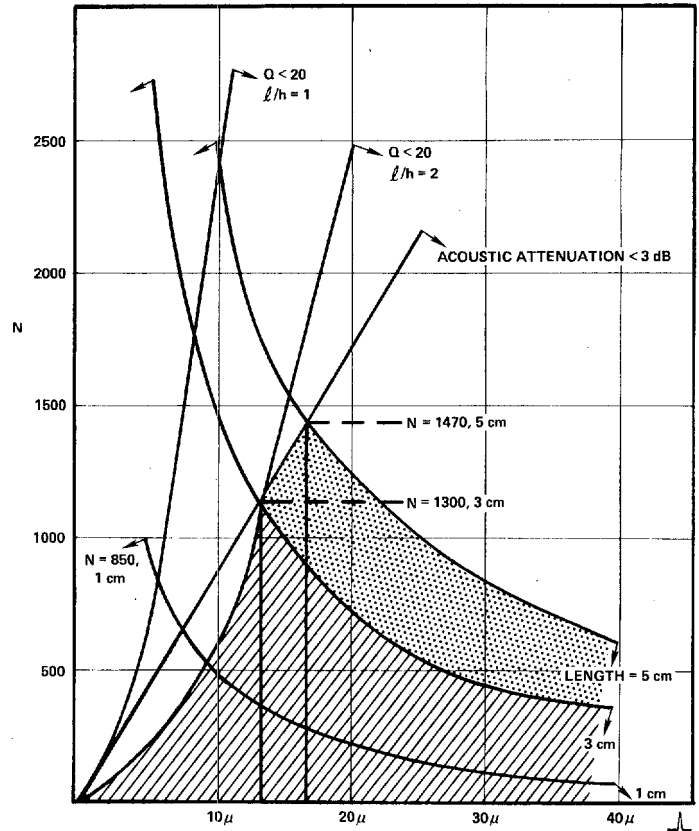
where we assumed $\Delta f = f_0/2$, which is the maximum fractional bandwidth. Another constraint on the number of resolvable elements can be obtained from the consideration of geometric beam spreading. An equation that relates the transducer length L to the near-field distance (equivalent to D) at the half-power points is

$$D = \frac{L^2}{2\Lambda_0}. \tag{19}$$

From (2) we have that

$$L = \frac{n\Lambda_0^2 Q}{2\pi\lambda}. \tag{20}$$

We now combine (19) and (20) and substitute the result into (18) to get

$$N \leqslant \left(\frac{\eta Q}{4\pi}\right)^2 \Lambda_0^2. \tag{21}$$

The third fundamental limit is the acoustic attenuation in the deflector which we will also express in terms of Λ_0. If γ is the attenuation in decibel per unit length, referenced to 1 GHz, and if we allow 3 dB of attenuation we have that

$$D \leqslant \frac{3}{\gamma} \left(\frac{\Lambda_0}{\Lambda_1}\right)^2 \tag{22}$$

where Λ_1 is the acoustic wavelength at 1 GHz. By substituting (22) into (18), we have

$$N \leqslant \frac{1.5}{\gamma\Lambda_1^2} \Lambda_0 \tag{23}$$
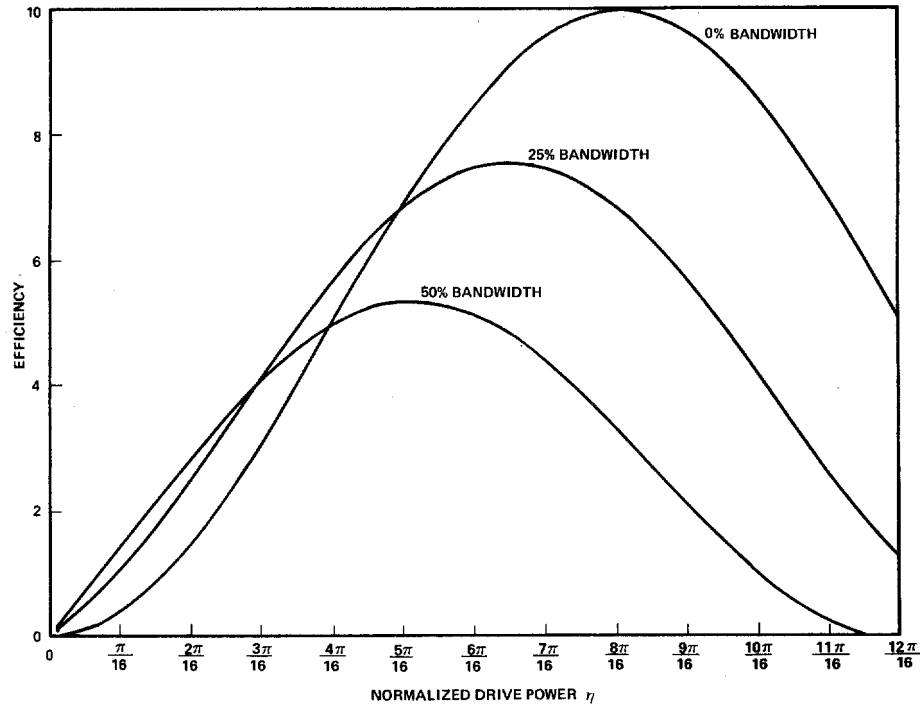
Fig. 7. Peak efficiency and bandwidth plots versus drive power.

The number of resolvable elements as limited by these three independent constraints is plotted as a function of the acoustic wavelength in Fig. 6. It is important to note that the maximum number of resolvable spots occurs at the minimum intersection point of the curves represented by (18), (21), and (23).

The design procedure for acousto-optic deflectors can now be summarized. Having selected the acousto-optic interaction material, we use (18), (21), and (23) to plot graphs of time-bandwidth product versus wavelength. The operating frequency or acoustic wavelength and other parameters can then be determined.

One application for acousto-optic deflectors is the generation of a random accessed spot or beam of light. Equation (17) shows, that for a fixed crystal length equivalent to the transit time τ, the bandwidth is key to achieving a large number of addressable positions or angles. We also want the diffraction efficiency to be high, but (3) shows that the diffraction efficiency is a function of Δk, the momentum mismatch parameter. In contrast to an acousto-optic modulator, the momentum mismatch for beam deflectors is due to the wide range of acoustic wave vectors. The momentum mismatch is given by

$$\Delta k = \frac{Q}{4} \frac{\Delta f}{f_0}. \tag{24}$$

In Fig. 7, we have plotted the value of I_1/I_0 versus η from (3) for values of $\Delta f/f_0 = 0$, $\Delta f/f_0 = 0.25$ and $\Delta f/f_0 = 0.5$. The most revealing result is that the efficiency is at nearly the same value of 50 percent at $\eta = \pi/4$ for all fractional bandwidths. This means that the light intensity is nearly the same for all addressed positions which is desirable. If we were to use more drive power in an attempt to gain more efficiency, we see that we can do so at low fractional bandwidths (i.e., small deflection angles), but we reach the peak value for $\Delta f/f_0 = 0.5$ at $\eta = 5\pi/16$. At larger values of η the diffraction efficiency continues to increase for the lower fractional bandwidths but decrease for the larger fractional bandwidths. Clearly the value

of $\eta \approx \pi/4$ is the point at which the intensity variation as a function of beam angle or position is minimized and the diffraction efficiency is approximately 50 percent.

A beam deflector can also be operated in a linear scanning mode by using a linear FM signal as the driving waveform. Considerations regarding diffraction efficiency as a function of drive power and fractional bandwidth are the same as those given above. An additional concern, however, is the degree of linearity required of the FM signal. As noted by Korpel in this issue, the presence of the FM signal in the beam deflector introduces a small amount of focal power into the system that must be considered when calculating the spot size that can be achieved. Dickson [19] gives a detailed analysis of the spot size and linearity requirement for the swept frequency mode.

When significant acoustic wave attenuation exists, an exponential shading will be imposed on the diffracted optical wave front. The far-field intensity pattern of a uniformly illuminated acousto-optic deflector subjected to acoustic wave attenuation is [20]

$$\frac{I}{I_0} = C_1 e^{-\gamma D} \left| \frac{\sin (\pi D x / \lambda F) - (j\gamma D/2)}{(\pi D x / \lambda F) - (j\gamma D/2)} \right|^2 \tag{25}$$

where C_1 is a constant, F is the lens focal length, D is the optical aperture, γ is the acoustic wave amplitude attenuation factor in nepers per centimeter, and x is the displacement distance in the far field output plane. The far field intensity pattern shown in Fig. 8 has a slightly larger half-power beamwidth and somewhat larger sidelobe intensity as the acoustic wave attenuation increases. An acoustic attenuation of less than 12 dB across the optical aperture is usually acceptable. The exponential factor in (25) indicates that the optical intensity is reduced due to the reduced average acoustic wave power in the interaction region. An increase of input power is therefore necessary to restore the optical diffracted intensity.

We now consider the effect of a nonuniform optical illumination incident on the acousto-optic beam deflector. The
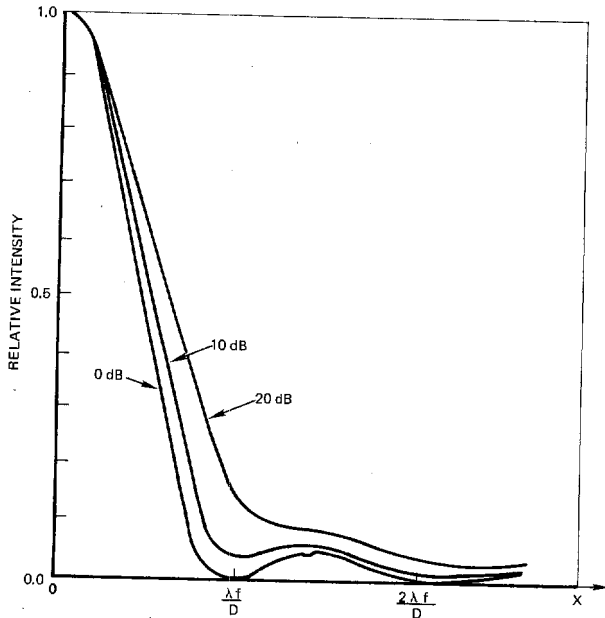
Fig. 8. The far-field intensity distribution of the diffracted optical beam with 0, 10, and 20 dB elastic attenuation across the optical aperture.

most frequently used source of light is a laser, which has a Gaussian intensity profile. If we couple the Gaussian illumination with the exponential attenuation, we have that

$$\frac{I}{I_0} = C_2 \exp\left(-\gamma D + \frac{(\gamma D)^2}{8}\right)\left[\frac{D^2}{4}\exp\left(-2\left(\frac{\pi Dx}{2\lambda F}\right)^2\right)\right] \quad (26)$$

where C_2 is a constant and D is the e^{-2} width of the Gaussian optical input beam. Since the factor in the brackets in (26) is identical to the far-field intensity distribution of the Gaussian illumination in the absence of attenuation, the far-field spot shape remains unchanged by the exponential attenuation.

Another important application of an acousto-optic deflector is as an electrical-to-optical signal modulator for wide-band signals. Rhodes and Turpin discuss a wide range of such applications in this issue. Of particular importance to the design of the device is a consideration of the linearity, diffraction efficiency and dynamic range of the device. Hecht [17] has made a careful analysis of the relationship between the diffraction efficiency and the resulting nonlinearities. Suppose that we apply a wide bandwidth signal to the transducer of a deflector having a time–bandwidth product N. We can then decompose the signal into N components, each having a small diffraction efficiency η_l. The approximate expressions for the overall efficiency, depletion, compression, cross-modulation, and intermodulation terms are given as follows.

$$\text{Diffraction Efficiency} \approx \eta_1\left[1 - \frac{1}{3}\eta_1 + \sum_{l=2}\frac{2}{3}\eta_l\right]$$

$$\text{Depletion} \approx \sum_{l=1}\eta_l$$

$$\text{Compression} \approx \frac{1}{3}\left[\eta_1 + 2\sum_{l=2}\eta_l\right]$$

$$\text{Cross-Modulation} \approx \frac{2}{3}\eta_2^2$$

$$\text{Third-Order Intermodulation} \approx \frac{1}{36}\eta_1^2\eta_2. \quad (27)$$

Depletion is the reduction of the undiffracted beam due to the finite intensities of the diffracted orders. Compression is the fractional deviation from a linear response to one frequency component due to all other signals present. Cross-modulation is the fractional change in the response of one signal due to the presence of the second signal. Third-order intermodulation is the output intensity of spurious signals caused by two input signals and generally limits the dynamic range of an optical signal processing system. A useful result that relates the available dynamic range, based on third order intermodulation products, compression and the number $N_1 < N$ of the frequency components that are saturated by the deflector is [18]

$$DR = \left[\frac{1 + 2N_1}{1 - C}\right]^2 \quad (28)$$

where DR is the dynamic range and C is the compression. If a small degree of compression is required, a large dynamic range is required to allow an appreciable number N_1 of the frequency components to saturate.

ADVANCED BEAM DEFLECTOR TECHNIQUES

Two techniques are presently available for the reduction of the Bragg angle deviation Δk in an acousto-optic beam deflector, offering an increase in the efficiency or a decrease in the required drive power.

The first technique is birefringent diffraction [21] which occurs in certain anisotropic crystals. The birefringent Bragg diffraction process is best described by the momentum diagram of Fig. 9 where the optical polarization is different between the incident and the diffracted optical beams. For the case of nearly perpendicular acoustic and optical diffracted beams, the phase matching of the k vectors can be approximately satisfied over a broad range of acoustic frequencies due to the tangential acoustic wave vector to the optical wave surface. A simple geometrical analysis in the Appendix (see also [12]) shows that the acoustic beam spread must be

$$\Delta\phi = \frac{\Delta k_x}{k_0}\frac{\lambda_1}{8n_1}\frac{\Lambda_0}{v^2}(\Delta f)^2 = \frac{\Lambda_0}{L_1} \quad (29)$$

where

$$L_1 = 4.4\left(\frac{f_0}{\Delta f}\right)L_0 \quad (30)$$

where L_1 is the effective interaction length for the anisotroptic diffraction acousto-optic deflector. The effective interaction length is improved by a factor of 8.8 for a fractional bandwidth of 0.5; the RF power is thus reduced because of the increase in interaction length. A typical example is the slow shear wave TeO_2 acousto-optic beam deflector.

For isotroptic materials, some improvement can be obtained using an acoustic beam steering technique. In this approach we cause the acoustic beam to track the Bragg angle requirement by the use of a phased acoustic transducer array [7], [16]. The simplest phased array uses a planar array as shown by Fig. 10, where the adjacent array elements differ in phase by a fixed quantity ψ. A composite acoustic wavefront can be obtained by connecting the adjacent individual acoustic wavefronts as shown in Fig. 10, corresponding to the first grating order acoustic field. It can be shown that this first-order acoustic wavefront tilts at an angle $\psi vS/2\pi f$, which is inversely proportional to the frequency. Since the Bragg angle is an
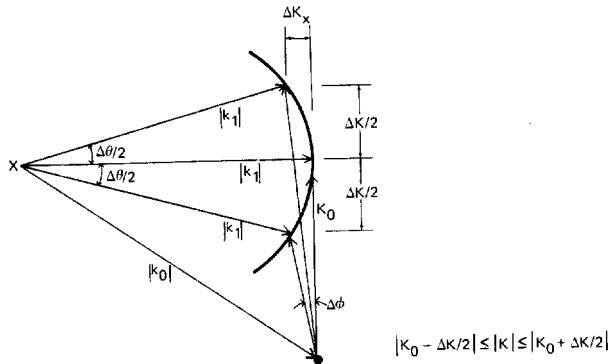
Fig. 9. Anisotropic Bragg direction diagram.

$$|K_0 - \Delta K/2| \leq |K| \leq |K_0 + \Delta K/2|$$
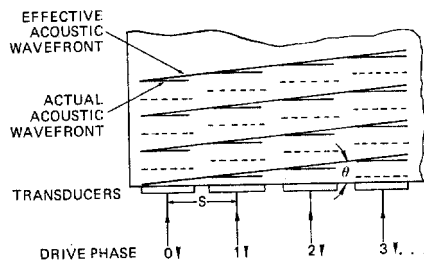
Fig. 10. Acoustic planar phased array configuration.

arcsin function of frequency, the acoustic beam will not track the Bragg condition exactly. The Bragg condition is satisfied at both ends of the bandwidth when the array element separation is [22]

$$S = \frac{n v^2}{(f_0^2 - \Delta f^2/4)\lambda}. \tag{31}$$

However, at the mid-band frequency, the error in the Bragg condition has its maximum value resulting in reduced performance. To keep the tracking error below a value that produces less than 3-dB variation in response over the bandwidth, the number of array elements m can be solved from the array equation in [22]. The gain over the single element device is approximately a factor of 4. Furthermore, the acoustic planar array produces many acoustic wavefront orders which reduce the acoustic power in the desired order; efficiency will be approximately another 3 dB lower. The overall improvement in performance for a flat array is about a factor of 2 over a single element transducer. At high frequencies, the transducer impedance is usually less than a few ohms, so that segmenting the transducer also has the advantage of transforming the impedance to a higher value closer to a 50-Ω system. To provide acoustic power concentration into the desired order of acoustic wavefront, a more advanced array structure [7], [23], where the array elements are made on steps of step height ($\Lambda_0/2$) each, can be employed, resembling a blazed grating in optics. However, such steps are difficult to fabricate at high frequencies.

ACOUSTO-OPTIC MATERIALS

The development of acousto-optic devices has reached a stage where performance is limited by materials and their fundamental parameters, particularly acoustic attenuation. Materials with high figures of merit generally have high attenuation while materials with low acoustic attenuation have relatively poor figures of merit. The widely used acousto-optic
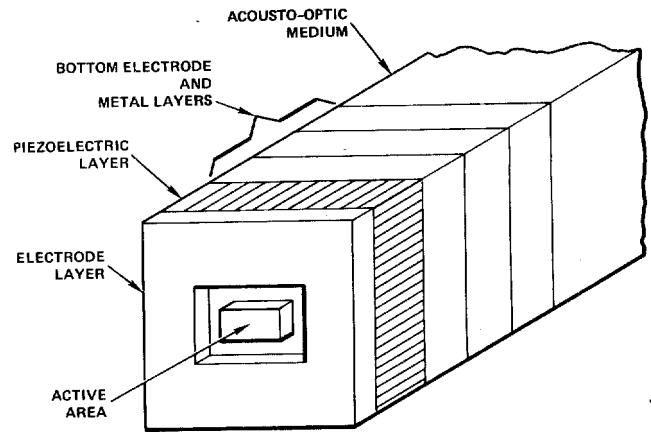
Fig. 11. Transducer assembly configuration with top electrode pattern (not to scale).

materials are fused quartz, TeO_2 and $LiNbO_3$. Development work on new infrared materials have been reported recently and should stimulate applications for infrared lasers. A list of the commonly used acousto-optic materials are given in Table I, [8], [9], [24].

TRANSDUCER DESIGN

The acoustic wave is launched into the acousto-optic material by a piezoelectric transducer that is bonded or deposited onto the substrate. The configuration shown schematically in Fig. 11, consists of top metallic electrode, the pieoelectric material, three metallic layers, and the acousto-optic medium. The RF field is applied across the piezoelectric material using the metallic layers as electrodes. The theory of transducer design has been reported by Meitzler and Sittig [25]–[27].

The performance of high-frequency transducers is highly dependent on the acoustic parameters of the layers that form the system, because these layers act as mismatched transmission lines. Each of these layers can be represented as two-port electrical and mechanical networks connecting the input and output variables of each layer [25]. For the piezoelectric layer, the input electrical variables are the voltage and the current whereas the output acoustic variables are the stress and the particle velocity. For the metal layers, the input and output variables are the stress and the particle velocities.

For a two-port electrical network, the input variables v_n and i_n and the output variables v_{n+1} and i_{n+1} are related by the matrix equation

$$\begin{pmatrix} V_n \\ i_n \end{pmatrix} = \begin{pmatrix} A_n & B_n \\ C_n & D_n \end{pmatrix} \begin{pmatrix} V_{n+1} \\ i_{n+1} \end{pmatrix}. \tag{32}$$

A tandem connection of n such networks is described by a matrix with components A, B, C, D obtained by matrix multiplication:

$$\begin{pmatrix} A & B \\ C & D \end{pmatrix} = \prod_1^n \begin{pmatrix} A_n & B_n \\ C_n & D_n \end{pmatrix} \tag{33}$$

The A_n, B_n, C_n, and D_n values are determined by the mechanical impedance and thickness of the nth section of the transducer assembly.

Meitzler and Sittig have applied this approach to Mason's [28] equivalent circuit of a piezoelectric layer, and have extended the procedure to include the other layers as well. The equivalent circuit of the transducer and acousto-optic medium

TABLE I
ACOUSTO-OPTIC PROPERTIES OF SELECTED CRYSTALLINE MATERIALS

Material	Density - ρ $(10^3 kg/m^3)$	Velocity - v $(10^3 m/s)$	Index - n	Attenuation - Γ (dB/μs GHz^2)	M_2 $(10^{-15} s^3/kg)$	M_3 $(10^{-15} m\text{-}s^2/kg)$
LiTaO$_2$	7.45	6.19	2.18	0.062	1.37	1.84
LiNbO$_3$	4.64	6.57	2.20	0.098	7.00	10.1
TiO$_2$	4.23	8.03	2.584	0.566	3.93	7.97
Sr$_{.75}$Ba$_{.25}$Nb$_2$O$_6$	5.40	5.50	2.299	2.20	38.6	48.8
GaP	4.13	6.32	3.31	3.80	44.6	93.5
TeO$_2$	6.00	4.20	2.26	6.30	34.5	32.8
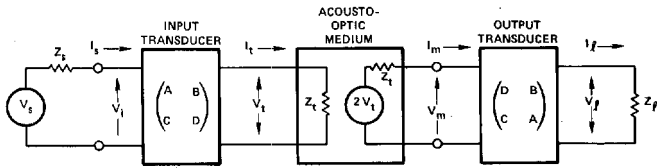
Fig. 12. Equivalent circuit representation of an acousto-optic device with two transducers.

configuration is shown in Fig. 12, where a transducer assembly is included at both ends of the acousto-optic medium. The source voltage and impedance are V_s and Z_s and the load voltage and impedance are V_l and Z_l. The mechanical impedance of the acousto-optic medium is Z_t. The insertion loss IL is given by

$$IL = 20 \log \left| \frac{V_s}{V_l} \right| + 20 \log \left(\frac{R_l}{R_s + R_l} \right) \qquad (34)$$

where

$$\frac{V_s}{V_l} = \left(\frac{1}{2R_l Z_t} \right) ((AZ_t + B) + R_s(CZ_t + D))$$

$$\cdot (A(Z_t + B) + R_l(CZ_t + D)) \quad (35)$$

and where Z_l and Z_s are taken to be purely resistive. If $Z_l = Z_s$, then the conversion loss of one transducer will be one half the IL.

The conversion loss represents the power reflected at the transducer due to the electrical impedance mismatch between the driver and the acousto-optic device. A conversion loss of 3 dB means that only one half of the RF electrical power applied to the transducer electrodes is converted to acoustic power if there are no dissipative losses in the transducer assembly.

Calculations for transducer impedance are performed with the aid of a computer program. The important outputs of the transducer computer program are the transducer electrical bandwidth and impedance. The values of H and L are determined from the acousto-optic requirements and the approximate thickness of the transducer is determined by the required center frequency of the acousto-optic device. The computer program also provides information on the bandwidth and impedance as a function of the properties of the bonding layers.

The most commonly used piezoelectric transducers are single crystal LiNbO$_3$ plate transducers [29], and ZnO thin film transducers [30]. Below 1 GHz, LiNbO$_3$ transducers have better performance mainly because of a higher coupling coefficient and a low electrical Q factor, resulting in a very simple tuning network. At 1 to 2 GHz, ZnO, and LiNbO$_3$ transducers have comparable performance parameters. For frequencies above 2 GHz, ZnO devices are in production [30], [31] whereas work with LiNbO$_3$ transducers has been limited to laboratory developments [32]. Based on our calculation, LiNbO$_3$ transducers should perform well even at the high frequencies and further development of the plate transducer technology should result in improved performance. Given a piezoelectric material and an acousto-optic material, the next most important parts of the transducer assembly are the metal layers. In Fig. 13, we show the conversion loss versus frequency for a transducer assembly whose parameters are given in the figure. The piezoelectric material is LiNbO$_3$, and the acousto-optic material is TeO$_2$. It is obvious that for this example, the tin metal layer gives a wider bandwidth than the indium layer.

The computer programs calculate the constructional parameters of the transducer layers. They also predict the resulting bandwidth, response and conversion losses. We now need to determine how to connect the transducer to the driving source through an impedance matching network.

IMPEDANCE MATCHING NETWORKS

In this section, we describe the use of microstrip elements in designing and fabricating impedance matching networks for acousto-optic devices. There are serious shortcomings in fabricating matching networks using lumped elements. At frequencies above 400 MHz it becomes increasingly difficult to realize the network design parameters because of the parasitic impedance of the inductor coil and the inductance of the capacitor leads. Such networks limit the bandwidth and tend to be lossy, thus restricting the ultimate performance of the acousto-optic device; in addition, they are difficult to reproduce. We have found that the use of microstrip techniques in fabricating matching networks with distributed elements has given excellent results.

When properly used, transmission line elements may be used to simulate inductors and capacitors. The detailed theory, along with the necessary charts and tables which allow one to

TOP
ELECTRODE : Al   1 μm
TRANSDUCER : LiNbO₃   5 μm
                 ⎰ Au   0.2 μm
BONDING LAYERS ⎨ In OR Sn 0.7 μm
                 ⎱ Au   0.2 μm
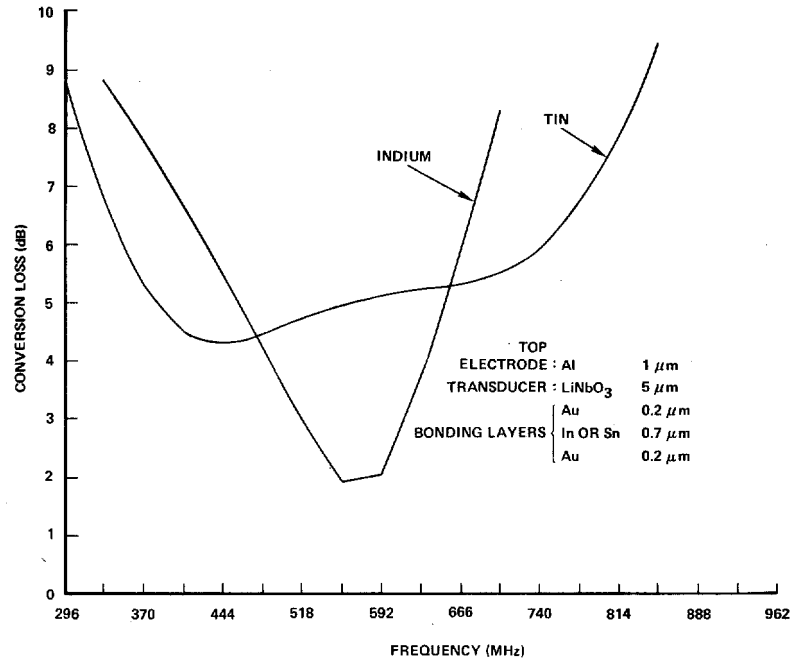
Fig. 13. Calculated conversion loss versus frequency for indium and tin
bonding layers.
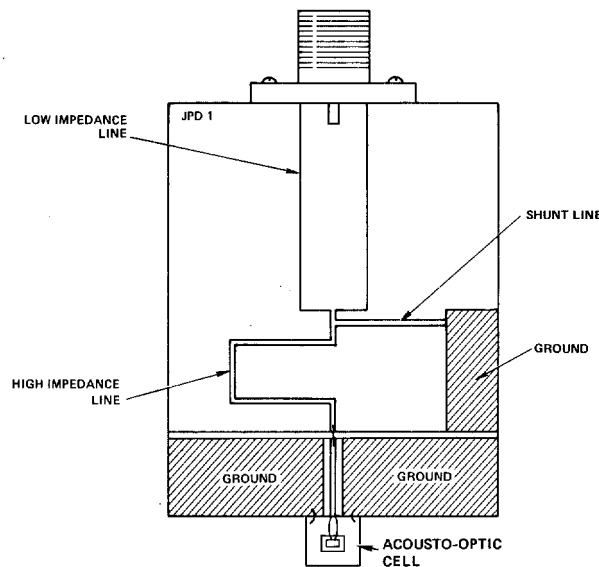
Fig. 14. Microstrip impedance matching network.

design a given circuit, is given in [33]. It is worth while to note the following:

1) the addition of a high characteristic impedance series microstrip will approximate the addition of a series inductor;
2) the addition of a low characteristic impedance series line will approximate the addition of a shunt capacitor;
3) the addition of a shunt line to ground can be treated as a shunt inductor.

To fabricate a matching network, the starting impedance of the acousto-optic cell (including all leads) must be measured with a network analyzer. The problem here is to design micro-strip matching networks which will match the impedances of these devices to the electronic driver. A matching network

consisting of a series high impedance line, a high impedance line shunted to ground, and a series low impedance line is shown in Fig. 14. This network is approximately equivalent to a series inductor, a shunt inductor and a shunt capacitor.

The proper dimensions of these microstrip elements are cal-culated for impedance matching at the center frequency of the cells according to the procedures given in [7]. The im-pedance of microstrip section is derived from the transmission line equations and is

$$Z = Z_0 \frac{Z_L + jZ_0 \tan \beta l}{Z_0 + jZ_L \tan \beta l}. \tag{36}$$

In (36), Z is the impedance of a microstrip element, Z_0 is its characteristic impedance, Z_L is the load impedance, l is the length of the microstrip element, and $\beta = 2\pi/\lambda$, where λ is the

TABLE II
ACOUSTO-OPTIC DEFLECTORS AND MODULATORS

Device Type	Material	Laser Wavelength	Center Frequency	Bandwidth	Aperture	Efficiency	Reference
Deflector	TeO_2 Slow Shear	0.633 μm	75 MHz	50 MHz	40 μs	80% max	Grossman [36] Merry [35]
Deflector	$LiNbO_3$	0.633 μm	1600 MHz	1050 MHz	1.0 μs	1.0%/watt	Hecht [37] Grossman and Young [38]
Deflector	$LiNbO_3$	0.633 μm	2500 MHz	1600 MHz	2.4 μs	1.8%/watt	Kirchner [31]
Modulator	TeO_2	0.633 μm	500 MHz	170 MHz (AM) 300 MHz (RF)	--	50% max	Grossman and Young [38]
Modulator	TeO_2	0.633 μm	750 MHz	250 MHz (AM) 600 MHz (RF)	--	30% max	Grossman and Young [38]

wavelength of the electrical signal on the microstrip line. The calculated dimensions are considered as starting values. The actual values used in fabricating the networks are obtained from the General Electric time sharing computer network on a program called "COMPACT." Among other things, COMPACT will compute the optimum circuit dimension over the frequency range specified when given the circuit configuration and starting dimensions. The quantity that is optimized is the return loss of the network. COMPACT does not calculate the circuit that will give the best match at a given frequency, but rather it defines the circuit with the best match over the entire frequency range specified by the user. It is perhaps worth stating here, that COMPACT will do the same thing for a lumped element network, but implementing this network in practice is very difficult, whereas implementing the microstrip network is relatively easy. Using the optimized dimensions for the circuit elements, the matching network circuit is then fabricated.

EXAMPLES OF ACOUSTO-OPTIC DEVICES

Acousto-optic modulators are widely used in applications for digital and analog modulation of laser beams. The design procedures outlined earlier apply for both types of modulators. For digital modulation, devices handling 200 Mbit/s date rates are used in a number of applications; as the data rate increases the efficiency decreases, but it is still acceptable for many applications at a rate of 500 Mbit/s. For analog modulation, the acousto-optic modulator system configuration is more complicated since the acousto-optic modulation transfer function is a nonlinear (sinusoidal) function of the drive voltage. For analog modulation, we add a bias level, at the carrier frequency, to the modulation frequency to improve linearity; this technique works very well and the maximum achievable bandwidth is on the order of 300 MHz.

Acousto-optic deflectors are made from TeO_2, $PbMO_4$, GaP, and $LiNbO_3$ crystalline materials. For broad bandwidth signal processing applications, $LiNbO_3$ deflectors have the best performance, because of the material's low acoustic attenuation. Table II is a list of $LiNbO_3$ devices fabricated by various co-workers in the technical community. The slow shear wave TeO_2 devices make use of the anisotroptic Bragg diffraction phenomena, and are of particular interest because it has extremely high figure of merit ($M_2 \approx 800$) and is the only device

that has over 2000 resolvable elements when operated as a deflector.

In addition to acousto-optic modulators and deflectors, special multiple array element transducers have been constructed for applications in signal processing, data storage, and beam deflectors. The maximum number of acousto-optic array elements constructed is 136 for a holographic recording system [39].

CONCLUSIONS

Acousto-optic device technology has matured significantly in the past ten years. In some signal processing applications the time–bandwidth product and the overall system throughput is now limited by the performance of photodetector arrays, not the acousto-optic devices. Other signal processing applications, however, require bandwidths well beyond 1 GHz and diffraction efficiencies of more than 10 percent. The discovery of new materials having higher figures of merit and less attenuation at high frequencies is needed to significantly improve the performance of both modulators and deflectors.

APPENDIX A
INTERACTION LENGTH CALCULATION FOR ANISOTROPIC CRYSTALS

Referring to Fig. 9, the incident light wave vector (k_0) interacts with the acoustic wave vector (K), resulting in the diffracted wave vector (k_1). The refractive indicies for the two wave vectors are n_0 and n_1, respectively, and n_1 is greater than n_0. For a given acoustic bandwidth, the change in the acoustic wave vector magnitude ΔK will result in the angular change of $\Delta\phi$ given by

$$\Delta\phi \cong \frac{\Delta K_x}{K_0}. \tag{A1}$$

From Fig. 9 it can be seen that

$$\Delta K_x = k_1 - k_1 \cos\left(\frac{\Delta\theta}{2}\right) \cong \frac{(\Delta K)^2}{8k_1}. \tag{A2}$$

Substituting (A2) into (A1) and noting that $K_0 = 2\pi/\Lambda_0$, $\Delta\phi$ is now expressed as

$$\Delta\phi = \frac{\lambda\Lambda_0(\Delta f)^2}{8n_i v^2}. \tag{A3}$$

For a finite transducer length L, its radiation spread angle is Λ_0/L which must be equated with $\Delta\phi$. Therefore,

$$\Delta\phi = \frac{\Lambda_0}{L} = \frac{\lambda\Lambda_0(\Delta f)^2}{8n_1 v^2}. \qquad \text{(A4)}$$

We define a characteristic length L

$$L_0 = \frac{1.8 n_1 v^2}{\lambda f_0 \Delta f}. \qquad \text{(A5)}$$

This length L_0 corresponds to a Q of about 22. Combining (A4) and (A5), it is seen that the interaction length L_1 is

$$L_1 = 4.4 \frac{f_0}{\Delta f} L_0. \qquad \text{(A6)}$$

REFERENCES

[1] P. Debye and F. W. Sears, "Scattering of light by supersonic waves," *Proc. Nat. Acad. Sci.*, vol. 18, pp. 409–414, 1932.

[2] R. Lucas and P. Biquard, "Proprietes milieux solides et liquides soumis aux vibrations elastiques ultra sonores," *J. Phys. Radium*, vol. 3, pp. 464–477, 1932.

[3] C. V. Raman and N. S. Nagendra Nath, "The diffraction of light by high frequency sound waves: Part I," *Proc. Indian Acad. Sci.*, vol. 2A, pp. 406–412, 1935; "Part II," vol. 2A, pp. 413–420, 1935; "Part III—Doppler effect and coherence phenomena," vol. 3A, pp. 75–84, 1936; "Part IV—Generalised theory," vol. 3A, pp. 119–125, 1956; "Part V—General considerations—Oblique incidence and amplitude changes," vol. 3A, pp. 359–365, 1936.

[4] W. R. Klein and B. D. Cook, "Unified approach to ultrasonic light diffraction," *IEEE Trans. Sonics Ultrasonics*, vol. SU-14, pp. 123–134, 1967.

[5] R. W. Dixon, "Photoelastic properties of selected materials and their relevance for applications to acoustic light modulators and scanners," *J. Appl. Phys.*, vol. 38, pp. 5149–5153, Dec. 1967.

[6] C. F. Quate, C. D. W. Wilkinson, and D. K. Winslow, "Interaction of Light and Microwave Sound," *Proc. IEEE*, vol. 53, pp. 1604–1623, Oct. 1965.

[7] A. Korpel, R. Adler, P. Desmares, and W. Watson, "A television display using acoustic deflection and modulation of coherent light," *Proc. IEEE*, vol. 54, pp. 1429–1437, Oct. 1966.

[8] D. A. Pinnow, "Guided lines for the selection of acousto-optic materials," *IEEE J. Quantum Electron.*, vol. QE-6, pp. 223–238, Apr. 1970.

[9] R. W. Dixon, "Photoelastic properties of selected materials and their relevance for applications to acoustic light modulators and scanners," *J. Appl. Phys.*, vol. 38, pp. 5149–5153, Dec. 1967.

[10] N. Uchida and Y. Ohmachi, "Elastic and photoelastic properties of TeO single crystal," *J. Appl. Phys.*, vol. 40, pp. 4692–4695, Nov. 1969.

[11] A. W. Warner, D. L. White, and W. A. Bonner, "Acousto-optic light deflectors using optical activity in paratellurite," *J. Appl. Phys.*, vol. 43, pp. 4489–4495, Nov. 1972.

[12] I. C. Chang, "Acousto-optic devices and applications," *IEEE Trans. Sonics Ultrasonics*, vol. SU-23, Jan. 1976.

[13] D. Maydan, "Acousto-optical pulse modulators," *IEEE J. Quantum Electron.*, vol. QE-6, pp. 15–24, Jan. 1970.

[14] J. W. Goodman, *Introduction to Fourier Optics*. New York: McGraw-Hill, 1968.

[15] S. K. Yao, to be published.

[16] E. I. Gordon, "A review of acousto-optical deflection and modulation devices," *Proc. IEEE*, vol. 54, pp. 1391–1401, Oct. 1966.

[17] D. L. Hecht, "Multifrequency acousto-optic diffraction'" *IEEE Trans. Sonics Ultrasonics*, vol. SU-24, Jan. 1977.

[18] A. VanderLugt, private communications, Feb. 1980.

[19] L. D. Dickson, "Optical considerations for an acousto-optic deflector," *Appl. Opt.*, vol. 11, no. 10, Oct. 1972.

[20] I. Gorog, J. D. Knox, and P. V. Goedertier, "A television rate laser scanner—I. General considerations," *RCA Rev.*, vol. 33, no. 4, Dec. 1972.

[21] R. W. Dixon, "Acoustic diffraction of light in anisotropic media," *IEEE J. Quantum Electron.*, vol. QE-3, pp. 85–93, Feb. 1967.

[22] S. K. Yao and E. H. Young, "Two-hundred (200) MHz bandwidth step-array acousto-optic beam deflector," presented at SPIE Symp., Aug. 1976.

[23] D. A. Pinnow, "Acousto-optic light deflection: Design consideration for first order beam steering transducers," *IEEE Trans. Sonics Ultrason.*, vol. SU-18, pp. 209–214, Oct. 1971.

[24] N. Uchida and N. Niizeki, "Acousto-optic deflection materials and techniques," *Proc. IEEE*, Aug. 1973.

[25] A. H. Meitzler and E. K. Sittig, "Characterization of piezoelectric transducers used in ultrasonic devices operating above 0.1 GHz," *J. Appl. Phys.*, vol. 40, pp. 4341–4352, Oct. 1969.

[26] E. K. Sittig, "Design and technology of piezoelectric transducers for frequencies above 100 MHz," in *Physical Acoustics Vol. IX*, W. P. Mason and R. N. Thurston, Eds. New York: Academic Press, 1972.

[27] ——, "Effects of bonding and electrode layers on the transmission parameters of piezoelectric transducers used in ultrasonic digital delay lines," *IEEE Trans. Sonics Ultrasonics*, vol. SU-16, pp. 2–10, Jan. 1969.

[28] W. P. Mason, *Electromechanical Transducers and Wave Filters*. New York: D. Van Nostrand, 1942 (1948, 2nd ed.), pp. 399–404.

[29] A. H. Meitzler, "Piezoelectric transducer materials and techniques for ultrasonic devices operating above 100 MHz," in *Ultrasonic Transducer Materials*, O. E. Mattiat, Ed. New York: Plenum, 1971.

[30] E. K. Kirchner and J. R. Yaeger, "Today's capabilities of microwave, acousto-optic devices," Aug. 1976.

[31] E. K. Kirchner, "Deposited transducer technology for use with acousto-optic bulk wave devices," *Proc. SPIE*, vol. 214 (Acousto-optic Bulk Wave Devices), Nov. 1979.

[32] H. C. Huang, J. D. Knox, Z. Turski, R. Wargo, and J. J. Hanak, "Fabrication of submicron LiNbO transducers for microwave acoustic (bulk) delay lines," *Appl. Phys. Lett.*, vol. 24, pp. 109–111, Feb. 1974.

[33] G. L. Mattaei, L. Young, and E. M. T. Jones, *Microwave Filters, Impedance-Matching Networks, and Coupling Structures*. New York: McGraw-Hill, 1964, chs. 4, 6, 9.

[34] R. M. Montgomery and E. H. Young, Jr., "Trends in acousto-optic modulators," *Proc. SPIE*, Aug. 1976.

[35] J. B. Merry, "High resolution acousto-optic deflector demonstrated in a laser scanner," *CLEOS*, Feb. 1978.

[36] B. G. Grossman and B. R. Reddersen, "High speed laser facsimile scanner," *Proc. SPIE*, Aug. 1979.

[37] D. L. Hecht, "Acousto-optic device techniques—400 to 2300 MHz," in *1977 Ultrasonics Symp. Proc.* (IEEE Cat. #377CH1264-ISU), 1977.

[38] E. H. Young and B. G. Grossman, private communications.

[39] A. M. Bardos, R. H. Nelson, H. N. Roberts, and C. A. Shuman, "Electro-optic components for wideband recording and reproduction," in *Proc. Electro-Optical Systems Design Conf.*, Nov. 1975.

Acousto-Optic Signal Processing: Convolution and Correlation

WILLIAM T. RHODES, MEMBER, IEEE

Invited Paper

Abstract—The use of acousto-optic devices in real-time signal convolution and correlation has increased dramatically during the past decade because of improvements in device characteristics and implementation techniques. Depending on the application, processing can be implemented via spatial or temporal integration. Two-dimensional signal processing (including image processing) is possible, in spite of the inherent one-dimensional nature of the acousto-optic device as a spatial light modulator.

I. INTRODUCTION

T HE ACOUSTO-OPTIC cell has a long history of application to optical processing and display, dating back at least to the late 1930's when Okolicsanyi proposed its use in projection television systems [1]. References to its use in converting electrical signals into spatial light distributions appear in a number of early papers on optical signal processing [2]–[4], and in the 1960's extended research programs were conducted on its application to the processing of radar and telecommunications signals [5]–[16]. Various techniques developed during this period have been described by Maloney in a highly readable paper in *IEEE Spectrum* magazine [17]. Developments of new techniques since 1970 have significantly enhanced the capabilities of acousto-optic cells in specific signal processing tasks. For example, through the application of time-integration acousto-optic processing methods, processing time–bandwidth products greatly exceeding the time–bandwidth product of the acousto-optic device itself can be achieved, and spatial filtering of two-dimensional (2-D) distributions—e.g., image deblurring—is possible.

This paper presents a tutorial review of acousto-optic signal processing methods, particularly those developed during the 1970's, as they relate to the linear shift-invariant filtering operations of convolution and correlation, both 1-D and 2-D. (See [18] for a complementary discussion of acousto-optic methods in signal spectral analysis.) We place major emphasis on systems aspects, choosing examples to illustrate key points. A Fourier optics point of view is stressed throughout [19]–[21].

II. USE OF ACOUSTO-OPTIC CELLS AS SPATIAL LIGHT MODULATORS

A. General Background

If the operation of different acousto-optic correlators and convolvers is to be understood, it is important that the basic

relationship between the driving electrical signal and the resultant modulation of light waves, both spatially and temporally, be clear. In order to facilitate a better understanding of the systems described in later sections, we therefore first review the basic characteristics of acousto-optic cells as spatial light modulators. We begin by considering briefly certain physical constraints that bear on the types of signal waveforms that can serve as input and the ways in which acousto-optic cells can be used.

To begin with, acoustic waves launched by the transducer into the cell frequently cannot be viewed, or otherwise detected optically, if they are imaged in conventional fashion. Like an unstained amoeba under a microscope, the acoustic wave structure remains unseen unless some special technique, such as phase contrast imaging or dark central field imaging, is used to render it visible [19, ch. 7].

As another point of great operational importance, we note that the electrical signals that drive acousto-optic cells must generally be bandpass in nature, with frequency content typically in the range of 1 MHz to 1 GHz. Reasonably large fractional bandwidths are acceptable, depending on the nature of the acousto-optic material and the transducer [22]. This restriction on the input signal waveform means that signals to be processed, if not originally bandpass in nature, must be placed on carriers in order to be suitable for input. The carrier can be modulated in both magnitude and phase, allowing complex signal processing. In many cases, an acousto-optic cell can be used directly in processing of radar and RF communication signals without the need for additional modulation.

Finally, it should be recalled that physical size of the cell and attenuation of sound waves in the cell material limit the practical duration of the signal contained in the cell at one instant in time to, typically, a few tens of microseconds. This prevents the use of acousto-optic devices in many speech and other voiceband signal processing operations, where the minimum useful time window is typically tens of milliseconds. (An exception occurs in spectrum analysis, where time-integration acousto-optic processing methods can yield useful short-time spectra with time windows in the tens-of-milliseconds range.)

B. Analytical Modeling

When used as a spatial light modulator, an acousto-optic cell is illuminated by a beam of light, usually collimated, and the wave field of that beam is modified by the sound waves in the cell via diffraction processes. The nature of the acousto-optic interaction is influenced by the thickness, in the direction of

light wave propagation, of the interaction region. Specifically, if this thickness is large compared to the distance between neighboring acoustic wavefronts in the cell, Bragg or volume effects are significant and conditions for diffraction of the incident light are modified. We begin by modeling "thin" interaction or Raman–Nath regime operation, then consider modifications necessary for Bragg regime modeling. Our analysis is 1-D in nature except where extension to two dimensions is necessary. In modeling the cell we assume that sound wave reflection at the end of the cell opposite the input transducer is suppressed, i.e., acoustic wave propagation is unidirectional.

With reference to Fig. 1, the signal-driven acousto-optic cell is characterized by a complex wave amplitude transmittance function $t(x, t)$, where x is the spatial coordinate along the axis of acoustic wave propagation and t denotes time. (We consistently use boldface notation to denote complex-valued quantities.) If we let $s(x)$ represent, to within a proportionality constant, the transducer-induced elastic strain field in the acousto-optic medium at time $t = 0$, $t(x, t)$ is given by [17]

$$t(x, t) = \exp [js(x - Vt)] \, \text{rect} \, (x/W) \qquad (1)$$

where V is the velocity of the strain field in the medium (the acoustic velocity), W is the width of the cell, and rect($\cdot$) denotes the unit rectangle function. The origin of the x-axis is placed at the middle of the cell. The strain field at the transducer end of the cell, $s[-(W/2) - Vt]$, is proportional to the input signal voltage $v(t)$; i.e.,

$$s[-(W/2) - Vt] = mv(t) \qquad (2)$$

where m is a proportionality constant. If (1) is rewritten in terms of $v(t)$, the resulting representation for $t(x, t)$ has the advantage of linking the acousto-optic cell transmittance and, thereby, any processor outputs directly to the input signal waveform. However, the form of (1) lends itself to a more compact analysis of the operation of processing systems considered initially and will, therefore, be used for the time being; i.e., $s(x - Vt)$ will itself in general be treated as the system input, with (2) providing the link to the driving electrical signal waveform. Pictorial reasoning is generally adequate in linking $s(x - Vt)$ and $v(t)$: if $s(\cdot)$ and $mv(\cdot)$ are plotted as functions of the same variable, they vary only by a horizontal scale factor (the sound velocity) and a delay (corresponding to the time required for the strain wave to propagate from the transducer to the optical axis at $x = 0$).

As suggested earlier, the driving signal waveform is normally an RF carrier that is modulated in magnitude and phase. We write the corresponding strain wave, for $t = 0$, as

$$s(x) = a(x) \cos [2\pi f_0 x + \alpha(x)]. \qquad (3)$$

Substituting for $s(x - Vt)$ in (1) and expanding the exponential in a power series, we obtain (with H.O. denoting higher order in s)

$$t(x, t) = \{1 + js(x - Vt) + \text{H.O.}\} \, \text{rect} \, (x/W)$$
$$= \{1 + ja(x - Vt) \cos [2\pi f_0(x - Vt)$$
$$+ \alpha(x - Vt)] + \text{H.O.}\} \, \text{rect} \, (x/W). \qquad (4)$$

If the modulation amplitude $a(x)$ can be assumed small, the higher order terms can be neglected,[1] and, on expanding the

cosine into exponentials, we obtain

$$t(x, t) = \{1 + ja(x - Vt) \exp [j\alpha(x - Vt)] \exp [j2\pi f_0(x - Vt)]$$
$$+ ja(x - Vt) \exp [-j\alpha(x - Vt)]$$
$$\cdot \exp [-j2\pi f_0(x - Vt)]\} \, \text{rect} \, (x/W), \qquad (5)$$

or, equivalently,

$$t(x, t) = \{1 + ja(x - Vt) \exp [j2\pi f_0 x] \exp [-j2\pi \nu_0 t]$$
$$+ ja^*(x - Vt) \exp [-j2\pi f_0 x] \exp [j2\pi \nu_0 t]\} \, \text{rect} \, (x/W) \qquad (6)$$

where ν_0 is the temporal frequency of the driving RF carrier, related to spatial frequency f_0 by $\nu_0 = f_0 V$, and where $a(x) = |a(x)|$, $\alpha(x) = \arg \{a(x)\}$.

It is of considerable use to us in later analyses to express the transmittance function $t(x, y)$ in terms of the analytic signal $\tilde{s}(x)$ associated with $s(x)$, defined by[2]

$$\tilde{s}(x) = a(x) \exp [j2\pi f_0 x]. \qquad (7)$$

Then $s(x) = \text{Re}\{\tilde{s}(x)\}$, and

$$t(x, t) = \{1 + j(\tfrac{1}{2})\tilde{s}(x - Vt) + j(\tfrac{1}{2})\tilde{s}^*(x - Vt)\} \, \text{rect} \, (x/W). \qquad (8)$$

Equations (6)–(8) serve as the principal basis for our subsequent analyses.

If the acousto-optic cell is illuminated by a monochromatic, normally incident, unit-amplitude plane wave, the complex wave amplitude of the transmitted wave $u(x, t)$ equals $t(x, t)$. It is instructive to consider the special case where $a(x - Vt) = 1$; i.e., the driving waveform is an unmodulated carrier. Under these circumstances, $u(x, t)$ is given by (from (6))

$$u(x, t) = \{1 + j \exp [j2\pi f_0 x] \exp [-j2\pi \nu_0 t]$$
$$+ j \exp [-j2\pi f_0 x] \exp [j2\pi \nu_0 t]\} \, \text{rect} \, (x/W). \qquad (9)$$

Let ν denote the optical frequency of the incident wave ($\sim 5 \times 10^{14}$ Hz): $\nu = c/\lambda$, c = speed of light, λ = wavelength. If we ignore the effects of the window function, the three terms of (9) represent, respectively, an undiffracted component at optical frequency ν traveling in the $+z$ direction (the zeroth order); a diffracted plane wave component at optical frequency ($\nu - \nu_0$) with propagation direction inclined through angle $\sin^{-1}(\lambda f_0)$ toward the $+x$-axis (the -1 order, taking the sign in accord with the frequency shift) and a diffracted plane wave component at optical frequency ($\nu + \nu_0$) with propagation direction inclined through angle $\sin^{-1}(\lambda f_0)$ away from the $+x$-axis (the $+1$ order). The directions of propagation and respective optical frequencies are noted in Fig. 1. The shift in frequency of the diffracted waves can be viewed in terms of conservation of photon and phonon momentum, Doppler shift, or as a natural consequence of the diffraction process. All points of view lead to the same result. The Doppler shift point of view is attractive in that it gives us on inspection the sign of the frequency shift.

The trio of diffraction orders in (9) (and the neglected higher order components as well) is characteristic of Raman–Nath regime operation of an acousto-optic cell. As Bragg regime operation is approached, either through an increase in acoustic frequency ν_0 or through a broadening of the acoustic beam,

---

[1] To the extent that $a(x)$ is not small, intermodulation products become significant and can, in some cases, adversely affect device performance. For an analysis of this [?]

[2] Strictly speaking, $s(x)$ is not an analytic signal as defined, but rather the exponential representation signal associated with $s(x)$. However, the difference between the two is ignorable for the narrow-band case of
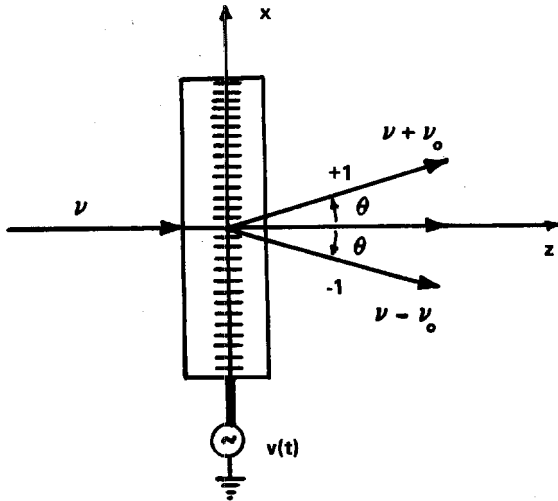
Fig. 1. Acousto-optic cell showing directions and center frequencies of diffracted waves.
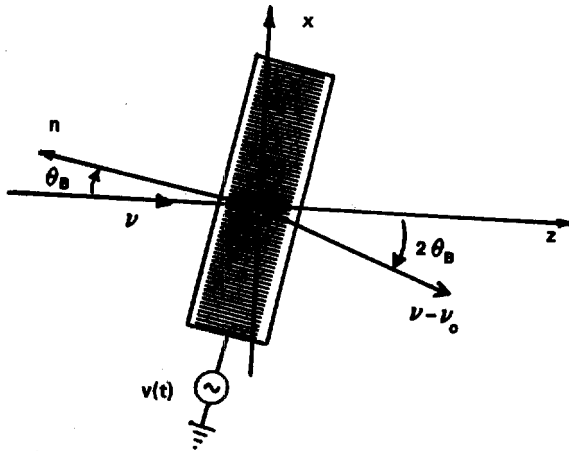

Fig. 2. Geometry for diffraction in Bragg regime.

the diffraction efficiency for normally incident illumination diminishes, ultimately to an insignificant level. To observe diffraction again, it is necessary to rotate the cell slightly in its plane, as shown in Fig. 2, until the angle the incident beam makes with the cell satisfies the Bragg condition:

$$\theta_B = \sin^{-1} (\lambda/2\Lambda) \qquad (10)$$

where Λ is the acoustic wavelength. In this regime, only one of the first order diffraction components is produced with significant magnitude. For the case illustrated in Fig. 2, this is the downshifted or -1 component at frequency $(\nu - \nu_0)$, and the effective transmittance of the cell can be represented by[3]

$$t(x, t) = \{1 + ja(x - Vt) \exp [j2\pi f_0 x]$$
$$\cdot \exp [-j2\pi\nu_0 t]\} \text{ rect } (x/W)$$
$$= \{1 + j(\tfrac{1}{2})\tilde{s}(x - Vt)\} \text{ rect } (x/W). \qquad (11)$$

If the cell is rotated through θ_B in the opposite direction, it is the upshifted or $+1$ diffraction component that is produced,

[3] A more accurate model would include a complex constant of proportionality with the second

and $t(x, t)$ can be represented by

$$t(x, t) = \{1 + ja^*(x - Vt) \exp [-j2\pi f_0 x]$$
$$\cdot \exp [j2\pi\nu_0 t]\} \text{ rect } (x/W)$$
$$= \{1 + j(\tfrac{1}{2})\tilde{s}^*(x - Vt)\} \text{ rect } (x/W). \qquad (12)$$

As noted by Korpel [25], relatively large fractional bandwidths for the complex modulation $a(x - Vt)$ can be accommodated while good Bragg discrimination against other orders is retained if phased array transducers are used. Bragg regime operation is common in acousto-optic processing, particularly since the 1960's, because of the greater diffraction efficiency that is generally possible. In particular, the modulation level $a(x - Vt)$ can be increased significantly without the production of complicating higher order diffraction components.

C. Phase to Amplitude Conversion

Essential for the operation of most acousto-optic processing systems is the conversion at one stage or another in the system of the temporal and spatial *phase* modulation of light, represented by (1), into some form of temporal and spatial modulation of light wave *intensity*. This can be accomplished in several ways using the spatial filtering system of Fig. 3. The cell is illuminated by a collimated beam of light; in the back focal plane of lens L_1 appears the spatial Fourier transform of $t(x, t)$. Successful operation of the spatial filtering system depends on the physical separation in the spatial filter plane of the Fourier transforms of the three terms of (7). This separation is assured by the bandpass nature of $s(x - Vt)$, and requires only that the spatial bandwidth of the modulation $a(x - Vt)$ be smaller than f_0 (equivalently, that the cutoff temporal frequency of $a(x - Vt)$ be smaller than ν_0), a condition virtually always satisfied in acousto-optic cell operation.

Two principal methods of conversion are described. Additional methods are described in [26]. In the *Zernike phase contrast method*, the optical phase of the undiffracted wave from the cell is shifted by $90°$ by a quarter-wave plate on the optical axis in the spatial filter plane. The result is an output plane wave amplitude given by (from (4))

$$u(x, t) = \{j + js(x - Vt)\} \text{ rect } (x/W),$$

with corresponding intensity, given by $|u(x, t)|^2$, equal to

$$I(x, t) = \{1 + 2s(x - Vt) + s^2(x - Vt)\} \text{ rect } (x/W). \qquad (13)$$

As desired, this intensity distribution contains the signal term $s(x - Vt)$. The output of a small photodetector at point x in the image plane will be proportional to $I(x, t)$. Only $s(x - Vt)$ itself contains temporal frequency content about the carrier frequency ν_0; thus, if the detector output is bandpass filtered, an output electrical waveform proportional to a delayed version of $v(t)$ can be obtained.

In the *half-plane stop method*, either the $+1$ or the -1 diffraction order is blocked in the spatial filter plane, with the resultant output intensity (with a $+1$ order stop)

$$I(x, t) = |1 + j(\tfrac{1}{2})\tilde{s}(x - Vt)|^2 \text{ rect } (x/W)$$
$$= \{1 + (\tfrac{1}{4})a^2(x - Vt) + 2s(t)\} \text{ rect } (x/W). \qquad (14)$$

Again, a bandpass filter following the output of a small image plane detector yields the modulation waveform, since the second term is low-pass in nature. If the acousto-optic cell is operating in the Bragg regime, no such filtering is required, the
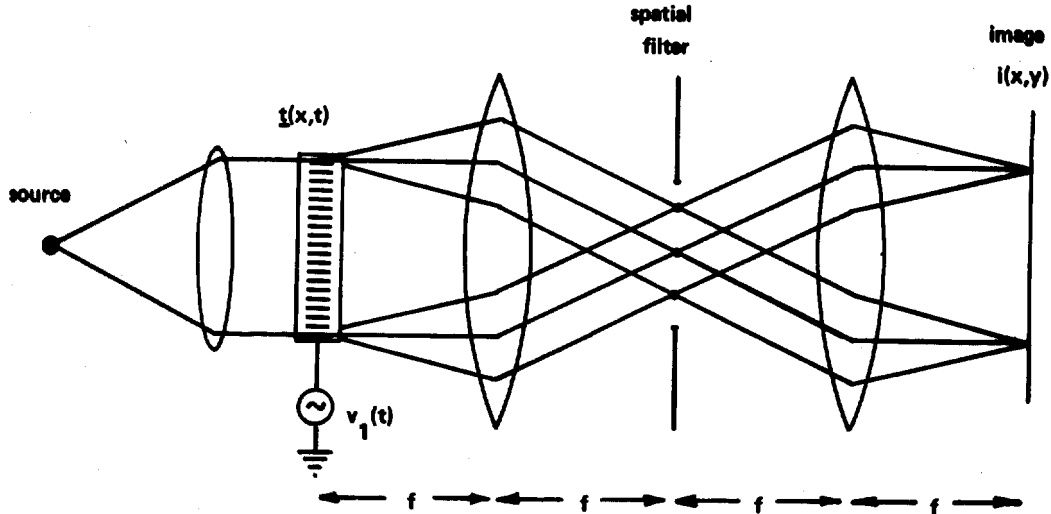
Fig. 3. Use of spatial filtering system to convert phase modulation to amplitude modulation.

It is important to note that neither complete temporal nor complete spatial coherence is required of the wave illuminating the acousto-optic cell in order for these conversion processes to operate, and indeed this is true of most of the correlators and convolvers to be discussed. This is evident if we consider the effects on the spatial filter plane distributions in Fig. 3 of enlarging the source of broadening its spectral bandwidth. In either case, the result is a smearing out of the three diffraction components in the Fourier plane. However, so long as these distributions do not overlap spatially, the desired filtering operation can still be performed. (For broad-band sources, it is necessary to use achromatic wave plates in the phase shifting methods.)

There are alternative methods for modulation conversion that do not require spatial filtering. For example, Meltz and Maloney note that simple propagation of the transmitted optical wave distribution through a distance $Z = \lambda^2/2\Lambda$ leads to the same result as the Zernike phase contrast method discussed above, assuming satisfactorily small modulation bandwidth [14]. In addition, if shear-wave acousto-optic cells are employed (for example, TeO_2), lensless conversion methods using birefringent waveplates and polarizers can be employed [16].

III. 1-D SPACE INTEGRATING CONVOLVERS AND CORRELATORS

A. Notation and Basic Relationships

Given two real-valued distributions $s_1(x)$ and $s_2(x)$, we desire to evaluate either their convolution or their cross correlation. Since the two operations are related through simple coordinate reversals, we concentrate on the cross correlation, this being the operation of greatest interest in radar and RF communications signal processing. In acousto-optic processing, $s_1(x)$, $s_2(x)$, and, therefore, their cross correlation are narrow-band signals—carriers modulated, in general, both in magnitude and in phase. As we shall see, acousto-optic correlators can be constructed to yield as output either the envelope of the correlation function or the entire complex modulated carrier.

Before considering specific examples of systems, we establish some basic notation and relationships for the correlation integral. The cross correlation of real s_1 and s_2 is given by

(infinite limits are assumed unless otherwise noted)

$$R_{12}(\tau) = \int s_1(x)s_2(x+\tau)\,dx \qquad (15a)$$

$$= \int s_1(x-\tau)s_2(x)\,dx. \qquad (15b)$$

Following the notation established in Section II, we write

$$s_1(x) = a_1(x)\cos[2\pi f_0 x + \alpha_1(x)] \qquad (16a)$$

$$= \mathrm{Re}\,\{\tilde{s}_1(x)\} \qquad (16b)$$

$$s_2(x) = a_2(x)\cos[2\pi f_0 x + \alpha_2(x)] \qquad (17a)$$

$$= \mathrm{Re}\,\{\tilde{s}_2(x)\} \qquad (17b)$$

where $\tilde{s}_1$ and $\tilde{s}_2$ are the analytic signals associated with s_1 and s_2, respectively. Exploiting the properties of the analytic signal representation, one can write the correlation of real waveforms $s_1(t)$ and $s_2(t)$ in terms of a complex correlation of $\tilde{s}_1(t)$ and $\tilde{s}_2(t)$:[4]

$$R_{12}(\tau) = \left(\tfrac{1}{2}\right)\mathrm{Re}\left\{\int \tilde{s}_1^*(x-\tau)\tilde{s}_2(x)\,dx\right\} \qquad (18a)$$

$$= \left(\tfrac{1}{2}\right)\mathrm{Re}\left\{\exp[j2\pi f_0\tau]\int a_1^*(x-\tau)a_2(x)\,dx\right\} \qquad (18b)$$

$$= \left(\tfrac{1}{2}\right)\mathrm{Re}\,\{\exp[j2\pi f_0\tau]\,r_{12}(\tau)\} \qquad (18c)$$

$$= \left(\tfrac{1}{2}\right)r_{12}(\tau)\cos[2\pi f_0\tau + \theta_{12}(\tau)] \qquad (18d)$$

where

$$r_{12}(\ ) = \int a_1^*(x-\tau)a_2(x)\,dx \qquad (18e)$$

$$r_{12}(\tau) = |r_{12}(\tau)| \qquad (18f)$$

$$\theta_{12}(\tau) = \arg\{r_{12}(\tau)\}. \qquad (18g)$$

[4] The proof is relatively easy if it is remembered that the analytic signal contains only positive frequency components.
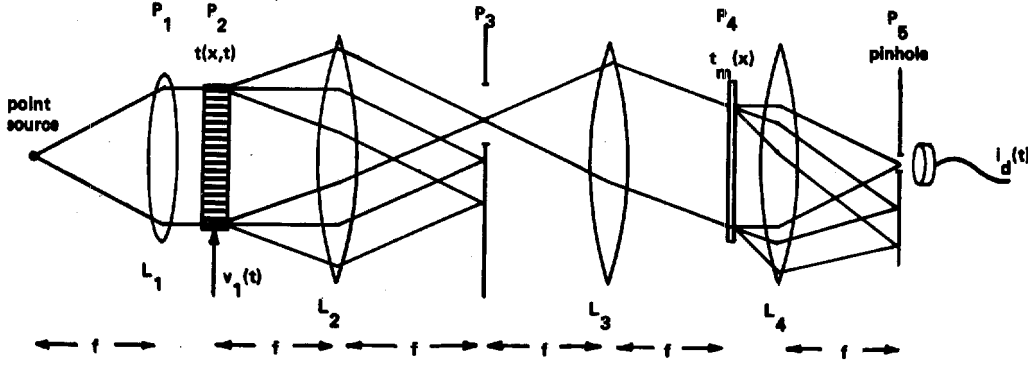
Fig. 4. Nonheterodyning correlator/convolver with single doubly diffracted component incident on pinhole detector.

It should be noted that a_1 and a_2 can represent real baseband signals (which are placed on a carrier for acousto-optic modulation) if α_1 and α_2 equal zero or pi. In that case, $R_{12}(\tau)$ is a pure amplitude-modulated carrier with the amplitude conveying the correlation of $a_1(x)$ and $a_2(x)$.

B. Nonheterodyning Space-Integrating Correlator

In the traditional form of acousto-optic correlator, the integral of (15) is an integration over a spatial coordinate. As a first example of a space-integrating correlator, consider the system of Fig. 4, which evaluates the square of the correlation envelope $r_{12}(\tau)$. The acousto-optic cell can be operated in the Bragg regime, though we assume Raman–Nath operation in our analysis. The complex wave amplitude of the cell is assumed to be given by (1) with $s(x - Vt) = s_1(x - Vt)$. The spatial filter mask in plane P_3 is constructed to pass only the frequency-upshifted +1 diffraction component, and the wave amplitude incident on the mask in plane P_4 therefore has the form (note that the sense of the x-axis has been reversed in this plane, consistent with the inversion undergone in imaging plane P_2 to plane P_4):

$$u_{\text{inc}}(x, t) = (\tfrac{1}{2})\tilde{s}_1^*(x - Vt)\,\text{rect}\,(x/W). \qquad (19)$$

The mask itself, which may be a phototransparency, is represented by amplitude transmittance

$$t_m(x) = [1 + s_2(x)]$$

$$= [1 + (\tfrac{1}{2})\tilde{s}_2(x) + (\tfrac{1}{2})\tilde{s}_2^*(x)]. \qquad (20)$$

The absence of a factor j in the second and third terms is consistent with the amplitude modulation characteristics of photomasks.

The wave transmitted by the mask has complex amplitude

$$u_{\text{trans}}(x, t) = u_{\text{inc}}(x, t)\,t_m(x)$$

$$= \{(\tfrac{1}{2})\tilde{s}_1^*(x - Vt) + (\tfrac{1}{4})\tilde{s}_1^*(x - Vt)\tilde{s}_2(x)$$

$$+ (\tfrac{1}{4})\tilde{s}_1^*(x - Vt)\tilde{s}_2^*(x)\}\,\text{rect}\,(x/W). \qquad (21)$$

To within a quadratic phase factor, the final lens Fourier transforms this distribution and the pinhole samples the resultant transform distribution at the origin, i.e., at zero spatial frequency. Of the three terms of (21), the first contains spatial carrier term $\exp[-j2\pi f_0 x]$ and the third contains $\exp[-j2\pi 2f_0 x]$. Only the second term, corresponding to a doubly diffracted wave component, has spatial frequency content about zero spatial frequency, and the wave amplitude
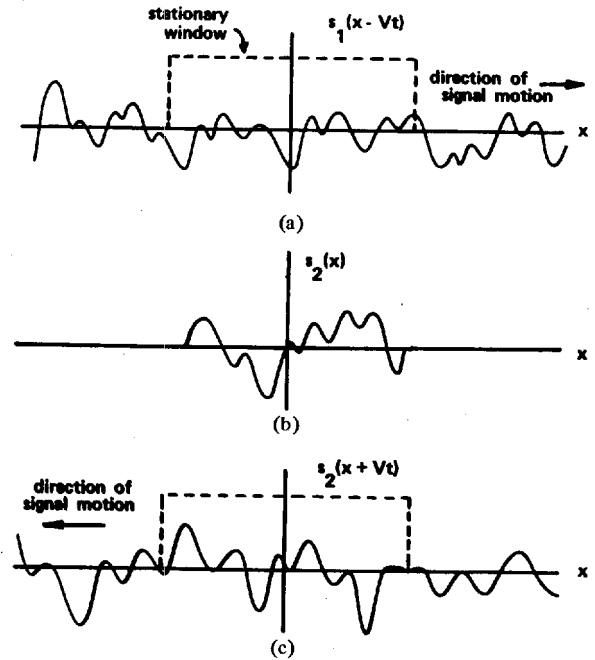
Fig. 5. Functions involved in correlation operation.

at the pinhole is thus given by

$$u_{\text{pinhole}}(t) = (\tfrac{1}{4}) \int \tilde{s}_1^*(x - Vt)\tilde{s}_2(x)\,\text{rect}\,(x/W)\,dx. \qquad (22)$$

Except for the window function, this function is proportional to $r_{12}(Vt)\exp[j2\pi\nu_0 t]$. The detector output $i_d(t)$ is proportional to the wave intensity $|u_{\text{pinhole}}|^2$; thus to the extent that the windowing effect of the finite cell length can be ignored (and dropping a proportionality constant),

$$i_d(t) = r_{12}^2(Vt). \qquad (23)$$

It should be noted that this system requires illumination from a point source because of the pinhole detection arrangement. The source may, however, have broad spectral bandwidth, subject to the spatial filtering requirements in plane P_3.

In a closely related system, the photomask is replaced with a second acousto-optic cell, driven from the bottom. Taking the axis inversion into account, the mask transmittance then becomes

$$t_m(x, t) = 1 + j\tilde{s}_2(x + Vt) + j\tilde{s}_2^*(x + Vt). \qquad (24)$$
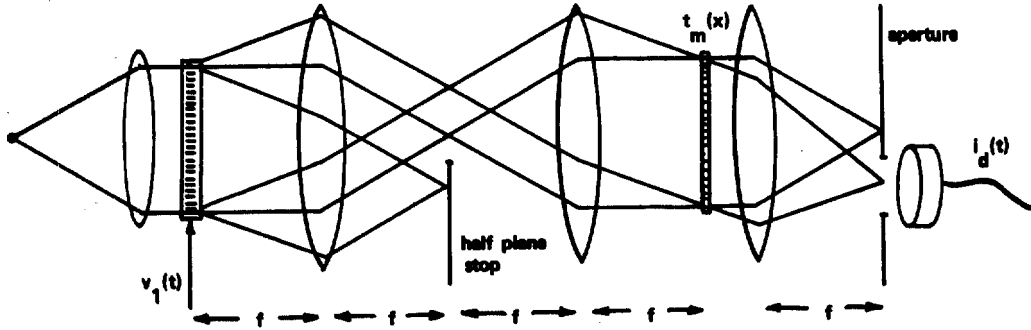
Fig. 6. Heterodyning correlator/convolver with zero and +1 diffraction component imaged on reference mask $t_m(x)$.

Proceeding as before, we find the detector output to be proportional to $r_{12}^2(2Vt)$, or, if the sound velocities are different, to $r_{12}^2[(V_1 + V_2)t]$, where the meaning of V_1, V_2 is obvious. Two-cell systems are convenient in that no photomask recording is required. It should be noted, however, that if such a system is to be used to correlate electrical signal waveforms $v_1(t)$ and $v_2(t)$, it is a *time-reversed* version of $v_2(t)$ that must drive the second acousto-optic cell. (This can be seen by considering the form of the spatial pattern induced in the cell that results, e.g., from a frequency-chirped input signal.) In certain cases a time-reversed version of $v_2(t)$ may be difficult to produce.

Window-imposed limitations on space-integration correlator (and convolver) operation are illustrated with the help of Fig. 5, which shows (a) the signal $s_1(x - Vt)$ moving past the window function, (b) the stationary phototransparency signal $s_2(x)$, and (c) acousto-optic signal $s_2(x + Vt)$ moving under a window. In order for the window to be ignorable, signal $s_1(x)$ must be no wider in extent than window width W. For matched filtering operations, this means that the duration T of the signal to be filtered should not exceed the acoustic transit time across the cell W/V. As noted earlier, this transit time rarely exceeds several tens of microseconds. For signals of greater duration, only partial correlation is possible with the space-integration method.

C. Heterodyning Correlators

With only minor modifications, the system of Fig. 4 can be made to yield the complete phase-bearing correlation function $R_{12}(\cdot)$ as output, not simply its envelope $r_{12}(\cdot)$. Processors that do this are generally referred to as heterodyne processors, since the information-bearing carrier is produced by the heterodyne mixing of two optical waves at the detector. For the example shown in Fig. 6, we allow the zeroth order to be passed by the spatial filter and replace the pinhole in front of the detector with an off-axis opening to pass one of the diffraction components. For analytical convenience we also introduce a 90° phase shift in the +1 diffraction component, although this is not essential. Proceeding as before but including the zeroth-order diffraction component, we have for the wave field transmitted by the mask

$$u_{\text{trans}}(x, t) = \{[1 + (\tfrac{1}{2})\tilde{s}_1^*(x - Vt)]$$
$$\cdot [1 + (\tfrac{1}{2})\tilde{s}_2(x) + (\tfrac{1}{2})\tilde{s}_2^*(x)]\} \text{ rect }(x/W). \quad (25)$$

Of the various product terms, only the singly diffracted components $(\tfrac{1}{2})\tilde{s}_1^*(x - Vt)$ and $(\tfrac{1}{2})\tilde{s}_2^*(x)$, both of which contain spatial carrier terms exp $[-j2\pi f_0 x]$, travel in the correct

nominal direction to pass the detector plane mask. Thus so far as the detector is concerned, we need consider only the wave field

$$u_d(x, t) = \{(\tfrac{1}{2})\tilde{s}_1^*(x - Vt) + (\tfrac{1}{2})\tilde{s}_2^*(x)\} \text{ rect }(x/W). \quad (26)$$

Since the detector responds only to the time varying energy flow in this wave field, we can write for $i_d(t)$, the detector output,

$$i_d(t) = \int |u_d(x, t)|^2 \, dx$$

$$= (\tfrac{1}{4}) \int |\tilde{s}_1^*(x - Vt)|^2 \text{ rect }(x/W) \, dx$$

$$+ (\tfrac{1}{4}) \int |\tilde{s}_2^*(x)|^2 \text{ rect }(x/W) \, dx$$

$$+ (\tfrac{1}{2}) \text{ Re }\left\{ \int \tilde{s}_1^*(x - Vt)\tilde{s}_2(x) \text{ rect }(x/W) \, dx \right\}. \quad (27)$$

The third term is, again to within limitations imposed by the window function rect (x/W), the desired cross correlation $R_{12}(Vt)$. Since $R_{12}(Vt)$ rides on a temporal frequency carrier $\nu_0 = Vf_0$, it can be separated by bandpass filtering from both the second term, which is at dc, and from the first term, which is a baseband term with twice the bandwidth of the modulation $a_1(t)$. As before, a second acousto-optic cell can be used for the signal s_2 as well.

A characteristic common to all heterodyning correlators and convolvers is the mixing at the detector of light waves with optical frequencies in two distinct bands (in the above case separated nominally by ν_0). In an alternate scheme described by Sprague in a review of acousto-optic correlators [27], the basic system of Fig. 4 is used, with the spatial filter passing the +1 and -1 diffraction components from the acousto-optic cell (shifted by $\pm\nu_0$, respectively) and blocking the zeroth order. The complex amplitude of the light wave transmitted by the mask is proportional to

$$u_{\text{trans}}(x, t) = \{[(\tfrac{1}{2})\tilde{s}_1(x - Vt) + (\tfrac{1}{2})\tilde{s}_1^*(x - Vt)]$$
$$\cdot [1 + (\tfrac{1}{2})\tilde{s}_2(x) + (\tfrac{1}{2})\tilde{s}_2^*(x)]\} \text{ rect }(x/W). \quad (28)$$

In this case, only the product terms $(\tfrac{1}{4})\tilde{s}_1(x - Vt)\tilde{s}_2^*(x)$ and $(\tfrac{1}{4})\tilde{s}_1^*(x - Vt)\tilde{s}_2(x)$ have nominal propagation directions along the z-axis. Thus the complex wave amplitude at the on-axis
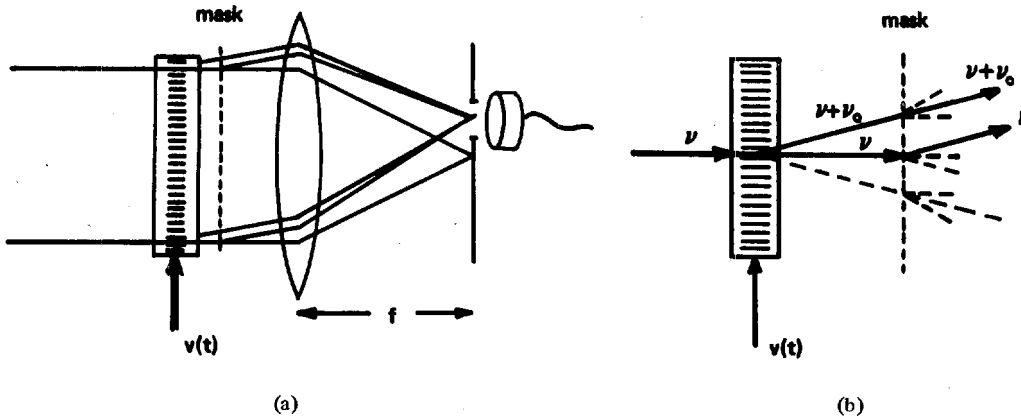
Fig. 7. Proximity imaging, or compact correlator/convolver: (a) basic system; (b) diagram showing relative optical frequencies and origins of components that reach detector.
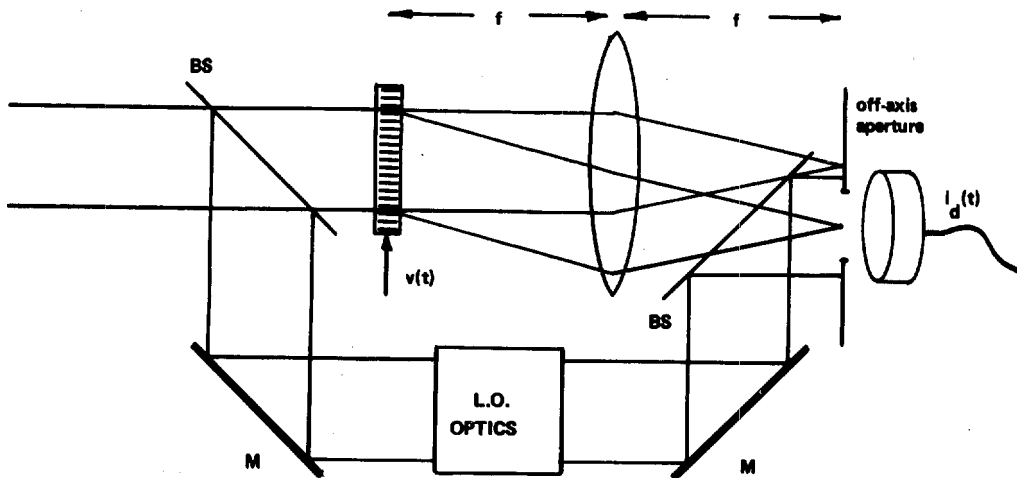
Fig. 8. Fourier plane heterodyne processor: M = mirror and BS = beamsplitter.

pinhole is given by

$$u_{\text{pinhole}}(t) = (\tfrac{1}{4}) \int [\tilde{s}_1^*(x - Vt)\tilde{s}_2(x)$$

$$+ \tilde{s}_1(x - Vt)\tilde{s}_2^*(x)] \, \text{rect} \, (x/W) \, dx$$

$$= (\tfrac{1}{2}) \, \text{Re}\left\{ \int \tilde{s}_1^*(x - Vt)\tilde{s}_2(x) \, \text{rect} \, (x/W) \, dx \right\}.$$

$$(29)$$

Ignoring the window effect, this is the desired correlation. The detector, responding to the intensity of the light at the pinhole, has output

$$i_d(t) = |R_{12}(Vt)|^2 = r_{12}^2(Vt) \cos^2 [2\pi\nu_0 t + \theta_{12}(Vt)]$$

$$= (\tfrac{1}{2})r_{12}^2(Vt) + (\tfrac{1}{2}) r_{12}^2(vT) \cos [2\pi 2\nu_0 t + 2\theta_{12}(Vt)].$$

$$(30)$$

The second term, on a carrier, can be extracted by bandpass filtering. Some additional processing is required to obtain $r_{12}(Vt)$ and, if desired, $\theta_{12}(Vt)$ as final outputs.

A number of heterodyne correlators have been described that do not require the careful imaging of the acousto-optic cell onto the phototransparency that is characteristic of the systems of Figs. 4 and 6. An example is illustrated in Fig. 7.

In this case the cell and mask are assumed to be sufficiently close together that they can be characterized by the product transmittance

$$t_{\text{prod}}(x, t) = t(x, t)\, t_m(x)$$

$$= \{[1 + (\tfrac{1}{2}) \exp [j\theta] \tilde{s}_1(x - Vt)$$

$$+ (\tfrac{1}{2}) \exp [j\theta] \tilde{s}_1^*(x - Vt)]$$

$$\cdot [1 + (\tfrac{1}{2})\tilde{s}_2(x) + (\tfrac{1}{2})\tilde{s}_2^*(x)]\} \, \text{rect} \, (x/W).$$

$$(31)$$

The phase factor $\exp [j\theta]$, which depends on the distance separating the mask and the acousto-optic cell, is chosen for convenience in analysis to equal $-j$. (For some other choice, the phase of the carrier of the cross correlation function changes.) With normally incident illumination of the acousto-optic cell, the light that passes the detector plane mask corresponds to the product terms containing spatial carriers of the form $\exp [j2\pi f_0 x]$, or the terms $(\tfrac{1}{2})\tilde{s}_1(x - Vt)$ and $(\tfrac{1}{2})\tilde{s}_2(x)$. The energy flux associated with these two waves, which governs the detector output, is given by

$$i_d(t) = \int |(\tfrac{1}{2})\tilde{s}_1(x - Vt) + (\tfrac{1}{2})\tilde{s}_2(x)|^2 \, \text{rect} \, (x/W) \, dx \quad (32)$$

which evaluates to the same form as (27).

In order for this kind of correlator (sometimes referred to as a compact configuration correlator) to function correctly, it is necessary that the basic form of the wavefield transmitted by the acousto-optic cell not change significantly over the propagation distance separating cell and mask. This in turn imposes constraints on that distance and on the bandwidth of the complex modulation $a_1(\cdot)$ [14]. This kind of processor geometry has been exploited extensively by researchers at the Harry Diamond Laboratory with planar Bragg mode acousto-optic processors, typically with a second, reverse direction acousto-optic device replacing the phototransparency [28].

D. Fourier-Plane Heterodyne Processing

We close this section with a description of one additional type of space-integrating optical processor, investigated by Whitman et al. [15], that emphasizes the diversity of ways in which acousto-optic cells can be employed for signal filtering. Shown in Fig. 8, this system places the detector in the Fourier transform plane of the acousto-optic cell, behind a mask that passes only the -1 diffraction component. Incident on the detector are two wave distributions, one given by the spatial Fourier transform of the distribution $\tilde{s}_1(x - Vt)$, the other— referred to as the local oscillator (L.O.) wave—being determined by the nature of the optical system in the second arm of the optical system. Letting ξ denote the Fourier plane coordinate and denoting the L.O. wave (for reasons that will become clear) by $(\frac{1}{2})\tilde{S}_2^*(-\xi)$, we thus have for the wave amplitude at the detector

$$u_d(\xi, t) = (\tfrac{1}{2})\tilde{S}_1(\xi) \exp\,[-j2\pi\xi Vt] + (\tfrac{1}{2})\tilde{S}_2^*(-\xi) \quad (33)$$

where $\tilde{S}_1(\xi) \exp\,[-j2\pi\xi Vt]$ is the spatial transform of signal distribution $\tilde{s}_1(x - Vt)$. The detector output is given by

$$i_d(t) = \int |u_d(\xi, t)|^2 \, d\xi \quad (34)$$

which, by Rayleigh's theorem, can be written as

$$i_d(t) = \int |(\tfrac{1}{2})\tilde{s}_1(x - Vt) + (\tfrac{1}{2})\tilde{s}_2^*(x)|^2 \, dx$$

$$= (\tfrac{1}{4}) \int |\tilde{s}_1(x - Vt)|^2 \, dx + (\tfrac{1}{4}) \int |\tilde{s}_2^*(x)|^2 \, dx$$

$$+ (\tfrac{1}{2}) \,\text{Re} \left\{ \int \tilde{s}_1(x - Vt)\tilde{s}_2(x) \, dx \right\} \quad (35)$$

where $\tilde{s}_2(x)$, the inverse spatial transform of $\tilde{S}_2(\xi)$, is the analytic signal associated with real signal $s_2(x)$. The first term of (35) is at baseband, the second at dc. The properties of analytic signals are such that the third, or ac term, denoted $i_{ac}(t)$, has the form of a convolution,

$$i_{ac}(t) = \int s_1(x - Vt)s_2(x) \, dx. \quad (36)$$

As a function of time, this term represents a filtered version of the input signal waveform $v_1(t)$, with the filter impulse response being governed by the function $s_2(x)$.

As noted in [15], a signal $v(t) = \cos 2\pi\nu_s t$ input to the acousto-optic cell produces a single spot of light, downshifted in frequency by ν_s...

mixes with the wave $\tilde{S}_2^*(-\xi)$ at point $\xi = \xi_s$ to produce an output beat signal. This beat signal is itself sinusoidal at frequency ν_s; however, its magnitude and phase are governed by the magnitude and phase of the L.O. wave at point ξ_s. Thus, $\tilde{S}_2(\xi)$ plays the role of a transfer function, leading to an alternate point of view of the processor. In [29], Korpel establishes various basic relationships between this transfer function point of view and the convolution point of view. Recently Florence and Rhodes [30] have described a generalization of the Fourier plane heterodyne processor wherein the L.O. wave field varies in optical frequency as a function of Fourier plane coordinate ξ. The mixing processes that result lead to signal input–output relationships described loosely as a nonlinear mapping of signal frequency components. The method can be used for certain kinds of bandwidth compression and expansion.

IV. 1-D TIME-INTEGRATING CONVOLVERS AND CORRELATORS

A. Introduction

Acousto-optic processors are well suited to wide-band signal processing, with acousto-optic correlators being particularly applicable to radar signal processing. Situations arise, however—for example, in direction finding of noise-like sources— where correlation times exceeding the transit time of the acousto-optic window are desirable or necessary. Extensions of the basic space-integrating methods discussed above have been investigated where correlation times are increased by the use of multiple cells with delay lines and by the use of folded-path acousto-optic devices [31]. Especially important in extending the capabilities of acousto-optic devices has been the development of an alternate class of acousto-optic processors, known collectively as time-integrating processors, that allow integration times of the order of tens of milliseconds and greater [32]–[41].

B. Two-Cell System

We begin with a description of the first processor of this class to be developed, reported by Montgomery in [32] and illustrated in Fig. 9. Because time-integration processing is characterized by integrations with respect to time rather than space, we modify our point of view from that taken in the previous section and emphasize t, the integration variable, by writing the acousto-optic cell transmittance directly in terms of the driving signal waveforms, $v_1(t)$ and $v_2(t)$. For convenience of notation we also move the x-axis origin from the optical axis to the bottom end of the cells. Under these circumstances, we can write (omitting a modulation proportionality constant and the window function)

$$t_1(x, t) = \exp\,[jv_1(t - x/V)] \quad (37a)$$

$$\doteq [1 + jv_1(t - x/V)] \quad (37b)$$

$$t_2(x, t) = \exp\,[jv_2(t + x/V - T)] \quad (38a)$$

$$\doteq [1 + jv_2(t + x/V - T)] \quad (38b)$$

where

$$v_1(t) = b_1(t) \cos\,[2\pi\nu_0 + \beta_1(t)] \quad (39)$$

$$v_2(t) = b_2(t) \cos\,[2\pi\nu_0 t + \beta_2(t)]. \quad (40)$$

In (38) the + sign denotes the reversed sound wave propagation direction, and T is the acousto-optic transit time W/V.
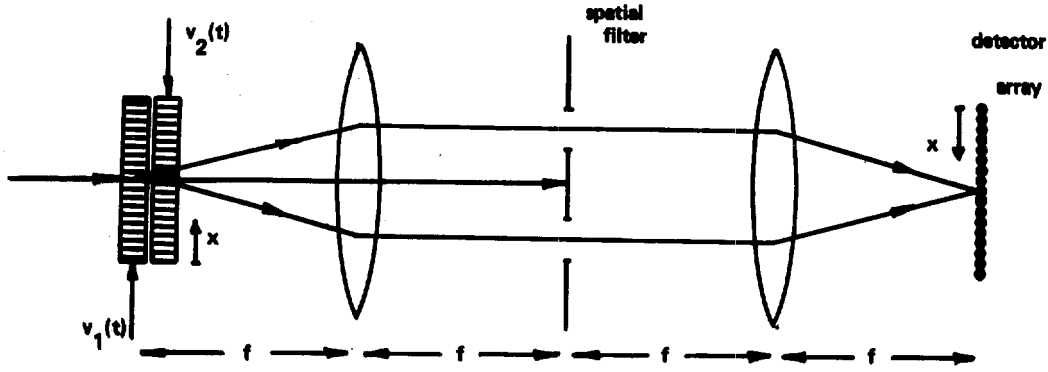
Fig. 9. Example of a two-cell time-integrating correlator/convolver. Rays show directions of principal diffraction components.

As before, we introduce the analytic signal representations for v_1, v_2, writing

$$v_1(t) = \text{Re } \{\tilde{v}_1(t)\} \qquad (41)$$

$$v_2(t) = \text{Re } \{\tilde{v}_2(t)\} \qquad (42)$$

where

$$\tilde{v}_1(t) = b_1(t) \exp[j\beta_1(t)] \exp[j2\pi\nu_0 t] \qquad (43a)$$

$$= b_1(t) \exp[j2\pi\nu_0 t] \qquad (43b)$$

$$\tilde{v}_2(t) = b_2(t) \exp[j\beta_2(t)] \exp[j2\pi\nu_0 t] \qquad (44a)$$

$$= b_2(t) \exp[j2\pi\nu_0 t]. \qquad (44b)$$

In terms of the analytic signals, the transmittance functions become

$$t_1(x, t) = \{1 + j(\tfrac{1}{2})\tilde{v}_1(t - x/V) + j(\tfrac{1}{2})\tilde{v}_1^*(t - x/V)\} \qquad (45)$$

$$t_2(x, t) = \{1 + j(\tfrac{1}{2})\tilde{v}_2(t + x/V - T) + j(\tfrac{1}{2})\tilde{v}_2^*(t + x/V - T)\}. \qquad (46)$$

Although the notation has been changed from that of Section III, it is important to note that the analytic signal terms $\tilde{v}_1$, $\tilde{v}_2$, $\tilde{v}_1^*$, and $\tilde{v}_2^*$ correspond directly to the acoustic wave terms $\tilde{s}_1$, $\tilde{s}_2$, $\tilde{s}_1^*$, and $\tilde{s}_2^*$ of earlier analyses. Specifically, as functions of x they lead to the same diffracted wave components as before and can be filtered out by appropriate spatial filter plane stops.

As a function of the real signals $v_1(t)$ and $v_2(t)$, the cross-correlation function $R_{12}(\tau)$ has the form

$$R_{12}(\tau) = \int v_1(t - \tau) v_2(t) \, dt \qquad (47)$$

which in terms of the analytic signals can be written as

$$R_{12}(\tau) = (\tfrac{1}{2}) \text{ Re}\left\{ \int \tilde{v}_1^*(t - \tau) \tilde{v}_2(t) \, dt \right\} \qquad (48a)$$

$$= (\tfrac{1}{2}) \text{ Re } \{\exp[j2\pi\nu_0\tau] r_{12}(\tau)\} \qquad (48b)$$

where

$$r_{12}(\tau) = \int b_1^*(t - \tau) b_2(t) \, dt. \qquad (49)$$

In practice, the two cells of Fig. 9 are typically operated in the Bragg regime with, for example, cell 1 being rotated

clockwise and cell 2 being rotated counterclockwise through the Bragg angle. Under these circumstances, the conjugated terms of (45) and (46) are suppressed, and the product transmittance has the form

$$t_{\text{prod}}(x, t) = [1 + j(\tfrac{1}{2})\tilde{v}_1(t - x/V)][1 + j(\tfrac{1}{2})\tilde{v}_2(t + x/V - T)]. \qquad (50)$$

If the cell pair is illuminated by a nominally collimated light beam, the pair of openings in the pupil plane mask pass only diffraction components corresponding to the terms $j(\tfrac{1}{2})\tilde{v}_1(t - x/V)$ and $j(\tfrac{1}{2})\tilde{v}_2(t + x/V - T)$, with a resultant detector plane intensity distribution given by

$$I_d(x, t) = |j(\tfrac{1}{2})\tilde{v}_1(t - x/V) + j(\tfrac{1}{2})\tilde{v}_2(t + x/V - T)|^2$$
$$= (\tfrac{1}{4})|\tilde{v}_1(t - x/V)|^2 + (\tfrac{1}{4})|\tilde{v}_2(t + x/V - T)|^2$$
$$+ (\tfrac{1}{2}) \text{ Re } \{\tilde{v}_1^*(t - x/V)\tilde{v}_2(t + x/V - T)\}. \qquad (51)$$

The detectors in the output plane array perform the integration with respect to time, integrating charge at a rate proportional to the incident light intensity. Thus letting $E_{\Delta T}$ denote the light energy delivered at point x on the detector array during an interval of time T, the output of the integrating detector at x is proportional to

$$E_{\Delta T}(x) = (\tfrac{1}{4}) \int_{\Delta T} b_1^2(t - x/V) \, dt + (\tfrac{1}{4}) \int_{\Delta T} b_2^2(t + x/V - T) \, dt$$
$$+ (\tfrac{1}{2}) \text{ Re}\left\{ \int_{\Delta T} \tilde{v}_1^*(t - x/V)\tilde{v}_2(t + x/V - T) \, dt \right\}. \qquad (52)$$

To the extent that ΔT can be assumed infinite, the first two terms of this expression evaluate to constants and the third to the desired correlation; thus,

$$E_{\Delta T}(x) = \text{bias} + R_{12}(2x/V - T). \qquad (53)$$

In practice, integration times are limited by dark current, which ultimately saturates the linear response of integrating photodetectors. Nevertheless, as suggested earlier, integration times of tens of milliseconds are possible with low noise CCD photodetector arrays, and these times can be extended by post-detection digital integration. The acousto-optic window no longer limits the signal duration, but it does impose a restriction on the correlation variable τ, limiting it to the range $0 \leq \tau \leq W/V$. This restriction can present difficulties in certain
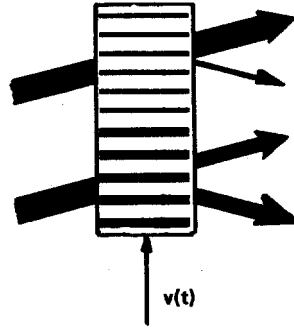
Fig. 10. Zeroth-order depletion.
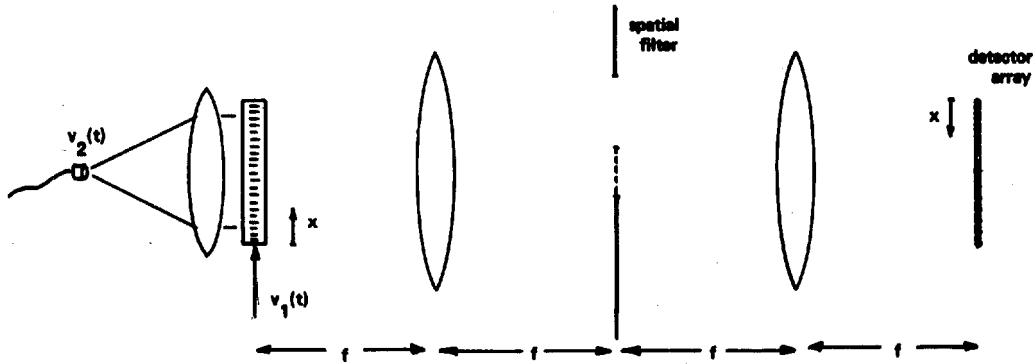
Fig. 11. Single-cell time-integration system. Dotted line in spatial filter denotes phase shifter.

areas of application when, for example, relative time delays between signals are unknown. Perhaps the major limitation of time-integration processors is the presence of the bias terms that attend the desired correlation function. These terms also drive the integrating detectors toward saturation and, because they are signal dependent (both as functions of time and of space), may be difficult to compensate with post-detection processing. In spite of these bias terms, however, excellent processing gain is achievable with time-integration methods when applied to matched filtering operations [27].

A possible drawback of the two-cell system just discussed relates to a phenomenon known as zeroth-order depletion. The basic idea is illustrated graphically in Fig. 10, which shows a bandpass acoustic wave diffracting light in the Bragg regime. Where the acoustic wave is weak, low-efficiency diffraction of the incident beam has relatively little effect on the intensity of the undiffracted component of the output. With high diffraction efficiency, however, a sufficiently large fraction of the incident wave is diffracted that the zeroth order—that part of the wave field that is to be diffracted by the second cell—is modulated both temporally and spatially rather than being constant. High diffraction efficiency operation results in reduced accuracy because of this phenomenon.

C. One-Cell System

Fig. 11 shows an alternate time-integration correlator, of a type described by Turpin [34] and by Kellman [35], that overcomes the zeroth-order depletion limitations of the two-cell system and is generally simpler to implement. The acousto-optic cell, illuminated with light from an LED or laser diode, is driven from the top by signal $v_1(t)$ and imaged onto the integrating detector array. The spatial filter plane mask shifts the phase of the zeroth order by $90°$ and blocks the frequency-downshifted diffraction component. The intensity of the

illumination is modulated by signal $v_2(t)$, such that

$$I_{\text{illum}}(t) = B + v_2(t), \tag{54}$$

where B is a bias sufficiently large to keep the sum $[B + v_2(t)]$ nonnegative. The detector plane intensity is thus given by

$$I_d(x, t) = I_{\text{illum}}(t) \left| 1 + (\tfrac{1}{2}) \tilde{v}_1(t - x/V) \right|^2$$

$$= [B + v_2(t)] [1 + (\tfrac{1}{4}) b_1^2(t - x/V) + v_1(t - x/V)] \tag{55}$$

with associated time-integrated intensity

$$E_{\Delta T}(x) = B\Delta T + \int_{\Delta T} \{ B v_1(t - x/V)$$

$$+ v_2(t)[1 + (\tfrac{1}{4}) b_1^2(t - x/V)\} \, dt$$

$$+ \int_{\Delta T} v_1(t - x/V) v_2(t) \, dt. \tag{56}$$

The first term in this expression is a spatially uniform bias, which builds up with the integration time ΔT; the second term, being governed by an integrand at the carrier frequency ν_0, is negligable for $\Delta T \gg 1/\nu_0$. The third term, for ΔT sufficiently large, is the desired correlation $R_{12}(\cdot)$ as a function of x/V.

D. One-Cell System with Electronically Inserted Reference

We note briefly a method suggested by Kellman for increasing the versatility and convenience of time-integration acousto-optic processors. The system employed is a simple modification of that of Fig. 11, in which input signal $v_1(t)$ is replaced by signal

$$v_1'(t) = b_1(t) \cos [2\pi(\nu_0 + \nu_c)t + \beta_1(t)] + A \cos 2\pi\nu_0 t \tag{57}$$

obtained from $v_1(t)$ by shifting the carrier frequency by an amount ν_c and adding a cosine signal at that same frequency.

With $v_1'(t)$ as the input, the acousto-optic cell transmittance, assuming Bragg regime operation, is given by

$$t(x, t) = 1 + j[A + (\tfrac{1}{2})\tilde{v}_1(t - x/V)] \exp [j2\pi\nu_c(t - x/V)]. \quad (58)$$

The cell is illuminated as before by the modulated diode and imaged, this time with a zeroth-order stop. The resultant detector plane intensity is given by

$$I_d(x, t) = [B + v_2(t)] \left| A + (\tfrac{1}{2})\tilde{v}_1(t - x/V) \right|^2$$

$$= [B + v_2(t)] [A^2 + (\tfrac{1}{4})b_1^2(t - x/V) + Av_1(t - x/V)]. \quad (59)$$

Assuming $\Delta T \gg 1/\nu_0$, the associated time-integrated intensity is approximated by

$$E_{\Delta T}(x) = A^2 B \Delta T + A \int_{\Delta T} v_1(t - x/V)v_2(t)\, dt \quad (60)$$

which is similar to the results for the previous system (which corresponds to setting A equal to unity), but now the ratio of the correlation term to the bias term is proportional to A^{-1} and can therefore be adjusted for optimum system performance [40].

E. Linear Intensity Modulation Method

As our final example, we describe a time-integration correlator/convolver that represents a significant departure from the other systems—both time-integrating and space-integrating—that we have considered to this point. The scheme, described by Sprague and Koliopoulos [33], relies on characteristics of acousto-optic cells operating in the Bragg regime at high diffraction efficiencies. For an acousto-optic modulator with sinusoidal driving signal $v(t) = b \cos 2\pi\nu_0 t$, the intensity of the diffracted wave I_{diff} for Bragg regime operation is given by $I_{\text{diff}} = I_{\text{illum}} \sin^2 (Kb)$, where I_{illum} is the intensity of the incident light and K is a constant. For low diffraction efficiency, $Kb \ll 1$ and I_{diff} is approximately equal to $(Kb)^2$, consistent with our earlier analyses. In Sprague's scheme, the driving signal is of the form $v(t) = [b_0 + b_1(t)] \cos 2\pi\nu_0 t$, where b_0 is chosen so as to place operation in the linear portion of the $\sin^2$ curve; i.e., $Kb_0 = \pi/4$. Under these circumstances, the diffracted wave, modulated both temporally and spatially, has the form

$$I_{\text{diff}}(x, t) = I_{\text{illum}} \sin^2 [K(b_0 + b_1(t - x/V))]$$

$$= I_{\text{illum}} [(\tfrac{1}{2}) + Kb_1(t - x/V)]. \quad (61)$$

The illuminating beam is modulated according to

$$I_{\text{illum}}(t) = B + b_2(t) \quad (62)$$

and the acousto-optic cell is imaged onto the detector plane with only the diffracted component passed. The resultant detector plane distribution is thus

$$I_d(x, t) = [B + b_2(t)] [(\tfrac{1}{2}) + Kb_1(t - x/V)] \quad (63)$$

with integrated intensity

$$E_{\Delta T}(x) = (\tfrac{1}{2}) B \Delta T + \int_{\Delta T} [(\tfrac{1}{2})b_2(t) + KBb_1(t - x/V)]\, dt$$

$$+ K \int_{\Delta T} b_1(t - x/V)b_2(t)\, dt \quad (64)$$
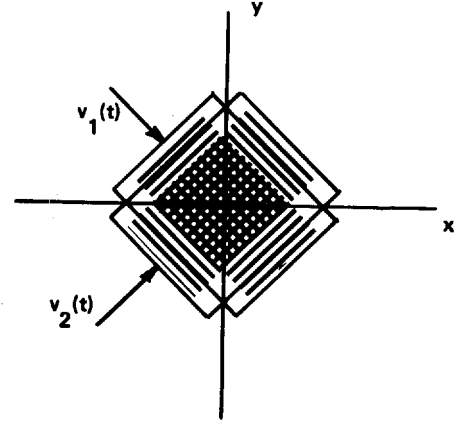
Fig. 12. Cross-ambiguity processor: Input cell geometry.

which consists again of a bias plus the desired correlation term. Because $Kb_1(t)$ is small, the signal-to-bias ratio of the output distribution is itself relatively low.

V. EXTENSIONS TO TWO DIMENSIONS

Although the great majority of acousto-optic processors have 1-D inputs and 1-D outputs, certain 2-D processing operations are possible. The classic example of 2-D acousto-optic processing involves the use of astigmatic imaging systems to allow multiple 1-D correlations or convolutions to be performed in parallel in a channelized system [3]. Systems employed are straightforward extensions of the space-integrating systems discussed in Section III, but the image of the 1-D acousto-optic cell signal $s(x - Vt)$ is spread out in the y-direction to illuminate a mask transparency that varies not only with x but also with y. The single output plane mask and detector become multiple masks and detectors at different distances above the x-axis.

A reasonably sophisticated 2-D acousto-optic processing operation on a *pair* of 1-D signals is the evaluation of the cross-ambiguity function. Given two analytic signals $\tilde{v}_1(t)$ and $\tilde{v}_2(t)$, their cross-ambiguity function is given by

$$\gamma_{12}(\tau, \nu) = \int \tilde{v}_1^*(t - \tau)\tilde{v}_2(t) \exp [j2\pi\nu t]\, dt \quad (65)$$

which can be viewed as the complex correlation of $\tilde{v}_1(t)$ with a frequency-shifted version of $\tilde{v}_2(t)$. A space-integration acousto-optic implementation, described by Said and Cooper [42], is explained with the help of Fig. 12. The two real bandpass signals $v_1(t)$ and $v_2(t)$ are input to a pair of crossed cells, with propagation directions at $45°$ to the x–y axes. The complex amplitude transmission of the acousto-optic cell pair is given by (ignoring the effect of the window)

$$t_{\text{pair}}(x, y, t) = [1 + js_1(\sqrt{2}\ [x + y - Vt])]$$

$$\cdot [1 + js_2(\sqrt{2}\ [x - y - Vt])]. \quad (66)$$

The cell pair is illuminated with a nominally collimated light beam and imaged, with all but one (doubly) diffracted wave component being stopped by a spatial filter plane mask. The transmitted component has the form

$$u_{\text{trans}}(x, y, t) = \tilde{s}_1^*(\sqrt{2}\ [x + y - Vt])\tilde{s}_2(\sqrt{2}\ [x - y - Vt]).$$

$$(67)$$

To pass this component, the spatial filter must consist of an

76
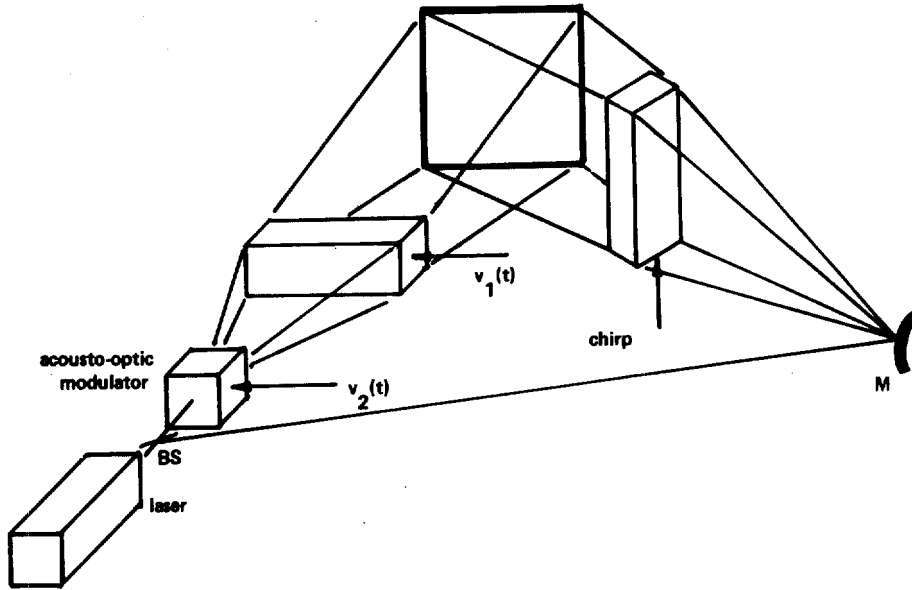
Fig. 13. Time-integration cross-ambiguity processor schematic.

opaque mask with an opening shifted vertically off axis. The wave distribution $u_{trans}(x, y, t)$ is now acted on by an astigmatic lens system that images in the vertical direction while Fourier transforming in the horizontal direction [3]. The resultant output wave amplitude is given by

$$u_{out}(u, y, t) = \int \tilde{s}_1^*(\sqrt{2}[x + y - Vt]) \tilde{s}_2(\sqrt{2}[x - y - Vt])$$

$$\cdot \exp [j2\pi u x] \, dx \quad (68)$$

which equals $\gamma_{12}(2\sqrt{2}\, y, u)$, as long as both signals are within the aperture. The observed intensity is the squared modulus of this distribution; if phase is to be preserved, interferometric means can be used.

An area of considerable current interest is the application of time integration acousto-optic techniques to 2-D signal processing applications [34], [37], [39]. We illustrate with a system described by Turpin [34] for cross-ambiguity function calculation. Fig. 13 is a schematic representation of this system, greatly simplified to illustrate the concept, not the optics. (The actual system is too complicated optically to illustrate easily, requiring a combination of spherical and cylindrical lenses as well as spatial filtering masks to remove unwanted diffraction components.) Light from the laser source, split by a beamsplitter, travels through two subsystems to be recombined interferometrically in the output plane. In the upper subsystem, the laser beam is first modulated in complex amplitude by an acousto-optic modulator, which is driven by narrow-band signal $v_2(t)$. The output of the acousto-optic modulator is a light beam (a single diffraction component from the cell) with complex amplitude $\tilde{v}_2(t)$. This beam is expanded in the horizontal, or x direction and recollimated so as to illuminate the entire width of the second acousto-optic cell. The output of this second cell, which is driven by signal $v_1(t)$, is expanded and recollimated in the vertical direction and imaged with appropriate spatial filtering in the horizontal direction. The result in the output plane is a complex wave amplitude distribution given by $\tilde{v}_1^*(t - x/V)\tilde{v}_2(t)$. Note that as a function of output plane coordinates this distribution varies only in the x direction.

Also incident on the output plane is a wave produced by the second subsystem. This wave is planar and is incident

at an angle that varies linearly with time in the y direction and is constant in the x direction. Such a wave, described analytically by $\exp [-j2\pi \alpha y t] \exp [-j2\pi \beta x]$, where α and β are constants, can be produced by driving the third acousto-optic cell with a sinusoid that is ramped linearly in frequency—a chirp.

The interference of the waves from the two subsystems produces the intensity distribution

$$I_d(x, y, t) = \left| \tilde{v}_1^*(t - x/V)\tilde{v}_2(t) + \exp (-j2\pi \alpha y t) \right.$$

$$\left. \cdot \exp (-j2\pi \beta x) \right|^2$$

$$= \left| \tilde{v}_1^*(t - x/V)\tilde{v}_2(t) \right|^2 + 1$$

$$+ 2 \, \text{Re} \left\{ \exp (j2\pi \alpha x)\tilde{v}_1^*(t - x/V)\tilde{v}_2(t) \right.$$

$$\left. \cdot \exp (j2\pi \beta y t) \right\}. \quad (69)$$

If this distribution is integrated with respect to time, the third term yields

$$2 \, \text{Re} \left\{ \exp (j2\pi \alpha x)\tilde{v}_1^*(t - x/V)\tilde{v}_2(t) \exp (j2\pi \beta y t) \right\}.$$

Assuming that the constant α is sufficiently large, this distribution takes the form of a sinusoidal fringe pattern whose magnitude and phase carry the magnitude and phase of the cross-ambiguity function. Specifically, assuming ΔT to be large, the integrated output intensity is given by

$$E_{\Delta T}(x, y) = \text{bias} + 2 \left| \gamma_{12}(x/V, y) \right|$$

$$\cdot \cos [2\pi \alpha x + \arg \{ \gamma_{12}(x/V, y) \}]. \quad (70)$$

It should be noted that the accompanying bias distribution is a function of spatial variable x. However, this distribution is spatially low pass in nature. If the output distribution is scanned with a television camera (the camera itself performing the time integration), the output video signal will contain a low-pass component, which can be filtered out, and a bandpass component, which conveys the desired ambiguity function. The tilting plane wave from the lower subsystem must be "restarted" periodically. Assuming it switches back to its starting angle instantaneously, there are certain values of y for which the optical phase of the wave changes continuously with time. For other values of y, however, the phase function $\exp [-j2\pi \beta y t]$ has periodic discontinuities as a function of time.
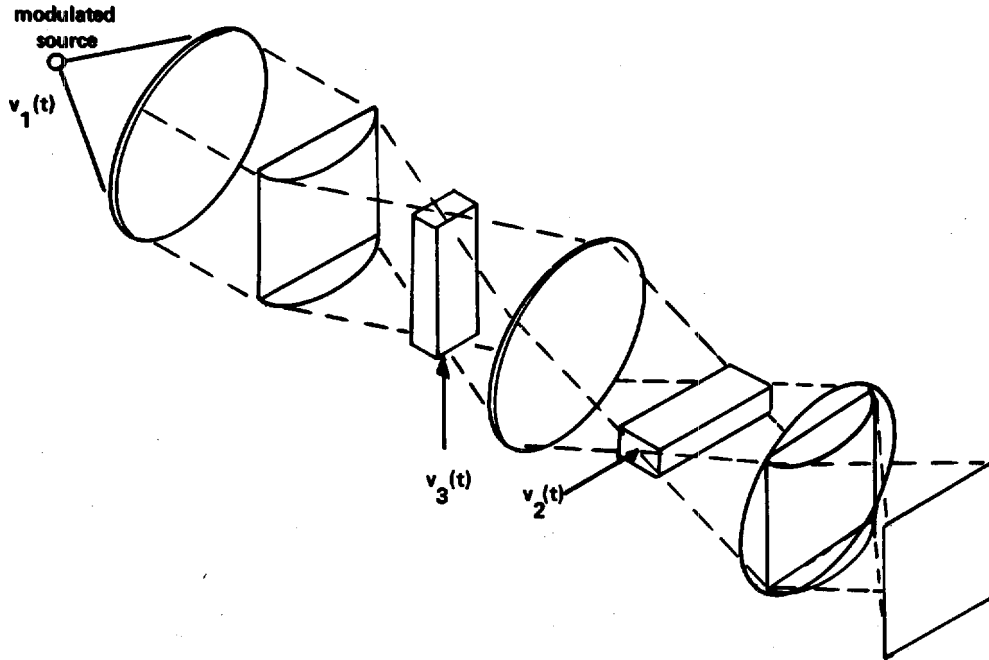
Fig. 14. 2-D triple product time-integration processor. Spatial filtering masks not shown.

Only for those values of y for which the wave phase changes continuously as a function of time is the desired ambiguity function produced. In essence the periodic tilts of the plane wave introduce a comb filter effect in the signal analysis. The total number of discrete frequencies represented by the comb can be shown to equal the time–bandwidth product of the third acousto-optic cell.

The scheme just described is complicated somewhat by the interferometer nature of the system. Not only must a laser be used as the light source, but system construction must be interferometrically stable. Kellman has investigated a class of 2-D time-integration processors based on a simpler, imaging-type architecture [40]. Fig. 14 shows the basic form of such systems. In essence, the two acousto-optic cells of the system are imaged onto each other and onto the output plane, which contains a 2-D array of integrating photodetectors. Intermediate spatial filtering, not shown in the figure for simplicity, leads to a term in the output plane intensity distribution that is given by

$$I(x, y, t) = v_1(t)v_2(t - x/V)v_3(t - y/V). \qquad (71)$$

The integrated intensity, as a function of x and y, is thus given by

$$E_T(x, y) = \text{bias} + \int_{\Delta T} v_1(t)v_2(t - x/V)v_3(t - y/V)\, dt. \qquad (72)$$

Depending on the form of $v_1(t)$, $v_2(t)$, and $v_3(t)$, this system, refered to as a *triple product processor*, can be used for cross-ambiguity calculation or for large time–bandwidth product spectrum analysis (see [18]).

We close this section with a description of a 2-D image processing technique currently under investigation by the author [43] that can be performed using acousto-optic devices. The operation of the overall system is shown schematically in Fig. 15: $f(x, y)$ represents the input image and $h(x, y)$ the spatial impulse response of the filter to be realized, given by
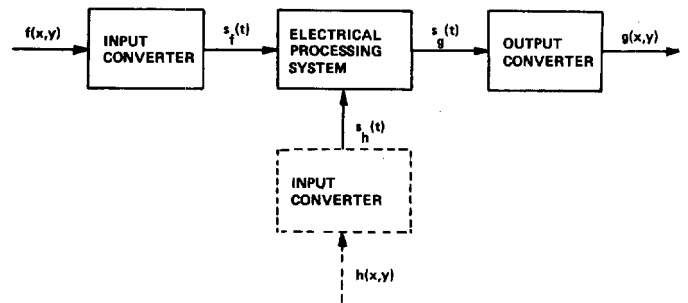
Fig. 15. Image processing system.

2-D convolution $g(x, y) = f(x, y) * h(x, y)$. An essential feature of the system operation is the conversion (invertible through sampling relationships) from 2-D to 1-D signal representations and back again. The acousto-optic system employed for input and output conversion serves the purpose of producing a set of sinusoidal fringes. These fringes, with intensity $I_f(x, y; t) = 1 + \cos[\omega_0 t + 2\pi(ux + vy)]$, result from the interference of light from a pair of mutually coherent light spots. These light spots are scanned in orthogonal directions by acousto-optic beam deflectors to produce fringes of controllable spatial frequency. Depending on the relative temporal frequencies of the two spots (also determined acousto-optically), the fringes may be stationary ($\omega_0 = 0$) or moving with constant phase velocity ($\omega_0 \neq 0$).

Consider the input conversion operation first. We assume that the image to be processed $f(x, y)$ exists as the intensity transmittance of a photo transparency. (It is significant that $f(x, y)$ is the *intensity* transmittance, as opposed to the complex wave amplitude transmittance, of the transparency, for this means that the system is insensitive to such things as emulsion thickness variations and the severely limited dynamic range of wave amplitude spatial light modulators.) This photo-transparency is transilluminated by the fringes and the trans-mitted light collected by a large photodetector. The detector

output is given by

$$s_d(t) = \int f(x, y) I_f(x, y; t) \, dx \, dy. \tag{73}$$

This signal consists of a dc bias plus an ac term, at frequency ω_0, given by

$$s_f(t) = |F(u, v)| \cos [\omega_0 t + \arg \{F(u, v)\}]$$

$$= \mathrm{Re} \{\exp (-j\omega_0 t) F(u, v)\} \tag{74}$$

where $F(u, v)$ denotes the 2-D Fourier transform of $f(x, y)$. As u and v are varied by changing the inputs to the acousto-optic beam deflectors, $s_f(t)$ conveys sequentially on a temporal carrier the magnitude and phase of the spatial transform of $f(x, y)$. In practice, u and v are scanned in a raster or spiral scan so as to effectively sample the entire transform $F(u, v)$. Scanning is sufficiently slow that $s_f(t)$ is a narrow-band signal.

The electrical signal waveform $s_h(t)$ can be generated in the same way or it can be stored. In any case, we assume it to have the form

$$s_h(t) = |H(u, v)| \cos [\omega_0 t + \arg \{H(u, v)\}] \tag{75}$$

where u and v are again scanned with time ($u = u(t)$, $v = v(t)$) and where $H(u, v)$ is the 2-D Fourier transform of impulse response $h(x, y)$.

The electrical processing system of Fig. 15 consists of an analog multiplier followed by a bandpass filter tuned to the double frequency $2\omega_0$. The output of the filter thus has the form

$$s_g(t) = |G(u, v)| \cos [2\omega_0 t + \arg \{G(u, v)\}] \tag{76}$$

where

$$G(u, v) = F(u, v) H(u, v) \tag{77}$$

i.e., $s_g(t)$ conveys the magnitude and phase of the product of the transforms of $f(x, y)$ and $h(x, y)$ and, therefore, corresponds to the time-signal representation of the desired output $g(x, y)$.

In order to produce output intensity distribution $g(x, y)$ from signal waveform $s_g(t)$, a second, synchronized acousto-optic system is used to produce a fringe pattern of the form

$$I_g(x, y, t) = |G(u, v)| \{1 + \cos [2\pi(ux + vy) + \arg \{G(u, v)\}]\} \tag{78}$$

where u and v are implicit functions of time. Noting that an integration with respect to time corresponds to an integration with respect to u and v, the time-integrated intensity distribution $\int I_g(x, y) \, dt$ is easily shown to equal a bias plus the (real) distribution $g(x, y)$. Contrast is low, but computer simulations have shown it to be adequate for many applications.

VI. CONCLUDING REMARKS

This paper has surveyed the major techniques developed to date for effecting signal convolutions and correlations with acousto-optic devices. The emphasis has been on a Fourier optics point of view; distinctions between different possible modes of operation—Bragg regime, Raman–Nath regime, linear in wave amplitude, linear in wave intensity, phase preserving, etc.—have received major emphasis in hopes of avoiding possible confusion. Although the treatment is by no means exhaustive, it should serve as an adequate basis for an under-

standing of most of the literature in this field. The support of the U.S. Air Force Office of Scientific Research for much of the author's research in acousto-optic signal processing is gratefully acknowledged.

REFERENCES

[1] F. Okolicsany, "The wave-slot, an optical television system," *Wireless Eng.*, vol. 14, pp. 527–536, Oct. 1937.

[2] F. Vilbig, "An apparatus for speech compression and expansion and for replaying visible speech records," *J. Acoust. Soc. Amer.*, vol. 22, pp. 754–761, Nov. 1950.

[3] L. J. Cutrona, E. N. Leith, C. J. Palermo, and L. J. Porcello, "Optical data processing and filtering systems," *IRE Trans. Inform. Theory*, vol. IT-6, pp. 386–400, June 1960.

[4] A. H. Rosenthal, "Application of ultrasonic light moduation to signal recording, display, analysis, and communication," *IRE Trans. Ultrasonics Eng.*, vol. UE-8, pp. 1–5, Jan. 1961.

[5] L. Slobodin, "Optical correlation technique," *Proc. IEEE*, vol. 51, p. 1782, Dec. 1963.

[6] M. Arm, L. Lambert, and I. Weissman, "Optical correlation technique for radar pulse compression," *Proc. IEEE*, vol. 52, p. 842, July 1964.

[7] J. S. Gerig and H. Montague, "A simple optical filter for chirp radar," *Proc. IEEE*, vol. 52, p. 1753, Dec. 1964.

[8] D. H. McMahon, "Pulse compression via Brillouin scattering in the Bragg limit," *Proc. IEEE*, vol. 55, pp. 1602–1612, Sept. 1967.

[9] M. B. Schulz, M. G. Holland, and L. Davis, Jr., "Optical pulse compression using Bragg scattering by ultrasonic waves," *Appl. Phys. Lett.*, vol. 11, pp. 237–240, Oct. 1967.

[10] J. H. Collins, E. G. H. Lean, and H. J. Shaw, "Pulse compression by Bragg diffraction of light with microwave sound," *Appl. Phys. Lett.*, vol. 11, pp. 240–242, Oct. 1967.

[11] M. King, W. R. Bennett, L. B. Lambert, and M. Arm, "Real-time electrooptical signal processors with coherent detection," *Appl. Opt.*, vol. 6, pp. 1367–1375, Aug. 1967.

[12] E. B. Felstead, "A simple real-time incoherent optical correlator," *IEEE Trans. Aerosp. Electron. Syst.*, vol. AES-3, pp. 907–914, Nov. 1967.

[13] R. W. Dixon, "Acoustic diffraction of light in anisotropic media," *IEEE J. Quantum Electron.*, vol. QE-3, pp. 85–93, Feb. 1967.

[14] G. Meltz and W. T. Maloney, "Optical correlation of Fresnel images," *Appl. Opt.*, vol. 7, pp. 2091–2099, Oct. 1968.

[15] R. Whitman, A. Korpel, and S. Lotsoff, "Applications of acoustic Bragg diffraction to optical processing techniques," in *Modern Optics (Proc. Symp. Modern Optics*, Microwave Res. Inst. Symposia Series, vol. XVII), Brooklyn, NY: Polytechnic Press, 1967, pp. 243–256.

[16] H. R. Carleton, W. T. Maloney, and G. Meltz, "Colinear heterodyning in optical processors," *Proc. IEEE*, vol. 57, pp. 769–775, May 1969.

[17] W. T. Maloney, "Acoustooptical approaches to radar signal processing," *IEEE Spectrum*, vol. 6, pp. 40–48, Oct. 1969.

[18] T. Turpin, "Spectrum analysis using optical processing" this issue, pp. 79–92.

[19] J. W. Goodman, *Introduction to Fourier Optics*. New York: McGraw-Hill, 1968.

[20] A. Papoulis, *Systems and Transforms with Applications in Optics.* New York: McGraw-Hill, 1968.

[21] A. Vander Lugt, "Coherent optical processing," *Proc. IEEE*, vol. 62, 1300–1319, Oct. 1974.

[22] I. C. Chang, "Acoustooptic devices and applications," *IEEE Trans. Sonics Ultrasonics*, vol. SU-23, pp. 2–22, Jan. 1976.

[23] D. L. Hecht, "Multifrequency acousto-optic diffraction," *IEEE Trans. Sonics and Ultrasonics*, vol. SU-24, pp. 7–18, Jan. 1977.

[24] M. I. Skolnik, *Radar Handbook.* New York: McGraw-Hill, 1970, ch. 3.

[25] A. Korpel, "Acousto-optics—A review of fundamentals," this issue, pp. 48–53.

[26] R. W. Damon, W. T. Maloney, and D. H. McMahon, "Interaction of light with ultrasound: phenomena and applications," in *Physical Acoustics*, W. P. Mason and R. N. Thurston, Eds., vol. 7, New York: Academic Press, 1970, pp. 273–366.

[27] R. A. Sprague, "A review of acousto-optic signal correlators," *Opt. Eng.*, vol. 16, pp. 467–474, Sept./Oct. 1977.

[28] N. J. Berg, J. N. Lee, M. W. Casseday, and B. J. Udelson, "Surface wave delay line acoustooptic devices for signal processing," *Appl. Opt.*, vol. 18, pp. 2767–2774, 1979.

[29] A. Korpel, "Acoustooptic signal processing," in *Optical Information Processing*, Yu. E. Nesterikhin, G. W. Stroke, and W. E. Kock, Eds. New York: Plenum, 1976, pp. 171–193.

[30] J. M. Florence and W. T. Rhodes, "Frequency-variant signal processing using a channelized optical system," submitted to *Opt. Lett.*

[31] M. Gottlieb, J. J. Conroy, and T. Foster, "Optoacoustic processing of large time-bandwidth signals," *Appl. Opt.*, vol. 11, pp. 1068–1077, May 1972.

[32] R. M. Montgomery, "Acousto-optical signal processing system," U.S. Patent 3 634 749, Jan. 1972.

[33] R. A. Sprague and C. L. Koliopoulos, "Time integrating acousto-optic correlator," *Appl. Opt.*, vol. 15, pp. 89–92, Jan. 1976.

[34] T. M. Turpin, "Time integrating optical processors," in *Real-Time Signal Processing*, F. Tao, Ed. (*Proc. SPIE*, vol. 154, 1978), pp. 196–203, 1978.

[35] P. Kellman, "Detector integration acousto-optic signal processing," in *Proc. 1978 Int. Optical Comp. Conf.* (*Digest of Papers*), (IEEE No. 78CH-1305-2C), pp. 91–95, 1978.

[36] ——, "Time integrating optical processors," in *Optical Processing Systems*, W. Rhodes, Ed. (*Proc. SPIE*, vol. 185, 1979), pp. 130–139, 1979.

[37] ——, "Time integrating optical signal processing," in *Acousto-Optic Bulk Wave Devices*, J. Houston, Ed. (*Proc. SPIE*, vol. 214, 1979), pp. 63–73, 1979.

[38] T. R. Bader, "Acoustooptic spectrum analysis: a high performance hybrid technique," *Appl. Opt.*, vol. 18, pp. 1668–1672, May 1979.

[39] J. D. Cohen, "Ambiguity processor architectures using one-dimensional acousto-optic transducers," in *Real-Time Signal Processing II*, T. F. Tao, Ed. (*Proc. SPIE*, vol. 180, 1979), pp. 134–142, 1979.

[40] P. Kellman, "Time integrating optical signal processing," Ph.D. dissertation, Stanford University, Stanford, CA, June 1979.

[41] P. S. Guilfoyle, D. L. Hecht, and D. L. Steinmetz, "Joint transform time-integrating acousto-optic correlator for chirp spectrum analysis," in *Active Optical Devices*, J. Tracy, Ed. (*Proc. SPIE*, vol. 202, 1979), pp. 154–162, 1979.

[42] R. A. K. Said and D. C. Cooper, "Crosspath real-time optical correlator and ambiguity function processor," *Proc. Inst. Elec. Eng.*, vol. 120, pp. 423–428, Apr. 1973.

[43] W. T. Rhodes, "Acousto-optic devices applied to image processing," in *Real-Time Signal Processing*, F. Tao, Ed. (*Proc. SPIE*, vol. 180, 1979), pp. 143–149, 1979.

Spectrum Analysis Using Optical Processing

TERRY M. TURPIN

Invited Paper

Abstract—Spectrum analysis is one of the most fundamental tools in science today. Its use in one form or another spans virtually every discipline. It was one of the first recognized applications of optical processing, and the usefulness of optical spectrum analysis has grown remarkably in the past decade. This is due to the fundamental simplicity, parallelism and intrinsic speed of optical spectrum analyzers, the maturity of the components now available, and the remarkable variety and versatility of the processing architectures that have been developed.

This paper presents six selected topics on spectrum analysis using optics. The topics were selected because they represent practical techniques with broad applicability and illustrate different aspects of the technology. The topics are grouped by architecture as space integrating and time integrating. The space integrating sections cover radiometry for detecting low-level signals in wide-band noise, programmable filtering of electrical signals for interference rejection applications, and an optical technique that is equivalent to 10^5–10^6 parallel filters for application where fast response, high resolution, and wide bandwidth of coverage are simultaneously required.

The time integrating sections cover the versatile time integrating spectrum analyzer, and its extension to the calculation of ambiguity surfaces which have important application to radar processing problems requiring simultaneous measurement of a radar return's time of arrival and possible Doppler frequency shift. This process also illustrates the parallel nature of optical operations, and introduces a fundamental concept, the use of one-dimensional optical components configured for performing two-dimensional operations. The discussion of this concept continues into two-dimensional time integrating spectrum analyzers that use two time integrating spectrum analyzers, each capable of resolving N elements, and combines them to produce N^2 resolvable elements in real time.

I. INTRODUCTION

SPECTRUM analysis is one of the most useful techniques in modern science. Virtually every discipline (astronomy, geology, medicine, etc.) makes use of it in one form or another. An important concept in spectrum analysis is "real-time" analysis. This means that a sequence of spectra are computed on either overlapping or adjacent data apertures, as opposed to "sampled" spectrum analysis where a single narrow-band filter is scanned across a relatively wide bandwidth. Note that the concept of real-time analysis implies that the calculation of one spectrum is complete in less time than is required to fill the input aperture.

Efficient digital algorithms have been developed that greatly reduce the work factor in spectral calculations, and special-
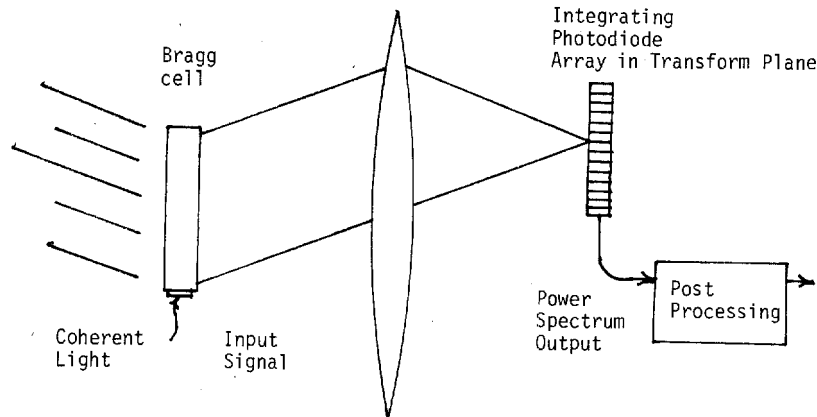
Fig. 1. Acousto-optic radiometer.

purpose digital hardware has been developed around these algorithms. Real-time spectrum analysis below 2 MHz bandwidth is predominantly performed in special-purpose digital equipment; however, above 10-MHz bandwidth, analog optical techniques dominate the field. This is largely due to the maturity of the component technology and the remarkable variety and versatility of processor architectures that have been developed.

Optical spectrum analysis is a practical option to builders of processing systems, providing wider processing bandwidths than previously possible. Spectrum analysis was one of the first recognized, and is today one of the most important functions performed by optics. Spectrum analyzers based on optics are currently available as off-the-shelf hardware. For those applications where off-the-shelf analyzers will not meet the system builder requirements, special-purpose optical systems have been built and are currently solving problems. In view of the importance of spectrum analysis to optical computing, this paper discusses selected techniques and applications that illustrate useful features of this technology.

Optical spectrum analyzers can be divided into two major classes based on the variable of integration for the Fourier transform operation. The "space integrating architecture" performs a Fourier transform with respect to a spatial variable. The "time integrating architecture" takes the transform with respect to a temporal variable "t." One- and two-dimensional transforms exist for both types. The techniques and practical examples of both time and space integrating architectures are presented, along with a brief discussion of some of the components that are currently used in optical spectrum analysis.

The space integrating topics include radiometry for the detection of low level signals in wide-band noise. This section illustrates the usefulness of postdetection integration on a photosensor for improved sensitivity. The radiometer is contrasted to an interference rejection filter that does no postdetection integration and illustrates a practical application of coherent detection in optical spectrum analysis. The final section under space integrating processors describes the two-dimensional Fourier transform of an analog signal which has been recorded on photographic film or its real-time equivalent in two-dimensional raster (TV-like) former. This process is equivalent to calculating 10^5–10^6 spectral coefficients in parallel and is treated from the point of view of combining small transforms (300–1000 spectral coefficients) into large transforms.

The time integrating section starts with the versatile time integrating spectrum analyzer. This technique is treated from the point of view of an array of oscillators each with a temporal frequency that increases linearly with its spatial coordinate "X" (distributed oscillator). Each oscillator mixes with the signal to be transformed and the result is integrated on a discrete photosensor array to produce a spectrum. This point of view leads naturally to the use of the other spatial dimension "Y" for multiple inputs and the extension of the time integrating spectrum analyzer to the calculation of ambiguity surfaces. Ambiguity surfaces have important applications to radar processing problems requiring simultaneous measurement of a radar return's time of arrival and Doppler shift.

The final topic under time integrating spectrum analysis is a discussion of the two-dimensional time integrating spectrum analyzer that uses two time integrating spectrum analyzers, each capable of resolving N elements, and combines them to produce a system capable of resolving N^2 elements. The two-dimensional time integrating spectrum analyzer is treated from a different point of view than the two-dimensional space integrating analyzer, however the underlying concepts are equivalent and interchangeable. The important point in both treatments is that very large Fourier transforms can be broken down into smaller transforms that are easily calculated. These smaller transforms can then be recombined to produce the desired result.

As an introduction to optical spectrum analyzers, consider the system in Fig. 1. Coherent light illuminates a one-dimensional spatial light modulator, in this case a Bragg cell. The light diffracted by the cell is collected by a lens and focused onto a photodiode array. The light amplitude at the photodiode is the spectrum of the information in the Bragg cell. This serves to illustrate the simplicity of at least one optical technique for calculating spectra. The remainder of this paper (after a brief discussion of some components) consists of a discussion of six selected topics in spectrum analysis.

II. SPECTRUM ANALYZER COMPONENTS: BRAGG CELLS AND PHOTOSENSORS

An optical processor (Fig. 1) must have a means of converting information (usually in the form of an electrical signal) into an optical format. It should also include a means for converting the optical output back into an electrical signal. Although there are important applications for off-line (non-real-time) optical processing using photographic film (for example in synthetic aperture radar [1]), the current trend is for real-time processing. The most practical and highly developed real-time input device for optical systems is the Bragg cell or acousto-optic cell [2]–[4]. This device is discussed briefly

because of its important position in today's processing architectures.

Bragg cells are currently available with bandwidths in excess of 10^9 Hz and are capable of holding more than 10^3 analog data samples. They provide a temporary storage register for the array of data to be processed. The high data rate, coupled with large dynamic range, availability from a variety of vendors, reasonable cost, and reproducible quality, have given the Bragg cell undisputed leadership at the input end of today's real-time optical systems. Real-time two-dimensional devices are being developed [5] offering greater storage capacity for the future, but none of these devices has reached the stage of engineering development of the Bragg cell. The maturity of Bragg cell technology is largely responsible for the transition of real-time optical computing from the research laboratory to modern information processing systems.

A Bragg cell [6] is illustrated in Fig. 1. It is a block of transparent material with a piezoelectric transducer bonded to one end. The other end is tapered to trap the acoustic waves and loaded to provide an effective acoustic termination. A piezoelectric transducer is sandwiched between electrodes and vibrates in synchronism with an applied voltage. The vibration is coupled mechanically into the crystal and propagates down the material at about 6 mm/μs for most crystalline solids[1]. In solids, shear waves or compression waves can be excited depending on the transducer type. In general, transducers used in acousto-optic applications have bandwidths spanning a single octave of frequencies or less. For center frequencies from 10^7 Hz to 1.5×10^9 Hz most cells use thin slices of lithium niobate as a transducer. The transducers are metal bonded onto the transparent material. For extremely high center frequencies (1.6–10 GHz) sputtered films of zinc oxide (ZnO) are used [7]. Although the ZnO transducers have the advantage of being easy to produce, particularly where very high frequency response is required, they tend to be less efficient in converting electrical energy into useful acoustic energy, with losses of 10–13 dB (for single octave operation) as compared with 1–2 dB for lithium niobate transducers.

When driven by an electrical signal the transducer excites an acoustic replica of that signal. This replica propagates down the long axis of the Bragg cell and produces compressions and rarefactions in the material [8]. The interaction between light and sound results from an increase in the index of refraction of the material at a compression and a decrease in index at a rarefaction. Light is scattered by these changes in index. There are two commonly used modes of operation. The classification is based on which optical parameter (amplitude or intensity) is proportional to the amplitude of the applied acoustic signal. For low-level input signals the diffracted light amplitude (a complex quantity possessing magnitude and phase) is proportional to the acoustic amplitude. The phase of the light as it propagates through the optical system is the dominant feature of the analysis. The definition of what is a low-level signal depends upon the required dynamic range. A signal that diffracts 10 percent of the incident light implies a 33-dB linear dynamic range, while if 1 percent of the light is diffracted the dynamic range is 53 dB [9].

In the second mode of operation (large signal), the intensity response of the cell is considered [10]. The diffracted intensity is given by

$$I_d = I_0 \sin^2 \xi/2 \qquad (1)$$

where ξ is proportional to the acoustic amplitude of a sinusoidal signal and hence to the electrical amplitude. If the sinusoidal signal (ξ) is amplitude modulated about the $I_d = I_0/2$ operating point, the change in intensity is proportional to the amplitude of the modulation. For example, if the modulation is $\pi/2 + Kf(t)$, the diffracted light intensity as a function of time is

$$I_d(t) = \frac{I_0}{2} + \frac{KI_0}{2} f(t) \qquad (2)$$

for small K.

The bias term $I_0/2$ is necessary because intensity can never be negative; the negative values are expressed as intensities below the bias. There is no consideration of phase in this mode of operation and spectrum analyzers based on this mode of operation do not require monochromatic or spatially coherent light.

At the other end of the system (Fig. 1) is the sensor, the device that converts the optical signal back into an electrical signal. One-dimensional photosensitive arrays are currently available in sizes from 64 to more than 1700 elements. Several of these arrays exhibit dynamic ranges greater than 10^4 to 1 (saturation signal to rms noise) in output voltage or current. Most of these devices (with one important exception described in the text) integrate the light intensity that falls upon them between the times that a photosite is readout. Although not as mature as Bragg cells, the one-dimensional photosensor [11], [12] arrays are well developed and are the most prevalent output device in optical processing.

As with input devices the two-dimensional output arrays are not nearly as well developed as their one-dimensional counterparts. At first glance, the vidicon based television camera appears attractive. Although these devices are useful for qualitative imaging applications, their usefulness as precision measurement instruments is limited by nonlinear sensitivity, geometric distortion, and space variant resolution.

Two-dimensional solid-state image sensors are available but only in commercial TV format. They have neither the quality (1000 to 1 dynamic range is extremely rare) or the variety of their one-dimensional counterparts [13]. This is understandable; the large area of the device results in yield problems. The complexity and constraints on the design are challenging. It is in the sensor area that the device development opportunities of greatest importance to optical processing are found.

III. SPACE INTEGRATING OPTICAL SPECTRUM ANALYSIS

The Fourier transform relationship (see Fig. 1) between the light amplitude distribution in the Bragg cell plane and the photosensor plane is well known [14], [15] and will not be repeated here. What will be discussed are two practical applications of the Bragg cell optical spectrum analyzer (radiometry and adaptive filtering), and a special case of the two-dimensional optical transform which is analogous to the digital fast Fourier transform (FFT) for discrete data.

A. The Acousto-Optic Radiometer Bank

The radiometer [16] is a tool for the detection of signals in noise where the noise power exceeds the signal power. It is used extensively in radio astronomy [17]. The simplest radiometer measures the total energy received over a given integration period; the device is illustrated in Fig. 2. The filter defines a noise bandwidth B. The output of the filter can be considered a string of noise pulses, each pulse of duration $1/B$. The
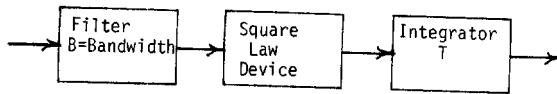
Fig. 2. Total power radiometer.

TABLE I
ACOUSTO-OPTIC RADIOMETER SPECIFICATIONS

Frequency Coverage = 10^9 Hertz

Bandwidth of Resolution Cell B = 2 x 10^6 Hertz

Number of Photodetectors = 1000 (oversampled 2:1)

Detector Integration Time = 500 milliseconds

Detector Capacity = 2 x 10^6 electrons

Detector Noise = 700 electrons rms

Equation for Sensitivity = S/N_{out} = 1000 $(S/N)^2_{in}$

square law detector converts these pulses to measures of instantaneous noise power. Let the mean of these pulses at the output of the square-law detector be M and standard deviation M [18]. Signals are assumed to be continuous, and if a signal of power S is present in the noise, the output of the square-law device has a mean $S + M$ and a standard deviation M. By the central limit theorem [19] the mean voltage out of the integrator will be proportional to $(BT)M$, where the time bandwidth product BT is the number of noise pulses averaged. The uncertainty (standard deviation) of this measurement is $\sqrt{BT}\,M$. The signal to noise out of the radiometer is defined as the ratio of the change in the output due to the presence of a signal BTS to the uncertainty in the measurement $\sqrt{BT}\,M$. Expressed as a power ratio

$$\left(\frac{S}{N}\right)_{out} = BT\frac{S^2}{M^2} \qquad (3)$$

but S/M is the signal to noise at the input, hence

$$\left(\frac{S}{N}\right)_{out} = BT\left(\frac{S}{N}\right)^2_{in}. \qquad (4)$$

As the number of samples averaged (BT) increases, output signal-to-noise ratio improves. Note that the output is a small change (BTS) on top of a large fixed bias (BTM). The averaging process produces an uncertainty (standard deviation) in the output voltage of $\sqrt{BT}\,M$.

The Bragg cell spectrum analyzer of Fig. 1 can implement an array of total power radiometers. Each point in the Fourier transform plane of Fig. 1 corresponds to a filter of bandwidth approximately equal to the reciprocal of the aperture of the Bragg cell (time delay). The light amplitude at a point in the transform plane is directly proportional to the acoustic amplitude of a sinusoidal signal component within the Bragg cell aperture. The optical detectors described previously generate photocharge proportional to light intensity and accumulate the photocharge until it can be read out (integrates the charge [20]). If a photodetector array is placed in the transform plane of Fig. 1, each filter (point in space) is followed by a square-law detector (intensity detector), and an integrator and the system of Fig. 1 becomes an array of radiometers; one for each resolution cell of the transform plane. Systems of this type are being experimentally implemented by NASA for millimeter-wave spectroscopy.

The acoustooptic radiometer takes advantage of the high-speed capabilities of the optics, and the storage and integration capabilities of the detectors. A typical system might have the specification in Table I. The wide-band input is channelized by the optics. The detectors provide the square law operation and integration that results in reducing a 10^9 Hz bandwidth signal to 2×10^6 samples/s, and results in an improvement in signal-to-noise ratio (SNR). For example, a signal at -10 dB SNR in one 2-MHz filter would appear at $+10$-dB SNR after integration. It is important to note that this assumes the $\sqrt{BT}\,M$ uncertainty at the output of the detector is large compared with the detector noise N_d

$$\sqrt{BT}\,M = kN_d \text{ (in electrons at the output)} \qquad (5)$$

where k is a constant on the order of 4. This sets a lower bound on input $M = kN_d/\sqrt{BT}$; if it is less than this, the sensitivity degrades due to the dominance of detector noise. The detector must also have wide dynamic range or the bias (BTM) term will saturate the array before the integration is complete.

When properly designed, the acousto-optic radiometer achieves theoretical performance. Additional dynamic range and sensitivity can be gained through digital integration of the output which has been conveniently reduced to a sample rate compatible with microprocessor technology. Assuming aperture weighting for side lobe reduction, the Bragg cell radiometer described in Table I is equivalent to performing a 1000 point transform every 500 ns, calculating the power spectrum, and averaging the results. It is equivalent to at least 5×10^9 complex multiplies per second [21].

B. Interference Rejection Filters

A different aspect of acousto-optic spectrum analysis is illustrated in the use of an optical spectrum analyzer as an interference rejection filter. The problem of rejecting relatively narrow-band interfering signals is becoming more important as the bandwidth of digital communications system increases. A technique for interference rejection is illustrated in Fig. 3. If all the switches are in position A the input signal is decomposed by the filterbank and recombined without distortion onto bus A with no output on B. If a filter contains a narrow-band interfering signal, the switch corresponding to that filter could be switched to B removing the signal from A. Fig. 4 illustrates the A spectrum before and after this filtering process. The notch in the broad-band signal has a negligible effect on the transmission.

The optical implementation of this technique is shown in Fig. 5 [22]. The signal (Fig. 4(a)) is applied to a Bragg cell. The cell is illuminated with coherent light and the spectrum of the signal is formed on a photodiode array. The light at each photodiode has an amplitude proportional to the amplitude of the corresponding acoustic frequency component in the Bragg cell. A given acoustic frequency component acts as a moving diffraction grating, hence the light diffracted by it is Doppler frequency shifted by the motion of this grating. The light frequency is shifted by the frequency of the acoustic signal. The acoustic signal component can be reconstructed by down converting the diffracted light to the acoustic frequency. This is achieved by adding the optical signal to an optical local oscillator (reference beam in Fig. 5). The result falls on a photodiode which responds to the square of the amplitude. This square-law process results in an electrical signal at the output of the diode with a frequency equal to the difference between the frequencies of the two optical inputs. This results

Bandpass Filter Bank
Bandwidth is Δf for Each Filter
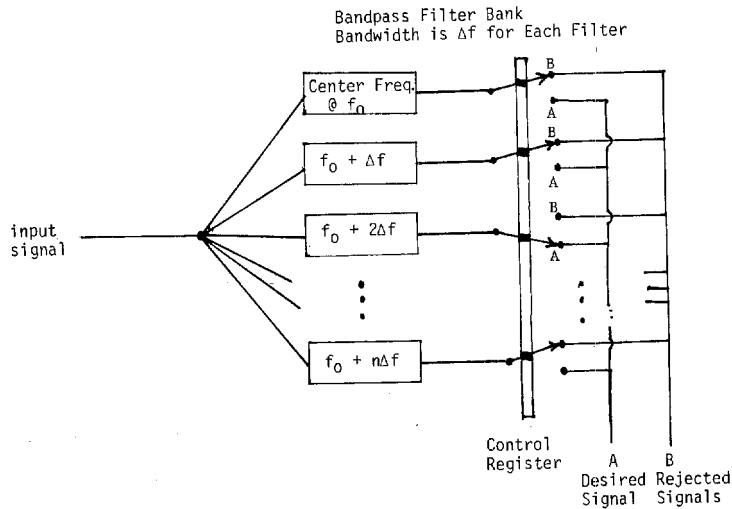
Fig. 3. Electrical equivalent of the interference rejection filter.
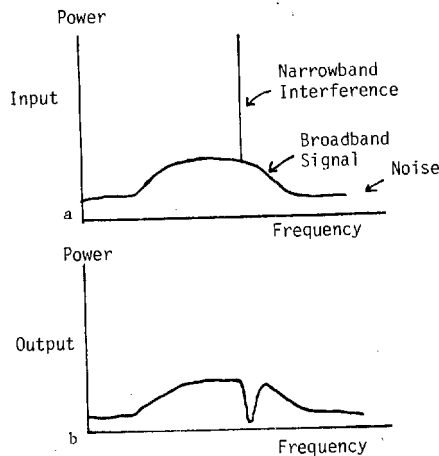
Fig. 4. Example of the output of an interference rejection filter.
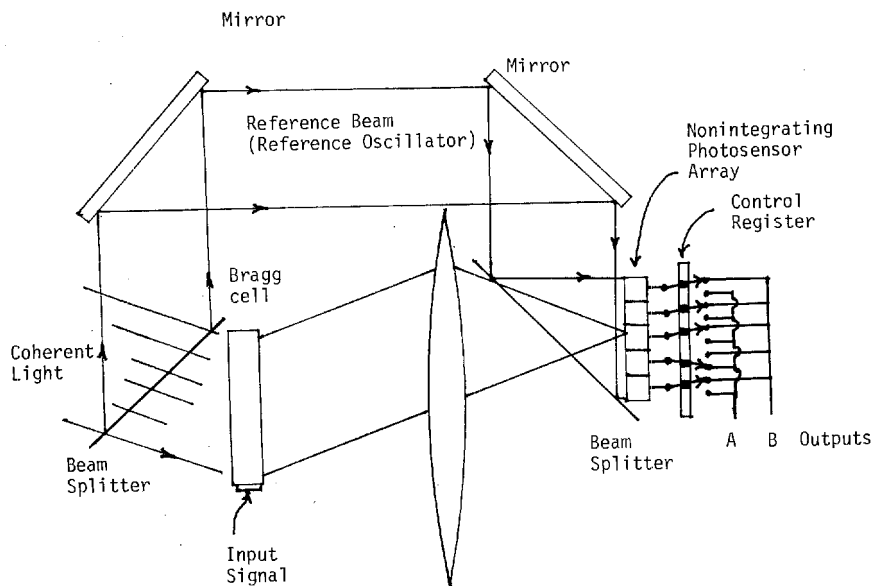
Fig. 5. Interference rejection filter.

in the recovery of the acoustic frequency component and hence the input RF frequency component. The signal component on each photodiode can be switched to either the A or B

output, depending on the state of an external control register (not shown).

A more precise description of the operations in the filter can

now be given. The broad-band signal including a narrow-band interfering signal is $f(t)$. This signal has been single sideband converted to the passband of the Bragg cell. The acoustic amplitude in the Bragg cell, and hence the diffracted optical signal amplitude at the exit port of the cell is proportional to $f(t - x/v)$, where x is the distance from the transducer, and v the acoustic velocity. The optical system takes the Fourier transform with respect to the spatial variable x

$$F(p, t) = \int_{-L}^{L} f\left(t - \frac{x}{v} - T\right) \exp -jpx \, dx \qquad u = t - \frac{x}{v} - T$$

(6)

$$F(p, t) = -v \exp jpv(T - t) \int_{t}^{t-2T} f(u) \exp jpvu \, du \qquad (7)$$

where $2L$ is Bragg cell length, and $2T$ is Bragg cell delay. $F(p, t)$ is seen to be the Fourier transform of the portion of $f(t)$ within the aperture of the Bragg cell. Associated with each spatial frequency p is a temporal frequency $w = pv$. The light at spatial position p has been frequency shifted by an amount equal to the corresponding temporal frequency. The integral in (7) is defined as $F(pv)$ and is the spatial distribution in the detector plane of Fig. 5. The detectors respond to light intensity rather than light amplitude, hence it is necessary to bring in a reference wave intersecting the frequency plane at a small angle "a" and having an amplitude "A." The total amplitude in the output plane is the sum of the reference wave and the transform of the signal

$$T(p, t) = A \exp jap - vF(pv) \exp jpv(T - t). \qquad (8)$$

The corresponding intensity is $|T(p, t)|^2$

$$|T(p, t)|^2 = A^2 + v^2 |F(pv)|^2$$

$$- 2Av \, \text{Re}\left[F(pv) \exp -jpv\left(t - T + \frac{a}{v}\right)\right] \quad (9)$$

where $\text{Re}(x)$ means the real part of x. The detector integrates this output over the spatial plane p

$$\int |T(p, t)|^2 \, dp = \int A^2 \, dp + \int |F(pv)|^2 \, dp$$

$$- 2Av \, \text{Re} \int F(pv) \exp -jpv\left(t - T + \frac{a}{v}\right) dp. \quad (10)$$

The original signal $f(t)$ is assumed to be real and to occupy an octave or less of bandwidth. Under these assumptions the first two terms of (10) do not contribute in-band frequency components to the reconstruction. The last term represents the reconstruction of the signal

$$2Av \, \text{Re} \int F(pv) \exp jpv\left(t - T + \frac{a}{v}\right) dp = 2Af\left(t - T + \frac{a}{v}\right).$$

(11)

If all of the detectors in Fig. 5 are switched to one position, the signal is reconstructed without distortion and with a time shift that is proportional to the angle of the reference beam. An on-axis reference beam reconstructs the signal without delay relative to the center of the Bragg cell. A tilted reference wave introduces a phase shift into each frequency component that is proportional to the frequency and varies linearly with frequency. From the Fourier shift theorem, a linear

phase variation in the frequency domain translates into a displacement in the time domain. The segmented detector allows the user the option of selecting the frequency components that take part in the reconstruction. The system of Fig. 5 can remove narrow-band interfering signals from the A output of the detector by switching undesired frequency components to B.

The same operation of programmable filtering could be performed by placing an array of optical switches in the transform plane and then taking a second optical Fourier transform to reconstruct an image of the signal in the Bragg cell. This image could be sampled with a narrow aperture to reconstruct the signal in time. The relative time delay would be determined by the position of the sampling aperture, and interfering signals could be blocked by activating the optical switches in the transform plane. Such a configuration has a more complex optical system and requires a spatial light modulator (optical switch). The construction of such a light modulator is a more complex process than the detector array development.

Three factors control the dynamic range of the system

1) quantum noise (the square root of the number of photons per reciprocal bandwidth);
2) the nonlinear effects in the Bragg cell;
3) detector noise.

Item 2) is given extensive treatment in an excellent paper by Hecht [9]. This paper shows that once a spurious free dynamic range has been selected, the maximum percentage of the input light that can be diffracted per frequency cell is fixed.

The rate of computation [23] in terms of complex multiplies per second for this system is on the same order as that for a radiometer of similar resolution and bandwidth.

C. Two-Dimensional Optical Transforms

As a final topic under space integrating optical spectrum analysis an analogy will be drawn between the FFT [24] that has resulted in a dramatic reduction in the computational workload of digital spectrum analyzers, and the large space bandwidth product optical spectrum analysis that results when a time series is written onto a spatial light modulator (such as photographic film) in a raster format and a two-dimensional Fourier transform is taken of the result [25].
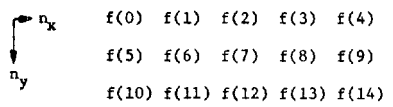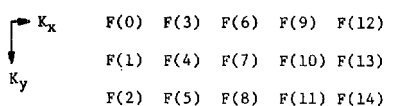
Historically the discovery of the large space bandwidth optical processor by Thomas [25] was independent of the FFT algorithm and only recently has this technique been recognized as an analog implementation of the FFT. This section will treat the large space bandwidth spectrum analyzer in terms of the FFT because the FFT is well known and used extensively. This approach also gives a straightforward geometric meaning to the FFT, and illustrates the process of formulating a large one-dimensional problem into a more manageable two-dimensional one. The usefulness of this technique in optical processing is that it permits more than 10^6 data points to be transformed to 10^6 spectral points in a single parallel operation.

Table II is a quick review of the steps involved in an FFT [26]. These steps can be implemented optically. Consider the signal $f(n)$ recorded on a two-dimensional spatial light modulator as a spatial transmittance function $\tilde{f}(x, y)$

$$\tilde{f}(x, y) = \sum_{n_x=0}^{L-1} \sum_{n_y=0}^{M-1} f(Ln_y + n_x)$$

$\cdot \delta(x - n_x \Delta x, y - n_y \Delta y)) * s(x, y)$ (12)

where $\delta(x, y)$ is the two-dimensional Dirac delta, $*$ denotes

TABLE II
THE FFT

The formation of an FFT	Comments
Given: $f(n)$ where $n = 0,1,2....N-1$, then:	(a) A discrete time series
$$F(k) = \sum_{n=0}^{N-1} f(n) e^{j\left(\frac{2\pi}{N} nk\right)}$$ for $k = 0,1,.......N-1$.	(b) The discrete Fourier transform. In general, an N point transform requires N^2 complex multiplications.
If $N = LM$, let $n = Ln_y + n_x$: $n_y = 0,1,2.....M-1$ $n_x = 0,1.......L-1$ If $k = MK_x + K_y$: $K_x = 0,1,2.....L-1$ $K_y = 0,1,2.....M-1$	The indices n and k are expressed in two-dimensional coordinates.
$F(K_x,K_y) =$ $$\sum_{n_x=0}^{L-1} \underbrace{\left(\sum_{n_y=0}^{M-1} f(Ln_y + n_x)\, e^{j\frac{2\pi}{M}n_yK_y}\right)}_{g(n_xK_y)} \cdot \underbrace{\left(e^{j\frac{2\pi}{N}n_xK_y}\right)}_{\text{Twiddle Factor}} \cdot \left(e^{j\frac{2\pi}{L}n_xK_x}\right)$$	(c) The sum is now L, M point transforms in n_y followed by M multiplies (by Twiddles) and M, L transforms in n_x for $LM^2 + ML^2 + N$ complex multiplies.
n_x $f(0)$ $f(1)$ $f(2)$ $f(3)$ $f(4)$ n_y $f(5)$ $f(6)$ $f(7)$ $f(8)$ $f(9)$ $f(10)$ $f(11)$ $f(12)$ $f(13)$ $f(14)$	If $L = M = R$, $N = R^2$, and the number of multiplies is reduced from R^4 to $(2R + 1)R$.
K_x $F(0)$ $F(3)$ $F(6)$ $F(9)$ $F(12)$ K_y $F(1)$ $F(4)$ $F(7)$ $F(10)$ $F(13)$ $F(2)$ $F(5)$ $F(8)$ $F(11)$ $F(14)$	Each of the M and L point transforms can be expressed in two-dimensional coordinates for greater reduction in the number of multiplications.

convolution, and $s(x, y)$ is the shape of the recorded data sample, Δx and Δy are the x and y separation of the samples, respectively

$$\tilde{F}(P_x, P_y) = \int \tilde{F}(x, y) \exp j(P_x x + P_y y)\, dx\, dy$$

$$= S(P_x, P_y) \sum_{n_x=0}^{L-1} \sum_{n_y=0}^{M-1} f(Ln_y + n_x)$$

$$\cdot \exp jP_y n_y \Delta y \exp jP_x n_x \Delta x \tag{13}$$

where $x = n_x \Delta_x, y = n_y \Delta_y$, let

$$\tilde{g}(n_x P_y) = \sum_{n_y=0}^{M-1} f(Ln_y + n_x) \exp jP_y n_y \Delta y.$$

There are two differences between equation (c) of Table II and (13), the spatial transform of two-dimensionally formatted data. First, the premultiplication by $S(P_x, P_y)$, the transform of the shape of a data sample, and second, the absence of the "twiddle factors" between the vertical and horizontal Fourier transforms. If $s(x, y)$ is smaller than the sample spacing in the x and y dimensions, then $S(P_x, P_y)$ will tend to be slowly varying and almost constant over the transform.

Table III shows the correspondence between the variables and functions in equation (c) and those in Fig. 6. Fig. 6 shows the two-dimensional transform implemented first as a vertical

transform (indicated by the cylinder lens) with imaging in the horizontal direction (imaging optics not illustrated) to produce an intermediate plane where $\tilde{g}(x, P_y)$ exists. And, finally the horizontal transform of $\tilde{g}(x, P_y)$ with the vertical P_y axis imaged to produce a two-dimensional transform $\tilde{f}(P_x, P_y)$. The twiddle factors in Table II when translated into spatial variables (Table III) represent a prism[2] (linear phase shift) in the plane where $\tilde{g}(x, P_y)$ exists. This prism has a shift of $0°$ along the $P_y = 0$ and $x = 0$ axis. In the (X, P_y) plane its phase increases linearly with P_y and x and corresponds to 2π at $(L\Delta x, 2\pi/\Delta y)$ as shown in Fig. 6. With the prism in place, the output of the two-dimensional transform is the same as the output of the FFT. The coefficient corresponding to (K_x, K_y) occurs at

$$(P_x, P_y) = [(2\pi/L\Delta x) K_x, (2\pi/M\Delta y) K_y].$$

The prism acts to produce a linear phase shift in the x direction; when transformed, this results in a translation of the position of the transform coefficients. If the prism is removed the values of the Fourier transform are not changed, they are only displaced in the P_x direction. Inspection of the twiddle factor shows the displacement due to the twiddle factor is

[2] This element is not strictly speaking a prism. It is a quadratic surface (an element of a lens or zone plate). In this application it introduces a linear phase shift in x for a fixed y and in this sense it behaves as a prism.

TABLE III
FFT CONVERSIONS

Optical	Digital
$P_y = \dfrac{2\pi}{M\Delta y} \; K_y$	$K_y = \dfrac{MP_y\,\Delta y}{2\pi}$
$P_x = \dfrac{2\pi}{L\Delta x} \; K_x$	$K_x = \dfrac{LP_x\,\Delta x}{2\pi}$
$P_y = 0, \dfrac{2\pi}{L\Delta y} \ldots\ldots \dfrac{2\pi}{\Delta y}\left(\dfrac{M-1}{M}\right)$	$K_y = 0, 1, 2, 3,\ldots\ldots\ldots M-1$
$P_x = 0, \dfrac{2\pi}{L\Delta x} \ldots\ldots \dfrac{2\pi}{\Delta x}\left(\dfrac{L-1}{L}\right)$	$K_x = 0, 1, 2, \ldots\ldots\ldots L-1$
$x = n_x\Delta x$	$n_y = 0, 1, 2,\ldots\ldots\ldots M-1$
$y = n_y\Delta y$	$n_x = 0, 1, 2,\ldots\ldots\ldots L-1$

Twiddle Factors

$$e^{j\frac{\Delta y}{L\Delta x}P_y X} \qquad\qquad\qquad e^{-j\frac{2\pi}{N}n_x K_y}$$
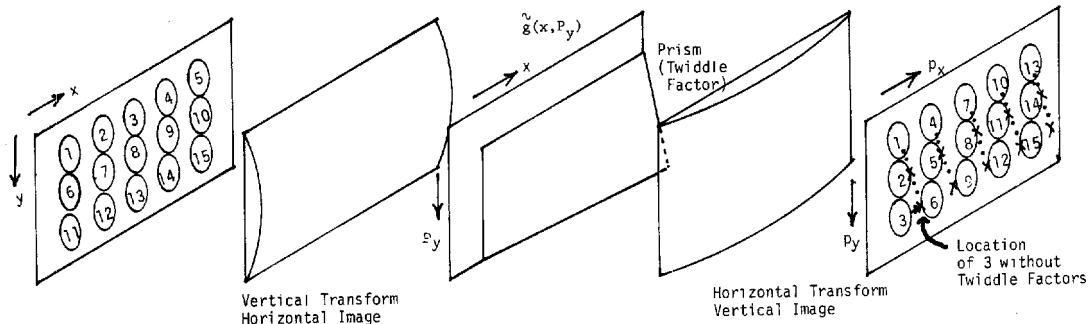
Fig. 6. Optical FFT.

$$\Delta P_x = (\Delta y / L\Delta x)P_y$$

$$F(K_x, K_y) = \tilde{F}(P_x, P_y) \qquad \text{evaluated at}$$

$$P_x = \frac{2\pi}{\Delta x}\left(\frac{1}{L}K_x + \frac{1}{N}K_y\right)$$

$$P_y = \frac{2\pi}{\Delta y}\frac{1}{M}K_y \qquad \text{(prism removed).} \qquad (14)$$

This translation of the transform coefficients when the prism is removed is shown as the dotted lines in the P_x, P_y plane of Fig. 6. The two-dimensional Fourier transform of the array in Fig. 6 produces the same result as the FFT but the result is slightly displaced in P_x due to the absence of the twiddle factors (prism), which is the same result that Thomas developed [25]. Markevitch [27] applied this technique to the two-dimensional Fourier transform of RF signals recorded on film in a television raster format. A similar result was also developed by Whitehouse [28], [29], for a nonoptical analog FFT.

In digital signal processing the fast algorithm reduces the number of complex multiplies required for the transform

calculations. In optical processing the multiplies are trivial but the two-dimensional format of the input permits N^2 input data samples to be transformed using a spatial light modulator with N resolution elements in each dimension.

The technique permits large transforms (10^6 or 10^7 points) to be taken with modest optical systems. The development from the FFT shows how small transforms can be combined into larger ones. Just as the FFT gains computational power from factoring into more than two dimensions, this approach suggests higher order optical factorings offer exciting research possibilities and the existence of alternative techniques for the recombination of the partial transforms. One such implementation will be described from a different point of view when the two-dimensional time integrating spectrum analyzer is discussed in the next section.

Using a real-time spatial light modulator at a rate of 100 transforms of 10^6 points/s, the computational equivalent of more than 2×10^9 complex multiplies per second can be performed. This is an impressive capability and in the future, with the development of integrated circuits as spatial light modulators [30], [31], it offers the hope for compact low cost spectrum analyzer modules.
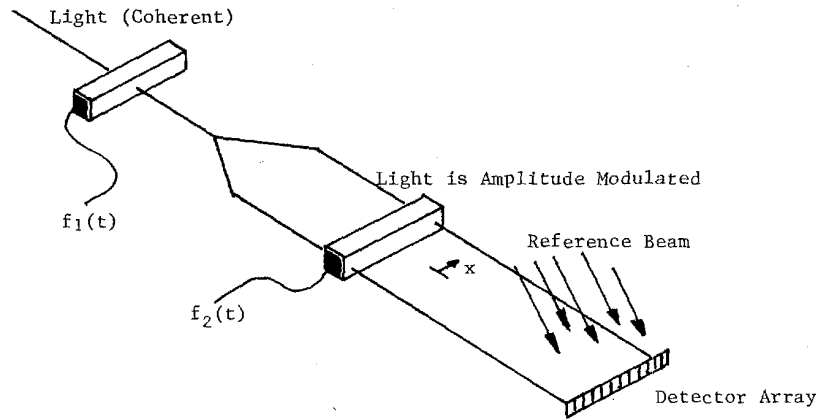
Fig. 7. Coherent I-D correlator.

IV. TIME INTEGRATING SPECTRUM ANALYSIS

In the previous sections, one- and two-dimensional spatial Fourier transforms were discussed. In each case the variable of integration was spatial. This implies the mechanism of data storage is also spatial. In the following section the time integrating alternative is described. The variable of integration and storage mechanism in these techniques is temporal.

Optical time integrating techniques have been developed using moving masks [32], [33] and fixed masks with moving integrators (photosensors) [34]. Acousto-optic and surface acoustic wave [35], [36] techniques permit the application of the time integrating concept to wide-band signal processing (100 MHz bandwidth and greater). Acousto-optic time integrating spectrum analysis in one dimension was introduced by Montgomery [35] in 1972, and later by Sprague and Koliopolous [36]. In 1978, acousto-optic time integrating spectrum analysis was extended to two dimensions with the development of the three product processor (TPP) [37], [38]. For a detailed clear treatment of various modes of operation of the TPP (such as coherent, incoherent, incoherent with an electronic reference, etc.), it would be difficult to improve on Kellman [39]. Cohen [40] describes a variety of acousto-optic implementations of cross ambiguity functions [41], a two-dimensional process involving spectrum analysis. Space integrating and time integrating architectures have been combined to produce hybrid two-dimensional spectrum analysis systems [42].

The time integrating correlator (TIC) is the foundation of the one-dimensional acousto-optic time integrating spectrum analyzer, and the TPP forms the foundation of two-dimensional techniques. The TIC and the TPP exist in coherent and incoherent versions. The coherent versions will be discussed because of the simplicity of analysis.

A. One-Dimensional Time Integrating Spectrum Analysis

The basis of acousto-optic time integrating spectrum analysis is the time integrating correlator. A coherent version of this correlator is shown in Fig. 7 [43]. Incoming light is modulated by $f(t)$ in the first cell. The diffracted light is then imaged onto the length of a second Bragg cell. The signal $g(t)$ interacts with the first diffracted beam to produce optical output proportional to $f(t) g^*(t - x/v)$ where v is the velocity of sound in the Bragg cell and x is the distance along the cell. The conjugation of g is the result of using the negative diffraction order in the second cell and the positive in the first. This distribution is then imaged onto an array of photodiodes that

integrate the light intensity until readout. An optical reference beam R is provided to produce an output intensity proportional to the amplitude of $f(t) g^*(t - x/v)$.

The sum of the signal and the reference at the detector is

$$A(x, t) = R + f(t) g^* \left(t - \frac{x}{v}\right). \tag{15}$$

The resulting intensity $I = A^*(x, t) A(x, t)$

$$I(x, t) = |R|^2 + 2 \text{ Re} \left[R f(t) g^* \left(t - \frac{x}{v}\right)\right]$$
$$+ \left|f(t) g \left(t - \frac{x}{v}\right)\right|^2 \tag{16}$$

(where Re means the real part of). The detector integrates this intensity to produce an output of $Z(x)$

$$Z(x) = \int_0^T \left(|R|^2 + \left|f(t) g \left(t - \frac{x}{v}\right)\right|^2 \right.$$
$$\left. + 2 \text{ Re} \left[R f(t) g^* \left(t - \frac{x}{v}\right)\right]\right) dt. \tag{17}$$

The first term represents a fixed bias. The second term is a signal dependent bias, and the third term represents the desired correlation. The signal dependent bias is particularly annoying when working with nonstationary signals. It causes the entire background level of the detector to move up and down with the input signal level. This necessitates the reestimation of the bias every integration period. One alternative is to tilt the reference wave R with respect to the detector. R becomes $Re^{jk\alpha x}$ for small angle α, and $k = 2\pi/\lambda$ where λ is the optical wavelength. This places the third term in (17) on a spatial carrier ($\cos k\alpha x$) which provides two advantages

1) the desired correlation term can be separated from the other terms with a bandpass filter, and
2) it alters (17) such that the desired term becomes the true complex correlation with phase represented by the spatial phase of the spatial carrier rather than just the real part of the complex correlation.

The major disadvantage is that many more detector elements are required to resolve the spatial carrier.

Spectrum analysis can be implemented with the time integrating correlator thru the use of the chirp transform algo-
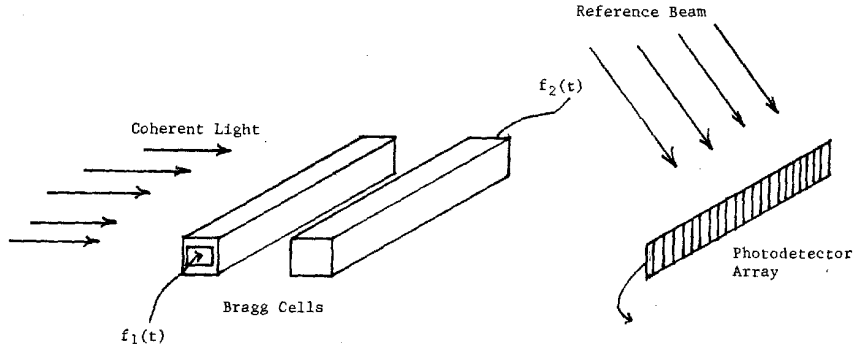
Fig. 8. Time integrating correlator.

rithm [44]. Let

$$f(t) = g(t) = 2 \cos \left(\omega_0 t + \frac{a}{2} t^2 \right)$$

$$= \exp j \left[\omega_0 t + \frac{a}{2} t^2 \right] + \exp -j \left[\omega_0 t + \frac{a}{2} t^2 \right]. \quad (18)$$

The positive diffraction from the first cell is

$$\exp j \left(\omega_0 t + \frac{a}{2} t^2 \right)$$

and the doubly diffracted light amplitude from the second cell is

$$A(x, t) = \left[\exp j \left(\omega_0 t + \frac{a}{2} t^2 \right) \right]$$

$$\cdot \left[\exp -j \left[\omega_0 \left(t - \frac{x}{v} \right) + \frac{a}{2} \left(t - \frac{x}{v} \right)^2 \right] \right]$$

$$A(x, t) = \left[\exp j \left(\frac{\omega_0 x}{v} - \frac{a}{2} \frac{x^2}{v^2} \right) \exp j \frac{ax}{v} t \right]. \quad (19)$$

The first term in (19) is spatial only, with a quadratic phase term that is characteristic of chirp algorithms. The second term is a distributed (in space) oscillator whose temporal frequency ax/v is a linear function of position x and chirp rate a. If $f(t)$ is multiplied by a signal to be analyzed $S(t)$, the output added to a reference beam of unit amplitude, and the resulting intensity integrated on a detector for a period of T, the output is twice the real part of $A(x)$

$$A(x) = \exp j \left(\frac{\omega_0 x}{v} - \frac{ax^2}{2v^2} \right) \int_0^T S(t) \exp j \frac{axt}{v} \, dt. \quad (20)$$

This is the Fourier transform of $S(t)$. The resolution is approximately $1/T$, the reciprocal of the detector integration time. The frequency range is 0 to $ax_{max}/v = a \, T_{max}$; where T_{max} is the maximum delay of the Bragg cell. The number of resolvable elements is $(aT \, T_{max})$. Since aT (the chirp bandwidth) cannot exceed the bandwidth of the cell plus the bandwidth of the signal, the upper bound on the number of resolvable elements is the time–bandwidth product of the Bragg cell. The quadratic phase term can be handled in several ways. For a fixed angular acceleration "a" it can be cancelled using a quadratic reference beam. A second alternative is to readout $A(x)$ and correct for the quadratic term by the post processing electronics. Fig. 8 illustrates a third alternative; chirp signals are applied to two Bragg cells that are located approximately

in the same plane. Equation (21) describes the product of the positive order $(e^{j\phi})$ diffracted light from the first cell with the negative order $(e^{-j\phi})$ light from the second cell. In this case all the quadratic phase terms cancel leaving an array of oscillators with a temporal frequency that depends on spatial position X without the quadratic phase term of (20). This system has an additional advantage in that it produces twice the number of resolution elements as the system in Fig. 7,

$$A(x, t) = e^{j\omega_0} \left[\left(t - \frac{T_{max}}{2} + \frac{x}{v} \right) + \frac{a}{2} \left(t - \frac{T_{max}}{2} + \frac{x}{v} \right)^2 \right]$$

$$\cdot e^{-j\omega_0} \left[\left(t - \frac{T_{max}}{2} - \frac{x}{v} \right) + \frac{a}{2} \left(t - \frac{T_{max}}{2} - \frac{x}{v} \right)^2 \right]$$

$$= e^{j} \left[\frac{2\omega_0 x}{v} \right] e^{j} \left[\frac{2ax}{v} \left(t - \frac{T_{max}}{2} \right) \right] \quad (21)$$

where T_{max} is maximum Bragg cell delay.

The time integrating optical system analyzer offers flexibility. By changing the detector integration time and chirp rate "a" the resolution of these devices can be scaled to cover a few hertz to tens of kilohertz.

B. Ambiguity Function

A special case of spectrum analysis is the cross ambiguity function [41]. This function

$$Q(\omega, \tau) = \int_{-\infty}^{\infty} f(t) g^*(t - \tau) e^{j\omega t} \, dt \quad (22)$$

is the spectrum of the product of two signals as a function of τ, the relative offset in time. Ambiguity functions have widespread applications in radar and represent the optimum response for a linear radar processing system with white noise. A pair of Bragg cells can form the array of products $f(t) g^*(t - x/v)$ as previously described. Similarly, a second pair of cells orthogonal to the first can form a product resulting in $e^{j(ayt/v)}$, a distributed oscillator. This implies that four Bragg cells configured as two orthogonal (in space) time integrating correlators could implement the integrand of the ambiguity function

$$f(t) g^* \left(t - \frac{x}{v} \right) \exp j \frac{ayt}{v}.$$

This distribution can be integrated on a two-dimensional photodetector to complete the calculation. There exist many physical implementations of this process; Fig. 9 illustrates two orthogonal correlators. The product of the time correlation
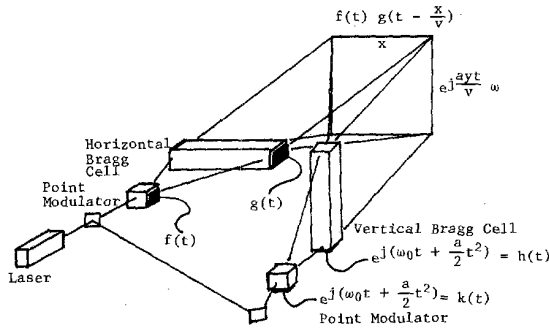
Fig. 9. Two-dimensional correlator.

integrand $f(t)g^*(t - x/v)$ and the distributed oscillator $e^{j(ayt/v)}$ takes place in the square law process on the detector. This is shown in (23) where the light amplitude from the orthogonal correlators are summed on the detector which responds to the resultant intensity

$$I(x, y, t) = \left| f(t)g^* \left(t - \frac{x}{v}\right) + \exp j \frac{ay}{v} t \right|^2$$

$$= 2 \operatorname{Re} f(t)g^* \left(t - \frac{x}{v}\right) \exp j \frac{ay}{v} t + 1$$

$$+ \left| f(t)g^* \left(t - \frac{x}{v}\right) \right|^2. \tag{23}$$

Once again the result contains the term of interest plus a signal dependent bias $|f(t)g^*(t - x/v)|^2$.

The multiplication can also be performed directly through multiple diffraction as illustrated in Fig. 10. In this configuration the signal $\hat{f}(t)$ which is applied to the point modulator is the product of the signals $f(t)$ and $K(t)$ in Fig. 9. The two point modulators of Fig. 9 have been combined into a single modulator in Fig. 10. The optical point modulator (Fig. 10) is illumated by coherent light and the resulting diffracted light expanded to fill a horizontal Bragg cell. The light diffracted by the second Bragg cell is modulated by $\hat{f}(t) g(t - x/v)$. The optical system compresses this light horizontally and expands it vertically through a third cell. The cylindrical optical system (not shown) then forms an image of the horizontal cell and the vertical cell onto a common output plane. The light amplitude at position x, y is modulated by $\hat{f}(t) g(t - x/v) h(t - y/v)$. As with the coherent correlator this result is added to a reference beam and the resulting intensity distribution is detected. This configuration is the coherent three product processor. Incoherent versions also exist and are described in detail by Kellman [38], [45]. The three product processor forms the following general operation

$$Z(x, y) = \int_0^T \hat{f}(t) g \left(t - \frac{x}{v}\right) h \left(t - \frac{y}{v}\right) dt. \tag{24}$$

Light at position (x_o, y_o) in the output plane has been modulated by $f(t) g(t - x_o/v) h(t - y_o/v)$. The integral is performed with a time integrating two-dimensional detector such as a charge coupled device or an electron beam addressed sensor (for example a vidicon). The cross ambiguity function is a special case of the general three product operation consisting of an array of products in one-dimension $f(t) g(t - x/v)$, and a spectrum analysis in an orthogonal dimension. A two-dimensional time integrating spectrum analyzer represents a
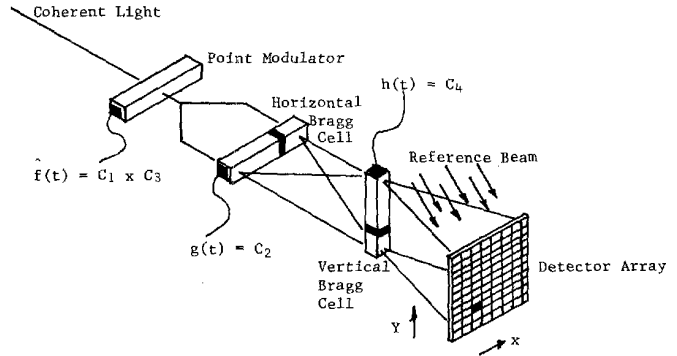
Fig. 10. Three product processor (TPP).
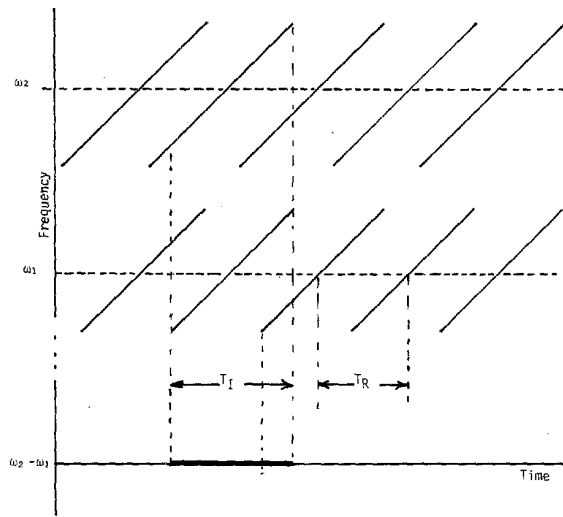
Fig. 11. Periodic chirp signals.

special case of the ambiguity function hence, can be implemented by the three product processor. This is the time integrating analog of the two-dimensional space integrating spectrum analysis previously described.

C. Two-Dimensional Time Integrating Spectrum Analysis

Consider the TPP (Fig. 10) where chirps C_1 and C_2 (Fig. 11) are applied to the horizontal and point modulators of the TPP, respectively. Chirp C_1 is multivalued [39] and must start T_{max} (the maximum cell delay) before C_2 to insure that the difference frequency is without gaps. Considering only the terms near $\omega_2 - \omega_1$ in frequency, the light amplitude due to C_1 and C_2 is $\hat{f}(x, t)$

$$\hat{f}(x, t) = \exp j \left[\omega_2 t + \frac{a}{2} t^2\right] \exp -j \left[\omega_1 \left(t - \frac{x}{v}\right) + \frac{a}{2} \left(t - \frac{x}{v}\right)^2\right]$$

$$= \exp j \left(\frac{\omega_1 x}{v} - \frac{a}{2} \frac{x^2}{v^2}\right) \exp j \left[(\omega_2 - \omega_1) + \frac{ax}{v}\right] t \tag{25}$$

for one period of the chirp. In Appendix A it is shown that N periods of $\hat{f}(x, t)$ can be written as

$$f(x, t) = T_i N e^{j\phi x}$$

$$\cdot \underbrace{\operatorname{sinc} \left(\frac{P(x) T_i}{2}\right)}_{C} * \underbrace{x \, [e^{jp(x)t}]}_{A} \underbrace{\left[\frac{\sin (p(x) NT_R/2)}{\sin (p(x) T_R/2)}\right]}_{B} \tag{26}$$

where $p(x) = \omega_2 - \omega_1 + ax/v$, a temporal frequency dependent on x, and $*x$ is the convolution in the x variable. T_i and T_R are the interaction period and the repetition period of the chirp as illustrated in Fig. 11.

Term "A" is an oscillator whose frequency is a linear function of position x. Term "B" spatially (and temporally) filters this oscillator into discrete spectral lines spaced $2\pi/T_R$ rad/s apart and of width $2\pi/NT_R$ rad/s. Convolution by term "C" spreads the lines spatially without affecting the temporal frequency. B is a spatial pattern only. Using $p(x) = \omega_2 - \omega_1 + ax/v$ to determine the spatial line width and line separation, the line separation is Δx when $p(x) - p(x + \Delta x) = 2\pi/T_R$.

$$\Delta x \text{ spacing} = \frac{2\pi v}{aT_R} \qquad (27)$$

Similarly,

$$\Delta x \text{ width} = \frac{2\pi v}{aT_i}$$

where width is measured from the peak to the first null of the appropriate distribution. If $T_i = T_R$ the peak of one oscillator falls at the first null of its adjacent oscillator. The general situation is illustrated in Fig. 12. The oscillators have a fixed frequency in the y direction and increment frequency in discrete steps by $2\Pi/T_R$ in the x direction (each step $\Delta x = 2\Pi v/aT_R$); $f(x, t)$ is an oscillator running at discrete frequencies that differ by multiples of $2\Pi/T_R$ as a function of x.

Consider the TPP in Fig. 10 where, in addition to chirp C_1 and C_2, chirps C_3 and C_4 are applied to the point and vertical modulators of the TPP respectively. C_3 and C_4 have chirp rates b and carrier frequencies ω_3 and ω_4, respectively. The product of these chirps as a function of y and t is

$$g(y, t) = \exp j \left(\frac{\omega_3 y}{v} - \frac{b}{2} \frac{y^2}{v^2} \right) \exp j \left[(\omega_4 - \omega_3) + \frac{by}{v} \right] t$$

$$= e_y^{j\phi} e^{jp(y)t} \qquad (28)$$

and only one period of this chirp is present. This is a continuous distributed oscillator whose frequency is a function of position y.

The resultant output of the three product processor with both the horizontal and vertical oscillators running is the product of the horizontal and vertical distributions

$$h(x, y, t) = g(y, t) f(x, t)$$

$$= T_i N \exp j(\phi_x + \phi_y) \text{ sinc} \left(\frac{p(x) T_i}{2} \right) *x$$

$$\cdot \left[\exp j[p(x) + p(y)] t \right] \left[\frac{\sin (p(x) NT_R/2)}{\sin (p(x) T_R/2)} \right] \quad (29)$$

The temporal frequency of this oscillator varies as a function of x and y. The frequency is $\omega = p(x) + p(y) = \omega_4 - \omega_3 + \omega_2 - \omega_1 + (ax + by)/vt$ when evaluated at $x = K(2\Pi v/aT_R)$, $K = 1, 2, \cdots$ defined by the horizontal oscillator whose frequencies are quantized by the periodic nature of the horizontal chirp.

Fig. 12 illustrates this oscillator for $N = 10$ and $a = bN$ with the origin set at zero. If a signal $S(t)$ falling within the passband of this oscillator is applied to the point modulator of the
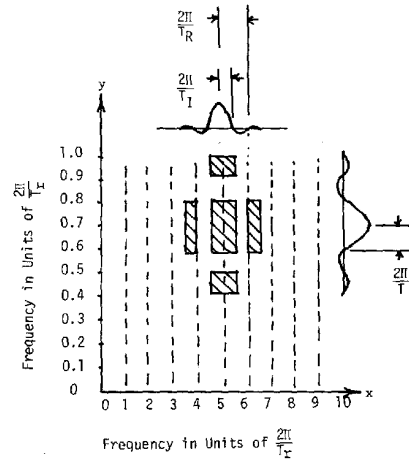
Fig. 12. Output of a two-dimensional time integrating Fourier transform.

TPP, and the output is mixed with a reference wave R and integrated on a two-dimensional detector the result is

$$\hat{S}(x, y) = \int_0^T |R + S(t) h(x, y, t)|^2 \, dt$$

$$= \int_0^T |R|^2 \, dt + \int_0^T |S(t) h(x, y, t)|^2 \, dt$$

$$+ 2 \text{Re} \left[\int_0^T S(t) h(x, y, t) \, dt \right]. \qquad (30)$$

The last term represents the spectrum analysis of $S(t)$ if evaluated along the line defined by $\delta(x - 2\Pi v/aT_R)$. These lines are commonly called coarse frequency loci. The term of interest is

$$S(x, y) = 2 \text{Re} \left[R \int S(t) e^{j(\Delta\omega + ((ax+by)t/v))} \, dt \right] \qquad (31)$$

where $\Delta\omega = \omega_4 - \omega_3 + \omega_2 - \omega_1$ is the frequency at the origin. Fig. 12 illustrates the spectrum of a signal at $\omega = 5.7 \times 2\pi/T_R$. Given a signal frequency ω rad/s the output in Fig. 12 will occur centered at the point (x, y)

$$x = \left[\text{int} \left(\frac{\omega T_r}{2\pi} \right) \right] \frac{2\pi}{T_r} \frac{v}{a} \text{ where int } (x) \equiv \text{the greatest integer} \leq x$$

$$y = \left[\frac{\omega T_r}{2\pi} - \text{int} \left(\frac{\omega T_r}{2\pi} \right) \right] \frac{2\pi v}{T_r b}. \qquad (32)$$

In Fig. 12, $a = 10b$. For example

$$x = 5 \frac{2\pi}{T_r} \frac{v}{a}$$

$$y = 7 \frac{2\pi}{T_r} \frac{v}{b}.$$

What has been accomplished is very similar to the two-dimensional spatial transformation described in Section III-D, where the optical analog to a FFT was developed. In the time integrating analog of the FFT it should not be surprising to

find a format similar to that for the space integrating form.

In one-dimensional time integrating spectrum analysis the upper bound on the number of resolvable elements was the time–bandwidth product of the cell (typically 1000). The two-dimensional time integrating analyzer has an upper bound of the product of the time–bandwidth products of the horizontal and vertical cells ($10^3 \times 10^3$ or 10^6).

Practical two-dimensional photodiode arrays having about 200 000 diodes exist; this, plus the 1000 to 1 dynamic range of these detectors, bound the performance of these systems. The attractive feature of this technique is the ability to do two-dimensional processing using one-dimensional real-time modulators which have achieved a degree of engineering refinement and reliability far beyond the available two-dimensional real-time modulators.

In Section III-C the two-dimensional spatial transform was treated as an analog of the FFT where a sequence of small transforms is combined into a large one through an orthogonal transform. In this section the two-dimensional time integrating transform was presented from the viewpoint of mixing two N long arrays of oscillators orthogonally in space to produce N^2 oscillators in two dimensions. The treatments are equivalent and interchangeable. Each gives a different point of view of what is mathematically the same process.

There is a fundamental difference between optical technology and other techniques. In most technologies, multiplies are expensive and storage relatively inexpensive. The reverse is true in optics. A three product processor can be built with current technology that will perform more than 10^{15} triple multiplies per second (10^9 Hz bandwidth Bragg cells with 1-μs aperture). A detector (storage device) with sufficient resolution and dynamic range and associated output rate has yet to be developed.

V. Summary

The acousto-optic radiometer bank illustrates the usefulness of square-law detection and temporal integration on photosensors to reduce data rate and enhance sensitivity. The interference rejection filter uses the same square law process on the photosensor to perform heterodyne detection. The result is not integrated temporally because the desired output is a filtered radio frequency signal. The third topic (optical FFT) takes a one dimensional set of data points, formats them into a two-dimensional array, then transforms in two dimensions and interprets the result in terms of the one-dimensional transform of the original array. Transforms of large arrays of data (greater than 10^6 points) can be implemented with this technique. Time integrating techniques are described in terms of time integrating correlators and distributed oscillators. A chirp algorithm is used to implement a distributed oscillator. One-dimensional time integrating spectrum analysis is described in terms of multiplying a signal by an array of oscillators (distributed oscillators) and integrating the result on a photosensor. The ambiguity function is treated as an array of one-dimensional spectrum analyzers operating on an orthogonal (in space) array of signals.

Finally, two-dimensional spectrum analysis is treated in terms of a two-dimensional array of oscillators produced by multiplying two orthogonal (in space) one-dimensional arrays of oscillators. The signal to be transformed is multiplied by this two-dimensional array of oscillators and the result integrated (in time) on a two-dimensional photosensor.

Appendix A

The expression for the interaction of two multivalued repeating chirp signals is $f(x, t)$ where

$$f(x, t) = \exp j \left(\frac{\omega_1}{v} x - \frac{a}{2} \frac{x^2}{v^2} \right) \sum_{n=-(N-1)/2}^{(N-1)/2} \mathrm{rect} \left(\frac{t - nT_R}{T_I} \right)$$

$$\cdot \exp j \left[(\omega_2 - \omega_1) + \frac{ax}{v} \right] [t - nT_R] \qquad (1A)$$

where rect (x) 1 for $|x| \leqslant \frac{1}{2}$, 0 for $|x| > \frac{1}{2}$, T_I is the duration of the interaction, and T_R is the repetition period of the chirps. ω_2 and ω_1 define the difference frequencies in the band of interest and also represent the frequency of the chirps at $x = 0$, $t = 0$. We define $\phi_x = (\omega_1/vx - ax^2/2v^2)$ as a fixed phase pattern and $p(x) = (\omega_2 - \omega_1 + ax/v)$ as a temporal frequency as a function of x. Then,

$$f(x, t) = e_x^{j\phi} \sum_{n=-(N-1)/2}^{(N-1)/2} (\exp jp(x)[t - nT_R]) \mathrm{rect} \left(\frac{t - nT_R}{T_I} \right)$$

$$(2A)$$

which is a repetitive signal and hence can be rewritten as the convolution of one period with a repetitive impulse train

$$f(x, t) = e^{j\phi} x$$

$$\cdot \int_{-\infty}^{\infty} \mathrm{rect} \frac{\xi}{T_I} \left(\sum_{n=-(N-1)/2}^{(N-1)/2} \delta(t - nT_R - \xi) \right) e^{jp(x)\xi} d\xi \qquad (3A)$$

where $\delta(x)$ = Dirac delta, $\int_{-\infty}^{\infty} f(x) \delta(x) dx = f(0)$. This is recognized as the Fourier transform of the product of two functions; hence it can be expressed as a convolution of transforms

$$f(x, t) = e_x^{j\phi} T_I$$

$$\cdot \mathrm{sinc} \frac{P(x) T_I}{2} *_x \left(e^{jp(x)t} \sum_{n=-N-1/2}^{N-1/2} \exp j \frac{ax}{v} (nT_R) \right) \qquad (4A)$$

where $*_x$ denotes convolution in the x variable. Using the identity

$$\sum_{n=-(N-1)/2}^{(N-1)/2} e_n^{j\theta} = N \frac{\sin N\theta/2}{\sin \theta/2}$$

equation (4A) becomes,

$$f(x, t) = (T_I N) e_x^{j\phi} \mathrm{sinc} \frac{P(x) T_I}{2} *_x \left(e^{jp(x)t} \frac{\sin \frac{p(x) NT_R}{2}}{\sin \frac{p(x) T_R}{2}} \right).$$

$$(5A)$$

References

[1] E. N. Leith, "Complex spatial filters for image deconvolution," Proc. IEEE, vol. 65, pp. 18–28, Jan. 1977.

[2] R. Adler, "Interaction between light and sound," *IEEE Spectrum*, pp. 42–54, May 1967.
[3] A. Korpel, "Acousto-optics—A review of fundamentals," this issue, pp. 48–53.
[4] E. H. Young, Jr., and S. K. Yao, "Design considerations for acousto-optic devices," this issue, pp. 54–64.
[5] D. Casasent, "Spatial light modulators," *Proc. IEEE*, vol. 65, pp. 143–155, Jan. 1977.
[6] N. Uchida and N. Zobukazu, "Acousto-optic deflection materials and techniques," *Proc. IEEE*, vol. 61, pp. 1073–1092, Aug. 1973.
[7] E. K. Kirchner and J. R. Yaeger, "Today's capabilities of micro-wave (0.2 to 18 gigahertz) acousto-optic devices," in *Proc. Acousto-Optic Device Development/Instrumentation/Applications Conf.* (Society of Photo-Optical Instrumentation Engineers), (San Diego, CA), pp. 4–11, Aug. 26–27, 1976.
[8] I. C. Chang, "Acousto-optic devices and applications," *IEEE Trans. Sonics Ultrason.*, vol. SU-23, Jan. 1976.
[9] D. L. Hecht, "Multifrequency acousto-optic diffraction," *IEEE Trans. Sonics Ultrason.*, vol. SU-24, Jan. 1977.
[10] Klein and Cook, "Uniform approach to ultrasonic light diffraction," *IEEE Trans. Sonics Ultrason.*, vol. SU-14, pp. 123–134, July 1967.
[11] D. F. Barbe, "Imaging devices using the charge coupled concept," *Proc. IEEE*, vol. 63, pp. 38–67, Jan. 1975.
[12] G. M. Borsuk, "Photodetectors for acousto-optic signal processors," this issue, pp. 100–118.
[13] A. J. Steckl, "Charge coupled devices," in *The Infrared Handbook*, Wolfe and Zissis, Eds. Washington, DC: Office of Naval Research, Department of the Navy, 1978, ch. 12.
[14] Goodman, *Introduction to Fourier Optics*. New York: McGraw-Hill, 1978.
[15] K. Preston, Jr., *Coherent Optical Computers*. New York: McGraw-Hill, 1972.
[16] Borsuk and Malarkey, "Wideband acousto-optic radiometery," in *Proc. SPIE Conf. Effective Utilization of Optics in Radar Systems*, Sept. 27–29, 1977.
[17] J. D. Kraus, *Radio Astronomy*. New York: McGraw-Hill, 1966.
[18] Davenport and Root, *Random Signals and Noise*. New York: McGraw-Hill, 1958.
[19] J. E. Freund, *Mathematical Statistics*. Englewood Cliffs, NJ: Prentice Hall, 1971.
[20] A. J. Steckl, "Charge coupled devices," in *The Infrared Handbook*, Wolfe and Zissis, Eds. Washington, DC: Office of Naval Research, Department of the Navy, 1978, ch. 12.
[21] K. Preston, "Trade-offs in optical computing," in *Proc. SPIE Conf. Effective Utilization of Optics in Radar Systems*, Sept. 27–29, 1977.
[22] A. Korpel, "Acousto-optics," in *Applied Solid State Science*, vol. 11, R. Wolfe, Ed. New York: Academic Press, 1972.
[23] K. Preston, Jr., "A comparison of analog and digital techniques for pattern recognition," *Proc. IEEE*, vol. 60, pp. 1216–1230, 1972.
[24] Bergland, "A guided tour of the fast Fourier transform," *IEEE*

Spectrum, vol. 6, pp. 41–52, 1969.
[25] C. E. Thomas, "Optical spectrum analysis of large space band-width signals," *Appl. Opt.*, vol. 5, pp. 1782–1790, 1966.
[26] Rabiner and Gold, *Theory and Application of Digital Signal Processing*. Englewood Cliffs, NJ: Prentice Hall, 1975.
[27] B. V. Markevitch, "Optical processing of wideband signals," presented at the 3rd Wideband Analog Recording Symp., *RADC*, Griffiss AirForce Base, NY, Sept. 1969.
[28] H. Whitehouse, "Signal processing with charge transfer devices," *IEEE Trans. Electron Devices*, vol. ED-23, p. 132, Feb. 1976.
[29] H. Whitehouse, "Optical and analog electronic signal processing," in *Proc. SPIE* (Huntsville, AL), vol. 128, pp. 165–171, Sept. 27–29, 1977.
[30] C. S. Gault, "Development of a charge-coupled device (CCD) addressed light modulator," in *Proc. SPIE Conf.*, vol. 185, pp. 93–95, 1979.
[31] Grinberg *et al.*, "Liquid-crystal electro-optical modulators for optical processing two-dimensional data," in *Proc. SPIE*, vol. 128, pp. 253, 266, Sept. 1977.
[32] W. T. Rhodes, "Acousto-optic signal processing—Convolution and correlation," this issue, pp. 65–79.
[33] K. Bromley, "An optical incoherent correlator," *Opt. Acta*, vol. 21, pp. 35–41, 1974.
[34] Monahan, Bocker, Branley, and Louie, "Incoherent electro-optical processing with CCD's," in *Proc. Dig. Int. Optical Computing Conf.* (Washington, DC), Apr. 1975.
[35] R. M. Montgomery, "Acousto-optical signal processing system," U.S. Patent 3 634 749, Jan. 1972.
[36] Sprague and Koliopoulos, "Time integrating acousto-optic correlator," *Appl. Opt.*, vol. 15, pp. 89–92, Jan. 1976.
[37] T. M. Turpin, "Time integrating optical processing," in *Proc. SPIE Symp. Real Time Signal Processing* (San Diego, CA), vol. 154, pp. 196–203, Aug. 1978.
[38] P. Kellman, "Detector integration acousto-optic signal processing," in *Proc. Int. Optical Computing Conf.* (London, England), pp. 91–95, Sept. 1978.
[39] ——, "Time integrating optical signal processing," Ph.D. dissertation, Stanford Univ., Stanford, CA, June 1979.
[40] J. D. Cohen, "Ambiguity processor architecture using one-dimensional acousto-optic transducers," in *Proc. SPIE Technical Symp. East* (Washington, DC), vol. 180, Apr. 1979.
[41] P. M. Woodward, *Probability and Information Theory with Applications to Radar*. New York, McGraw-Hill, 1953.
[42] T. R. Bader, "Coherent optical hybrid techniques for spectrum analysis," in *Proc. SPIE*, vol. 185, pp. 140–146, 1979.
[43] R. Sprague, "Review of acousto-optic signal correlators," in *SPIE Proc. Acousto-Optics* (San Diego, CA), vol. 90, pp. 136–147, Aug. 1976.
[44] Rabiner, Schafer, and Rader, "The chirp Z-transform algorithm and its application," *Bell Syst. Tech. J.*, pp. 1249–1292, May–June 1969.
[45] P. Kellman, "Time integrating optical processors," in *Proc. SPIE* (Huntsville, AL), vol. 185, pp. 130–139, May 22–23, 1979.

Integrating Acousto-Optic Channelized Receivers

PETER KELLMAN, MEMBER, IEEE, HARRY N. SHAVER, MEMBER, IEEE, AND
J. WILLIAM MURRAY, MEMBER, IEEE

Abstract—The subject of this paper is acousto-optic channelized receivers with large noncoherent processing gain. A receiver model is developed and the output statistics are derived for signal plus noise input. Noise equivalent bandwidths and signal detection sensitivity are calculated. The implications of large average noise power are discussed. Experimental measurements are in agreement with the theory presented.

I. INTRODUCTION

ACOUSTO-OPTIC (AO) techniques for power spectral measurement have been exploited for a variety of signal analysis applications [1]. Application of AO techniques to integrating channelized receivers with large noncoherent processing gain is the subject of this paper. Particular emphasis is given to detection of signals buried in noise. The key attributes of AO technology for this application are wide instantaneous bandwidth, a large number of spectral samples, and high-detection sensitivity.

The AO channelized receiver realizes high sensitivity and multiple-signal handling ability by means of channelization. Increased sensitivity may be achieved through noncoherent integration [2]. Special attention to receiver noise loading, system stability, and linearity is required to achieve significant processing gain. A receiver model is developed and the output mean and variance are calculated for signal plus noise input. The treatment in this paper relates the noise equivalent channel bandwidth to optical parameters. The degradation in signal detection sensitivity due to noise arising in the photodetection process is derived. It is shown that a tradeoff between noncoherent processing gain and output dynamic range exists due to the increase in average noise power bias with increasing integration. Implications of average noise power loading to receiver design are discussed. Receiver processor considerations such as digital quantization noise and threshold settability are included. Experimental noise measurements are in agreement with the theory presented.

II. ACOUSTO-OPTIC CHANNELIZED RECEIVER MODEL

A conceptual diagram of the AO channelized receiver is shown in Fig. 1. A first-order theory of operation is reviewed. A transparent ultrasonic delay line (Bragg cell) is utilized to convert a wide-band electrical input to a proportional optical pattern by means of a traveling pressure wave. Spatial variation created in the refractive index is used to modulate coherent light, and the diffracted spectral components are separated by a lens. The Fourier transform of the input signal results as a light distribution in the focal plane of the lens. This light distribution is detected photoelectronically, produc-

ing a charge distribution proportional to the instantaneous power spectrum of the input signal. Integrated charge packets at discrete photosites are then multiplexed to produce a sampled data waveform.

An expression for the detected output voltage samples is now derived in terms of the input signal $u(t)$. The sliding window power spectrum at time t can be written as

$$\left| \int_{-\infty}^{\infty} w(\tau)\, u(t-\tau)\, \exp(-i2\pi f\tau)\, d\tau \right|^2$$

where the window function $w(t)$ determines the spectral resolution. The complex window function $w(t)$ represents both amplitude and phase factors. Contributions to the amplitude window function include the finite delay length, uniformity of illumination, acoustic attenuation, and diffraction. Phase contributions include lens aberrations, optical surface inaccuracies, and focusing errors.

Utilizing a discrete array of photodetectors gives rise to a sample spectrum

$$\int_{-\infty}^{\infty} H(f-f_k) \left| \int_{-\infty}^{\infty} w(\tau)\, u(t-\tau)\, \exp(-i2\pi f\tau)\, d\tau \right|^2 df$$

where f_k is the frequency corresponding to the kth detector and $H(f)$ is a spectral weighting function that describes the spatial response of an individual detector element. This weighting function includes the contribution of electrical crosstalk between channels that may occur in the readout process. In particular, the inefficiency of charge transfer devices broadens the spectral weighting. Variation between array elements has been neglected.

The instantaneous power spectrum is integrated in time producing a voltage

$$X_{jk} = \int_{jT}^{(j+1)T} \int_{-\infty}^{\infty} H(f-f_k)$$

$$\cdot \left| \int_{-\infty}^{\infty} w(\tau)\, u(t-\tau)\, \exp(-i2\pi f\tau)\, d\tau \right|^2 df\, dt \quad (1)$$

where j denotes the sample time and T equals the integration period.

The output sampled data value

$$Z_{jk} = X_{jk} + Y_{jk} \quad (2)$$

includes an additive detection noise contribution Y_{jk}. Detection noise has both thermal and shot components. Shot noise depends on the average optical power and is therefore signal
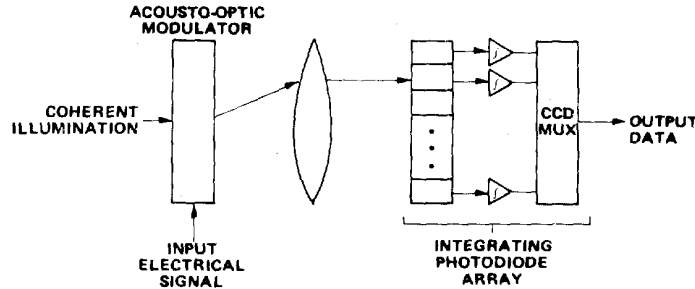
Fig. 1. AO channelized receiver concept.

Fig. 2. Simplified channel model.

dependent. Thermal noise, due to random agitation of electrons and reset charge uncertainty, is independent of the optical signal. The relative importance of thermal versus shot noise depends on the number of photo electrons. It will be shown that shot noise effects are negligible for devices with more than several hundred rms thermal noise electrons.

A simplified model of a single receiver channel is shown in Fig. 2. This model is useful in first order calculations of receiver sensitivity and noise figure. However, it will be shown this simple channel model is not precise since it does not include the effect of a spectral weighting function $H(f)$.

III. NOISE EQUIVALENT BANDWIDTH

The output detection statistics are calculated based on the receiver model described in the previous section, equations (1) and (2). Detailed derivation is lengthy, therefore, only important results are stated in the text (derivations are outlined in Appendix A). Signal-to-noise ratios are defined and noise equivalent bandwidths are derived. The noise equivalent bandwidth is expressed in terms of the input window and spectral weighting functions. The equivalent bandwidth is signal dependent due to spectral averaging. Two cases are analyzed: sinusoid plus noise and random signal plus noise.

Consider a signal plus noise input

$$u(t) = s(t) + n(t) \tag{3}$$

where $n(t)$ is zero mean white Gaussian noise with noise power spectral density $N_0/2$ (i.e., the noise autocorrelation is

$$R_n(\tau) = E\{n(t)\,n(t-\tau)\} = (N_0/2)\delta(\tau)).$$

The mean output,

$$\mu_Z = E\{Z_{jk} = X_{jk} + Y_{jk}\} = E\{X_{jk}\}$$
$$= \mu_X = \mu_s + \mu_n \tag{4}$$

is the sum of the mean output signal power μ_s and the mean output noise power μ_n. It may be shown that μ_n is given by

$$\mu_n = \frac{N_0 T}{2} \int G(f)\,df \int H(f')\,df' \tag{5}$$

where $G(f)$ is the magnitude squared of the Fourier trans-

formed window function,

$$G(f) = \left| \int w(\tau)\exp(-i2\pi f\tau)\,d\tau \right|^2. \tag{6}$$

The output noise variance σ_Z^2 is given by

$$\sigma_Z^2 = \sigma_X^2 + \sigma_Y^2. \tag{7}$$

The detector noise variance σ_Y^2 degrades the output signal-to-noise ratio. Detection sensitivity loss is examined in the following section.

For a sinusoidal input,

$$s(t) = A\cos[2\pi f_0 t + \phi] \tag{8}$$

the mean output signal power can be written as

$$\mu_s = \frac{A^2 T}{4}\mathcal{H}(f_k - f_0) \tag{9}$$

where $\mathcal{H}(f)$ is the convolution between the functions G and H,

$$\mathcal{H}(f) = \int G(f-f')H(f')\,df'. \tag{10}$$

The variance for a sinusoid plus noise input $\sigma_{X_{s+n}}^2$ can be expressed in terms of the variance for noise only input $\sigma_{X_n}^2$ in the familiar form

$$\sigma_{X_{s+n}}^2 = \sigma_{X_n}^2 (1 + 2\,\mathrm{SNR}_i) \tag{11}$$

where

$$\sigma_{X_n}^2 = \left(\frac{N_0}{2}\right)^2 T \int \mathcal{H}^2(f)\,df \tag{12}$$

and the input signal-to-noise ratio $\mathrm{SNR}_i = A^2/2B_s N$ is measured in the noise equivalent bandwidth B_s. The noise equivalent bandwidth B_s for the case of sinusoid plus noise input, equals

$$B_s = \frac{\int \mathcal{H}^2(f)\,df}{\mathcal{H}^2(0)}. \tag{13}$$

The signal-to-noise ratio of the variable X_{jk} can be defined as

$$\mathrm{SNR}_X = \mu_s^2/\sigma_{X_n}^2 \tag{14}$$

where the mean noise power μ_n has been subtracted. The output signal-to-noise ratio SNR_X can be related to the input signal-to-noise ratio SNR_i as

$$\mathrm{SNR}_X = B_s T\,\mathrm{SNR}_i^2. \tag{15}$$

KELLMAN *et al.*: INTEGRATING AO CHANNELIZED RECEIVERS

It has been assumed that the input frequency $f_0 = f_k$. An alternative definition for output signal-to-noise ratio uses the signal plus noise variance, yielding

$$\frac{\mu_s^2}{\sigma_{X_{s+n}}^2} = B_s T \frac{SNR_i^2}{1 + 2\,SNR_i} \tag{16}$$

which is approximately the same as (15) for low input signal-to-noise ratio. The latter definition exhibits linear behavior for a sinusoid input at high signal-to-noise ratio.

The processing gain may be defined as the ratio of the input signal-to-noise ratio without integration, to the input signal-to-noise ratio with integration in order to achieve the same detection probability. The processing gain is proportional to $\sqrt{B_s T}$.

The above formulation for sinusoid plus noise input is approximately valid for signals with narrow-band modulation. However, as the modulation bandwidth approaches the channel bandwidth, the signal spectrum interacts with the spectral weighting and thereby alters the effective time–bandwidth product.

Consider the case of a random Gaussian input signal $s(t)$ with uniform spectral density $S/2$, independent of the additive noise $n(t)$. The input signal-to-noise ratio in an arbitrary bandwidth is $SNR_i = S/N_0$. It can be shown that the mean and variance are

$$\mu_X = \mu_n (1 + SNR_i) \tag{17}$$

and

$$\sigma_{X_{s+n}}^2 = \sigma_{X_n}^2 (1 + SNR_i)^2. \tag{18}$$

The signal-to-noise ratio defined by Equation (14) becomes

$$SNR_X = \frac{\mu_n^2}{\sigma_{X_n}^2} SNR_i^2 = B_n T\, SNR_i^2 \tag{19}$$

where the noise equivalent bandwidth B_n is given by

$$B_n = \frac{\left[\int G(f)\,df \int H(f)\,df\right]^2}{\int \mathcal{H}^2(f)\,df}. \tag{20}$$

Using the alternative definition of signal-to-noise ratio (16), we have

$$\frac{\mu_s^2}{\sigma_{X_{s+n}}^2} = B_n T \frac{SNR_i^2}{(1 + SNR_i)^2}. \tag{21}$$

By this definition, the output signal-to-noise ratio never exceeds $B_n T$ for the case of random noise input.

Noise equivalent bandwidths have been derived for sinusoidal and wideband random input signals. The discrepancy between noise equivalent bandwidths B_s and B_n is due to averaging the spectral power. It can be shown that B_s is less than or equal to B_n. For Gaussian functions $G(f)$ and $H(f)$ the ratio B_n/B_s equals 2.

The probability of detection and false alarm depend on the probability distribution of the detection statistic. The distribution of the variable Z_{jk} is approximately Gaussian for large time–bandwidth product. In the preceding calculations, it has been assumed that the time–bandwidth product is much greater than one. Probability densities for noise only and signal plus noise inputs are illustrated in Fig. 3. This figure illustrates the relatively large mean noise level μ_n with respect
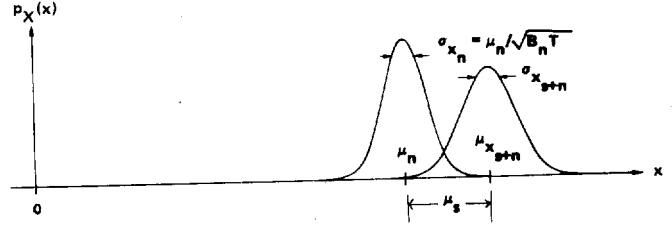
Fig. 3. Representative probability densities.

to the standard deviation σ_{X_n} that occurs as a consequence of integration. Receiver operating characteristics, i.e., probability of detection versus probability of false alarm, are easily calculated for Gaussian statistics.

IV. RECEIVER NOISE LOADING

The mean noise power level relative to the standard deviation increases with integration resulting in a bias. The presence of bias results in a tradeoff between receiver sensitivity and dynamic range. Evaluation of signal-to-noise ratio loss due to detection noise and the effect of average noise power loading are quantified below.

Receiver noise figures are typically determined by the receiver front end, since subsequent stages are preceded by sufficient gain in order to overcome additional noise. The integrating AO channelized receiver may likewise be operated with sufficient gain to overcome photodetection noise, provided that the mean noise level is tolerable.

Define the relationship between receiver noise σ_{X_n} and detection noise σ_Y as

$$\sigma_{X_n} = K\sigma_Y. \tag{22}$$

At this noise setting the mean noise level becomes

$$\mu_n = \sqrt{B_n T}\, \sigma_{X_n} = K\sqrt{B_n T}\, \sigma_Y. \tag{23}$$

If the detector dynamic range DR is defined as the maximum signal divided by the rms detector noise without input noise loading (i.e., $DR = Z_{max}/\sigma_Y$), then the receiver dynamic range with noise loading $\widetilde{DR} = (Z_{max} - \mu_n)/\sigma_Z$ can be expressed as

$$\widetilde{DR} = \frac{DR}{\sqrt{1 + K^2}} - \sqrt{\frac{K^2}{1 + K^2} B_n T}. \tag{24}$$

Equation (24) defines a tradeoff between dynamic range and processing gain $\sqrt{B_n T}$ for a fixed value of K. A further consideration is that the shot noise component becomes more significant with increasing mean noise level. Shot noise effects are treated in Appendix B.

The output signal-to-noise ratio degradation due to detector noise can be expressed through the ratio

$$\rho^2 = \frac{SNR_X}{SNR_Z} = 1 + \left(\frac{\sigma_Y}{\sigma_{X_n}}\right)^2 \tag{25}$$

where $SNR_Z = \mu_s^2/\sigma_Z^2$. The input sensitivity loss ρ equals,

$$\rho = \sqrt{\frac{1 + K^2}{K^2}}. \tag{26}$$

The receiver dynamic range can be written in terms of ρ as

$$\widetilde{DR} = \sqrt{\frac{\rho^2 - 1}{\rho^2}}\, DR - \frac{1}{\rho} \sqrt{B_n T}. \tag{27}$$

Equations (26) and (27) are plotted in Figs. 4 and 5. Fig. 4 illustrates the large sensitivity loss that occurs as the detector noise exceeds the noise contribution due to the input. In Fig. 5 the detector dynamic range value is assumed to be $DR = 1000$ peak/rms (30 dB). For example, with $B_n = 1$ MHz, $T = 10$ ms, $DR = 1000$, and $\rho = 1.26$ (1 dB); the receiver dynamic range equals $\widetilde{DR} = 529$ (27.2 dB), therefore, noise loading has reduced the effective dynamic range by 2.8 dB.

The presence of a mean noise power output resulting from noncoherent integration places stringent requirements on system linearity and gain stability in order to realize the expected improvement in detection sensitivity. Susceptibility to gain variation depends to a large extent on the specific detection algorithm.

The effect of gain uncertainty is illustrated for the simplest detection scheme, a fixed threshold. The threshold must detect differences between the mean noise μ_n and signal plus noise $\mu_n + \mu_s$. If the gain changes by the fraction $(\Delta G/G)$, then the output signal level for a noise only input signal will be biased by $(\Delta G/G)\sqrt{B_n T}$ standard deviations. To maintain a probability of false alarm (P_{fa}) that does not exceed a specified value, the threshold level must necessarily be set for the condition where the gain is at (or greater than) its maximum value G_{max}. If the gain decreases then the input signal power required to provide a specified probability of detection (P_d) increases. The maximum loss in receiver sensitivity occurs when the gain changes to its minimum value G_{min}. For sinusoid plus noise input this can be computed from the relation

$$\max\{\text{loss}\} = 1 + Q$$

$$+ \left[1 - \sqrt{\frac{\text{TNR}_X}{\text{SNR}_X}}\right]\left[\sqrt{1 + 2Q\sqrt{\frac{\text{SNR}_X}{B_s T}}} - 1\right]$$

$$(28)$$

where

$$Q = \frac{\Delta G}{G_{min}}\sqrt{\frac{B_n T}{\text{SNR}_X}}\left[1 + \sqrt{\frac{\text{TNR}_X}{B_n T}}\right]$$

$$\Delta G = G_{max} - G_{min}$$

$$\sqrt{\text{TNR}_X} = \frac{1}{\sigma_{X_n}}[(\text{Threshold Level}|P_{fa}) - \mu_n].$$

For example, with $B_n T = 10000$, and P_d, P_{fa} corresponding to an output signal-to-noise ratio of 10 dB, a decrease in gain of 1 dB will reduce the input sensitivity approximately 10 dB. Techniques such as noise riding thresholds and Dicke switching have been exploited to overcome gain sensitivity [3]. However, these approaches generally suffer operational restrictions, reduced sensitivity, and increased complexity.

V. DIGITAL PROCESSING

The ability to set precise thresholds and to estimate the noise statistics is required for signal detection. The functions of signal detection and accurate receiver calibration can be implemented through digital processing of the channelized receiver data. Further sensitivity improvement and increased dynamic range may be realized by digital integration with extended precision.

Define the digitized receiver output as

$$\hat{Z}_{jk} = Z_{jk} - \epsilon_{jk} \qquad (29)$$
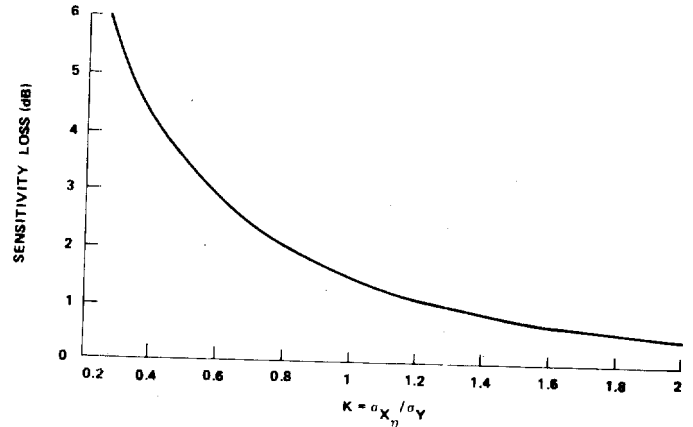
Fig. 4. Sensitivity loss versus receiver noise loading.
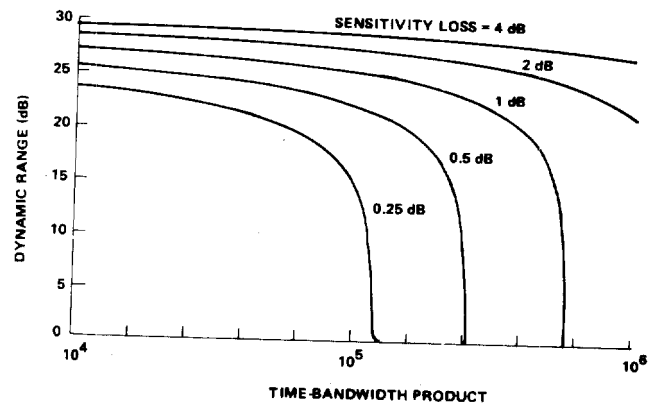
Fig. 5. Dynamic range versus time–bandwith product.

where ϵ_{jk} is the quantization error. The quantization error may be modeled [4] as zero mean independent noise, uniformly distributed with variance $\sigma_q^2 = q^2/12$, where q is the quantization step size. The assumption that the quantization error is independent of the signal is valid provided that the rms noise σ_{X_n} is comparable with the quantization step size q. The digital data has mean μ_X and variance

$$\sigma_{\hat{Z}}^2 = \sigma_X^2 + \sigma_Y^2 + \sigma_q^2. \qquad (30)$$

In a manner similar to the development in Section IV, define the relationship between receiver noise standard deviation and detection plus quantization noise as

$$\sigma_{X_n} = K'\sqrt{\sigma_Y^2 + \sigma_q^2}. \qquad (31)$$

The loss in sensitivity is then given by equation (26) and the dynamic range by equation (27) with the quantity K' replacing K. With this modification the curves of Figs. 4 and 5 apply to the digitized signal.

Digital integration improves the receiver sensitivity and increases the dynamic range. The mean noise spectrum estimate is improved and the precision of threshold settability increases with digital integration. However, additional bits must be maintained in the accumulation process in order to derive these benefits. Linear analog-to-digital conversion is used in order to subtract the mean noise spectrum prior to nonlinear distortion.

The digital integrated data can be written as,

$$V_{mk} = \sum^{(m+1)J} \hat{Z}_{jk} \qquad (32)$$

where J is the number of samples integrated. The mean and variance are given as

$$\mu_V = J\mu_X \qquad (33)$$

and

$$\sigma_V^2 = J\sigma_Z^2. \qquad (34)$$

The output signal-to-noise ratio SNR_V has improved linearly with the number of samples integrated J. The input sensitivity improvement through digital integration equals $\sqrt{J}$ for low-input signal-to-noise ratio SNR_i. The dynamic range and threshold sensitivity also increase by the factor $\sqrt{J}$. For example, if the quantization step equals the rms noise ($q = \sigma_{X_n}$) at $J = 1$, then at $J = 4$ there are two quantization levels per noise standard deviation.

The integrating AO channelized receiver provides a direct means for estimating the mean background spectral energy. The background signal may simply be the front end receiver noise as modified by the passband ripple or it may be the average signal environment. If 90-percent confidence is to be obtained that the measurement error in any of say 1000 channels will not exceed one-fourth the standard deviation of the noise in that channel (i.e., [Prob {measurement error $\leqslant \frac{1}{4}$ standard deviation}]^{1000} = 0.9), then the background measurement should be integrated at least 240 times longer than the signal data. The integration settings and detection algorithm are a function of the operational requirement and the spectral environment.

VI. NOISE MEASUREMENTS

The model presented in Section II was substantiated experimentally. Measurements of noise statistics, means and standard deviations, were made on several frequency channel outputs. These measurements were made parametrically on front end receiver noise level and detector integration time. A probability density analyzer was used to record probability densities and cumulative distributions of a frequency channel with signal plus noise input at several signal-to-noise ratios. Measured noise equivalent bandwidths B_s and B_n, agreed with the theory presented in Section III.

The AO channelized receiver had 500 MHz instantaneous bandwidth with 1000 channels spaced at 0.5-MHz intervals. The minimum integration period was 0.25 ms and the detector dynamic range was 33 dB. Analog-to-digital conversion had 10 bits accuracy at a sample rate of 4 MHz.

The front end gain was increased until the noise input to the receiver dominated. The mean noise level was measured for several values of $K = \sigma_{X_n}/\sigma_Y$, and for several integration times. The rms detector noise σ_Y was independent of the detector integration time T. A plot of output noise standard deviation σ_Z versus mean noise level μ_Z is shown in Fig. 6. The ratio μ_Z^2/σ_Z^2 depends linearly on the integration time T. The increase in bias required in order to achieve a constant noise variance is demonstrated. The noise equivalent bandwidth B_n was calculated to be 1.24 MHz for noise input.

Histograms of a single frequency channel output are shown in Fig. 7. The input noise level was set such that $\sigma_{X_n} = 4 \sigma_Y$. At this setting the maximum sensitivity loss due to detection noise is $\rho = 0.13$ dB. An input CW signal increased the mean output, thereby shifting the probability distribution and increasing the variance. The detector noise only distribution is included for reference. Clearly, the receiver noise dominates.

Equation (11) relating the output variance with sinusoid plus noise to the variance with noise only input can be writ-
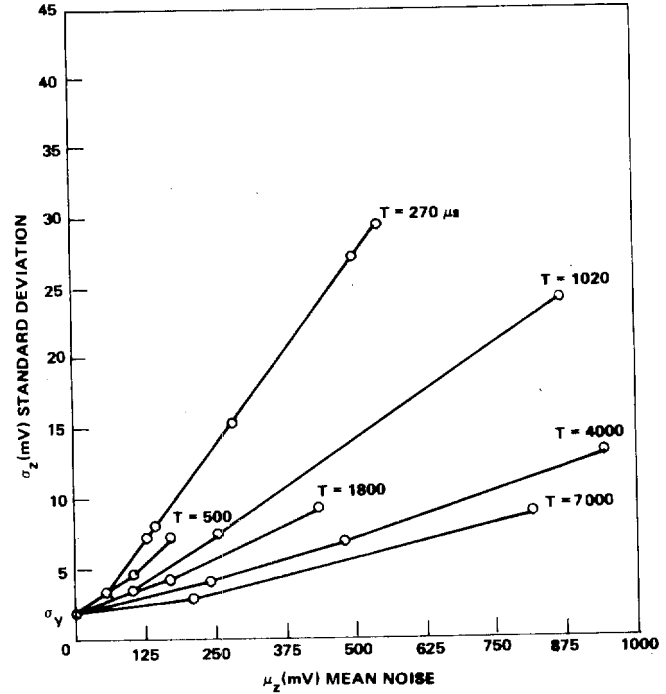

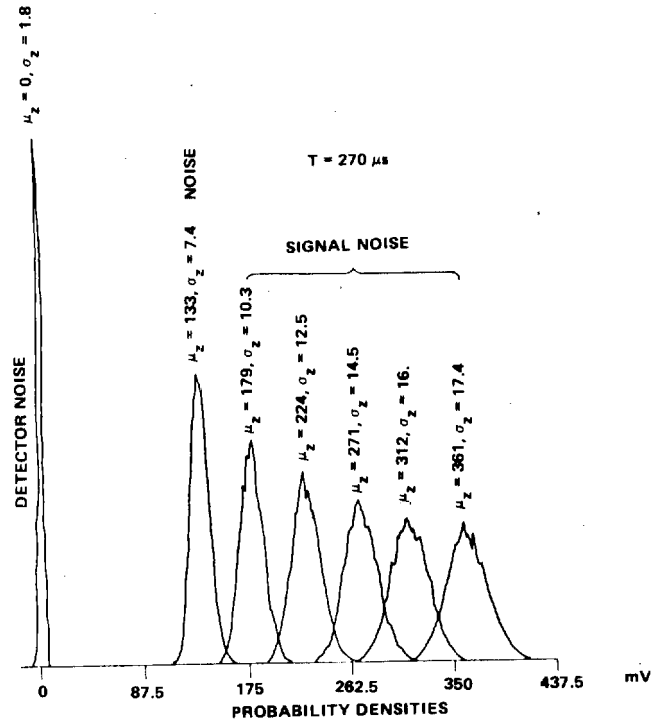Fig. 6. Standard deviation versus mean noise.

Fig. 7. Probability densities.

ten in terms of measurable quantities μ_s and μ_n as

$$\sigma_{X_{s+n}}^2 = \sigma_{X_n}^2 (1 + 2\alpha\mu_s/\mu_n) \qquad (35)$$

where

$$\alpha = \sqrt{B_n/B_s}.$$

The noise equivalent bandwidth B_s was calculated by a least squares with noise only input and over this the factor α was

1.38 and the noise equivalent bandwidth was approximately $B_s = 650$ kHz. The experimental value for B_s agrees well with calculations based on a truncated Gaussian window function and trapezoidal spectral weighting model.

The CW input sensitivity can be written as $S = \text{SNR}_Z + kTB_s + NF - \sqrt{B_s T}$. The measured sensitivity was $S = -122$ dBm for 0-dB output signal-to-noise ratio, $T = 0.25$ ms, and $NF = 5$-dB wideband front end noise figure. The measured sensitivity at $JT = 0.256$ s was $S \simeq -137$ dBm ($J = 1024$ samples averaged).

VII. CONCLUSION

The integrating AO channelized receiver has been applied to the detection of signals buried in noise. A receiver model has been developed and detection statistics were analyzed for sinusoid plus noise and random signal plus noise inputs. Signal-to-noise ratios were defined and noise equivalent bandwidths were derived in terms of input window and spectral weighting functions. The noise equivalent bandwidth was determined to be signal dependent due to spectral averaging. Detection sensitivity and dynamic range were calculated as a function of processing gain and receiver noise loading. Digital processing of channelized receiver data may be used to achieve further sensitivity improvement and increased dynamic range. Linearity and gain stability become increasingly important for large processing gain. Experimental results are in agreement with the statistical model presented. An AO channelized receiver with high sensitivity and wide instantaneous bandwidth has been demonstrated.

APPENDIX A
OUTLINE FOR DERIVATION OF NOISE STATISTICS

A.1 Mean Noise Power

The output variable X_{jk} defined by (1) can be rewritten as

$$X_{jk} = \int_{jT}^{(j+1)T} \iiint_{-\infty}^{\infty} H(f - f_k)w(\alpha)w^*(\beta)u(t - \alpha)u(t - \beta)$$
$$\cdot \exp[-i2\pi f(\alpha - \beta)]\, d\alpha\, d\beta\, df\, dt. \quad (36)$$

For noise only input, i.e., $u(t) = n(t)$, the mean output becomes

$$\mu_n = E\{X_{jk}\}$$
$$= \int_{jT}^{(j+1)T} \iiint_{-\infty}^{\infty} H(f - f_k)w(\alpha)w^*(\beta)R_n(\alpha - \beta)$$
$$\cdot \exp[-i2\pi f(\alpha - \beta)\, d\alpha\, d\beta\, df\, dt. \quad (37)$$

For zero-mean white Gaussian noise with autocorrelation $R_n(\tau) = (N_0/2)\delta(\tau)$ the mean output reduces to

$$\mu_n = \frac{N_0 T}{2} \int_{-\infty}^{\infty} |w(\alpha)|^2\, d\alpha \int_{-\infty}^{\infty} H(f)\, df. \quad (38)$$

Equation (38) is equivalent to (5) through use of Parseval's theorem,

$$\int_{-\infty}^{\infty} G(f)\, df = \int_{-\infty}^{\infty} |w(\alpha)|^2\, d\alpha$$

where $G(f)$ is the magnitude squared of the Fourier transformed window function defined by (6).

A.2 Mean Signal Power

For sinusoid input, $u(t) = A \cos[2\pi f_0 t + \phi]$, the output is (using (36))

$$X_{jk} = \frac{A^2}{2} \int_{jT}^{(j+1)T} \iiint_{-\infty}^{\infty} H(f - f_k)w(\alpha)w^*(\beta)$$
$$\cdot \{\cos[2\pi f_0(\alpha - \beta)] + \cos[4\pi f_0 t - 2\pi f_0(\alpha + \beta) + 2\phi]\}$$
$$\cdot \exp[-i2\pi f(\alpha - \beta)]\, d\alpha\, d\beta\, df\, dt. \quad (39)$$

Integrating with respect to t, the output becomes

$$X_{jk} \simeq \frac{A^2 T}{4} \iiint_{-\infty}^{\infty} H(f - f_k)w(\alpha)w^*(\beta)$$
$$\cdot \{\exp[-i2\pi(f + f_0)(\alpha - \beta)]$$
$$+ \exp[-i2\pi(f - f_0)(\alpha - \beta)]\}\, d\alpha\, d\beta\, df \quad (40)$$

where the term with frequency $2f_0$ has approximately integrated to zero. Integrating $d\alpha d\beta$ and using (6) yields

$$X_{jk} \simeq \frac{A^2 T}{4} \int_{-\infty}^{\infty} H(f - f_k)[G(f + f_0) + G(f - f_0)]\, df$$
$$\simeq \frac{A^2 T}{4} [\mathcal{H}(f_k - f_0) + \mathcal{H}(f_k + f_0)] \quad (41)$$

where $\mathcal{H}(\cdot)$ is defined by (10). For $f_k \approx f_0$ the term $\mathcal{H}(f_k + f_0)$ is vanishingly small. The mean signal power

$$\mu_s = E\{X_{jk}\} = X_{jk}$$

for deterministic sinusoidal input, resulting in (9).

A.3 Output Variance for Noise Only Input

The variance of the output variable X_{jk} can be calculated as

$$\text{var}\{X_{jk}\} = E\{X_{jk}^2\} - [E\{X_{jk}\}]^2. \quad (42)$$

For noise only input, the mean-square output equals

$$E\{X_{jk}^2\} = \iint_{jT}^{(j+1)T} \iiiint_{-\infty}^{\infty}$$
$$\cdot H(f - f_k)H(f' - f_k)w(\alpha)w^*(\alpha')w(\beta)w^*(\beta')$$
$$\cdot E\{n(t - \alpha)n(t' - \alpha')n(t - \beta)n(t' - \beta')\}$$
$$\cdot \exp[-i2\pi f(\alpha - \beta)] \exp[-i2\pi f'(\alpha' - \beta')]$$
$$\cdot d\alpha\, d\alpha'\, d\beta\, d\beta'\, df\, df'\, dt\, dt'. \quad (43)$$

Using the relation for the fourth moment of a jointly Gaussian random process,

$$E\{n(t_1)n(t_2)n(t_3)n(t_4)\} = E\{n(t_1)n(t_2)\}\, E\{n(t_3)n(t_4)\}$$
$$+ E\{n(t_1)n(t_3)\}\, E\{n(t_2)n(t_4)\}$$
$$+ E\{n(t_1)n(t_4)\}\, E\{n(t_2)n(t_3)\}$$

and substituting the noise autocorrelation function, the mean-

square output becomes

$$E\{X_{jk}^2\} = \left(\frac{N_0}{2}\right)^2 \int_{jT}^{(j+1)T} \int_{-\infty}^{\infty} \cdots \int H(f - f_k)H(f' - f_k)$$

$$\cdot w(\alpha)w^*(\alpha')w(\beta)w^*(\beta') \cdot [\delta(\alpha - \beta)\delta(\alpha' - \beta')$$

$$+ \delta(t - t' + \alpha' - \alpha)\delta(t - t' + \beta' - \beta)$$

$$+ \delta(t - t' + \alpha' - \beta)\delta(t - t' + \beta' - \alpha)]$$

$$\cdot \exp[-i2\pi f(\alpha - \beta)] \exp[-i2\pi f'(\alpha' - \beta')]$$

$$\cdot d\alpha \, d\alpha' \, d\beta \, d\beta' \, df \, df' \, dt \, dt'. \quad (44)$$

Integrating the term $\delta(\alpha - \beta)\delta(\alpha' - \beta')$ yields the mean noise power, μ_n^2. Subtracting the mean noise power and using the result

$$\int_{jT}^{(j+1)T} \int f(t - t') \, dt \, dt' = T \int_{-T}^{T} (1 - |\tau|/T)f(\tau) \, d\tau \quad (45)$$

the variance can be written as

$$\text{var}\{X_{jk}\} = \left(\frac{N_0}{2}\right)^2 T \int_{-T}^{T} \int_{-\infty}^{\infty} \cdots \int H(f - f_k)H(f' - f_k)$$

$$\cdot w(\alpha)w^*(\alpha')w(\beta)w^*(\beta')(1 - |\tau|/T)$$

$$\cdot [\delta(\tau + \alpha' - \alpha)\delta(\tau + \beta' - \beta)$$

$$+ \delta(\tau + \alpha' - \beta)\delta(\tau + \beta' - \alpha)] \exp[-i2\pi f(\alpha - \beta)]$$

$$\cdot \exp[-i2\pi f'(\alpha' - \beta')] \, d\alpha \, d\alpha' \, d\beta \, d\beta' \, df \, df' \, d\tau.$$

$$(46)$$

The term $(1 - |\tau|/T)$ may be approximated by unity for T large with respect to the width of $w(\cdot)$. Define the autocorrelation of the input window function as

$$R_w(\tau) = \int_{-\infty}^{\infty} w(t)w^*(t - \tau) \, dt \quad (47)$$

and the Fourier transform of the spectral weighting function as

$$h(t) = \int_{-\infty}^{\infty} H(f) \exp(-i2\pi ft) \, df. \quad (48)$$

Performing the integration results in

$$\text{var}\{X_{jk}\} \simeq \left(\frac{N_0}{2}\right)^2 T \int_{-\infty}^{\infty} |h(\tau)R_w(\tau)|^2 \, d\tau \quad (49)$$

where the autocorrelation function (47) is approximated by a finite time estimate, and the function $\mathcal{H}(\cdot)$ vanishes for large argument. The variance for noise only input described by (49) is equivalent to (12) by Parseval's theorem.

A.4 Output Variance for Sinusoid Plus Noise Input

For the case of sinusoid plus noise input

$$u(t) = s(t) + n(t)$$

where

$$s(t) = A \cos[2\pi f_0 t + \phi]$$

the mean-square output equals

$$E\{X_{jk}^2\} = \int_{jT}^{(j+1)T} \int_{-\infty}^{\infty} \cdots \int H(f - f_k)H(f' - f_k)$$

$$\cdot w(\alpha)w^*(\alpha')w(\beta)w^*(\beta') \cdot E\{[s(t - \alpha)s(t - \beta)$$

$$+ n(t - \alpha)n(t - \beta) + s(t - \alpha)n(t - \beta)$$

$$+ s(t - \beta)n(t - \alpha)] \cdot [s(t' - \alpha')s(t' - \beta')$$

$$+ n(t' - \alpha')n(t' - \beta') + s(t' - \alpha')n(t' - \beta')$$

$$+ s(t' - \beta')n(t' - \alpha')]\} \exp[-i2\pi f(\alpha - \beta)]$$

$$\cdot \exp[-i2\pi f'(\alpha' - \beta')] \, d\alpha \, d\alpha' \, d\beta \, d\beta' \, df \, df' \, dt \, dt'.$$

$$(50)$$

The expectation $E\{\cdot\}$ is comprised of 16 terms. By inspection 8 terms vanish since the noise has zero mean and has zero third moment. The terms $s(\cdot)s(\cdot)s(\cdot)s(\cdot)$ and $n(\cdot)n(\cdot)n(\cdot)n(\cdot)$ become μ_s^2 and $\mu_n^2 + \sigma_{X_n}^2$, respectively. The terms $s(t - \alpha)s(t - \beta)n(t' - \alpha')n(t' - \beta')$ and $s(t' - \alpha')s(t' - \beta')n(t -\alpha)n(t - \beta)$ are both equal to $\mu_s\mu_n$. The terms $s(t -\alpha)s(t' - \alpha')n(t - \beta)n(t' - \beta')$ and $s(t - \beta)s(t' - \beta')n(t - \alpha)n(t' - \alpha')$ are both equal to $(A^2 N_0 T/4)\mathcal{H}(f_k - f_0)\mathcal{H}(f_k + f_0)$ which is approximately zero for $f_k \approx f_0$. The final two terms $s(t - \alpha)s(t' - \beta')n(t' - \alpha')n(t - \beta)$ and $s(t' - \alpha')s(t - \beta)n(t - \alpha)n(t' - \beta')$ are both equal to $(A^2 N_0 T/8)[\mathcal{H}^2(f_k - f_0) + \mathcal{H}^2(f_k + f_0)]$. The term $\mathcal{H}^2(f_k + f_0)$ may be dropped for $f_k \approx f_0$. Combining terms, the mean square output is

$$E\{X_{jk}^2\} \approx \sigma_{X_n}^2 + (\mu_s + \mu_n)^2 + \frac{A^2 N_0 T}{4} \mathcal{H}^2(f_k - f_0) \quad (51)$$

and the output variance is given by

$$\sigma_{X_{s+n}}^2 \approx \sigma_{X_n}^2 \left[1 + \frac{A^2 N_0 T}{4\sigma_{X_n}^2} \mathcal{H}^2(f_k - f_0)\right]. \quad (52)$$

The variance can be rewritten as

$$\sigma_{X_{s+n}}^2 \approx \sigma_{X_n}^2 \left[1 + \frac{A^2}{B_s N_0}\right] \quad (53)$$

where the noise equivalent bandwidth B_s is defined by (13) and $f_k = f_0$. The output variance (53) is equivalent to (11) with the input signal-to-noise ratio SNR_i measured in a bandwidth B_s.

APPENDIX B
SHOT NOISE CONSIDERATION

Shot noise results from the photon statistics of the average optical power and is, therefore, signal dependent. The relative importance of shot versus thermal noise depends on the number of thermal noise electrons. The variance of the shot process equals the average number of electrons. Therefore, the expected variance equals $\mu_s + \mu_n$ (measured in electrons). For noise only input ($\mu_s = 0$), the ratio of detector noise variance σ_Y^2 to receiver noise variance $\sigma_{X_n}^2$ is given by

$$\left(\frac{\sigma_Y}{\sigma_{X_n}}\right)^2 = \frac{\sigma_{\text{shot}}^2 + \sigma_{\text{th}}^2}{\sigma_{X_n}^2} = \frac{\mu_n}{\sigma_{X_n}^2} + \frac{\sigma_{\text{th}}^2}{\sigma_{X_n}^2} = \frac{\sqrt{B_n T}}{\sigma_{X_n}} + \left(\frac{\sigma_{\text{th}}}{\sigma_{X_n}}\right)^2$$

where σ_{shot}^2 and σ_{th}^2 are the shot and thermal noise variances, respectively, and all quantities are measured in electrons.

If the ratio of receiver noise to thermal noise is set equal to K, then

$$\left(\frac{\sigma_Y}{\sigma_{X_n}}\right)^2 = \frac{\sqrt{B_n T}}{K\sigma_{th}} + \frac{1}{K^2}.$$

For example, using $B_n T = 1000$ and $K = 1$, the shot and thermal components are equal for $\sigma_{th} = \sqrt{B_n T} \simeq 32$ electrons rms. The shot noise becomes less significant with signal plus noise input since the random contribution of shot noise due to the mean signal power μ_s is less than the increase in output variance due to the signal, see (11).

REFERENCES

[1] T. M. Turpin, "Spectral analysis using optical processing," this issue, pp. 79–92.
[2] A. D. Whalen, *Detection of Signals in Noise.* New York: Academic Press, 1971.
[3] J. D. Kraus, *Radio Astronomy.* New York: McGraw-Hill, 1966.
[4] A. V. Oppenheim and R. W. Schafer, *Digital Signal Processing.* Englewood Cliffs, NJ: Prentice-Hall, 1975, pp. 413–418.

Photodetectors for Acousto-Optic Signal Processors

GERALD M. BORSUK, SENIOR MEMBER, IEEE

Invited Paper

Abstract—A description of devices, architecture, and performance criteria is presented for solid-state CCD and photodiode sensors useful in acousto-optic processing systems. Special attention is given to sensors used in both bulk and integrated optical acousto-optic instantaneous Fourier transform systems. The device physics of silicon photodetectors is presented in detail including discussion and analysis of quantum efficiency, responsivity, crosstalk, charge handling capacity, data rate, optical to electrical transfer function, noise sources, dynamic range, and sensitivity. A description of new technologies, such as VHSIC and GaAs IC's which are applicable to sensor technology for AO signal processing systems is also presented.

I. INTRODUCTION

PHOTODETECTORS for acousto-optic (AO) signal processing have unique requirements which until recently have not been addressed by the image detection community. This has been the case because the performance of AO signal processors has been limited by the optical apparatus rather than by the photodetector. This situation is no longer the case and has spurred on new development of photodetectors specifically for acousto-optical signal processing.

Although the architecture may vary depending upon the AO signal processing function, the common ingredients in these systems are an optical source, a light modulator(s), Fourier
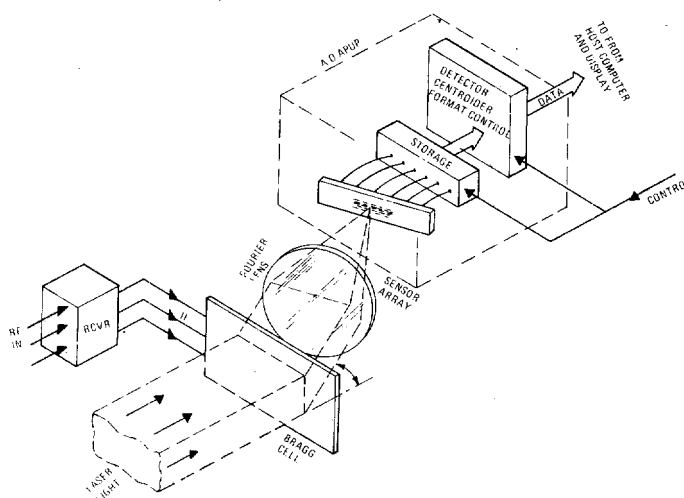
Fig. 1. A block diagram of a representative AO signal processing system.

transform optics, and a photodetector(s). The optical source is usually a GaAs laser diode or visible emitting gas laser although noncoherent sources, such as light-emitting diodes (LED's), are sometimes used. The light modulator consists of one or more AO Bragg devices. The photodetector is usually a silicon photodiode or charge-coupled device (CCD) array. Fig. 1 shows these components in typical AO system architecture.

The performance criteria for photodetectors for AO signal processing systems are different than for scene imaging applications. Specifically, broad-band spectral response is less important than uniform quantum efficiency at a specific wavelength. Other key differences between imaging and signal processing photodetectors are dynamic range, and data rate. The dynamic range of a typical visible scene in daylight is usually no greater than 25–30 dB (i.e., three orders of magnitude in light intensity) [1]. AO signal processors which use noncoherent detection (i.e., optical energy detection, optical phase and amplitude lost) may analyze electrical input signals over a 50-dB range. This range corresponds to an electrical signal output dynamic range of the photodetector of 100 dB due to the square-law relationship between incident light power and sensor output electrical power developed across a load resistor. AO signal processors which utilize coherent detection (i.e., optical amplitude and phase preserved) exhibit a linear transfer function between the input electrical signal and the resulting electrical output from the detector. Therefore an input voltage dynamic range of 50 dB corresponds to the same voltage range at the output of the detector.

The bandwidth requirements of photodetector arrays for AO signal processing are also different than those of typical scene imaging devices. A major application of AO processors is in the Fourier transformation of signals from the time domain into the frequency domain [2]. The time necessary to display the complete transform at the image plane is directly related to the AO aperture. State-of-the-art AO systems can produce a complete Fourier transform of 400–500 points approximately every microsecond. Thus the photodetector array for AO spectrum analysis systems must be capable of reading out every detector element within a microsecond or it will degrade the performance of the processor. A 500-pel photodetector accessing all elements sequentially every microsecond requires an output sample data rate of 500 MHz which is not consistent with the performance or requirements of scene imaging devices. Their access (or integration) times per pel usually range from 1 to 100 ms (without cooling) [3]. Conversely, other forms of AO signal processing, such as radiometric spectrum analysis [4], and time integrating correlator systems [5], benefit from photodetectors which are capable of long integration times. The requirement for new photodetectors has thus been brought about by the advancement in the state-of-the-art of AO processing.

II. SYSTEM CONSIDERATIONS

The photodetector is but one part of AO signal processors. In general, the AO processor can be analyzed simply as a black box in which input electrical signals are operated upon by a specific transform (see for example, [6]) yielding an electrical output. Signal processing functions, such as convolution and correlation, can be readily implemented using AO techniques. One of the most important and useful transforms performed using AO systems is the instantaneous Fourier transform. It can be implemented both in one and two spatial dimensions to perform the transformation of time-domain signals into the frequency domain. This AO implementation is considered here for two specific cases: total power radiometry, and narrow-pulse spectrum analysis.

The AO total power radiometer is a spectrum analyzer which performs as a bank of filters with each filter having its signal integrated by the pels of the photodetector. The Fourier analysis is thus a spatial domain transform while the power in each Fourier component is integrated in the time domain by the detector. The output signal-to-noise ratio (SNR) can be written as

$$\left(\frac{S}{N}\right)_{\text{out}} = \left(\frac{S}{N}\right)_{\text{RF}}^2 \left(\frac{S}{N}\right)_{\text{optics}} \sqrt{B\tau} \left(\frac{S}{N}\right)_{\text{Det}} \qquad (1)$$

where $\sqrt{B\tau}$ is the noncoherent correlation gain. The term B is the bandwidth of one filter of the bank while τ is the integration (or exposure) time. Two detector criteria are required to operate the system [7]

$$(R_{D_\lambda} \Phi\tau)\sqrt{B\tau} < Q_T \qquad (2)$$

and

$$[\overline{Q_T^2} \, (\text{NES})]^{1/2} \ll (R_{D_\lambda} \Phi\tau) \qquad (3)$$

where R_{D_λ} is the responsivity, Φ is the irradiance, τ is the detector integration time, Q_T is the total charge handling capacity of a pel, and $[\overline{Q_T^2} \, (\text{NES})]^{1/2}$ is the rms number of equivalent noise electrons at the input (these terms are explained in detail in Section IV.) In this mode of operation the effective processing gain $\sqrt{B\tau}$ is limited by the dynamic range of the detector

$$\sqrt{B\tau} \leqslant \frac{Q_T}{[\overline{Q_T^2}(\text{NES})]^{1/2}} \qquad (4)$$

Therefore, the lower the inherent noise of the detector, the larger the possible processing gain. (Noncoherent integration post processing can also be used to further increase the processing gain.)

The spectrum analysis of narrow pulsed signal is an important application of AO technology. The most important aspects of this technique are the measurement of time of arrival of signals being analyzed and their duration. These parameters are interrelated to the bandwidth of the sensor processor and the Nyquist theorem, since the method for readout of all solid-state sensor arrays for AO signal processing involve sampled data. Consider, for example, the three critical time parameters associated with AO spectrum analyzer performance. They are the exposure time, the pulse duration of signals to be analyzed, and the effective acoustic transit time of the signals in the Bragg device. The access (or exposure) time is the time period corresponding to one pel sample (although, the electrical data rate from the sensor may be reduced in frequency without loss of information by parallel processing as in the case of the line array detectors described in Section III.) The access time of the photosensor determines the precision with which the time of arrival and duration of any signal can be measured. Independently, the relationship between the acoustic transit time and the actual duration of the signal determine the precision with which the frequency of the pulse can be measured. The uncertainty in time of arrival of a signal or its duration is then just the access time of the sensor. If the signal's pulse duration is much less than the acoustic transit time the defracted optical signal will be spread across the array. It is then possible that no pel will have sufficient signal to noise ratio to indicate detection.

III. CATEGORIES OF DEVICES

There exist three generic types of photodetectors for AO signal processing: two-dimensional vacuum tube sensors; two-dimensional solid-state sensors; and one-dimensional solid-state sensors. Vacuum tube sensors, such as intensified vidicons,
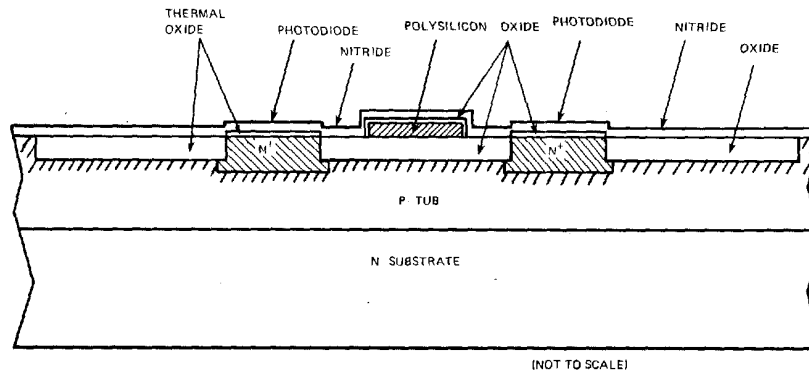
Fig. 2. A cross section of the 5050 silicon photodetector fabricated for
use with integrated optical and bulk AO real-time spectrum analyzers.

can exhibit near single photon shot noise performance. How-
ever, the poor geometric accuracy of the raster readout re-
quires scan correction by a separate processor to fully utilize
the optical processing capability of large time-bandwidth
systems. One technique for performing this scan correction
in coherent optical signal processors uses a precision diffrac-
tion grating as an optical reference in conjunction with a digital
computer and memory [8]. Other forms of vacuum tube
sensors combine solid state arrays in electron-beam semicon-
ductor (EBS) configuration [9]. These devices are capable of
achieving single-photon shot-noise limited performance. Such
devices and other vacuum tube sensors will not be treated in
more detail here. Solid-state sensors are emphasized because
of their inherently smaller size, longer life, and lower operating
voltages.

Two-dimensional solid-state sensors used for optical signal
processing are either CCD or charge-inspection device (CID)
area imagers. These devices do not suffer from geometric
distortion since the readout mechanism is colocated with the
sensing element in a planar structure. The two basic types of
CCD area imagers are the line transfer device and the frame
transfer device. Either of these types can be operated in time
delay and integrate mode. The CID is a unique device capable
of an ordered sequential pel readout or a random addressing of
pels. A review of the operation of these devices is presented in
[10] while [11] presents the recent state-of-the-art. The major
limitations of these solid-state devices for use in AO signal pro-
cessing is the limited number of pels ($\sim 10^5$ pels) [12], the long
access time to an individual pel, ($\geqslant 1$ ms for a large array) and
the low dynamic range (typically 20–30 dB). Recent work
aimed at improving the device yield and quantum efficiency of
large frame transfer imagers has resulted in a device which uses
a virtual phase clocking [13]. The device has a simpler gate
construction than other types of area CCD arrays and a larger
effective collection area per pel.

The two basic categories of linear array photodetectors
useful for AO signal processing are the photodiode and the
metal-oxide-semiconductor (MOS) depletion mode sensor.
The mechanisms for accessing photodiode line arrays are
either self-scanned MOS shift registers, random address MOS
switches, or CCD parallel-in/serial-out shift registers. MOS
depletion mode sensors are usually coupled directly to CCD
shift registers by direct charge injection.

An example of a commercially available randomly address-
able photodiode linear array is the Reticon CP1006 device
[14]. The device consists of two interdigitated rows of 256
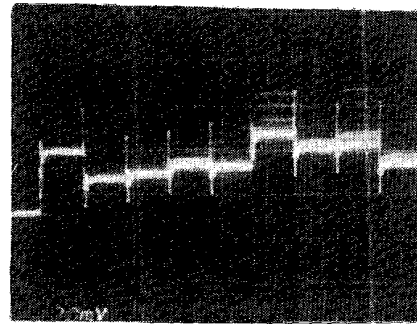
Fig. 3. Signal output from the integrated optical real-time spectrum
analyzer when two simultaneous RF pulses are applied to its input.

photodiodes with a pitch of 50 μm (so called 2P configura-
tion). Its dynamic range is 20 dB for noncoherent detection
processors. The array can be sequentially scanned or any pel
can be read at the strobe rate of 1 MHz [15]. The device
has been used in bulk AO RF spectrum surveillance and identifi-
cation systems [16]. The random access feature enables pre-
determined frequency slots to be addressed without the time
delay of sequentially scanning all pels. An example of a com-
mercially available photodiode array with CCD PI/SO shift
registers is the Reticon CP1023 device [17]. The device
has 256 pels on an 18-μm pitch. The device has four indepen-
dent outputs of 64 pels each, capable of a 6-MHz data rate
(10.6-μs access time). Its specified dynamic range is 30 dB
for noncoherent detection systems.

A self-scanned photodiode line array specifically designed
for use with integrated and bulk optical real time spectrum
analyzers has been built and tested both separately [18],
[19] and as an integral part of a working integrated optical
spectrum analyzer [20]. The sensor has 140 pels on a 12-μm
pitch, ϕP architecture (pels side by side) and a single photo-
diode for zeroth-order beam dumping. The array is composed
of seven groups of 20 pels each. Each group is addressed in
parallel by a ten-stage dynamic PMOS shift register. Each
group has two electrometer output circuits. One circuit out-
puts odd pels while the other circuit outputs even pels during
each clock cycle. Using this scheme, fourteen parallel samples
are available every clock cycle. The device operates at a clock
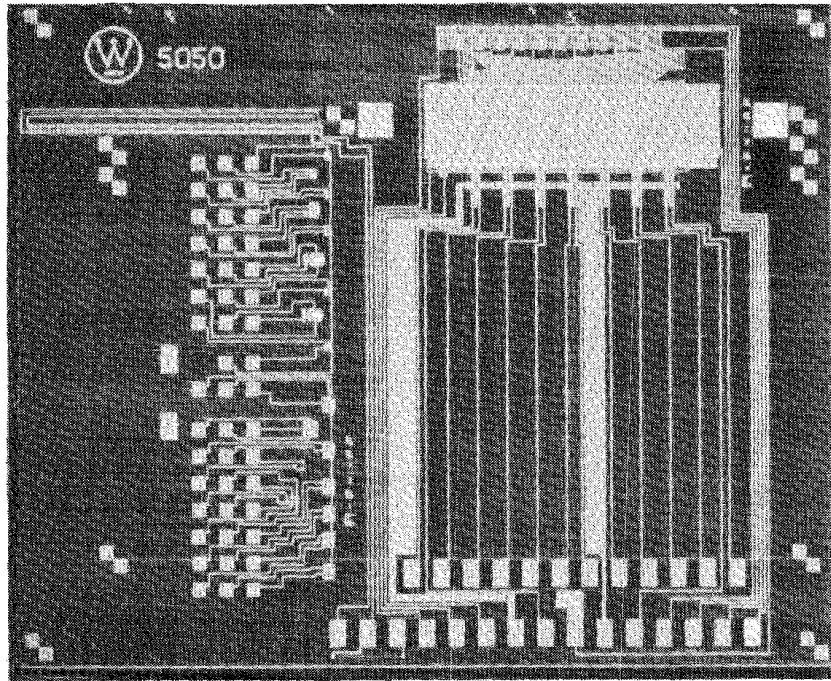
Fig. 4. Photomicrograph of the 5050 silicon photodetector designed
specifically for AO spectrum analyzers.

rate of 5 MHz resulting in an access (or integration) time of 2 μs. Large charge handling capacity is achieved by having large parasitic and photodiode junction capacitance. The measured dynamic range of the device is 41 dB for 2-μs access time. The pel to pel electrical crosstalk is limited by isolating the N+ photodiode elements in a boron tub made by ion implantation (a tub is a region of opposite carrier concentration to that of the substrate material in which device structures are fabricated.) Holdover crosstalk is reduced by using a common source reset switch. A cross section of the device is shown in Fig. 2. The tub junction is 6 μm deep. This type of tub structure limits crosstalk by cutting off the diffusion of both deeply absorbed photons and thermally generated carriers, at the expense of reduced quantum efficiency. An oscillograph of the output of the detector when two simultaneous RF pulses of 1.0-μs pulse duration, 4.17-kHz repetition rate, and 680- and 700-MHz frequencies are applied to the integrated optical spectrum analyzer is shown in Fig. 3 [21]. A photomicrograph of the sensor is shown in Fig. 4.

A MOS depletion mode linear array photodetector which is accessed by PI/SO CCD shift registers has been described [22]. The device is intended for use with an integrated optical spectrum analyzer. It consists of four groups of 25 pels on a pitch of 8-μm with a 2P architecture. It is designed to be readout in four parallel channels, each channel addressing 25 pels or in two parallel channels each channel addressing 50 pels.

IV. Device Physics

The fundamental process in a photodetector is the generation of free charge carriers by a direct or indirect band-gap transition due to absorption of photons in a semiconductor material. The three classes of photodetectors are photoconductors, depletion-layer devices, and avalanche photodiodes. For the purpose of line or area photodetector arrays for AO signal processing, only depletion-layer devices fabricated using

silicon integrated circuit technology have been developed extensively (although a GaAs photodiode line array for AO has been made [23] and is discussed in Section VI-B.) These devices form their photocharge collecting depletion regions either by reverse biased p-n junctions or by electric fields (i.e., CCD's). Excellent review papers and books exist in the literature describing the device physics of these photodetectors [10], [24]. Therefore, only those physical processes that are of critical importance for AO signal processing photodetectors are presented here in detail. They include quantum efficiency, responsivity, crosstalk, charge handling capacity, data rate, optical to electrical transfer function, noise sources, dynamic range, and sensitivity. As an example, a generalized expression which shows how these various sensor parameters interrelate to optical parameters has been derived for an AO space-integrating spectrum analyzer [4] and is given here in detail

$$Q_T \;=\; \underset{\substack{\uparrow \\ \text{Charge} \\ \text{Capacity}}}{[R_{D\lambda}]} \; \underset{\substack{\text{deflected} \\ \text{optical} \\ \text{power density}}}{\left[\frac{\delta P_s P_0 \gamma}{(\pi HP/4)\Delta f}\right]} \; \underset{\text{exposure time}}{[\tau_e]} \; \underset{\substack{\text{transfer} \\ \text{function}}}{[M_D]}$$

$$=\; \underset{\substack{\text{dynamic} \\ \text{range}}}{\left[\frac{Q_T}{\overline{Q}_T(\text{NES})}\right]} \; \underset{\text{sensitivity}}{\overline{Q}_T(\text{NES})}. \tag{5}$$

This expression describes the parameters associated with a given pel of the sensor. The term δ is the efficiency of the optoelectric interaction expressed as the fraction of light deflected per applied watt per instantaneous system bandwidth, Δf. P_s

is the RF signal power of a single tone applied to the AO device which is required to cause saturation of a given pel. P_0 is the power of the optical source. The term γ is the transmission loss in the optics including that due to optical apodization. The term $(\pi HP/4)$ is the area of a resolvable spot where H is the height of the pel element and P is its pitch. This term implicitly includes the optical modulation transfer function (MTF) of the system. The criteria for choosing H and P for a specified optical resolution are considered in Section V-A for bulk systems and V-B for integrated optical systems. The term M_D is the product of the modulus of the electrical transfer function and the sensor MTF. The electrical transfer function is a measure of the fidelity of the sensor's signal processor readout with respect to frequency (data rate), amplitude, and phase of the sampled data. The combined MTF is a measure of the sensor electrical crosstalk performance and its optical-to-electrical transfer characteristic.

A. Quantum Efficiency

Quantum efficiency is defined as the number of signal carriers collected by the detector divided by the number of photons that have impinged upon the detector. The factors which influence quantum efficiency are the optical transmission of the insulating layers that cover the detectors, junction depths for photodiode arrays, depletion layer thicknesses, bulk lifetime, surface recombination velocity, optical absorption coefficient, and pel-to-pel isolation techniques. The absolute quantum efficiency of a detector is determined by the collection efficiency of the individual regions of the semiconductor that make up the device multiplied by the transmission efficiency of the external optical layers and isolation techniques. A representative cross section of a silicon photodiode sensor array for AO signal processing is shown in Fig. 2 for example.

The first semiconductor region is an N+ layer. In this region, several mechanisms contribute to quantum efficiency. Surface recombination of minority carriers, characterized by the surface recombination velocity, causes a loss in efficiency since carriers created by absorption of photons at or very near the surface can be lost by hole–electron recombination. This loss is important for short wavelength photons which have a high absorption coefficient. Similarly, recombination in the bulk volume of the N+ layer causes loss of carriers. Bulk recombination loss is characterized by the minority carrier lifetime [25]. However, in the N+ region a gradient of ionized donar atoms gives rise to an electric field that aids in separating electron-hole pairs once created. The second region is the depletion layer which spreads from the N+ junction into the P-type layer. Carriers created within this region experience a high electric field and are almost immediately collected. The carriers in the undepleted P tub experience no built-in electric field if this region is considered to be of uniform doping. Only diffusion and recombination affect quantum efficiency in this region. The thickness of this layer is important because it limits pel-to-pel electrical crosstalk. Photons which are absorbed below the tub-substrate junction are not collected by any photodiode and therefore cannot contribute to crosstalk. However, the price paid for this crosstalk improvement is a loss in quantum efficiency. The equations which describe the quantum efficiency in these three regions are quite complex. Gary [26] and more recently Van de Wiele [27] describe both numerical and simplified analytical expressions for the quantum efficiency in these regions.

The quantum efficiency of the photodetector is also in-

fluenced by the technique used to isolate or define pels. In the example shown in Fig. 2, adjacent pel isolation is provided by the potential maximum formed between N+ diffusions. In this example, all photons absorbed between pels are collected. However, two other techniques are possible. The first is a heavily doped channel stop diffusion or ion implant. This type of diffusion is necessary in MOS-CCD type structures to define pel elements but results in substantial recombination of absorbed photogenerated charge in this region. Another technique is to isolate pels by the preferential etching of narrow grooves in $\langle 110 \rangle$ silicon [28]. This technique also results in an effective decrease in quantum efficiency since photons which impinge in the area of the grooves are not collected. The degradation in quantum efficiency for both cases sited above can be described by a factor n_{ISO}, which is simply the ratio of photoactive device area to total pel area.

The loss of efficiency due to optical reflection and absorption in the insulating layers covering the active region of photodiodes can be minimized by choosing their thickness to be $(\frac{1}{4})$ λ and requiring their refractive index to be the square-root value of the bulk semiconductor. The refractive index of silicon at optical wavelengths is 3.4 while that of Si_3N_4, a commonly deposited dielectric layer, is 1.9. Therefore, silicon nitride is a reasonable material to use for antireflection coating of silicon sensors. In practice, however, silicon nitride is never placed directly on silicon because of surface passivation problems. Usually a 100 Å layer of thermal oxide is grown before a silicon nitride deposition. To avoid spurious optical reflections, the surface of the photodetector active region should also be made planar. This is particularly important if the sensor is to be used as a coherent detector.

A total quantum efficiency which combines all the effects above can be expressed as

$$n = (n_{ISO}\, n_{REF})(n_{N+} + n_{Dep} + n_r). \tag{6}$$

Consider, for example, the following key silicon photodiode device parameters

X_j 18 μm—tub-substrate junction depth;
S 5 cm/s—surface recombination velocity;
α 600 cm^{-1} @ 8500 Å absorption coefficient or
3800 cm^{-1} @ 6328 Å absorption coefficient.

Sensors with these parameters can have a total quantum efficiency of 0.48 for λ = 8500 Å light and 0.82 for λ = 6328 Å. The lower quantum efficiency for longer wavelength light is due to a large fraction of photons being absorbed below the tub substrate junction.

The quantum efficiency of a MOS-CCD can be determined using the terms in (6) but noting that there exists no junction so n_{N+} is equal to zero. The quantum efficiency of CCD's is in general lower than for photodiodes due to the lower transmissivity of the gate material covering the depletion collection area. Polysilicon is usually used as the transparent gate although tin oxide is sometimes used and is of higher transmissivity [29].

B. Responsivity

Silicon photodiodes and CCD's have a narrow-band response in the near infrared and visible region of the optical spectrum given by the relationship

$$R_\lambda = \frac{qn}{h\nu} \tag{7}$$

where h is Planck's constant, ν is the optical frequency, q is the electronic charge and n is the total quantum efficiency. The units of spectral response are amperes per watt or current density per irradiance input. The detector responsivity at a specific wavelength is given by the relationship

$$R_{D_\gamma} = A R_\lambda = \frac{A q n}{h\nu} \qquad (8)$$

where A is the active area of a pel. The units of responsivity are charge per exposure input or coulombs per microjoule per square meter. As an example, consider the pel elements of a detector to be 12 μm $\times$ 20 μm and n to be 0.5 at $\lambda = 8500$ Å and 0.80 at 6328 Å. The responsivity is

$$R_{D_\lambda} = 8.2 \times 10^{-17} \text{ coulombs}/\mu J/m^2 \Rightarrow 513 \; e^-/\mu J/m^2$$

at 8500 Å and

$$R_{D_\lambda} = 9.8 \times 10^{-17} \text{ coulombs}/\mu J/m^2 \Rightarrow 610 \; e^-/\mu J/m^2$$

at 6328 Å.

C. Crosstalk Between Pels

An important consideration in the use of photodetectors for AO signal processing is the relationship between the sensor resolution and the resolution of the optical system. The key physical property of the semiconductor which determines to what extent photons incident upon a given pel contribute to signal charge within that pel or adjacent pels is the absorption coefficient. Fig. 5 shows the measured intrinsic absorption coefficient for silicon and germanium as a function of wavelength [30]. Also shown are the emission wavelength of some laser sources used for AO signal processing. The photon flux density $\Phi(x)$ as a function of the depth into the semiconductor is given by an exponential function

$$\Phi(x) = \Phi(0) \, e^{-\alpha x}. \qquad (9)$$

A large value of α means that most of the impinging photons will be absorbed near the surface of the semiconductor. Small values of α means that most will be absorbed deeper in the bulk.

Photon generated charge that are absorbed in the bulk silicon beyond the depth of the diode junction and its associated depletion layer must diffuse to the depletion region in order to contribute to the signal. In the diffusion process, the signal charge will migrate beyond the bounds of the illuminated pixel and be collected by neighboring pels resulting in crosstalk. Fig. 6 depicts a two-dimensional model for this process [31]. A more accurate model must also include the third dimension defining the height of the pels. The two-dimensional model described here will yield accurate results only for the case of the height of the pel small compared to the pitch. The following assumptions have been made in the model.

1) The probability density of photon absorption as a function of depth into the silicon is given by

$$P_A(x) = \alpha e^{-\alpha x}$$

where α is the absorption coefficient presented earlier.

2) All charge generated within the diode and its depletion layer is collected at that pel and cannot contribute to crosstalk.

3) Charge generated in the bulk of the silicon beyond the depletion layer has equal probability of diffusing in any direction.

4) Recombination effects are negligible in the undepleted
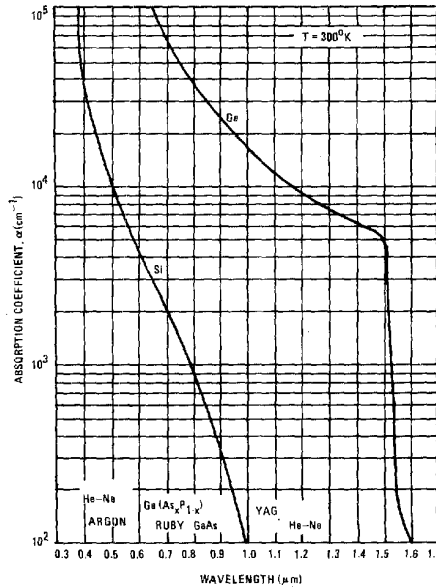
Fig. 5. The measured intrinsic absorption coefficient for silicon and germanium as a function of wavelength.
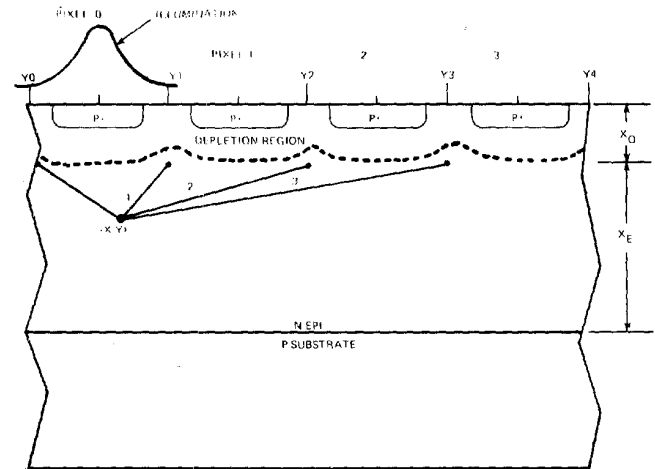
Fig. 6. Cross section of a photodiode array used to describe a two-dimensional model for electrical crosstalk.

tub (i.e., the diffusion length is large compared to the pitch distance and absorption depth).

5) The pel is illuminated with a spot which has circular symmetry and a Gaussian irradiance profile. The spot's $1/e^2$ width is equal to the pel pitch.

Let $P_{Ci(x,y)}$ denote the probability that detector i will collect charge generated by photon absorption at point (x,y). At distances beyond the depletion depth

$$P_{Ci(x,y)} = \frac{\Phi_i(x,y)}{2\pi} = \frac{1}{2\pi}\left[\tan^{-1}\left(\frac{y - y_i}{x - x_0}\right) + \tan^{-1}\left(\frac{y_{i+1} - y}{x - x_0}\right)\right]. \qquad (10)$$

If x is less than the depletion depth x_0, then

$$P_{C0}(x, y) = 1$$

and

$$P_{Ci}(x, y) = 0, \qquad i = 1, 2, 3, \cdots.$$
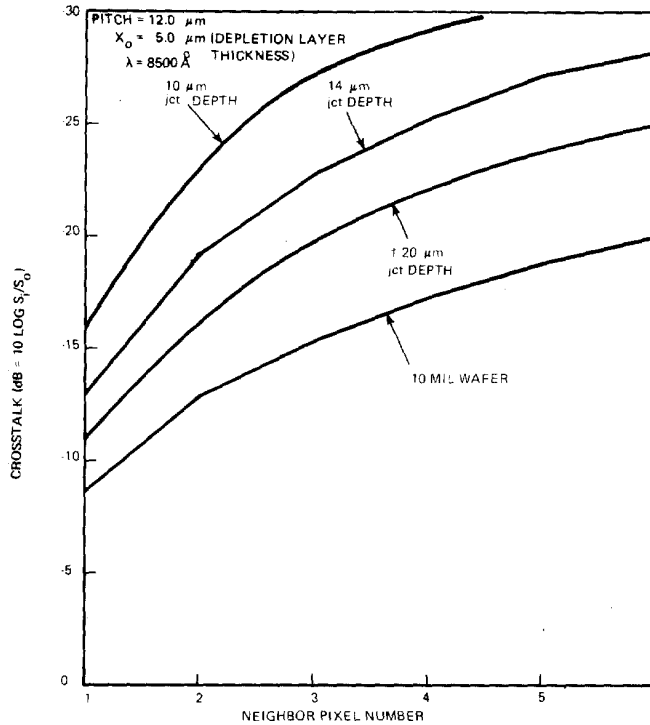
Fig. 7. Calculated results describing the crosstalk between neighboring pels as a parametric function of tub junction depth.

Let $H(y)$ denote the Gaussian irradiance profile given by

$$H(y) = H_0 \exp\left[-\tfrac{1}{2}(y/\sigma)^2\right] \tag{11}$$

where σ is the standard deviation of the irradiance profile. The signal collected by the illuminated pel is determined by combining the above equations and integrating

$$S_0 = \int_{y_0}^{y_1} H(y)\left[(1 - e^{-\alpha x_0}) + \int_{x_0}^{x_E} P_{C0}(x,y)\,P_A(x)\right]dx\,dy \tag{12}$$

and that by the ith pel

$$S_i = \iint_{x_0}^{x_E} H(y)\,P_{Ci(x,y)}P_A(x)\,dx\,dy, \quad i = 1, 2, 3, \cdots \tag{13}$$

where x_0 is the depth of the depletion boundary and x_E is the depth of the top layer or the back surface of the wafer.

The crosstalk to any pel T_i is then given by

$$T_i = 10 \log\left[S_i/S_0\right] \tag{14}$$

where i is the subscript denoting the neighbor element for which crosstalk has been calculated (i.e., $i = 1$ for nearest neighbor).

Numerical evaluation of this formulation for two dimensions using the six point Gauss–Legendre quadrature formula has been used to calculate the predicted crosstalk performance of a silicon array using the model described above. The results are shown in Fig. 7 for 8500 Å light. The plots show the improvement possible in pel isolation by making the tub thickness smaller. An analysis of crosstalk for CCD sensors is presented in [32].

D. Charge Capacity

The charge capacity of either a photodiode or MOS-CCD structure is of importance in devices for AO signal processing because it sets the upper bound of photon generated charge which can be stored by the detector in a sample interval. The difference between this value and the inherent noise of the detector sets the maximum dynamic range of the system. First, the charge handling capacity of photodiodes will be described and then that of buried channel CCD's.

The maximum charge handling capacity of a photodiode neglecting diode edge effects, is the product of the diode's capacitance and applied voltage. The capacitance is the sum of the diode's junction capacitance C_j, and parasitic capacitance C_P, while the maximum reverse bias V_R is the voltage applied to the diode during reset. The total charge capacity is then

$$Q_T = C_P V_R + \int_0^{V_R} C_j\,dV. \tag{15}$$

The value of the junction capacitance can be found from the relationship

$$C_j = \frac{C_{j0}}{[1 + V/V_{bi}]^{1/2}} \tag{16}$$

where C_{j0} is the junction capacitance at zero bias, V_{bi} is the built-in voltage and V is the voltage on the diode. The value of the parasitic capacitance can be found from the relationship

$$C_P = \frac{\kappa_0 \epsilon_0 A_P}{x_0'} \tag{17}$$

where κ_0 is the relative permittivity of the insulating material, x_0' is its thickness and A_P is the area of the capacitor. Replacing C_j in (15), and assuming the reasonable initial condition that $V_R \gg V_{bi}$, the maximum charge handling capability of a

photodiode in units of charge reduces to the expression

$$Q_T = 2(V_{bi}V_R)^{1/2}C_{jo} + C_P V_R. \qquad (18)$$

Typical realizable values for the terms in (18) for a silicon photodiode array are

$$C_{jo} = 0.01 \text{ pF}$$
$$V_{bi} = 0.6 \text{ V}$$
$$C_P = 0.1 \text{ pF}$$
$$V_R = 10 \text{ V}$$

which yields a charge capacity of 5 to $10 \times 10^6 \, e^-$.

The charge capacity of a shallow n-type buried channel CCD is given by the relationship [10]

$$Q_T \cong 0.75 \, N_D t_j A \qquad (19)$$

where N_D is the donor concentration of the channel, t_j is the n-p junction thickness, and A is the area of the photon collecting CCD gate. Using values of $N_D = 3 \times 10^{16}$ cm, $t_j = 0.3 \, \mu\text{m}$, and $A = 10^{-6}$ cm^2, the number of photocarriers which the typical shallow buried channel CCD can hold is $\sim 7 \times 10^5$ electrons.

E. Intrinsic Detector Transfer Characteristics

The use of photodetectors for AO signal processing place a premium on the fidelity of the sensor's amplitude and time transfer characteristics. The intrinsic time response of both CCD's and photodiode arrays to pulsed optical signals is dependent upon the time necessary for photogenerated carriers to be collected. In the depletion region of both CCD's and photodiodes, the free carriers are collected quickly. The average transit time t_0 for an electron in the depletion region is given by the relationship

$$t_0 = \frac{X_d}{2V_s} = \frac{2\kappa_s \epsilon_0 (V + V_{bi})/q N_A}{2V_s} \qquad (20)$$

where X_d is the depletion width, V_s is the saturation velocity of electrons, κ_s is the relative dielectric constant of silicon, ϵ_0 is the permittivity of free space, V_{bi} is the built-in junction voltage, V is the reverse bias on the diode, and N_A is the acceptor impurity concentration. As an example, for $N_A = 10^{16}$ cm^{-3} and $V = 10$ V, the average electron transit time in the depletion region is 5.6 ps. However, in the volume outside the depletion region the free carriers must diffuse to the depletion region. In imaging arrays which do not have a tub-substrate junction to cutoff deeply absorbed photons, the diffusion time of charge to the pel can be many microseconds. Photocarriers from a short optical pulse will then be collected over this time interval. If the exposure time is comparable to the optical pulse width, a temporal signal degradation will result. This time delay can cause degradation in AO spectrum analyzer systems whose processing period is less than several microseconds. This form of signal degradation is one contributor to the so called holdover crosstalk. The use of the tub-substrate junction to enhance pel-to-pel crosstalk performance is thus also important to limit temporal crosstalk in both CCD's and photodiode arrays.

The physical mechanism of electron-hole creation by the absorption of photons is identical for both MOS-CCD's and photodiodes. However, the linearity of the charge-to-voltage conversion can be substantially different depending upon the design of the sensor. The major reason for a nonlinear charge-to-voltage conversion in CCD or photodiode arrays is the junction depletion capacitance because it is voltage dependent.

In the case of CCD's, this capacitance is at the output sensing node. In the case of photodiodes, every pel has both a junction and a parasitic capacitance.

The linearity of a photodiode's response is dependent upon the ratio of the nonlinear junction capacitance to the parasitic capacitance. The response of photodiodes that are intensely illuminated within one exposure interval is quite complex. The diodes can be driven into forward bias. In the ideal case, their voltage response to light intensity then has a logarithmic transfer function similar to solar cells. However, in realizable photodiodes they act like leaky integrators in this mode.

The MOS CCD converts charge to voltage at the electrometer output by discharging junction depletion capacitance. This junction capacitance is made small by design to achieve high signal charge sensitivity. The junction is strongly reversed biased so that signal charge discharges it only slightly and it thus approximates a linear response. If the incident light intensity is very high, the MOS CCD register will spill charge into adjacent pels causing blooming. This phenomenon can be limited by adding to the sensor structure a drain such that excess charge is removed before blooming can occur.

IV. DETECTOR DYNAMIC RANGE AND NOISE

The linear dynamic range of photodetectors for AO signal processing can be expressed as the ratio of the maximum charge capacity of a pel to the rms number of noise electrons, both expressed here in units of charge

$$D_{\text{DET}} = \frac{Q_T}{[\overline{Q_T^2}(\text{NES})]^{1/2}}. \qquad (21)$$

The relationship between system dynamic range and sensor dynamic range is defined by

$$D_{\text{system}} \leqslant K D_{\text{DET}} \qquad (22)$$

where K is a function related to the system transfer function. The inequality indicates that the system dynamic range may be limited by the detector. The noise equivalent signal (NES) is defined as the input exposure density, $E(\text{NES})$, which will make the SNR equal to unity at the sensor output

$$E(\text{NES}) = \frac{[\overline{Q_T^2}(\text{NES})]^{1/2}}{R_{D_\lambda}} \; (\mu\text{J}/\text{m}^2) \qquad (23)$$

where $[\overline{Q_T^2}(\text{NES})]^{1/2}$ is the rms number of noise photoelectrons in coulombs and R_{D_λ} is the responsivity previously defined. The NES is separable into two components: temporal noise and fixed pattern noise. This separation can be expressed in terms of rms noise electrons by the expression

$$\frac{[\overline{Q_T^2}(\text{NES})]^{1/2}}{q} = \frac{1}{q}[\overline{Q}_{\text{Temporal}}^2 + \overline{Q}_{\text{spatial}}^2]^{1/2} \qquad (24)$$

where q is the electronic charge in coulombs. A summary of these noises sources is presented in Table I for CCD's and photodiode arrays and discussed in detail below. The choice between selecting a photodiode, a CCD, or a photodiode/CCD for a given AO system application is dependent principally upon tradeoffs between speed of operation, sensitivity, and dynamic range. In general, for low temporal noise performance (e.g., $\overline{Q}_T(\text{NES})/q < 200 \, e^-$) and moderate dynamic range (10^2), CCD's are superior to photodiode arrays principally because of the low output sensing capacitance at the electrometer as opposed to the photodiode capacitance. On

TABLE I

	CCD	PHOTODIODE
INTRINSIC	BULK TRAPS LEAKAGE PHOTON SHOT	LEAKAGE PHOTON SHOT
CIRCUIT	TRANSFER INEFFICIENCY $\sqrt{\frac{kT}{C}}$ JOHNSON-NYQUIST IN OUTPUT RESET OPERATION	$\sqrt{\frac{kT}{C}}$ JOHNSON-NYQUIST IN DIODE RESET OPERATION
		MOS ELECTROMETER SIGNAL PROC. AMP FIXED PATTERN A/D QUANTIZING NOISE

principally limited by amplifier noise common to both CCD's and photodiode arrays to about 500–1000 e^-, making the higher dynamic range (10^5) obtainable with photodiodes attractive.

Several optoelectrical techniques exist to extend the dynamic range of the photodetector. One technique utilizes two linear photodetector arrays and a beam splitter [33]. Light intensity is divided unequally between the two detectors. After the photodetector which receives the majority of light intensity saturates, the second detector array output is utilized. In this way the dynamic ranges of the two detector arrays can be combined to yield a total detection range which is the sum of the dynamic range of the individual photodetector arrays. Another elegant optical scheme for extending the detector dynamic range of a one-dimensional processor uses a two-dimensional detector array illuminated by means of a cylindrical lens through a stepped density filter [34]. The rows of the detector parallel to the direction of changing optical transmissivity become a measure of the optical intensity while the columns of the array represent the one dimensional spatial transform of the processor.

A. Detector Temporal Noise

There are several fundamental sources of temporal uncorrelated noise in photodetector arrays. They include the Johnson–Nyquist thermal noise associated with the charging of capacitors through a resistance, the shot noise due to leakage current, the shot noise of surface and bulk traps in MOS-CCD's, and the signal shot noise arising from quantum fluctuations of impinging photons. Other mechanisms that contribute to the overall temporal noise properties of detectors are peculiar to the specific circuit implementation of the detector. They include electrometer amplifier noise, noise due to transfer inefficiency in MOS-CCD's, and analog and digital processor noise.

The noise associated with the charging of capacitors is of importance since this mechanism is used repeatedly in photodetector arrays for the conversion of signals from charge to voltage or vice versa. Referring to Fig. 8, a capacitor whose initial charge is zero is to be charged to a voltage V_0 through a resistor R by closing a noiseless switch. The voltage across the capacitor (assuming the capacitance is independent of voltage) can be expressed as a function of time by the
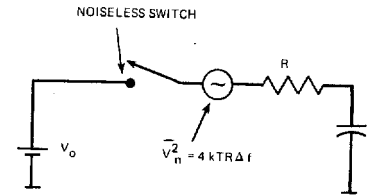

Fig. 8. Schematic representation of the charging of a capacitor through a noiseless switch showing the Johnson–Nyquist thermal noise source.

relationship

$$V(t) = V_0 (1 - e^{-t/RC}) \tag{25}$$

or in terms of the mean charge on the capacitor

$$Q_m(t) = CV_0 (1 - e^{-t/RC}). \tag{26}$$

Barbe has shown that the variance from the mean value of $Q(t)$ is given by the relationship [10]

$$\overline{Q(t)}^2 = kTC(1 - e^{-2t/RC}) \tag{27}$$

or in terms of voltage as:

$$\overline{V(t)}^2 = \frac{kT}{C} (1 - e^{-2t/RC}) \tag{28}$$

Signal detection of photodetector arrays usually involve two operations. The first is the fast charging of a capacitor through the action of a low resistance switch. Ideally the second operation is the discharging of the capacitance by signal charge generated by light when the switch is off. In fact, thermally generated leakage current and the emptying of surface and bulk traps also contribute to the process and thus add shot noise. The $RC/2$ time constant associated with the variance of the voltage (or charge) is different for the two conditions. For example, in the charging mode the time constant associated with the variance of the voltage for a typical MOS switch operating in the subthreshold (or triode) region charging a total capacitance of 0.2 pF (representing depletion and parasitic capacitance) is $(10^4 \ \Omega \times 0.2 \ \text{pF})/2 = 1$ ns. The time necessary for the capacitor to reach better than 99 percent of V_0 is $5 RC = 10$ ns. Consequently, the mean deviation at the end of the charging time, $t = 5 RC$, is

$$\overline{V}_n = \left(\frac{kT}{C}\right)^{1/2} \tag{29}$$

in voltage or

$$\overline{Q}_n = (kTC)^{1/2} \tag{30}$$

in charge.

Assuming that the low resistance switch is turned off at the end of the charging period ($R_{off} > 10^{12} \ \Omega$), the $RC/2$ time constant of the variance is now 0.1 s. This phenomenon can be used to obviate the noise source by the sequential sampling and differencing of signals commonly called correlated double sampling (CDS) [35]. Physically, an ideal capacitor has no sources of noise and hence the voltage set across it is as exact as is the ability to measure it.

The junction and depletion capacitances associated with semiconductors are not ideal because of the presence of leakage current and intraband traps. Leakage (or dark) current can

be described by the relationship [36].

$$i_L = q n_i \left(\frac{A_B w_j}{\tau_{G\text{-}R}} + A_s S \right) + i_D \qquad (31)$$

where n_i is the intrinsic carrier density ($n_i \sim \exp(-E_G/kT)$). A_B and A_S are the areas of the bulk junction and surface, w_j is the width of the depletion region, $\tau_{G\text{-}R}$ is the bulk generation-recombination lifetime, and S is the surface recombination velocity. Typical values for silicon integrated circuits are $\tau_{G\text{-}R} = 100\text{–}300$ μs and $S = 1\text{–}5$ cm/s. The diffusion current, i_D, is due to the diffusion of carriers to the depletion region which are thermally generated in the neutral bulk within a diffusion length $L = \sqrt{DT_0}$. A typical value for L in silicon integrated circuits is ~ 250 μm. Therefore, without a junction structure for limiting this diffusion of carriers to the depletion region, the entire bulk semiconductor can contribute leakage current to the collecting region. The effect of the leakage current is two fold. First, the semiconductor depletion capacitance is discharged in time. Second, the generation process is random, and this contributes a temporal noise associated with the sensing of the charge or voltage on the capacitance. The process obeys Poisson statistics and can therefore be described as shot noise

$$\overline{Q_n^2}(\text{Leakage}) = q i_L \tau \qquad (32)$$

where τ is the sample time interval. The sample time interval can correspond to the exposure time of the detector as photo-generated charge is integrated or it can correspond to the time interval associated with the processing of photogenerated signals.

Another source of shot noise associated with photodetectors which shift charge signals by using buried channel CCD shift registers is bulk trapping noise. This source of circuit noise can be very small because the trapping occurs with deep lying energy levels with time constants greater than 10 μs. An expression for high signal level bulk trapping noise is given by [10]

$$\overline{Q_n^2}(\text{trap}) = M N_S \frac{N_t}{N_D} (1 - e^{-\tau/\tau_e}) e^{-\tau/\tau_e} \qquad (33)$$

where M is the number of analog stages, N_S is the number of signal charge, and N_t is the density of bulk traps in the charge collecting volume. The term N_D is the doping density of the buried channel, τ is the time the charge packet is under a gate, and τ_e is the emission constant for a bulk trap. If the bulk trapping noise is computed for the MOS sensor element then $M = 1$ and τ is the exposure time. If it is being computed for the CCD shift register, then M is equal to the number of transfers and τ is the transport clock period. An MOS-CCD detector for use with a high-speed AO processor (i.e., short exposure time and high-speed readout) suffers little noise contributed by bulk traps. However, bulk traps can be the predominant detector noise source in a well designed, cooled CCD for use in long integration time AO systems such as time-integrating correlators and radiometers.

The shot noise due to the random fluctuations in signal photons incident upon the detector is given by the relationship

$$\overline{Q_n^2}(h\nu) = q R_{D\lambda} \Phi \tau \qquad (34)$$

where $R_{D\lambda}$ is the responsivity previously defined and Φ is the irradiance (or photon flux).

(a) Photodiode Read-Out Circuit
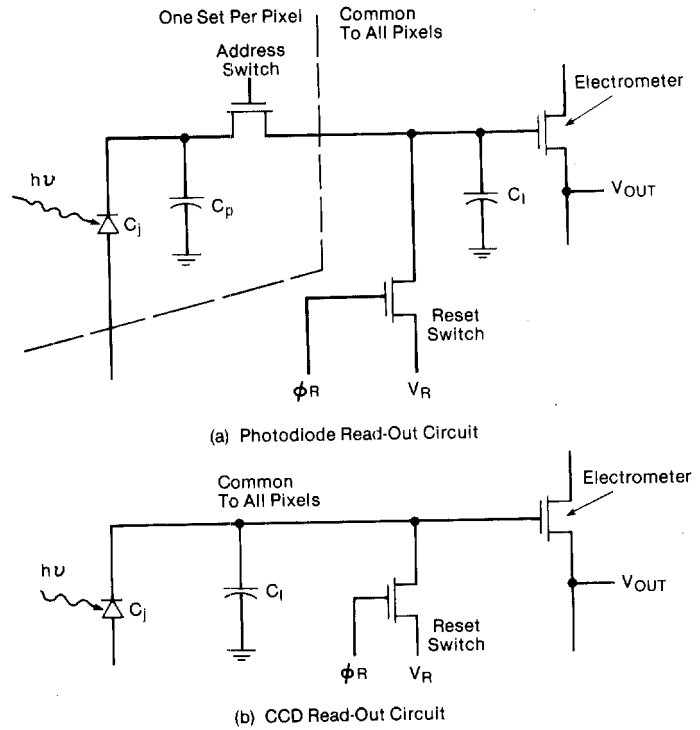
(b) CCD Read-Out Circuit

Fig. 9. Schematic representation of photodiodes and CCD arrays showing the key difference between circuit elements.

Temporal circuit noise sources common to both CCD and photodiode arrays arise principally at the output electrometer where charge is converted to voltage, and in the subsequent analog signal processing amplifiers. The first temporal noise source of the detector output circuitry is the $(kTC)^{1/2}$ noise created by the discrete resetting of the combined gate and parasitic capacitances on the MOS electrometer. The values and sources of these capacitances are not the same for CCD's and photodiode arrays. Fig. 9 shows the critical difference between a CCD and a photodiode array.

There are three contributors to the total capacitance in the photodiode case. They are the junction capacitance C_j the photodiode parasitic oxide capacitance C_p and the gate and parasitic capacitance of the electrometer gate C_I. The sum $(C_p + C_j)$ is directly proportional to the charge handling capacity of the photodiode and is sometimes made large by design to achieve large signal handling capability. In this case, signal detection is achieved by the discharging the capacitor by photon-generated carriers. The signal charge is then the difference between the original number of coulombs placed on the capacitor by the reset action and that number less those removed by recombination with photogenerated charge. A net increase in dynamic range of $\sqrt{C_j + C_p}$ can be achieved at the expense of low light level sensitivity by adding parasitic capacitance at each diode. This method of increasing diode capacitance is preferred to increasing junction capacitance because the latter also adds leakage current. The detector sensitivity suffers however since the $(kTC)^{1/2}$ noise also goes up with increased capacitance. The MOSFET electrometer capacitance C_I is directly proportional to the white noise density for both CCD's and photodiodes. Therefore, if $1/f$ noise is neglected, it is always of advantage to make C_I as small as possible.

In the case of CCD sensors, the signal charge is directly pro-

portional to the number of photons incident upon the detector. The sensing of this signal charge is then performed by a diode whose capacitance is independent of the charge handling capacity of the array. The smaller is this capacitor, the greater is the sensitivity of the device to low light (charge) levels and the smaller is the $(kTC)^{1/2}$ noise associated with the resetting of the combined gate and capacitance of the electrometer $(C_G + C_P)$. Therefore, if $(kTC)^{1/2}$ is the dominant noise source, CCD arrays will have greater sensitivity than photodiode arrays unless CDS is used.

The second temporal noise source is due to the MOSFETs which are typically used as both the on-chip electrometer and the signal processing amplifiers. Their noise variance can be expressed in terms of an equivalent input noise charge by the relationship

$$\overline{Q}_n^2 = E_n^2 \Delta f_n C_I^2 \qquad (35)$$

where Δf_n is the noise bandwidth and C_I is the input capacitance of the transistor. The term E_n^2 is the input noise density in (V^2/Hz) which is composed of white noise and $1/f$ noise [37]

$$E_n^2 = 4kT \left(\frac{2}{3} \frac{1}{g_m} \right) + \frac{K_0 I_{DS}^a}{g_m^2 f^b}. \qquad (36)$$

The $1/f$ noise term (last term on RHS) is an empirical relationship. The term I_{DS}^a is the drain current of the MOSFET in the high current pentode regime of operation. K_0 is a device-related constant inversely proportional to gate area. The terms a and b are experimentally determined such that the data fits the equation and have a range typically of 0.5 to 2 for a and about unity for b. The term g_m is the transconductance of the transistor defined here for the pentode operating regime as

$$g_m = \left(2\mu C_{ox} \frac{W}{L} I_{DS}^a \right)^{1/2} \qquad (37)$$

where μ is the carrier mobility, W/L is the transistor width-to-length ration, C_{ox} is the gate capacitance per unit area, and I_{DS}^a is the source-to-drain current. The frequency f_a at which the $1/f$ noise density equals the white noise density level is given by

$$f_a = \frac{3}{8} \left(\frac{K_0 I_{DS}^a}{kT} \right) g_m. \qquad (38)$$

This frequency usually ranges from 10 kHz to 100 kHz for MOSFET's. In particular, measurements made at Westinghouse on p-channel enhancement mode MOSFET's used for photosensor amplifiers are typically no more than 60 kHz [38].

The amplifier input capacitance C_I consists of the parallel combination of parasitic and gate capacitance. It can be shown that for minimum noise, the parasitic capacitance should be made equal to the gate capacitance. Substituting (36) and (37) into (35), and using the above condition, the noise variance in terms of charge at the input of the amplifier can be written as

$$\overline{Q}_n^2 (\text{Elect}) = \left(\frac{8kT(2 C_{ox} W)^{3/2} L^{5/2}}{3(\mu I_{DS}^a)^{1/2}} + \frac{K_0 I_{DS}^a (2C_{ox} W) L^3}{\mu I_{DS} f^b} \right) \Delta f_n. \qquad (39)$$

The substitution of only (36) into (35) yields the result

$$\overline{Q}_n^2 (\text{Elect.}) = \left[4kT \left(\frac{2}{3} \right) \left(\frac{C_I}{g_m/C} \right) + \frac{K_0 I_{DS}^a}{g_m/C} \right] \Delta f_n. \qquad (40)$$
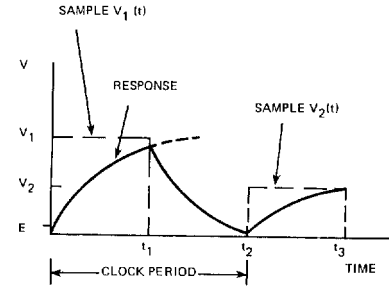

Fig. 10. Sampled data output response showing the effect of inadequate amplifier bandwidth.

This formulation indicates the importance of having a high g_m/C_I at the electrometer. The higher the g_m/C_I, the more sensitive is the detector output to photo generated charge as well as the inherent charge noise sources (e.g., leakage, traps, etc.) and the less sensitive to off-chip amplifier noise.

The sensor's output amplifier bandwidth B_0 and its relationship to noise bandwidth Δf_n is an important subject because of the discrete sample nature of the analog voltage or current signals reconstructed at the output of the sensor. Although a bandwidth of only half the sample rate is required to prevent aliasing, an effective loss in gain and accuracy is introduced if the signal processing amplifiers lack sufficient bandwidth to reconstruct the discrete samples. Referring to Fig. 10, the relationship between amplifier gain, bandwidth, and sample rate is given by

$$A_V(\text{eff}) = A_V [1 - \exp(-\pi B_0/f_c)] \qquad (41)$$

when B_0 is the -3-dB bandwidth of the sensor amplifiers and f_c is the clock frequency. If the amplifier has a bandwidth much greater than the sample rate, the discrete output samples will be an excellent representation of photogenerated charge packets collected by the sensor during an exposure time, but the noise power is increased due to the larger bandwidth. However, if the amplifier bandwidth is insufficient, the relationship between discrete charge packets and output voltage samples will not be perfect (for a general description of this effect for periodic waveforms see [39]). Thus a sample accuracy, S_A can be defined as the ratio of the output sample value obtained for a specific amplifier bandwidth to that obtained for the case $B_0 \gg f_c$. An exact expression for sample accuracy depends upon considering all previous samples in time since the output response is composed of a transient (continuously changing optical signals) and steady state response. However, a reasonable simplification is to consider only the last previous sample in time. This leads to the following expression for the accuracy S_A,

$$S_A = \left[1 - \frac{V_1}{V_2} \exp(-\pi B_0/f_c) \right] \qquad (42)$$

where V_1 is the amplitude of the Nth signal sample at the time t_1 and V_2 is the next sample at time t_3. An error, E, can be defined for achieving a specified accuracy by the relationship

$$E = (1 - S_A) = \frac{V_1}{V_2} \exp(-\pi B_0/f_c). \qquad (43)$$

Therefore, the bandwidth as a function of clock frequency and sample error can be written as

$$B_0 = \frac{f_c}{\pi} \left[\log \frac{V_1}{V_2} - \log E \right]. \qquad (44)$$

As an example, consider an error of 0.01 percent is required and that V_1/V_2 is equal to 0.5. The required bandwidth is then 2.7 times the clock rate, or 5.4 times the maximum signal frequency.

The relationship between signal processor amplifier noise and bandwidth can be obtained as an equivalent input noise by evaluating the integral equation

$$\overline{Q}_n^2(P) = C_I^2 \int_0^\infty |T(jf)|^2 E_n^2 \, df \qquad (45)$$

where $T(jf)$ is the transfer function of the electronics. The equivalent input noise density, E_n^2, has been shown earlier to be composed of white and $1/f$ noise components while the transfer function is dependent upon the amplifier gain-frequency characteristics and characteristic response of the sampled data. The transfer function can be written as

$$T(jf) = \frac{T_0}{(1 - e^{-jf\tau})} \left[\frac{(1 - e^{-j\tau sf})}{jf}\right] \left(\frac{1}{1 + j(f/B_0)}\right) (1 - e^{-jf\tau'}).$$

$$(46)$$

The first term on the right is due to periodic sampling while the second term is due to the relationship between the data sample hold time τ_s and the clock period $T_0 = 1/f_c$. The third term is the characteristic rolloff of a one pole filter response (typically achieved in operational amplifiers by the addition of a feedback capacitance) where B_0 is the -3 dB bandwidth. The last term is the characteristic frequency response of a correlated double sampled filter circuit [34]. The term τ' is the time between the clamp and sample operation of a given pel in the sample interval. Some reasonable assumptions can be made to evaluate the combined transfer function of (46). The frequency characteristic of a one-pole filter can be written as $\{1/[1 + (f/B_0)^2]\}$. The frequency characteristic of a CDS filter with $\tau' = (\frac{1}{2})T_0$ is given by the relationship $(1 - \cos \pi f/f_c)$. The frequency characteristic of a sample and hold circuit inherent in any analog-to-digital (A/D) converter is $(\text{sinc}^2 \pi f/f_c)$ for $\tau_H = T_0$. The CDS filter has double zeros at $f = 2nf_c$, $n = 0, 1, 2, 3, \cdots$ which suppress $1/f$ noise, while the sample-and-hold circuit has zeros at $f = kf_c$, $k = 1, 2, 3, \cdots$, which suppress clock noise. The relationship between these functions is shown in Fig. 11.

The effectiveness of a CDS circuit in removing the $(kTC)^{1/2}$ noise of the output electrometer is dependent upon the off resistance of the resetting switch and the time interval [40]

$$\overline{Q}_{\text{eff}}^2(\text{CDS}) = kTC_I[2(1 - e^{\tau'/R_{\text{off}}C_I}].\qquad (47)$$

This relationship shows that effectively all of the $(kTC)^{1/2}$ can be removed if $R_{\text{off}}C_I \gg \tau'$. However, if the opposite is the case, $(kTC)^{1/2}$ noise will not be removed but will increase by the factor $\sqrt{2}$. Therefore, for AO radiometry applications which require long integration times, the off-resistance of the reset switch must be very high to effectively use CDS. Values of 10^{12} Ω for this type switch are realizable. On the other hand, for AO spectrum analysis systems in which fast access time is required, the integration time is usually in the micro-second range. Therefore, CDS can be used effectively to remove $(kTC)^{1/2}$ noise in these applications. However, for high speed detection, the noise bandwidth must be large. The amplifier noise can then be the dominant noise component over the $(kTC)^{1/2}$ noise associated with sensor reset operations. In such cases, the implementation a CDS circuit is justified
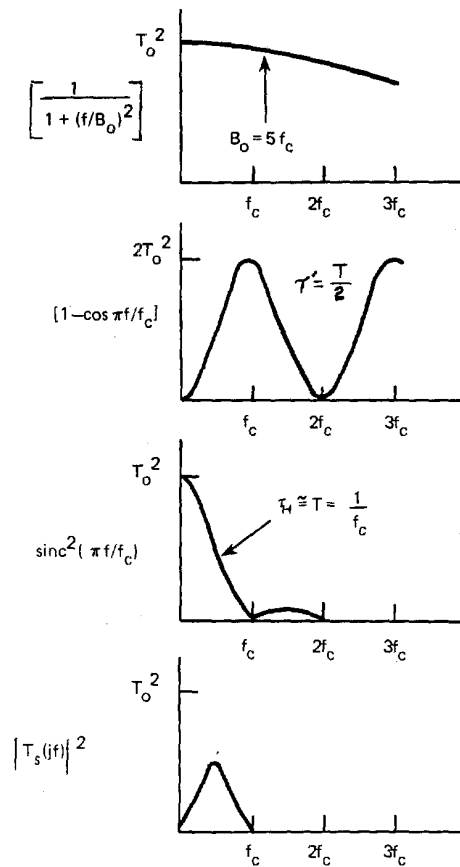

Fig. 11. The first cycle components of the transfer function of sampled data sensors.

only if the $1/f$ noise density is large. It can be shown that the effectiveness of CDS in removing $1/f$ noise goes as f_a/f_c^2 which means that at high clock rates CDS filters $1/f$ noise very effectively. A recent treatment of the response of a CDS circuit to $1/f$ noise is presented in [41].

An important source of temporal circuit noise which cannot be ignored is that which arises from the A/D quantization of signals at the sampled data output of the detector. The variance of this noise is given by the relationship [42]

$$\overline{Q}_n^2(\text{A/D}) = \frac{Q_I^2}{12} \qquad (48)$$

where Q_I is the quantizing interval. For photodetectors which have a linear transfer function between exposure density and output signal, Q_I is given by the relationship

$$Q_I = \frac{\Delta E}{\Delta B} \; (\mu J/m^2 \, /\text{bit}) \qquad (49)$$

where ΔE is the mean change in exposure density and ΔB is the mean change in output bits of the A/D.

B. Fixed Pattern Noise

Fixed pattern (or spatial) noise is due to unequal gain and/or different dc offsets between pels of photodetectors and correlated noise due to digital feedthrough from switching circuits. The effect of fixed pattern noise is to reduce the dynamic range of the system since any serial block signal processing performed on the detector's output must include the variance between pels due to nonuniform response.

The characterization of fixed pattern noise is best performed by experimental techniques. In the dark, the standard deviation about the mean of the sampled signal voltage of the array, V_{dc}, can be measured. Measuring the gain nonuniformity is somewhat more tedious. The array is uniformly illuminated with light at several levels of irradiance. At each level, the output voltage of each pel is measured and its dc offset is subtracted to obtain a normalized response. The standard deviation of the normalized response can then be obtained for each irradiance level and used to set an upper boundary on input optical irradiance. Using this largest value, a worst case noise voltage due to nonuniform gain is determined. The two noise voltages can be converted into an effective noise charge at the sensor input by the relationship

$$[\overline{Q_n^2}(\text{spatial})]^{1/2} = \frac{C_T}{A_V(\text{eff})}[\overline{V_{dc}^2} + \overline{V_G^2}]^{1/2} \qquad (50)$$

where C_T is the effective sensor input capacitance and A_V (eff) is the voltage gain from sensor element to output. For detector systems with linear transfer functions, spatial nonuniformities are dominated by dc offsets which are typically in the range of 10–20 mV.

The most common sources of unequal offsets in photodetectors are

1) nonuniform leakage current in the sensor region;
2) nonuniform leakage current in the analog shift register;
3) threshold voltage offsets;
4) nonuniform reset switch feed through.

The most common sources of unequal gain in photodetectors are

1) nonequal volumes for photogenerated carriers;
2) differences in integrating capacitance of the photocollecting node;
3) nonuniform amplifier gains in the analog signal processing chain.

The effect of fixed pattern noise can be removed at some expense. A signal processor capable of adding or subtracting a predetermined offset level and multiplying by a predetermined weighting coefficient to each pel can be used to improve photodetector fixed pattern performance. The processor must have sufficient capacity to store all offset levels and multiplication coefficients. It must also be able to operate at the maximum data rate of the detector or suffer the loss of information. Signal processors of this type have been built for use with bulk AO spectrum analyzer systems but are substantially larger in volume than the optical processing part of the system.

C. Signal-to-Noise Ratio

The SNR of the detector for noncoherent detection can be written as

$$\left(\frac{S}{N}\right)_{\text{DET}} = \frac{R_{D_\lambda}\Phi\tau}{[\overline{Q_T^2}(\text{NES}) + qR_{D_\lambda}\tau]^{1/2}}. \qquad (51)$$

The contributions to the equivalent noise charge may be summarized in terms of rms noise electrons by the relationship

$$\frac{[\overline{Q_T^2}(\text{NES})]^{1/2}}{q} = \frac{1}{8}[kTC_T + \overline{Q_n^2}(\text{Leakage}) + \overline{Q_n^2}(\text{traps})$$

$$+ \overline{Q_n^2}(\text{Elect.}) + \overline{Q_n^2}(P) + \overline{Q_n^2}(\text{AID})$$

$$+ \overline{Q_n^2}(\text{spatial})]. \qquad (52)$$

Techniques to improve detector SNR are the following. The Johnson–Nyquist $\sqrt{kTC_T}$ can be removed by CDS. Trap noise

is only present in CCD's and can be limited by careful device processing. The noise contribution of the post electrometer amplifier processor may be reduced by having a high g_m/C_I at the electrometer. Section IV-B described an experimental method for measuring the spatial contribution of noise to the NES. The combined contribution of all temporal noise sources can also be related to a measured sensor output voltage by the relationship

$$\frac{[\overline{Q_n^2}(\text{temporal})]^{1/2}}{q} = \frac{C_T\overline{V}_0(\text{temporal})}{qAv(\text{eff})} \qquad (53)$$

where $\overline{V}_0$ is the rms noise voltage over the noise bandwidth measured for a specific pel of the sensor. This measurement can be made by commanding a sample-and-hold device to sample the same pel of the sensor every exposure time, low-pass filtering of the sample and hold signal to the noise bandwidth, and then measuring the result with a true rms voltmeter whose bandwidth is at least the noise bandwidth. Since there is no viable mechanism for achieving photoelectric gain in present solid-state photodiode and CCD sensor arrays, single photon shot-noise limited performance cannot be achieved. (Present silicon avalanche photodiodes do not have uniform gain characteristics as a function of reset voltage and temperature and are thus not presently considered for large arrays.) However, examination of (51) shows that an improvement in SNR by a factor of $(\tau)^{1/2}$ can be achieved when $qR_{D_\lambda}\Phi\tau \gg \overline{Q_T^2}$ (NES). The detector is then photon shot noise limited. This mode of operation is possible by adjustment of either the irradiance Φ or the integration time τ. The practical limit to this improvement is set by the finite charge handling capacity of the array (i.e., the sensor output saturates) and by the photon shot noise due to optical scattering (which has been neglected in the expressions presented here).

V. PITCH AND DETECTOR PEL REQUIREMENTS

A. Bulk Acousto-Optic Processors

The number of resolvable spots N can be expressed by:

$$N = \frac{\Delta f}{B} = \left(\Delta f\frac{d}{v_a}\right)kh(x) \qquad (54)$$

where k_0 is a factor which accounts for optical aperture weighting and beam shape while $h(x)$ is a factor which specifies resolution. The term d is the width of the limiting optical aperture in the system while v_a is the velocity of sound in the Bragg device. The term Δf is the instantaneous AO bandwidth of the Bragg device while B is the bandwidth of a resolvable element.

The term k_0 is equal to $W_t W_a/1.22$ for a circularly symmetrical beam. W_t and W_a are the weighting functions for truncation of the Gaussian beam and aperture apodization respectively. The term $h(x)$ is unity if resolution is specified by the Rayleigh criterion. This specification is arbitrary and defines as resolvable two adjacent equal intensity spots separated by a dip of -0.97 dB. If greater resolution between adjacent spots is required, h will be less than unity. For example, if a -3 dB dip in intensity is required between adjacent spots of a uniformly illuminated circular aperture, a factor of 1.15 ($h(x) = .87$) greater resolution than is obtained using the Rayleigh criterion is necessary. The requirement to measure the dip between diffracted spots sets the minimum number of pels M_p at twice the number of resolvable spots for AO processor sensors. The pitch P (center-to-center pel spacing) of the array can be determined by equating the following geometric expression:
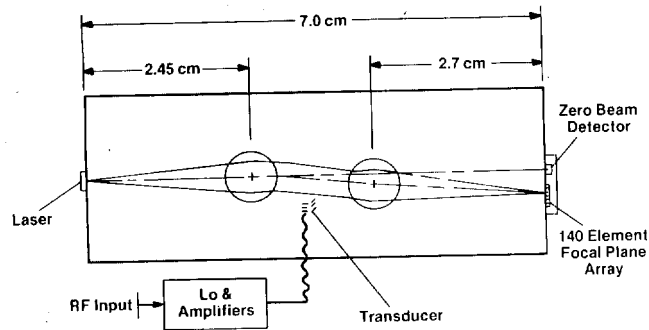
$$\frac{M_p P}{2F} \qquad (55)$$

Fig. 12. Schematic representation of a real-time IOC spectrum analyzer.

to the half angle of optical deflection obtained over a bandwidth Δf, given by $\theta/2 = (\lambda/2v)\Delta f$ where F is the focal length of the transform lens in the system. Using the small angle approximation, the expression for P is then given by

$$P = (\lambda F/2dk)\frac{1}{h(x)}. \qquad (56)$$

In this analysis, the limiting optical aperture is set by the beam expander rather than by the rectangular aperture of the AO device. The beam expander output is circularly symmetrical. Optical truncation and apodization of the beam cross section can be performed at this point before cylindrical optics channel the light through the AO device. The beam is then passed through additional cylindrical and spherical optics which reconstruct circularly symmetric spots and far-field patterns. An advantage of this optical arrangement over the use of an anamorphic beam expander is that apodization of the circularly symmetric beam expander output by modification of the Gaussian cross-section intensity profile results in circularly symmetric spots at the photosensor. A circular spot shape is advantageous because it minimizes the height H of the pel elements for a given spot diameter. The minimum height H of the pel elements is set equal to the diameter of the spot specified as twice the radius of the first zero of the far field diffraction pattern and can be expressed by

$$H = 2F\lambda/dk_0. \qquad (57)$$

The area of a pel is simply the product of H and P while the aspect ratio is the ratio of H to P equal to $4h(x)$. The pitch of the array can be matched to the required spot dimension by the choice of the focal length of the final lens. However, the optimum sensor design for AO systems need match the aspect ratio as well. For example, if resolution is specified by the Rayleigh criterion, $h(x)$ equals one. The resulting aspect ratio is four. Typical values for commercially available photosensor arrays are of the order of 1–1.4. Note however, that the more stringent the requirements on resolution, the lower the value of the aspect ratio.

B. Integrated-Optic Processors

Integrated optical circuits (IOC) consist of both active and passive optical devices formed on planar dielectric waveguides. Optical signal processing functions can be performed by the combination of these elements. Because of their inherent planer construction they are well suited to performing one-dimensional real-time spectrum analysis and spatial or time integrating correlation/convolution functions [20], [43], [44].

Fig. 12 shows a schematic diagram of a real-time IOC spectrum analyzer. The proposed IOC spectrum analyzer detector intended for use with a bulk system and one intended

for use with an IOC system is in the detector pitch and the mounting of the detector to the IOC. The pitch of the detector, as in the bulk case, is proportional to the focal length of the transform lens and to the frequency resolution given by [45]

$$P = \frac{\lambda(\Delta f)F}{N_{\text{eff}} V_s'} \qquad (58)$$

where N_{eff} is the effective index of refraction for a given optical mode within the waveguide and V_s' is the acoustic velocity of the surface acoustic wave (SAW) across the optical aperture. However, unlike bulk optical systems, the focal length F is limited principally by waveguide attenuation and the inefficiency of waveguide reflectors. The smaller the pitch the more advantageous is the detector for IOC. Typical commercially available photodetectors described in Section III have a pitch $\geqslant 18$ μm, while the two detectors designed specifically for use with IOC, have a pitch of 12 μm and 8 μm. Reducing pel pitch below these dimensions must await new technology developments associated with integrated circuit lithography and processing.

The mounting of the detector to the IOC requires precision butt coupling. The sensor must be brought to within several micrometers of the edge of the integrated optical planar guide to avoid light loss and optical crosstalk due to the rapid divergence of the beam. The divergence of the beam is determined by the numerical aperture of the waveguide. To prevent light from being reflected back into the waveguide where it will undergo internal reflections and possibly return to the detector array in adjacent pels, the detector array used for the IOC spectrum analyzer can be placed at a 45° angle to the edge. Light reflected off the surface of the detector cannot then re-enter the waveguide. Fig. 13 shows a schematic representation of this arrangement, while Fig. 14 shows the actual photodetector as an integral part of a working IOC spectrum analyzer.

VI. ADVANCED MICROELECTRONICS FOR ACOUSTO-OPTIC SIGNAL PROCESSING

The technology challenge of applying advanced microelectronics to AO signal processing is just beginning. Substantial innovation in the design and fabrication of microelectronic circuits to perform high-speed processing over a wide dynamic range of optical signals in both linear and area arrays are required at this time. Optical processing systems have demonstrated the capability of performing 10^{15} complex multiplications per second. Much of this computational power is useless without the development of advanced photodetector systems detectors but have as an integral part of their design high speed
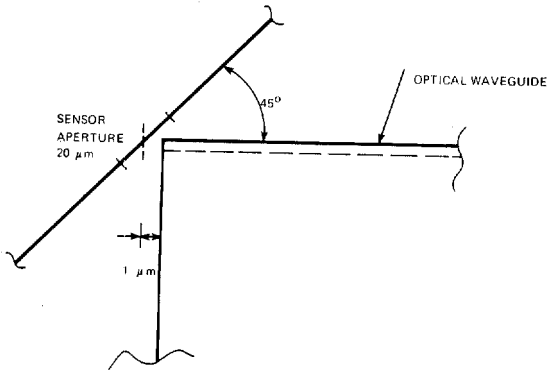
Fig. 13. Schematic representation of a butt coupled sensor to an IOC.

Fig. 16. Photomicrograph of an experimental groove isolated photo-diode array fabricated in ⟨110⟩ silicon.
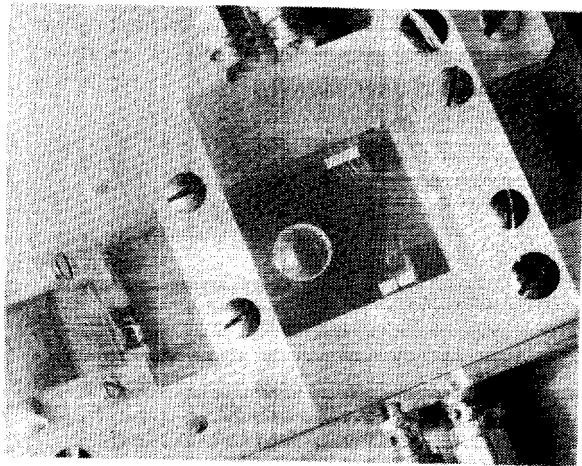

Fig. 14. Photograph showing a sensor butt coupled to a working IOC spectrum analyzer.
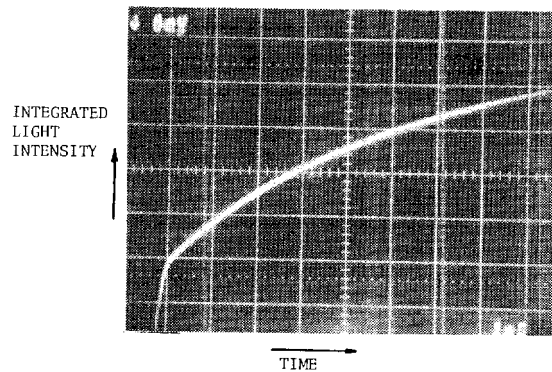
Fig. 17. Optical response of one pel of the array showing the linear to logarithmic response during an integration interval.

Fig. 15. Block diagram of advanced AO processors utilizing VHSIC technology.
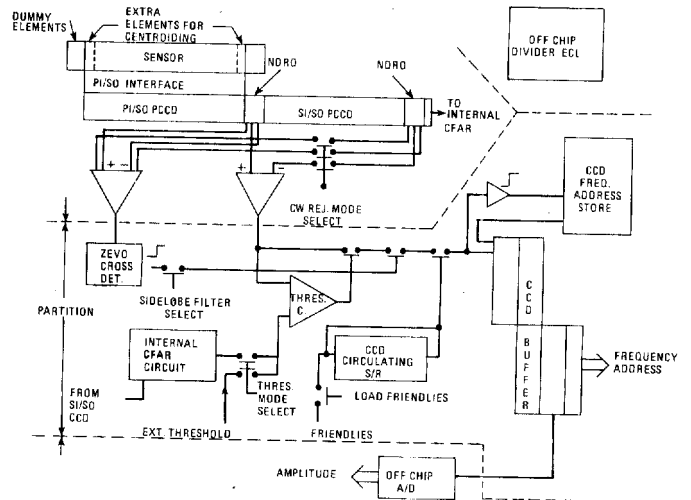
Fig. 18. Schematic representation of a high-speed detector preprocessor for use with AO instantaneous spectrum analyzers.

data processing. Two potential technology candidates for these advanced "smart" sensors are silicon very high speed integrated circuits (VHSIC) and GaAs microelectronic integrated circuits.

A. Very High Speed Integrated Circuits Technology

The VHSIC program is a Department of Defense initiative to develop high speed, low power digital silicon integrated circuits composed of greater than 10^4 digital logic gates per die. This transistor density requires the technological development of new lithographic and processing techniques. A figure of merit for VHSIC is 5×10^{11} (Gate-Hz)/cm^2. The effective utilization and implementation of VHSIC circuits requires accurate device and circuit models and computer aided design (CAD). VHSIC technology will impact optical signal processing in two ways as illustrated in Fig. 15. The first benefit is the use of VHSIC techniques in implementation of photosensor

circuits. Specifically, the capability to accurately define lines and spaces of 1 μm will allow fabrication of small pitch, high density photosensor arrays. This capability can also support the fabrication of high-speed peristaltic analog CCD's and amplifiers to perform the high-speed scanning and subsequent processing of large arrays. Finally, the ability to accurately control the concentration, depth, and lateral diffusion of impurity dopants in the circuit will invite the development of novel detector and signal processing structures. The second benefit of VHSIC is the potential development of a high-speed digital processor which performs many specialized functions
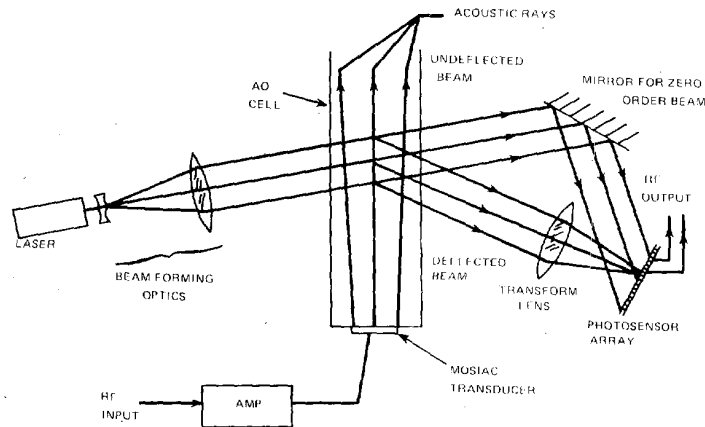
Fig. 19. Schematic representation of the AO exciser processor.
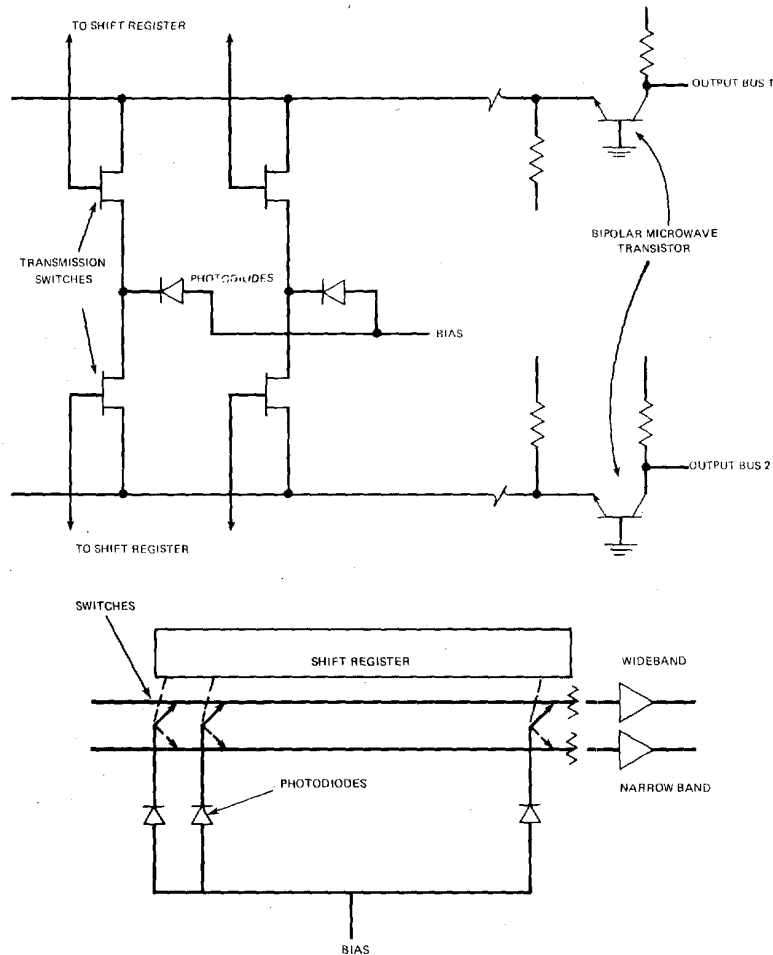
Fig. 20. A schematic representation of a switching photodiode array.

unique to the AO signal processing requirement. Such an AO VHSIC processor could be used to perform detection algorithms and pattern (signature) recognition algorithms of optically processed data as well as remove fixed pattern noise and other dilatorious properties of the sensor.

An advanced high speed detector preprocessor silicon microelectronic circuit for use with integrated and bulk real time AO spectrum analyzers is being developed [46]. The circuits will be capable of analyzing and sorting by amplitude, fre-

quency and time of arrival wide dynamic range optical signals presented at its focal plane. The photosensor part of the circuit utilizes narrow grooves to isolate diodes dielectrically. This unique geometry serves to limit adjacent pel electrical crosstalk and to allow operation of the diode sensors into their nonlinear forward biased region so that high optical dynamic range can be achieved. A photomicrograph of an experimental groove isolated photodiode array fabricated on ⟨110⟩ silicon is shown in Fig. 16 while the linear to log response of a partic-
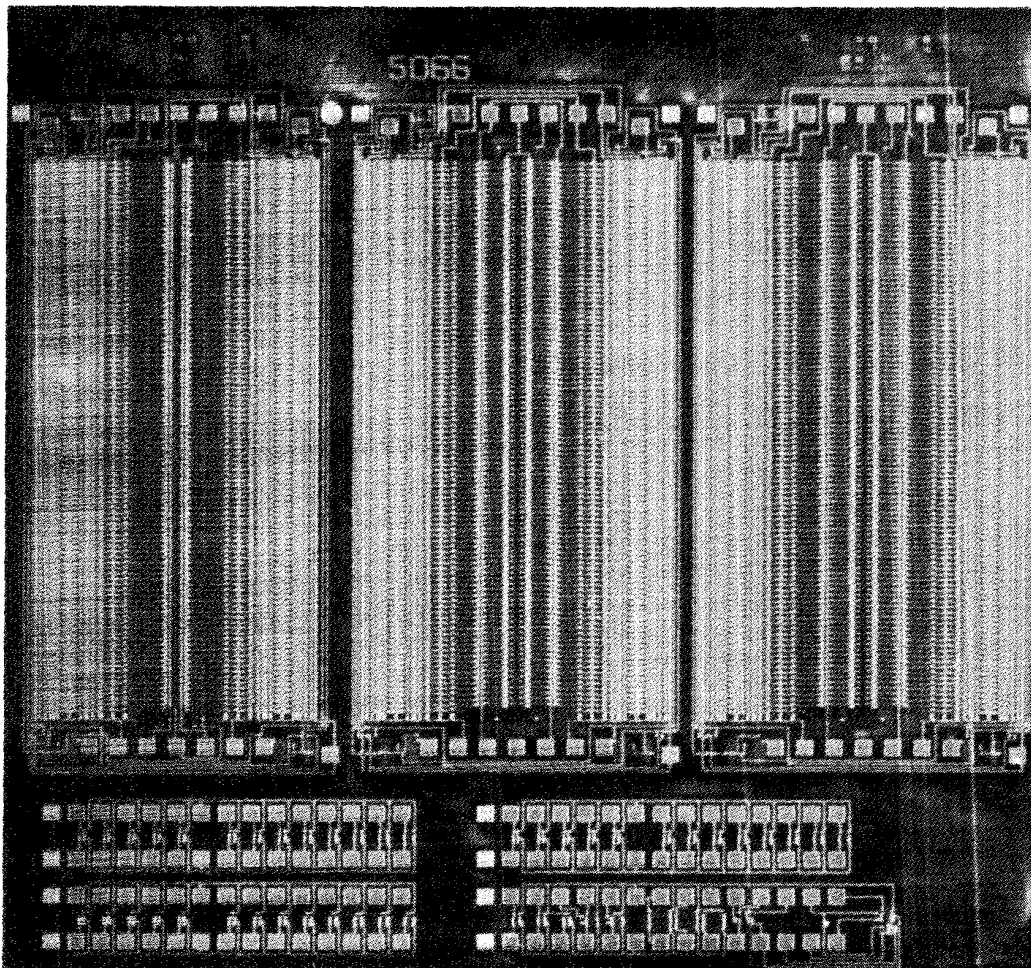
Fig. 21. Photograph of the exciser photodetector.

ular element of this array to HeNe 6328 Å laser light illumination is shown in Fig. 17 [47]. The signal processor utilizes high-speed peristaltic CCD's with on-chip bipolar transistor amplifiers for analog implementations of comparators and analog buffers, low noise short channel MOS charge to voltage amplifiers and CCD internal nondestructive readout charge to current amplifiers [48], [49]. A line to line differencing scheme is utilized to cancel fixed pattern noise in the sensor as well as remove CW signals. A schematic diagram of this circuit is shown in Fig. 18.

Another example of an advanced custom silicon microelectronic circuit which enables a unique AO phenomenon to be utilized is the AO exciser processor [50]. The processor utilizes the coherent property of laser light to allow reconstruction of time domain signals that have been transformed by the Bragg AO interaction. A schematic representation is shown in Fig. 19. Laser light incident on the Bragg device is diffracted in spatially resolved spots as in the ubiquitous AO spectrum analyzer. However, since the optical frequency of each deflected spot is doppler shifted in frequency proportional to the input electrical signal the superposition of reference laser light upon these spots results in optical mixing [51], [52]. A photodetector array of sufficient instantaneous bandwidth placed to intercept these spots will have a time domain output signal of identical frequency spectrum content but possibly amplitude shaded by a weighting function.

If an array of photodiodes is placed at the image plane and a means for either adding or deleting the response from any one diode to a common output bus is implemented, excision of particular frequencies in the time domain can readily be achieved. Fig. 20 is a representation of such a switching photo-array along with a schematic. Fig. 21 shows the actual silicon device built to perform this function [53], [54]. The positions of the switches, determining to which output bus each photodiode is connected, are set by loading serially a binary bit stream into the device's shift registers. The switch positions are then held in this state until new data is entered. Using this type of AO system, made possible by a unique photodetector, narrow-band signals are separated from broad-band signals over a wide instantaneous bandwidth. This function is useful as a prewhitening filter in spread spectrum communication systems, as well as for ECM signal processors to increase sensitivity in a jamming and a dense emitter radio frequency environment.

B. GaAs Technology

The use of GaAs integrated circuits for advanced high-speed sensor/processors is possible. A line array of GaAs detectors for use with an integrated optical spectrum analyzer has been fabricated and tested [23]. The detectors were fabricated as electroabsorption avalanche photodiodes. Measurements on individual diodes yielded noncoherent dynamic ranges of
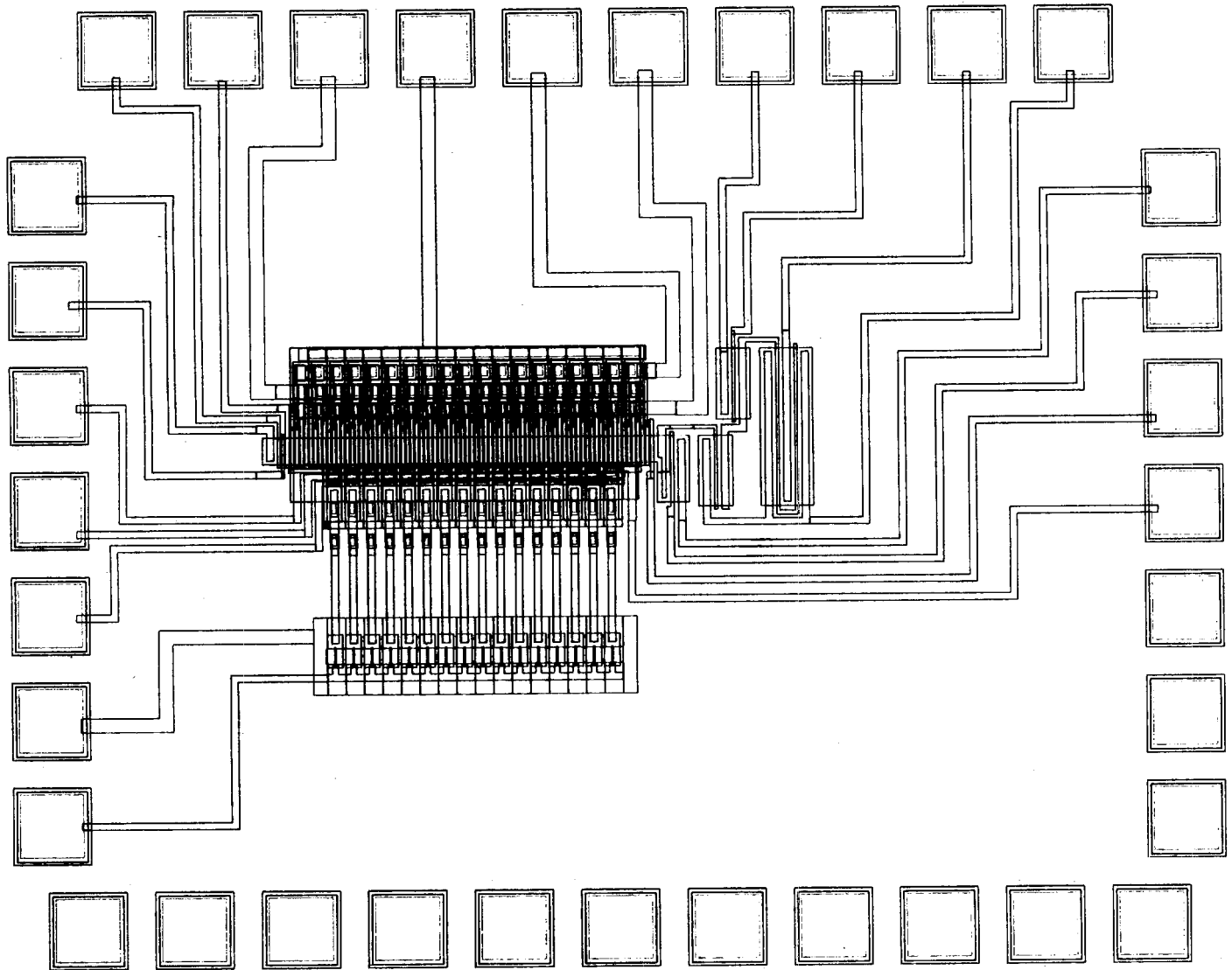
Fig. 22. GaAs photodiode/CCD.

57 dB. These detectors consisted of a line array of individually readout photodiodes. The ability to marry GaAs detectors with high-speed GaAs CCD's and digital logic functions may eventually be feasible as this technology matures [55]. A schematic representation of a 16-pel photodiode/CCD linear GaAs array is shown in Fig. 22 [56]. The device utilizes a Schottky diode as the sensor connected to a Schottky gate mesa-type GaAs CCD. Mesa-type GaAs CCD's have been operated at high speeds (500 MHz) in a continuous clocking mode [57].

VII. Conclusion

A description of the properties and use of solid state photo-detectors for AO signal processing has been presented. Special attention has been given to the device physics which describe the noise properties of these sensors because of their importance in determining the ultimate performance of the entire system. The different categories of device architectures have also been explained because of their differences to those typically used in scene imaging sensors. Although there have been some new sensors specifically made for AO applications, the photodetector still represents at this time the limit to

performance of AO systems. New silicon VHSIC and GaAs sensor/processors will be developed in the future that allow the full potential of these unique optical signal processors to be achieved.

References

[1] W. K. Middleton, *Vision Through The Atmosphere.* Toronto, Canada: University of Toronto Press, 1952.
[2] D. Hecht, "Spectrum analysis using acousto-optic devices," *Opt. Eng.*, vol. 16, pp. 461–466, Oct. 1977.
[3] Corresponding to leakage current density of 1–10 nA/cm².

[4] G. M. Borsuk, M. H. White, E. C. Malarkey, "Wideband acousto-optic radiometry," *Proc. SPIE Optics in Radar Systems*, vol. 128, pp. 344–352, Sept. 1977.

[5] R. A. Spague, "A review of acousto-optic correlations," *Opt. Eng.*, vol. 16, pp. 467–474, Oct. 1977.

[6] T. M. Turpin, "Spectrum analysis using optical processing," this issue, pp. 79–92.

[7] ——, "Time integrating optical processing," in *Proc. SPIE Symp. Real Time Signal Processing* (San Diego, CA), vol. 154, pp. 196–203, Aug. 1978.

[8] ——, "Real time,input transducer for coherent optical processing," *Int. Optical Computing Conf.* (Apr. 9–11, 1974, Zurich, Switzerland).

[9] J. B. Barton, J. J. Cuny, D. R. Collins, "Performance analysis of EBS-CCD imaging tubes/status of ICCD development," in *Proc. 1975 Int. Conf. Application of Charge Coupled Devices*, pp. 133–146, Oct. 1975.

[10] D. F. Barbe, "Imaging devices using the charge-coupled concept," *Proc. IEEE*, vol. 63, pp. 38–67, Jan. 1975.

[11] "Advances in CCD and imaging, Session II," in *Proc. ISSCC*, 1980.

[12] M. M. Blouke, J. F. Breitzmann and J. E. Hall, "Three Phase, backside illuminated 500 X 500 CCD imager," in *Proc. 1978 ISSCC*, p. 36, 1978.

[13] J. Hynecek, "Virtual Phase CCD Technology," in *Proc. 1979 IEDM*, p. 611.

[14] Reticon data sheet "512 random access line scanner-CP 1006," Feb. 2, 1980.

[15] G. Weckler, private communication, Apr. 1980.

[16] R. Ekstein, "ELINT sensor design goals," in *Proc. SPIE Conf. Workshop Acousto-Optic Bulk Wave Devices* (Monterey, CA), Nov. 27–29, 1979.

[17] Reticon Data Sheet "CP 1023 tapped 256 CCPD," Mar. 18, 1980.

[18] G. M. Borsuk, A. Turley, G. E. Marx, E. C. Malarkey, "Photosensor array for integrated optical spectrum analyzer systems," *Proc. SPIE*, vol. 176, p. 109, 1979.

[19] G. E. Marx and G. M. Borsuk, "Evaluation of a photosensor for integrated optics spectrum analyzers," in *Tech. Dig. 1980 Topical Meet. Integrated and Guided Wave Optics* (Incline Village, NV), vol. ME 6, 1980.

[20] D. Mergerian *et al.*, "Working integrated optical RF spectrum analyzer," *Appl. Opt.*, vol. 19, no. 18, Sept. 15, 1980.

[21] D. Mergerian, unpublished, Mar. 1980.

[22] J. Y. M. Lee, B. Chen, "Detector array for an integrated optic spectrum analyzer," Extended abstracts, vol. 80-1, *Spring Meet. Electro-Chemical Soc.*, May 11–16, 1980.

[23] "GaAs waveguide detector array for A IOC spectrum analyzer," Semiconductor Res. Lab, Washington University, St. Louis, MO, Final Rep. N064351-1 July 31, 1979.

[24] *Solid State Imaging*, Jespers, Van De Wiele, and White, Eds., NATO Advanced Study Institute Series, Series E, Applied Sciences, no. 16 (Leyden, The Netherlands: Noordhoff, 1976).

[25] A. S. Grove, *Physics and Technology of Semiconductor Devices*. New York: Wiley, 1967, p. 121.

[26] P. A. Gary, "Modeling and optimization of a silicon photosensor for a reading aid," Stanford Electronics Lab., Tech. Rep. No. 4822-1, May 1967.

[27] F. Van DeWiele, "Photodiode quantum efficiency," in *Solid State Imaging*, NATO Advanced Study Institute Series, Series E, no. 16 (Leyden, The Netherlands: Noordhoff, 1976).

[28] N. Bluzer, private communication, 1979.

[29] D. McCann *et al.*, "Buried-channel CCD imaging arrays with tin-oxide transparent gates," in *Proc. 1978 ISSCC*, p. 30, 1978.

[30] W. C. Dash and R. Newman, "Intrinsic optical absorption in single crystal germanium and silicon at 77° K and 300° K," *Phys. Rev.*, vol. 99, p. 1151, 1955.

[31] A. Turley, unpublished, 1978.

[32] R. H. Dyck, W. Steffe, "Effects of optical crosstalk in CCD image sensors," in *Proc. Int. Conf. Application of CCD's*, pp. 1–55, Oct. 1978.

[33] U.S. Patent 3 962 577.

[34] U.S. Patent 3 934 153.

[35] M. H. White, D. R. Lampe, F. Blaha, and I. Mack, "Characterization of surface channel CCD image arrays at low light levels," *IEEESC*, vol. 9, p. 3, Feb. 1974.

[36] M. H. White, "Photodiode sensor array," in *Solid State Imaging*, NATO Advanced Study Institute Series, Series E, N016.

[37] P. R. Gray and R. G. Meyer, Analysis and design of integrated circuits. New York: Wiley, 1977.

[38] A. Turley, private communication, 1979.

[39] C. D. McGillen and G. R. Cooper, *Continuous and Discrete Signal and System Analysis*. New York: Holt, Rinehart, and Winston, 1974, pp. 238–241.

[40] R. W. Brodersen and S. P. Emmons, "The measurement of noise in buried channel charge-coupled devices," in *1975 Int. Conf. Application of CCD's* (Oct. 29, 1975), p. 331.

[41] R. J. Kansy, "Response of a correlated double sampling circuit to 1/f noise," *IEEE J. Solid-State Circuits*, vol. SC-15, p. 373, June 1980.

[42] B. Gold and C. M. Rader, *Digital Processing of Signals*. New York: McGraw-Hill, 1969, p. 104.

[43] S. H. Chang and J. T. Boyd, "An integrated optical channel waveguide—CCD transversal filter," *IEEE Electron Device Lett.*, vol. EDL-1, Mar. 1980.

[44] C. S. Tsai, C. C. Lee and B. Kim, "A review of recent progress on guided wave acousto-optics with applications to wideband communication and signal processing," *Tech. Dig. 1980 Topical Meet. Integrated and Guided-Wave Optics* (Incline Village, NV), vol. ME1-1, 1980.

[45] M. C. Hamilton, D. A. Wille, and W. J. Miceli, "An integrated optical RF spectrum analyzer," *Opt. Eng.*, vol. 16, no. 5, p. 475, Sept.-Oct. 1977.

[46] Navy Contract N00173-79-C-0485.

[47] J. Kim, unpublished, Apr. 1980.

[48] G. M. Borsuk, M. H. White, N. Bluzer and D. R. Lampe, "Design and analysis of new high speed peristaltic CCD's," in *Proc. 1978 Conf. Application of CCD's* (Oct. 25–27), 1978.

[49] R. J. Brewer, "The low light level potential of a CCD imaging array," *IEEE Trans. Electron Devices*, vol. ED-27, p. 401, Feb. 1980.

[50] Navy Contract N00039-78-R-0417.

[51] W. J. Thaler, "Frequency modulation of a HeNe laser beam by ultrasonic waves in quartz," *Appl. Phys. Lett.*, vol. 5, no. 2, p. 29, July 16, 1964.

[52] G. M. Borsuk and W. J. Thaler, "Frequency-moduated laser communication system," *IEEE Trans. Sonics Ultrason.*, vol. SU-17, Oct. 1970.

[53] F. Kub, unpublished, Mar. 1980.

[54] N. Bluyer, F. Kub, and G. M. Borsuk, "Steering of high frequency low level photocurrents between summing busses beyond the $gm/2\pi c$ limit," *Proc. IEDM*, Dec. 1980.

[55] R. C. Eden and I. Deyhimy, "Application of GaAs integrated circuits and charge-coupled devices (CCD's) for high speed signal processing," in *Proc. SPIE Acousto Optic Bulk Wave Devices*, vol. 214, p. 39, 1979.

[56] F. Kub, Unpublished, May 1980.

[57] I. Deyhimy *et al.*, "An ultra high speed GaAs CCD," in *Tech. Dig. 1979 IEDM*, p. 619, 1979.

Contributors

Gerald M. Borsuk (SM'78) was born in Newark, NJ, on December 15, 1944. He received the B.S., M.S., and Ph.D. degrees in physics from Georgetown University, Washington, DC, in 1966, 1970, and 1972, respectively.

Since 1977, he has been employed by the Westinghouse Electric Corporation, Advanced Technology Laboratories, Baltimore, MD, and is Manager of the Solid State Device Physics Department primarily involved in research and development concerning charge-coupled devices and optical techniques for signal processing. Prior to joining Westinghouse, he worked for the ITT Electro Physics Laboratory, Columbia, MD.

*
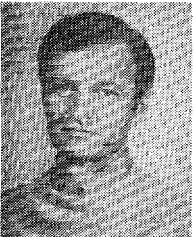
Berthold K. P. Horn received the B.Sc. (elec. eng.) degree from the University of the Witwatersrand, Johannesburg, South Africa, and the S.M. and Ph.D. degrees from the Massachusetts Institute of Technology (M.I.T.), Cambridge, MA, in 1965, 1968, and 1970 respectively.

He has taught at both the University of the Witwatersrand and M.I.T. He has been Associate Professor in the Department of Electrical Engineering and Computer Science of M.I.T. since June 1976. He directs the machine vision and machine manipulation work of the M.I.T. Artificial Intelligence Laboratory. His present interests also include locomotion, tomography, image understanding, exact color reproduction, and the protection of wildlife.

*

Peter Kellman was born in New York City, NY, on November 29, 1952. He received the B.S. degree in electrical engineering from Carnegie-Mellon University, Pittsburgh, PA, in 1975, and the M.S. and Ph.D. degrees in electrical engineering from Stanford University, Stanford, CA, in 1977 and 1979, respectively.

He joined ESL, Incorporated, a subsidiary of TRW, Sunnyvale, CA, in 1975 and has worked on the development of automatic signal search and collection systems using acousto-optic signal processing technology. He is currently manager of Acousto-Optic System Development.

Dr. Kellman is a member of the IEEE Acoustics Speech and Signal Processing and Communications Societies, Society of Photo-Optical Instrumentation Engineers, and the Optical Society of America.

*

Adrianus Korpel (SM'67–F'75) received the B.S., M.S., and Ph.D. degrees in 1953, 1955, and 1969, respectively, from the University of Technology, Delft, The Netherlands, all in electrical engineering.

From 1955 to 1960 he was with the Postmaster's General Research Laboratories, Melbourne, Australia. In 1960 he joined Zenith Radio Corporation, Chicago, IL, where in 1975, he became Director of research in engineering physics. Since 1977 he has been with the University of Iowa, Iowa City, as a faculty member of the Department of Electrical and Computer Engineering. He has worked in the areas of coherent optics, acousto-optics, and acoustic imaging. His present research interests include nonlinear phenomena.

Dr. Korpel is a member of both the Optical Society of America and the Acoustical Society of America.

*

J. William Murray (S'59–M'63) received the B.S.E.E. degree in 1960 from the University of Washington, Seattle, and the M.E.E. degree in 1962 from New York University, New York.

As a Member of Technical Staff at Bell Telephone Laboratories, Whippany, NJ, from 1960 to 1966, he participated in development of signal and data processing equipment, and associated computer software, for operation, testing, and simulation of antiballistic missile radar systems, and for measurement of antenna patterns of large multifunction phased-array radars. From 1966 to 1977 he was employed by the Applied Technology Division of Itek Corporation, Sunnyvale, CA. During this period he was primarily concerned with development of system designs for radar warning systems for use on military tactical aircraft. This included development of computer-based interferometer systems for providing highly accurate azimuth and elevation direction finding information. Since 1977 he has been a Member of Technical Staff at ESL, Incorporated, a subsidiary of TRW, Sunnyvale, CA. His current responsibilities are primarily in connection with system design of specialized computer-based signal processing systems. This includes development of systems for performing real-time analysis, display, and collection of the multichannel output signals available from acousto-optic channelized receivers.

Mr. Murray is a member of Tau Beta Pi.

*

William T. Rhodes (S'70–M'71) was born in Palo Alto, CA, on April 14, 1943. He received the B.S. degree in physics in 1966 and the M.S. and Ph.D. degrees in electrical engineering in 1968 and 1971, respectively, from Stanford University, Stanford, CA.

In 1971 he joined the faculty of the Georgia Institute of Technology where he is currently an Associate Professor teaching in the areas of modern optics, communications, and signal processing. He is coauthor of a book on lasers and their applications and is editing a book on optical information processing. In 1976 he was a Humboldt Research Fellow at the University of Erlangen in West Germany. His research is in the areas of image formation and processing and in hybrid optical/electronic signal processing. He is an associate editor for *Optics Letters* and serves on the editorial boards of *Optica Acta* and *Optical Engineering*.

Dr. Rhodes is currently the Chairman of the IEEE Computer Society Technical Committee on Optical Processing and the Vice Chairman of the Optical Society of America Technical Group on Information Processing and Holography.

*

Harry N. Shaver (S'53–M'57) was born in Bisbee, AZ, on June 25, 1935. He received the B.S.E.E. and M.S. degrees in electrical engineering from the University of Arizona, Tucson, in 1957 and 1959, respectively, and the degree of Engineer from Stanford University in 1965.

He joined ESL, Incorporated, a subsidiary of TRW, Sunnyvale, CA, in 1972 and has been active in the areas of signal search, automatic signal recognition, and optical signal processing. He is currently Manager of the Signal System Technology Department.

Mr. Shaver is a member of Tau Beta Pi, Pi Mu Epsilon, Sigma Pi Sigma, and Phi Kappa Phi.

*

Allan W. Snyder received the B.Sc. degree from the Pennsylvania State University, University Park, the S. M. degree from the Massachusetts Institute of Technology, Cambridge, MA, the M.S. degree from Harvard University, Cambridge, MA, the Ph.D. degree from University College London, England, and the D. Sc. degree from the University of London, London, England, in the fields of biology, electrical engineering, and applied physics.

At present he holds the chair of optical physics and vision research in the Institute of Advanced Studies at the Australian National University. He is Head of the Department of Applied Mathematics, a department devoted to interdisciplinary fields including membrane biophysics, optics and vision. He is also a professor in the Department of Neurobiology. During the academic years of 1974 and 1977 he was a Visiting Professor at the Technische Hochschule, Darmstadt, Germany, and at the Yale University School of Medicine, New Haven, CT, respectively. His industrial appointments include nine months with Peter Kiewitt as a Communication Engineer on the ice cap in Greenland (1960), a Research Scientist with the Sylvania Applied Research Laboratory (1963-1967), Consultant to the British Post Office (1967-1969), the Standard Telecommunications Laboratory, England (1969-1970), Telecom Australia (1972) and the French Centre National d'Etudes des Telecommunications (1976) all concerned with optical fibers. He conceived and jointly organized the first international workshop on photoreceptor optics in Darmstadt, Germany, 1974, and the first international workshop on optical waveguide theory in Lannion, France, 1976. He was one of the four invited members on the 1977 Marconi International Fellowship Committee. In addition to more than 150 papers, he is the co-author of *Photoreceptor Optics* (Springer Verlag, 1975) and *Optical Waveguide Theory* (Chapman and Hall, 1981) and was the Guest Editor of the 1977 special issue of *Optical and Quantum Electronics.*

Professor Snyder has been the recipient of a National Science Foundation fellowship in biophysics, the John Simon Guggenheim Fellowship in visual neurobiology, the research medal of the Royal Society of Victoria and the Edgeworth David Medal.

*

Terry M. Turpin received his B.S.E.E. degree from the University of Akron, Akron, OH, in 1966, and a M.S. degree in electronic engineering from Catholic University, Washington, DC, in 1970.

From 1967 to the present, he has been actively involved in optical processing research and development with the Department of Defense. He has had extensive experience with one- and two-dimensional optical processing systems and hands-on experience with a wide variety of electro-optical components.

Shi-Kay Yao (S'68-M'74-SM'80) was born in China on June 30, 1945. He received the B.S. degree in electrical engineering from National Taiwan University, Taipei, Republic of China, in 1967, and the M.S. and Ph.D. degrees in electrical engineering from Carnegie-Mellon University, Pittsburgh, PA, in 1969 and 1974, respectively.

He is currently Senior Scientist at the TRW Technology Research Center, Torrance, CA, contributing to the development of optoelectronic devices and fiber optical communication. Prior to this, he was manager of Optical Signal Processing at the Electronics Research Center of Rockwell International, Anaheim, CA, from 1976 to 1980, where his major contributions were in Integrated Optics, waveguide optical lenses, waveguide photodetectors, and surface acousto-optic devices using ZnO piezoelectric thin film. He was with Harris Corporation from 1974 to 1976 working on acousto-optic devices and surface acoustic wave devices. He has been working on optical image processing (1968-1970), laser communication (1970-1973) as part of his Ph.D. dissertation requirement, and integrated optical switching devices on $LiNbO_3$ (1973-1974) as post doctorate research, at Carnegie-Mellon University. He is the author or co-author of over 40 journal articles, technical presentations and holds several U.S. patents.

Dr. Yao is currently the Treasurer of the Los Angeles chapter of IEEE Quantum Electronics and Applications Society. He is a member of the Optical Society of America, Eta Kappa Nu, and Sigma Xi.

*

Eddie H. Young, Jr. received the B.S. degree (with honors) in electrical engineering from the University of Illinois, Urbana, in 1961 and the M.S. and Ph.D. degrees in electrical engineering from the University of Texas, Austin, in 1963 and 1968, respectively.

He is currently Director of the Optical Systems at Harris GSG leading engineering activities in optical systems and optical devices development. Prior to this, he was involved in the study of acoustic and optical interaction in bulk and surface waves for applications in signal processing. He first became interested in surface wave acoustics while on a Summer National Science Foundation postdoctorate residence at Stanford Microwave Laboratory. Subsequently, he was funded a NSF Grant to continue research at Old Dominion University. He also received a grant from NASA to work on a computer-aided network and analysis program. He spent 2 years as an Assistant Professor of Electrical Engineering at Old Dominion University, Norfolk, VA. At the University of Texas, his doctoral dissertation and graduate studies primarily involved plasmas and electromagnetic theory. In particular, he is involved in the fabrication of acoustic cells, and in the analysis and experimentation of the cells for correlation and spectrum analysis. In addition, some basic research is carried out in surface wave devices. He has written numerous technical papers.

Dr. Young is a member of the Eta Kappa Nu, Tau Beta Pi, and Sigma Xi.

Proceedings Letters

Quasi-Optics of the Waves Guided by a Slab of Uniaxially Anisotropic Dielectric

S. R. SESHADRI

Abstract—A ray optical method is given for deducing the dispersion relation and the group velocity of the TM wave guided by a slab of uniaxially anisotropic dielectric with particular emphasis on confirming the correctness of the reverse lateral displacement of the ray on total reflection at an interface separating the dielectric from the free space.

A planar slab of uniaxially anisotropic magnetoionic medium occupying the region $-\infty < x, y < \infty$, and $-d < z < d$ is situated in free space as shown in Fig. 1. The magnetization is in the z direction and is normal to the surfaces of the slab. All the field quantities are assumed to be independent of y and have the harmonic time dependence of the form $\exp(-i\omega t)$. With suitable normalizations, inside the slab, the TM waves (H_y, E_x, E_z) are governed by the following relations:

$$\left[\frac{1}{\epsilon}\frac{\partial^2}{\partial x^2} + \frac{\partial^2}{\partial z^2} + \omega^2\right] H_y(x, z) = 0 \tag{1}$$

$$E_x = \frac{1}{i\omega}\frac{\partial H_y}{\partial z}, \quad E_z = -\frac{1}{i\omega\epsilon}\frac{\partial H_y}{\partial x} \tag{2a, b}$$

and $\epsilon = 1 - 1/\omega^2$. The fields in the free space outside the slab are also governed by (1) and (2) with $\epsilon = 1$. We restrict our attention to frequencies below the plasma frequency, that is $\omega < 1$ and $\epsilon < 0$.

Assuming a plane wave solution of the form $H_y(x, z) \sim \exp[i(\beta_x x + \beta_z z)]$, from (1) we obtain the dispersion relation

$$\omega^2 \beta_x^2/(1 - \omega^2) - \beta_z^2 + \omega^2 = 0. \tag{3}$$

Also, we assume that β_x is positive real. For $\omega < 1$, β_z is also real. For the sake of convenience, we take β_z to be also positive. The group velocity $v_g = \hat{x}v_{gx} + \hat{z}v_{gz}$ in the unbounded uniaxially anisotropic dielectric can be deduced from (3) as

$$v_{gx} = \frac{-\omega\beta_x}{(1 - \omega^2)[1 + \beta_x^2/(1 - \omega^2)^2]} < 0$$

$$v_{gz} = \frac{\beta_z}{\omega[1 + \beta_x^2/(1 - \omega^2)^2]} > 0. \tag{4a, b}$$

It follows from (4a) that the wavevector and the ray given by the direction of the group velocity are inclined in opposite directions to the z axis which is normal to the surfaces of the slab. If θ_p and θ_g are, respectively, the angles of incidence of the wavevector and the ray with the surfaces of the slab as shown in Fig. 1, we obtain that

$$\tan\theta_p = \beta_x/\beta_z \quad \tan\theta_g = |v_{gx}|/v_{gz} = \omega^2\beta_x/(1 - \omega^2)\beta_z \tag{5a, b}$$

A plane TM wave is incident on the interface $z = d$ between the slab and the free space from the side of the slab. There is a reflected wave in the slab and a transmitted field in the free space. The magnetic field in the slab is of the form

$$H_y(x, z) = [A_1 \exp\{i\beta_z(z - d)\} + A_2 \exp\{-i\beta_z(z - d)\}] \exp(i\beta_x x) \tag{6}$$

where β_z can be expressed in terms of β_x from (3). From (1) with $\epsilon = 1$, we find the transmitted magnetic field in the free space to be of the form

$$H_y(x, z) = A_3 \exp\{-\alpha_z(z - d)\}\exp(i\beta_x x) \tag{7}$$

where $\alpha_z = (\beta_x^2 - \omega^2)^{1/2}$. We assume that $\beta_x > \omega$ and α_z is positive real leading to a total reflection in the slab. Applying the boundary conditions that H_y and E_x are continuous at the interface $z = d$ yields

$$A_2/A_1 = \exp(-i2\phi) \tag{8}$$

where

$$\tan\phi = \frac{\alpha_z}{k_z} = \frac{(\beta_x^2 - \omega^2)^{1/2}}{[\omega^2 + \omega^2\beta_x^2/(1 - \omega^2)]^{1/2}}. \tag{9}$$

Since $v_{gz} > 0$, A_2/A_1 given in (8) is the reflection coefficient both for the phase and the ray.

By considering a space-like wave packet and a time-like wave packet separately, we can establish [1], [2] that the ray on total reflection at a plane interface between the uniaxially anisotropic dielectric and the free space undergoes a lateral displacement in the x direction as given by

$$2x_s = 2\partial\phi/\partial\beta_x = 2\omega^2/\beta_x\beta_z\alpha_z > 0 \tag{10}$$

and an associated time delay as given by

$$2t_s = -2\partial\phi/\partial\omega = \frac{2\omega}{\beta_z\alpha_z}\left[1 + \frac{\alpha_z^2}{(1 - \omega^2)}\right] > 0. \tag{11}$$

In (8)–(11), ϕ is a function of the independent variables β_x and ω. The incident ray is directed in the $-x$ direction and the lateral displacement determined in (10) is in the $+x$ direction. Thus the ray on total reflection has a reverse lateral displacement. Felsen [3] has previously obtained this result by a systematic evaluation of the integral representation of the field excited by a simple source in a half space of the uniaxially anisotropic dielectric. The lateral displacement can be either in the forward or in the reverse direction but the associated time delay should always be positive. The positive time delay obtained in (11) confirms the correctness of the reverse lateral displacement deduced in (10).

The dispersion relation of the TM wave guided along the slab can be deduced using the zig-zag model for the propagation of the phase fronts of a homogeneous plane wave inside the slab [4]. The zig-zagging wave-normal directions of the successively and totally reflected homogeneous plane wave inside the slab are shown by the line $P_1P_2P_3P_4$ in Fig. 1. The dashed line P_1P_4 represents a phase front. The closure condition is that the resultant phase change between any two points on a phase front along the zig-zagging wave-normal directions including the phase changes occurring on total internal reflection at the two interfaces is equal to an integral multiple of 2π. Symmetry considerations show that the phase change introduced by the total internal reflection is the same for the two interfaces. Since the distance $P_1P_2P_3P_4 = 4d\cos\theta_p$, the total phase change from P_1 to P_4 along the zig-zagging wave-normal directions is obtained as $4\beta d\cos\theta_p - 4\phi$ where β is the magnitude of the wavenumber in the wave-normal directions. Since
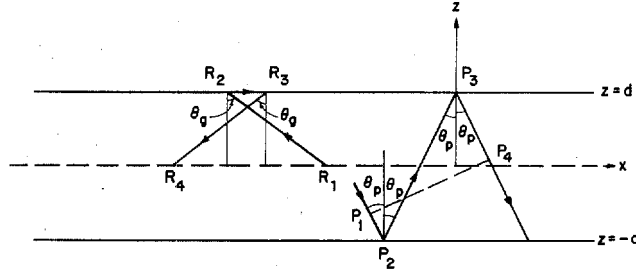
Fig. 1. Geometry of a planar slab of the uniaxially anisotropic dielectric showing the zig-zagging wave-normal directions and the associated zig-zagging ray directions.

$\beta \cos \theta_p = \beta_z$, the closure condition is given by

$$4d[\omega^2 + \omega^2 \beta_x^2/(1 - \omega^2)]^{1/2} - 4\phi = 2\pi n \qquad (12)$$

where n is an integer. This closure condition is the dispersion relation of the TM wave guided by the slab. The allowable values of β_x and the associated discrete values of the angle of incidence θ_p are given by the dispersion relation (12), together with (9) and (5a).

For the guided wave, in view of (12), ω becomes an implicit function of β_x. The group velocity V_g of the guided wave is in the x direction and the x component V_{gx} of V_g is given by $d\omega/d\beta_x$ as obtained from (12). Taking the derivative of (12) with respect to β_x and using (4a) and (5b), we determine the group velocity of the guided wave to be given by

$$-V_{gx} = \frac{d \tan \theta_g - \partial\phi/\partial\beta_x}{d \tan \theta_g/(-v_{gx}) - \partial\phi/\partial\omega}. \qquad (13)$$

Associated with the zig-zagging wave-normal directions are the zig-zagging ray directions. The direction of the ray is different from the corresponding wave-normal direction, as already indicated. On total reflection at an interface between the uniaxially anisotropic dielectric and the free space, a ray undergoes a *reverse* lateral shift. In Fig. 1 $P_1P_2P_3P_4$ is a part of the zig-zagging wave-normal directions incident on the interface at an angle θ_p. $R_1R_2R_3R_4$ represents the corresponding ray directions incident on the interfaces at an angle θ_g. R_1R_4 is on the midplane $z = 0$ of the slab. Since the reflections at the two interfaces are identical, $R_1R_2R_3R_4$ forms a unit cell in the periodic pattern of the zig-zagging ray directions. The times taken for the ray to advance from R_1 to R_2, from R_2 to R_3, and from R_3 to R_4 are given by $d \tan \theta_g/(-v_{gx})$, $-2\partial\phi/\partial\omega$, and $d \tan \theta_g/(-v_{gx})$, respectively. Hence, the time taken for the ray associated with the guided wave to advance from R_1 to R_4 along the actually ray direction is given by $2[d \tan \theta_g/(-v_{gx}) - \partial\phi/\partial\omega]$. In this time the ray associated with the guided wave advances in the $-x$ direction from R_1 to R_4. The distance from R_1 to R_4 is given by $2[d \tan \theta_g - \partial\phi/\partial\beta_x]$. The minus sign in front of $\partial\phi/\partial\beta_x$ specifically takes account of the fact that the lateral displacement is in the reverse direction. Hence the ray method [2] gives the group velocity of the guided wave as

$$-V_{gx} = \frac{d \tan \theta_g - \partial\phi/\partial\beta_x}{d \tan \theta_g/(-v_{gx}) - \partial\phi/\partial\omega} \qquad (14)$$

which is identical to that obtained in (13) from the dispersion relation. The correctness of the group velocity deduced via the ray method confirms the *reverse* direction of the lateral displacement of the ray resulting from the total reflection at the interface between the anisotropic dielectric and the free space.

The reverse lateral displacement was first obtained by Felsen [3]. Since the geometry is uniform in the longitudinal direction, the reversal of the ray in the longitudinal direction is somewhat intriguing. But, the positive time delay associated with the reverse lateral displacement and the correctness of the group velocity of the wave guided by a slab deduced by the ray method which explicitly includes the reverse lateral displacement confirm the correctness of the reverse lateral displacement.

REFERENCES

[1] H. K. V. Lotsch, "Reflection and refraction of a beam of light at a plane interface," *J. Opt. Soc. Amer.*, vol. 58, no. 4, pp. 551–561, Apr. 1968.
[2] H. Kogelnik and H. P. Weber, "Rays, stored energy, and power flow in dielectric waveguides," *J. Opt. Soc. Amer.*, vol. 64, no. 2,

pp. 174–185, Feb. 1974.
[3] L. B. Felsen, "Lateral waves on an anisotropic plasma interface," *IRE Trans. Antennas Propagat.*, vol. AP-10, pp. 347–349, May 1962.
[4] S. R. Seshadri, *Fundamentals of Transmission Lines and Electromagnetic Fields.* Reading, MA: Addison-Wesley, 1971, pp. 428–436.

Comments on "Resolution of Coherent Sources Incident on a Circular Antenna Array"

EDMUND K. MILLER

In the above letter,[1] a technique is presented for using a circular array of N equally spaced antennas to obtain the azimuths and strengths of M ($M \le N/2$) far-field sources. The procedure involves two basic steps: 1) use of a FFT (assuming N is a power of 2) to transform the N individual antenna-element strengths; 2) solution of an Mth-order linear system composed of the transformed data to find the coefficients of an Mth-order polynomial whose roots provide the azimuth angles.

It is the purpose of this brief letter to mention that step 2 above is identical to Prony's Method [1], a procedure which underlies much of modern signal processing. Although the approach in the above letter differs from the more direct approach presented in [1], both lead to the same result as can be seen by comparing their respective starting equations, which are sums of exponentials, and the subsequent linear system and polynomial solutions. For example, the (12), in the above letter, which has the form (redefining the Q_j's to eliminate the alternating minus signs of the author)

$$W_{M+i} = \sum_{j=1}^{M} Q_j W_{j-1+i}, \qquad 0 \le i \le M - 1 \qquad (1)$$

can be seen to be the same as the linear predictor which arises in Prony's method. In (1), the W_k come from step 1 above, and the Q_j are the linear predictor coefficients, solved for from (1), which form the polynomial

$$p^M + Q_1 p^{M-1} + \cdots Q_M = 0 \qquad (2)$$

whose roots provide the source directions (via their complex logarithms).

As Moody points out, basically the same technique works for finding the azimuth angles of far-field sources from linear arrays of equally spaced elements [2]. Furthermore, the azimuth and elevation angles of far-field sources can be found from a similar approach using planar arrays and receiving antennas [3]. Other applications for which Prony's Method has been used include the synthesis of nonuniformly spaced linear arrays [4]; the imaging of linear source distributions from their far fields [5]; and the extraction of the complex resonance frequencies (poles) of objects from the impulse or spectral responses [6], [7].

Reply[2] by M. P. Moody[3]

I wish to thank E. K. Miller for his very useful comments and for the list of references supplied relating to Prony's Method, of which I have not been hitherto aware.

Although he has shown that the method derived was not, after all, novel, it is hoped that the application of the method with deconvolution in solving the resolution problem (epoch detection) of overlapping pulses may be found to be of use.

Since submitting the original correspondence, I have become aware of another closely related method which, from the literature available, does not appear to have been linked with Prony's Method. I refer to Burg's so called maximum entropy method [8], [9] (also known as the autoregressive power spectral density estimate or Linear Prediction Spectral Estimate) and have included some recent references for the benefit of readers in this field [10]–[12]. The method was derived by Burg based on maximizing entropy, but results in a set of equations (also known as modified Yule–Walker equations) which bear a re-

semblance to Prony's matrix equation. Since Burg's method is equivalent to modeling the data as the impulse response of an Nth-order recursive digital filter (IIR filter) whose Z coefficients are the unknowns in the matrix equation [13], the positions of poles can be found on the Z plane by solution of the resulting polynominal in Z. Some work has also been carried out combining autoregressive with zero-producing moving average (ARMA) processes with good results in noisy conditions [14].

REFERENCES

[1] F. Hildebrand, *Introduction to Numerical Analysis*. New York: McGraw-Hill, 1956, pp. 378–382.
[2] J. M. Kelso, "Measuring the vertical angles of arrival of HF skywave signals with multiple modes," *Radio Sci.*, vol. 7, pp. 245–250, 1972.
[3] C. J. Benning, "Adaptive array beamforming and steering using Prony's method," in *Proc. Annu. Symp. USAF Antenna R&D*, AFAL (Univ. of Illinois, Allerton, IL), 1969.
[4] E. K. Miller and D. L. Lager, "Radiation field analysis and syntheses using Prony's method," *Electron. Lett.*, vol. 14, pp. 180–181, 1978.
[5] E. K. Miller, D. L. Lager, and J. T. Okada, "Imaging of linear source distributions," Lawrence Livermore Laboratory, Rep. UCRL-52822, Nov. 1979.
[6] A. J. Poggio, M. J. Van Blericum, E. K. Miller, and R. Mittra, "Evaluation of a processing technique for transient data," *IEEE Trans. Antennas Propagat.*, vol. AP-26, pp. 165–173, Jan. 1978.
[7] J. N. Brittingham, E. K. Miller, and J. L. Willows, "Pole extraction from real-frequency information," *Proc. IEEE*, vol. 68, pp. 263–273, Feb. 1980.
[8] J. P. Burg, "Maximum entropy power spectral analysis," presented at the 37th Annu. Meet. Society of Exploration Geologists (Oklahoma City, OK), Oct. 31, 1967.
[9] ——, "Maximum entropy spectral analysis," Ph.D. dissertation, Stanford University, Stanford, CA, 1975.
[10] D. N. Swingler, "A comparison between Burg's maximum entropy method and a nonrecursive technique for the spectral analysis of deterministic signals," *J. Geophys. Res.*, vol. 84, no. B2, pp. 679–685, Feb. 1979.
[11] S. Holm and J. M. Hovem, "Estimation of scalar ocean wave spectra by the maximum entropy method," *IEEE J. Oceanic Eng.*, vol. Oe-4, pp. 76–83, July 1979.
[12] S. M. Kay, "The effects of noise on the autoregressive spectral estimator," *IEEE Trans. Acoust., Speech and Signal Processing*, vol. ASSP-27, pp. 478–485, Oct. 1979.
[13] A. van den Bos, "Alternative interpretation of maximum entropy spectral analysis," *IEEE Trans. Inform. Theory* (Corres.), vol. IT-17, pp. 493–494, July 1971.
[14] M. Kaveh, "High resolution spectral estimation for noisy signals," *IEEE Trans. Acoustics, Speech and Signal Processing* (Corres.), vol. ASSP-27, pp. 286–288, June 1979.

Electrostatic Fields Inside Two Planar Distributions of Potential

D. A. DE WOLF

Abstract—The potentials and fields inside two parallel planar distributions of potential can be written as Green's function integrals. Each Green's function can be evaluated numerically by decomposing it into two series of terms (one for large and one for small distances) which converge rapidly within their intervals of use. The accuracy of truncation after a few terms is evaluated.

I. INTRODUCTION

The calculation of electron trajectories in electron devices requires knowledge of interior electric fields determined by boundary voltages. In many such devices, the shape of the boundary voltage plates is too complicated for analytical determination of the interior fields. With the advent of digital electronic computers, it has become feasible to generate accurate numerical solutions to potentials and fields in the interior of electron devices, but the cost of generating enough field points, or of regenerating trajectory points when needed, for calculating electron trajectories can increase rapidly with increasing volume. For many applications, especially for devices which approximate a sandwich of planar distributions of boundary voltages over large areas, the cost can become prohibitive. In this work, we propose a semianalytical, seminumerical technique to overcome this difficulty. We shall assume that two parallel planar distributions of voltage form the boundary (if necessary, two planar grids of voltages can be generated numerically to

bound a convenient part of the interior). Unlike a previous communication [1], the two voltage distributions may be different.

A Green's function connecting an arbitrary interior point to all grid points of the two planes can be calculated for interior potential and fields. It can be expressed as either of two series expansions (one for large, the other for small distances). Only a few terms of each are needed for reasonable accuracy. The problem is essentially reduced to a two-dimensional integral over the two planar boundary distributions.

II. ANALYSIS

Let the two bounding plates by located at $y_i = \pm Y$ (plus sign for $i = 1$, minus sign for $i = 2$). Let $V_i(x_0, z_0)$ be the voltage distribution on plate i. Consider an interior point $r = (x, y, z)$ and define $R_i = (x - x_0, y - y_i, z - z_0)$ as the distance vector between r and a point on plate i. The methods of [1] then yield for potential $\Phi(r)$,

$$\Phi(r) = \sum_{i=1}^{2} \iint dx_0 \, dz_0 \, V_i(x_0, z_0) \, G(R_i)$$

$$G(R_i) = \frac{1}{2\pi} \int_0^\infty dK K J_0(K R_p) \frac{\sinh[K(Y \pm y)]}{\sinh(2KY)} \tag{1}$$

where $R_p = [(x - x_0)^2 + (z - z_0)^2]^{1/2}$ is the parallel component of R_i. Further development of the Green's function $G(R_i)$ can be pursued, as in [1], to obtain,

$$G(R_i) = \frac{1}{2\pi Y^2} [G_1(\xi, \eta) - G_2(\xi, \eta)]$$

$$G_1(\xi, \eta) \equiv \sum_{m=0}^{\infty} \left\{ (4m + 1 \mp \eta)/[(4m + 1 \mp \eta)^2 + \xi^2]^{3/2} \right\}$$

$$G_2(\xi, \eta) \equiv \sum_{m=0}^{\infty} \left\{ (4m + 3 \pm \eta)/[(4m + 3 \pm \eta)^2 + \xi^2]^{3/2} \right\} \tag{2}$$

where $\xi = [(x - x_0)^2 + (z - z_0)^2]^{1/2}/Y$ and $\eta = y/Y$ are dimensionless versions of variables R_p and y, and where we retain the convention that the upper sign holds for $i = 1$ and the lower for $i = 2$. The convergence of (2) requires at least as many terms as are given by the integer closest to the ratio $R_p/4Y$. Hence distant source points require relatively many terms in the Green's function. It is desirable to supplement (2) by an expansion that handles distant source points more economically. Fortunately an alternative exists. Rewrite $G(R_i)$ as,

$$G(R_i) = \frac{1}{4\pi Y^2} \int_0^\infty dt t J_0(\xi t) \left[\frac{\cosh(\eta t)}{\cosh(t)} \pm \frac{\sinh(\eta t)}{\sinh(t)} \right]. \tag{3}$$

Utilizing the fact that the Bessel function of the first kind and zero order $J_0(\xi t)$ can be written as the real part of a Hankel function that goes to zero sufficiently rapidly when $t \to \infty$, we may deform the integration in the complex t plane to one along the positive imaginary axis that contains infinitesimal half circles around the singularities of $1/\cosh(t)$ and $1/\sinh(t)$.[1] The resulting series is

$$G(R_i) = \frac{1}{2\pi Y^2} [G_c(\xi, \eta) - G_s(\xi, \eta)]$$

$$G_c(\xi, \eta) \equiv \pi \sum_{m=0}^{\infty} (-1)^m (m + \tfrac{1}{2}) \cos[(m + \tfrac{1}{2})\pi\eta] K_0[(m + \tfrac{1}{2})\pi\xi]$$

$$G_s(\xi, \eta) = \pm \pi \sum_{m=0}^{\infty} (-1)^m m \sin(m\pi\eta) K_0(m\pi\xi) \tag{4}$$

with the upper sign for $i = 1$ and the lower for $i = 2$. The smallest argu-

[1] It may be helpful to bear in mind that the real part of an integral of a complex function along the positive imaginary axis results. The infinitesimal half circles yield real contributions, whereas the connecting pieces along the imaginary axis only yield purely imaginary contributions to the integral. Hence only the former contribute to the real part of the integral.

TABLE I
POTENTIAL

η \ ξ		0	0.5	1	1.5	2
-0.5	A	.04709	.03817	.02227	.01076	.00478
	E	.04735	.03843	.02232	.01076	.00478
-0.25	A	.08358	.06420	.03402	.01522	.00648
	E	.08397	.06459	.03399	.01522	.00648
0	A	.1452	.1006	.04519	.01820	.00735
	E	.1458	.1011	.04520	.01820	.00735
0.25	A	.2727	.1532	.05305	.01873	.00713
	E	.2734	.1539	.05309	.01873	.00713
0.5	A	.6297	.2184	.05178	.01582	.00569
	E	.6305	.2192	.05173	.01582	.00569

TABLE II
HORIZONTAL FIELD

η \ ξ		0	0.5	1	1.5	2
-0.5	A	0	.0308	.0290	.0168	.07952
	E	0	.0308	.0294	.0168	.07952
-0.25	A	0	.0638	.0513	.0255	.01117
	E	0	.0638	.0511	.0255	.01117
0	A	0	.1342	.0605	.0333	.01320
	E	0	.1342	.0804	.0333	.01320
0.25	A	0	.2993	.1142	.0375	.01335
	E	0	.2993	.1147	.0375	.01335
0.5	A	0	.6743	.1356	.0344	.01105
	E	0	.6743	.1350	.0344	.01105

TABLE III
VERTICAL FIELD

η \ ξ		0	0.5	1	1.5	2
-0.5	A	-.1184	-.0902	-.0461	-.01974	-.00812
	E	-.1189	-.0907	-.0462	-.01974	-.00812
-0.25	A	-.1822	-.1212	-.0471	-.01548	-.00535
	E	-.1827	-.1217	-.0468	-.01548	-.00535
0	A	-.3343	-.1744	-.0406	-.00775	-.00143
	E	-.3348	-.1749	-.0410	-.00775	-.00143
0.25	A	-.7683	-.2471	.0184	.00423	.00331
	E	-.7688	-.2476	.0182	.00423	.00331
0.5	A	-.2559	-.2369	.0346	.01934	.00810
	E	-.2559	-.2375	.0347	.01934	.00810

$$g_\xi(\xi, \eta) = \pi^2 \sum_{m=0}^{\infty} (-1)^m \left\{ (m + \tfrac{1}{2})^2 \cos\left[(m + \tfrac{1}{2})\pi\eta \right] K_1[(m + \tfrac{1}{2})\pi\xi] \right.$$

$$\left. \mp m^2 \sin(m\pi\eta) K_1(m\pi\xi) \right\}. \tag{7}$$

The sign convention is retained in (6) and (7): upper sign for $i = 1$ and lower sign for $i = 2$.

Calculations of the three Green's functions of (4) and (5) for $y = 1$ are shown in Tables I–III in the rows marked "E" for values of ξ and for $|\eta| \leqslant \tfrac{1}{2}$. The rows marked "$A$" give approximations for the $m < 3$ partial sums in (4), (6), and (7). The description of this half space $|\eta| \leqslant \tfrac{1}{2}$ by just a few terms appears to be accurate to well within a percent.

REFERENCE

[1] D. A. de Wolf, "A useful potential solution $V(x, y, z)$ for symmetric rectangular stepwise constant-potential boundaries at $y = \pm Y$," Proc. IEEE, vol. 66, pp. 85–86, Jan. 1978.

Correction to "Criteria for the Separation of Real and Complex Natural Modes of Dynamical Systems"

F. M. REZA

In the above letter,[1] (15) and (16) contain misprints. The correct version is

$$\| \sqrt{C} R \sqrt{C} \|^2 \lessgtr 4 \| \sqrt{C} L \sqrt{C} \|.$$

Frequency Domain Least-Mean-Square Algorithm

S. SHANKAR NARAYAN AND A. M. PETERSON

Abstract—Frequency domain adaptive filtering can be performed by Fourier transforming the input-signal vector and weighting the contents of each frequency bin. By reducing the eigenvalue spread of the data autocorrelation matrix, frequency domain filtering promises great improvements in convergence rate over the conventional time-domain adaptive filtering.

Adaptive filters are being widely used in a variety of applications, including noise cancellation [1], linear prediction filtering [2], and spectral estimation [3]. Filters of this type are generally implemented in the time domain in tapped-delay-line (TDL) form, and the Widrow-Hoff adaptive least-mean-square (LMS) algorithm [4] is used to obtain the filter parameters. The purpose of this letter is to describe a frequency domain equivalent of the time domain adaptive filter. This

ment of a Bessel function in (4) is $\pi\xi/2 \approx 1.6\xi$. Since $K_0(x)$ goes as $x^{-1/2} \exp(-x)$ for large x, we find that the sum of all these terms converges rapidly with increasing m when $\xi \geqslant 1$. Hence (4) is the desired alternative to (2) for large ξ.

Similar expansions for the electric field are easily worked out [$E(r)$ is the negative gradient of the potential $\Phi(r)$]. Each component of the electric field defines a new Green's function,

$$G_y(R_i) = \frac{1}{2\pi Y^3} g_\eta(\xi, \eta)$$

$$G_x(R_i) = \frac{(x - x_0)}{2\pi Y^4} g_\xi(\xi, \eta)$$

$$G_z(R_i) = \frac{(z - z_0)}{2\pi Y^4} g_\xi(\xi, \eta) \tag{5}$$

and we shall simply give the expansions of g_ξ and g_η for $\xi < 1$ and $\xi \geqslant 1$.

Small ξ ($\xi < 1$):

$$g_\eta(\xi, \eta) = \sum_{m=0}^{\infty} \left\{ \frac{\xi^2 - 2(4m + 1 \mp \eta)^2}{[(4m + 1 \mp \eta)^2 + \xi^2]^{5/2}} + \frac{\xi^2 - 2(4m + 3 \pm \eta)^2}{[(4m + 3 \pm \eta)^2 + \xi^2]^{5/2}} \right\}$$

$$g_\xi(\xi, \eta) = 3 \sum_{m=0}^{\infty} \left\{ \frac{4m + 1 \mp \eta}{[(4m + 1 \mp \eta)^2 + \xi^2]^{5/2}} \right.$$

$$\left. - \frac{4m + 3 \pm \eta}{[(4m + 3 \pm \eta)^2 + \xi^2]^{5/2}} \right\}. \tag{6}$$

Large ξ ($\xi \geqslant 1$):

$$g_\eta(\xi, \eta) = \pi^2 \sum_{m=0}^{\infty} (-1)^m \left\{ (m + \tfrac{1}{2})^2 \sin\left[(m + \tfrac{1}{2})\pi\eta \right] K_0[(m + \tfrac{1}{2})\pi\xi] \right.$$

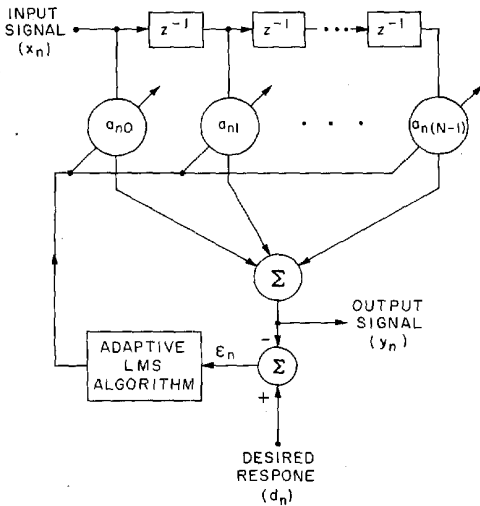$$\left. \pm m^2 \cos(m\pi\eta) K_0(m\pi\xi) \right\}$$

Fig. 1. A conventional TDL adaptive filter.

method promises great improvements in convergence rate over the time domain approach.

The general form of the TDL adaptive filter [4] is shown in Fig. 1. Its function is to weight and sum the delayed samples of the input signal x_n to form an adaptive output. The input signal vector X_n and the weight vector A_n at the time of nth iteration are defined as

$$X_n = [x_n \, x_{n-1} \cdots x_{n-(N-1)}]^T \tag{1}$$

and

$$A_n = [a_{n0} \, a_{n1} \cdots a_{n(N-1)}]^T \tag{2}$$

respectively. The corresponding filter output is

$$y_n = X_n^T A_n \tag{3}$$

The error ϵ_n is the difference between the desired response d_n and the output y_n

$$\epsilon_n = d_n - y_n. \tag{4}$$

In the LMS adaptive algorithm, the mean-square error $(\overline{\epsilon_n^2})$ is minimized by continuously updating the weight vector A_n as each new data sample is received, according to the expression

$$A_{n+1} = A_n + 2\mu X_n \epsilon_n \tag{5}$$

where μ is a positive constant that governs the rate of convergence, and proper choice of this constant ensures stability of the adaptive process.

It can be shown [5] that for stationary input and sufficiently small μ, the speed of convergence of the algorithm is dependent on the ratio of maximum to minimum eigenvalues, $\lambda_{max}/\lambda_{min}$, of the data auto-correlation matrix R_{XX},

$$R_{XX} = E(X_n X_n^T). \tag{6}$$

Slow convergence rate can be expected when this ratio is large. This eigenvalue spread is bounded by the relation [2],

$$1 \leqslant \frac{\lambda_{max}}{\lambda_{min}} \leqslant \frac{\displaystyle\max_{0 \leqslant \omega \leqslant 2\pi} |X(e^{j\omega})|^2}{\displaystyle\min_{0 \leqslant \omega \leqslant 2\pi} |X(e^{j\omega})|^2} \tag{7}$$

where $X(e^{j\omega})$ is the z-transform of the input signal x_n evaluated at $z = e^{j\omega}$. Therefore, an approach to accelerate the convergence rate would be to reduce the spectral dynamic range of the input signal. This can be achieved by implementing adaptive filtering in the frequency domain, and this will be described below.

A block diagram of the frequency domain adaptive filter is shown in Fig. 2. The input signal is filtered by a bank of band-pass filters, implemented digitally by the discrete Fourier transform (DFT). The filtered signals are weighted and summed to produce the time domain output signal. Fig. 3 is a symbolic representation of the frequency domain adaptive filter. The vector Z_n

$$Z_n = [z_{n0} \, z_{n1} \cdots z_{n(N-1)}]^T \tag{8}$$
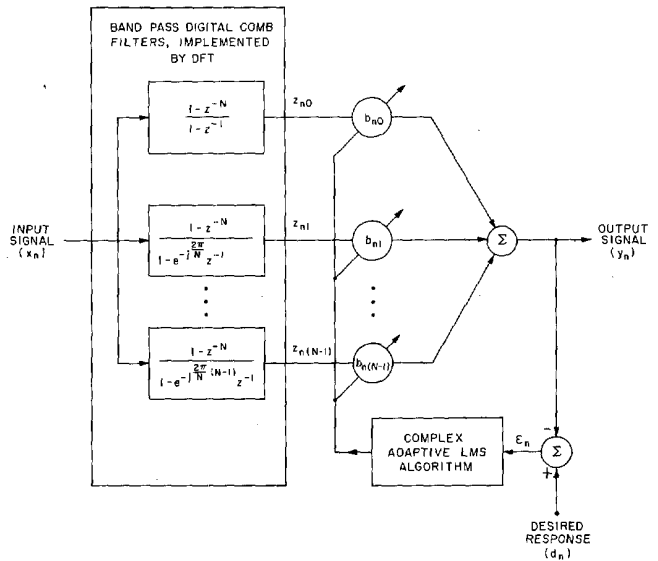
Fig. 2. A frequency-domain adaptive filter.
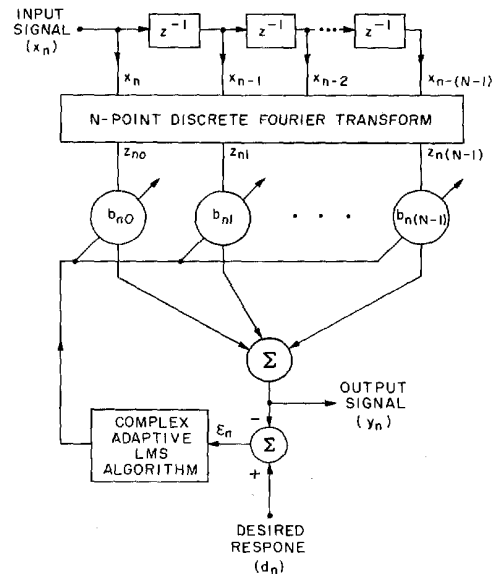
Fig. 3. A symbolic representation of frequency-domain adaptive filter.

is related to the input vector X_n by the orthogonal transformation

$$Z_n = W X_n \tag{9}$$

where W is an $N \times N$ DFT matrix [6] whose (p, q)th element is $e^{(-j2\pi pq/N)}$. The output and the corresponding error signal are

$$y_n = Z_n^T B_n \tag{10}$$

and

$$\epsilon_n = d_n - y_n \tag{11}$$

respectively, where

$$B_n = [b_{n0} \, b_{n1} \cdots b_{n(N-1)}]^T \tag{12}$$

is the frequency domain weight vector. The complex LMS algorithm [7] is used to recursively update the weight vector B_n. The weight vector update equation is

$$B_{n+1} = B_n + 2\mu \Lambda^{-2} \epsilon_n \overline{Z}_n \tag{13}$$

where μ is the adaptive step size and Λ^2 is an $N \times N$ diagonal matrix

whose (i, i)th element is equal to the power estimate (computed by averaging with a moving window) of the ith DFT output z_{ni}. When both the input and the desired signals are real, the components of the weight vector B_n satisfy the relation

$$b_{ni} = \bar{b}_{n(N-i)}, \qquad i = 1, 2, \cdots, \frac{N}{2}. \tag{14}$$

This fact can be used to reduce the computational requirements for weight vector updating. The inverse of matrix Λ^2 exists as long as the data auto-correlation matrix R_{XX} is positive definite. The use of $\mu\Lambda^{-2}$ in controlling the adaptive step size is functionally equivalent (as far as the adaption process is concerned) to normalizing the power in each of the DFT bins to unity before weighting. This has the same effect as that of pre-whitening the input signal, compressing the eigenvalue spread, and this results in faster convergence of the weight vector.

The frequency domain LMS algorithm is being used in adaptive line enhancers [1] and speech processing [2]. Early experimental studies have been encouraging, and the results will be presented in future publication. Theoretical analysis of this algorithm is under way.

REFERENCES

[1] B. Widrow *et al.*, "Adaptive noise cancelling: Principles and its applications," *Proc. IEEE*, vol. 63, pp. 1692–1716, Dec. 1975.
[2] J. Makhoul, "Linear prediction: A tutorial review," *Proc. IEEE*, vol. 63, pp. 561–580, Apr. 1975.
[3] L. Griffiths, "Rapid measurement of digital instantaneous frequency," *IEEE Trans. Acoust., Speech, Signal Processing*, vol. ASSP-23, pp. 209–222, Apr. 1975.
[4] B. Widrow, "Adaptive filters," in *Aspects of Network and System Theory*, R. Kalman and N. DeClaris, Eds. New York: Holt, Rinehart, and Winston, 1971, pp. 563–587.
[5] B. Widrow *et al.*, "Stationary and non-stationary learning characteristics of the LMS adaptive filter," *Proc. IEEE*, vol. 64, pp. 1151–1162, Aug. 1976.
[6] A. V. Oppenheim and R. W. Shafer, *Digital Signal Processing*. Englewood Cliffs, NJ: Prentice-Hall, 1975.
[7] B. Widrow *et al.*, "The complex LMS algorithm," *Proc. IEEE (Lett.)*, vol. 63, pp. 719–720, Apr. 1975.

An Autoregressive Moving Average Tone Detector

C. R. GUARINO

Abstract—A new method for estimating tones in an arbitrary spectrum is presented. An autoregressive-moving average estimator is formulated and transformed into a linear regression problem. Many of the shortcomings of an "all pole" model are overcome and simulated test results indicate that the estimates are not particularly sensitive to additive noise. The main advantages of this new method are computational simplicity and robustness in noise environments. The algorithm can be useful in all areas where spectral information must be extracted in a computationally efficient fashion.

I. INTRODUCTION

The purpose of this paper is to present a new method for estimating the predominant frequency from a finite number of noisy discrete-time observations. The classical approach involves a transformation into the frequency domain via a discrete Fourier transform and searching for a peak. Much literature exists detailing this method [1]–[3]. The major disadvantage is that even using the fast Fourier transform (FFT) algorithm, the computational burden can be large. In addition, computing the spectrum at every point provides more information than is necessary in many applications.

More recently, an algorithm has been proposed which estimates the peak frequency without performing a discrete Fourier transform (DFT) [4]. Essentially, the first three spectral moments are measured, the power, power mean frequency, and mean-square bandwidth. Estimation is predicated on implementing a quadrature detector which could introduce problems in balancing each channel.

The maximum-entropy spectral estimation method popularized by Burg has many advantages [5], [6], if only a peak frequency is of interest. The method presented here has several similarities with the Burg algorithm. Like the Burg method, it postulates a power spectrum of a particular structure. However, instead of assuming an all-pole structure, it assumes a more general pole-zero structure. Estimation of the pole-zero coefficients is based on a variation of the procedure presented in [7]. It will be shown that computationally fewer operations are required than with the DFT algorithm if the number of data points is large.

This algorithm's greatest usefulness will be in those applications where the frequency containing the largest energy density is unknown. Radar and Sonar measurement systems, in addition to modem testing, suggest themselves as possible application areas.

II. DERIVATION

One way to motivate the derivation is to assume that an $H(S)$, representing the Laplace transform of the transfer function of a linear time-invariant system must be designed which has a clearly defined peak in frequency. In general, a second-order $H(s)$ is given by

$$H(S) = \frac{d_1 s + d_2}{S^2 + 2\sigma S + (\sigma^2 + \Omega^2)}. \tag{1}$$

The pole locations are at $S_{1,2} = -\sigma \pm j\Omega$ where if σ is positive and Ω real, a stable system with a peak at Ω results. $H(S)$ can be mapped into the Z-domain yielding an $H(Z)$ of the following form:

$$H(Z) = \frac{a_0 + a_1 Z^{-1}}{1 + b_1 Z^{-1} + b_2 Z^{-2}}. \tag{2}$$

For the purposes of this paper, the numerator term provides little information except that a_0 and a_1 are two parameters which must be estimated. The denominator contains information relating to the peak frequency; b_1 and b_2 can be expressed in terms of σ and Ω as follows:

$$b_1 = -2e^{-\sigma} \cos \Omega \tag{3}$$

$$b_2 = e^{-2\sigma} \tag{4}$$

The impulse response recursion equations for $H(Z)$ are

$$h_n = -\sum_k b_k h_{n-k} + a_n, \quad 1 \leqslant n \leqslant 2 \tag{5}$$

$$h_n = -\sum_k b_k h_{n-k}, \qquad n > 2 \tag{6}$$

which indicates that h_n is a nonlinear function of the (b_k) and (a_k). This minimization is a difficult nonlinear programming problem even for the comparatively simple case of two poles and two zeros.

The approach taken in this paper relies upon transforming a nonlinear estimation problem into a linear regression problem. This is accomplished in the following fashion. Equation (2) can be expanded in matrix form as

$$
\begin{bmatrix} h_0 \\ h_1 \\ h_2 \\ \vdots \\ h_n \end{bmatrix} =
\begin{bmatrix}
1 & 0 & 0 & 0 & \cdots & 0 \\
0 & 1 & h_0 & 0 & & \\
0 & 0 & h_1 & h_0 & & \\
0 & 0 & h_2 & h_1 & & \vdots \\
& & h_3 & & & \\
\vdots & \vdots & \vdots & \vdots & & \\
0 & 0 & h_{N-1} & h_{n-2} & \cdots & 0
\end{bmatrix}
\begin{bmatrix} a_0 \\ a_1 \\ -b_1 \\ -b_2 \\ 0 \\ \vdots \\ 0 \end{bmatrix}
\tag{7}
$$

$$\hat{h} = \hat{A}\,\hat{\Gamma} \tag{8}$$

where (h_i) is the impulse response given by the Maclaurin series expan-

sion of $H(Z)$ as

$$H(Z) = \sum_{i=0}^{N-1} h_i Z^{-i}. \tag{9}$$

Equation (8) can be solved by the least squares normal equations given by

$$\tilde{\Gamma} = (A^T A)^{-1} A^T \hat{h}. \tag{10}$$

As is well known, the ordinary least squares estimators of $\tilde{\Gamma}$ of the generalized linear regression model are unbiased and consistent. In addition, the maximum likelihood estimators of the regression coefficients, $\tilde{\Gamma}$, are equivalent to the least squares estimators.

Equation (10) can be readily solved for $\tilde{\Gamma}$ leading to the following equations for $\tilde{b}_1$ and $\tilde{b}_2$.

$$\tilde{b}_1 = - \left\{ k_3 h_1 + k_5 \sum_{i=0}^{N-2} h_i h_{i+1} + k_6 \sum_{i=0}^{N-3} h_i h_{i+2} \right\}$$

$$\tilde{b}_2 = - \left\{ k_4 h_1 + k_6 \sum_{i=0}^{N-2} h_i h_{i+1} + k_7 \sum_{i=0}^{N-3} h_i h_{i+2} \right\} \tag{11}$$

where

$$k_3 = - \left[h_0 \sum^{N-3} h_i^2 \right] \Big/ D$$

$$k_4 = \left[h_0 \sum^{N-3} h_i h_{i+1} \right] \Big/ D$$

$$k_5 = \left[\sum^{N-3} h_i^2 \right] \Big/ D$$

$$k_6 = - \left[\sum h_i h_{i+1} \right] \Big/ D$$

$$k_7 = \left[\sum^{N-2} h_i^2 - h_0^2 \right] \Big/ D$$

$$D = \left[\sum^{N-2} h_i^2 \right] \left[\sum^{N-3} h_i^2 \right] - \left[\sum^{N-3} h_i h_{i+1} \right] - \left[\sum^{N-3} h_i^2 \right] h_0^2. \tag{12}$$

III. Computational Considerations

Equations (11) and (12) have been expressed in a form that is suitable for exposition but not for computation. It can be observed that many variables are simple functions of other, already computed, variables. For instance, if $\sum^{N-3} h_i^2$ has already been computed, then

$$\sum_{i=0}^{N-2} h_i^2 = \sum_{i=0}^{N-3} h_i + h_{N-2}^2$$

which involves just a single multiplication and addition.

If a measure of an algorithm's complexity is the total number of operations involved, then the complexity of this algorithm is linear in N. Depending on the method used to compute operations, the total number of operations is given by $K * N$ where K varies between 3 and 5 and N is the length of the input data record. For the DFT using the FFT, the number of computations varies as $N \log_2 N$. For large data records ($N > 32$) the autoregressive-moving average (ARMA) method has an advantage.

IV. Experimental Results

A computer program was written to test the accuracy of three methods of estimating a pure tone. The methods are, DFT processing [1], the method of moments [4] and the method presented in this paper. A pure sinusoidal was generated located approximately at the center of the normalized frequency spectrum (frequency normalized with respect to the sampling rate.) The sinusoid was added to a Gaussian random
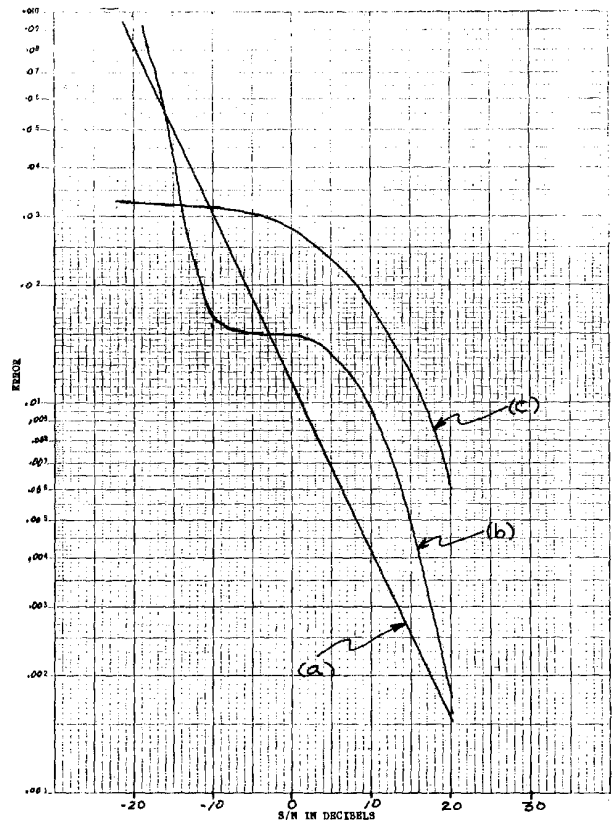
Fig. 1. Error performance of three frequency estimators. (a) ARMA estimation (b) DFT estimation (c) method of moments.

process of variable intensity. The error was computed as the magnitude of the difference between the true and estimated frequency divided by the true frequency. The results of this experiment are shown in Fig. 1. It can be noticed that on a logarithmic scale the error is linear for the ARMA method. In addition, the errors for large and small S/N ratios is smaller for the ARMA than for the DFT method.

V. Conclusion

A method has been presented which can efficiently and accurately estimate the peak frequency in an arbitrary spectrum. Simulated testing has shown the viability of the method.

Many alterations to the ARMA method of frequency estimation can be suggested. One modification is to use a weighted least squares formulation where the weight are determined by the errors of the estimates. The estimation is then a two step process.

Alternately, following the development of [7], the problem can be solved recursively. The frequency can then be estimated adaptively permitting a continuous tracking of the peak frequency.

References

[1] D. C. Rife and G. A. Vincent, "Use of the discrete Fourier transform in the measurement of frequencies and lends of tones," Bell Syst. Tech. J., vol. 49, pp. 197–228, Feb. 1970.

[2] R. B. Blackman and T. W. Tukey, The Measurement of Power Spectra from the Point of View of Communications Engineering. New York: Dover, 1959.

[3] L. C. Palmer, "Course frequency estimation using the discrete Fourier transform," IEEE Trans. Inform. Theory, vol. IT-20, pp. 104–109, Jan. 1974.

[4] J. N. Denenberg, "Spectral moment estimators: A new approach to tone detection," Bell Syst. Tech. J., vol. 55, pp. 143–155, Feb. 1976.

[5] J. P. Burg, "Maximum entropy spectral analysis," presented at the 37th Meet. Soc. Exploration Geophysicists, Oklahoma City, OK, Oct. 31, 1967.

[6] T. J. Ulrych, D. E. Smylie, O. G. Jensen, and G. K. C. Clarke, "Predictive filtering and smoothing of short records by using maximum entropy," J. Geophys. Res., vol. 78, pp. 4959–4964, 1973.

[7] C. R. Guarino, "Adaptive signal processing using FIR and IIR filters," Proc. IEEE, pp. 957–959, June 1979.

A Method for Improving the Classification Speed of Clustering Algorithms Which Use a Euclidean Distance Metric

J. D. CURLE AND J. J. HILL

Abstract—Many pattern recognition computer programs use one of the clustering algorithm techniques. Often these algorithms use a Euclidean distance metric as a similarity measure.

A scheme is proposed where both the Euclidean metric and a more simple city-block metric are utilized together to reduce overall classification time. The relation between the Euclidean and city-block distances is introduced as a scalar function. The bounds of the function are given and used to decide whether classification of each pattern vector is to be achieved by the computationally slow Euclidean distance or the faster city-block distance. The criteria is that the classification should be identical to the original Euclidean only scheme.

I. Introduction

Given a specific n-dimensional pattern vector, one of the important operations required of a clustering algorithm is to select from the K class references, the class reference which is closest to the pattern. The closeness can be expressed by one of the many forms of distance metric [1].

Many clustering algorithms produce optimum results if the Euclidean metric is used [2]. This metric can be expressed as

$$E(X, Z_j) = [(X - Z_j)^T (X - Z_j)]^{1/2}$$

where X represents the n-dimensional vector to be classified and Z_j represents the jth class reference point. The task is to compute and select

$$\text{MIN } E(X, Z_j), \quad j = 1, 2, \cdots, K.$$

For each pattern vector there are K computations.

The unweighted city-block distance metric can be computed more quickly than the Euclidean metric because no multiplications are involved (this is especially true for computers using software multiplication). The unweighted city-block metric is given by

$$C(X, Z_j) = \sum_{k=1}^{n} |X_k - Z_{jk}|$$

where k is the kth component of the n-dimensional vector.

However, for a scheme which is optimum using a Euclidean metric, inferior classification accuracy would result if a city-block metric was used, albeit with an improvement in classification speed.

Under certain conditions on the data, the minimum of the K Euclidean distances corresponds to the minimum of the K city-block distances. Under these conditions identical classification of the pattern vector is produced for both measures. The fact that the magnitudes of the two distances may be different does not affect classification.

If it could be deduced for a particular pattern vector, that the smallest of the set of Euclidean distances corresponded to the smallest of the set of city-block distances, then the city-block distances could be computed instead of the Euclidean and a saving in classification time would result.

A method of deciding which one of the distances to employ is given below.

II. A Minimum Euclidean Distance From a City-Block Ratio

Consider two city-block distances, designated C_1 and C_2. A logic decision is to be made to either use the smaller of C_1 and C_2 to obtain a classification, or to reject them, and compute and utilise the smallest Euclidean distance. Lemmas 1 and 2 will be given without proof since this is beyond the scope of this letter.

Lemma 1: The relationship between the Euclidean and city-block metrics is given by

$$C_j = E_j \cdot g_j(\theta n) \tag{1}$$

where $g_j(\theta n)$ is a scalar function of the orientation of E_j with respect to the axes of the n-dimensional space containing X and Z_j.

Lemma 2: $g_j(\theta n)$ is a bounded function

$$1 \leqslant g_j(\theta n) \leqslant \sqrt{n} \tag{2}$$

where n represents the dimension of the space. From (1)

$$\frac{E_1}{E_2} = \frac{C_1 \cdot g_2(\theta n)}{C_2 \cdot g_1(\theta n)}. \tag{3}$$

From (2)

$$\frac{1}{\sqrt{n}} \leqslant \frac{g_2(\theta n)}{g_1(\theta n)} \leqslant \sqrt{n}. \tag{4}$$

Now $E_1/E_2 > 1$ implies that $E_1 > E_2$, which is the information required by the classifier. But from (3)

$$\frac{C_1 \cdot g_2(\theta n)}{C_2 \cdot g_1(\theta n)} > 1 \text{ gives the same information.}$$

Rearranging gives the logic condition

$$\text{IF } \frac{C_1}{C_2} > \frac{g_1(\theta n)}{g_2(\theta n)} \text{ then } E_1 > E_2. \tag{5}$$

It is impractical to compute $g_1(\theta n)/g_2(\theta n)$ since this operation requires more time than to compute E_1 and E_2 directly.

However, from (4) and (5) the following logic condition is valid

(a) $\text{IF } \dfrac{C_1}{C_2} > \sqrt{n}, \text{ then } E_1 > E_2.$

Corollaries

(b) $\text{IF } \dfrac{C_1}{C_2} = \sqrt{n}, \text{ then } E_1 \geqslant E_2$

(c) $\text{IF } \dfrac{C_1}{C_2} < \dfrac{1}{\sqrt{n}}, \text{ then } E_1 < E_2$

(d) $\text{IF } \dfrac{C_1}{C_2} = \dfrac{1}{\sqrt{n}}, \text{ then } E_1 \leqslant E_2.$

These are the test conditions which decide whether a city-block or a Euclidean distance is to be used for the classification of a particular pattern vector X. Note that to provide the tests two city-block distances must be computed initially.

If test (a) is TRUE, then no Euclidean distances E_1 and E_2 need be computed and E_2 is considered as the smaller of the two distances by inference.

It can be seen that test (c) gives the same information as test (a), but in (a) $C_1 > C_2$ and in (b) $C_1 < C_2$. It can easily be arranged that C_1 represents the larger of the pair and therefore tests (c) and (d) become redundant.

For any practical classification scheme, when several distances to a point are equal, some rule arbitrarily decides which distance is to be used to classify the point. Under condition (b), E_2 is never greater than E_1, but may be equal to it. Thus a convenient rule is to select E_1 as the distance for classification from any pair of equal distances. This allows tests (a) and (b) to be combined in a single test

(e) $\text{IF } C_1 \geqslant C_2 \cdot \sqrt{n}, \text{ then } E_1 > E_2.$

A selection algorithm using this test is given below

1) compute all the city-block distances from X to $Z_j, j = 1, 2, \cdots, K$;
2) select the smallest pair of C_j and store their magnitudes and class references;
3) carry out test (e);
4) if TRUE $X \epsilon \omega j, C_j < C_i \forall i \neq j$ (ωj = class no. j); go to (6);
5) if FALSE
    (a) compute all $E_j, j = 1, 2, \cdots, K$;
    (b) select the smallest of all E_j;
    (c) $X \epsilon \omega j, E_j < E_i \forall i \neq j$;
6) get next point (pattern vector); go to (1).

III. CONCLUSIONS

An algorithm has been described which produces a classification according to a Euclidean distance metric by selectivity using either a Euclidean metric or an unweighted city-block metric. The unweighted city-block metric can be used instead of the Euclidean metric with no difference in classification if the pattern to be classified is suitably distributed with respect to the class reference points.

A test condition (e) has been given which allows selection of the Euclidean metric if the test is FALSE. Provided enough TRUE results are obtained from the test condition this method can be considerably faster than an algorithm using only a Euclidean (or the square of the Euclidean) distance.

REFERENCES

[1] E. Diday and J. C. Simon, *Digital Pattern Recognition*. New York: Springer-Verlag, 1976.
[2] J. T. Tou and R. C. Gonzalez, *Pattern Recognition Principles*. Reading, MA: Addison-Wesley, 1974.

Load Frequency Sampled-Data Control Via Lyapunov's Second Method

GORO SHIRAI

Abstract—This letter presents a sampled-data load frequency control based on the second method of Lyapunov. The proposed method is simple and practically feasible for implementation. A numerical illustration on a two-area load frequency control system is presented in order to verify the practicality of the proposed method.

I. INTRODUCTION

One of the important control problems in the operation of interconnected power systems is the load frequency control (LFC). The aim of LFC is to maintain a continuous balance between electric generation and a varying load demand by adjusting the outputs on regulating units in response to frequency deviation, net tie-line power flow deviation, and plant variables. In recent years considerable interest has been shown in the application of modern control theory to the problems of LFC [1]–[3]. In general, the controllers designed by means of the above theory yield to continuous time control systems. Continuous time LFC strategies will increase the number of signals sent to power stations. Therefore, these control systems lead to complexity. In order to settle these matters, sampled-data optimum LFC strategies are also proposed [4]–[5]. The objective of this letter is to develop a simple and easily implemantable LFC strategy. For the sake of this purpose, a sample-data control strategy based on the second method of Lyapunov is proposed.

II. BASIC THEORY

Consider a continuous time dynamic system described by

$$\dot{x} = Ax + Bu \qquad (1)$$

where $x \in R^n$ is the state of the system and $u \in R^m$ is the control. In (1), A and B are $n \times n$ and $n \times m$ matrices, respectively. Constraints are imposed on the control variables,

$$|u_i| \leq c_i < \infty, \qquad i = 1, 2, \cdots, m. \qquad (2)$$

In order to synthesize a sampled-data controller, let us transform (1) into the discrete-time equation represented by

$$x(t_{k+1}) = \Phi(T) x(t_k) + \Delta(T) u(t_k) \qquad (3)$$

where it was assumed that $t_{k+1} - t_k = T = $ constant for all k, and

$$\Phi(T) = \exp(AT) \qquad (4)$$

$$\Delta(T) = \int_0^T (\exp A\lambda) B \, d\lambda. \qquad (5)$$

If the autonomous system $x(t_{k+1}) = \Phi(T) x(t_k)$ is asymptotically
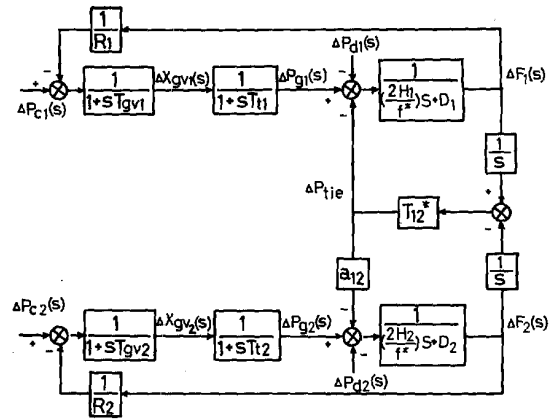
Fig. 1. Block diagram of two-area system.

(a)

(b)
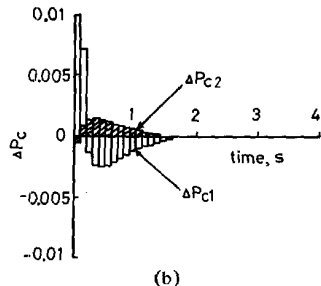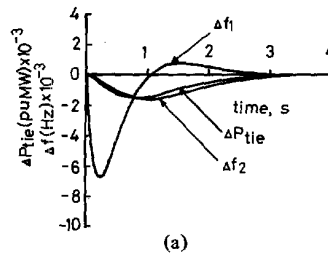
Fig. 2. Responses for proposed method ($T = 0.1$ s) (a) Δf_1, Δf_2 and ΔP_{tie}. (b) ΔP_{c1} and ΔP_{c2}.

(a)

(b)
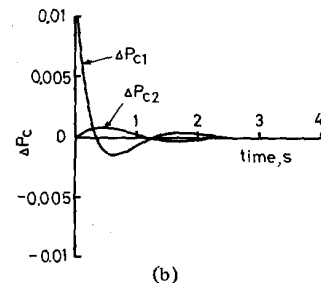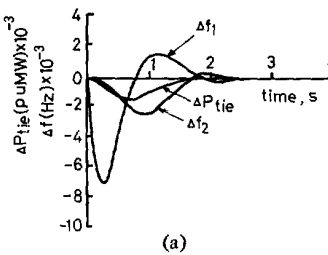
Fig. 3. Responses for conventional optimal control strategy (a) Δf_1, Δf_2 and ΔP_{tie}. (b) ΔP_{c1} and ΔP_{c2}.

stable, a Lyapunov function for the system can be represented by

$$V(x) = x'Px \qquad (6)$$

in which P is a positive-definite symmetric matrix. The prime denotes the transpose of a matrix. The difference $\Delta V(x(t_k), t_k)$ of (6) is given by

$$\Delta V(x(t_k), t_k) = V(x(t_{k+1}), t_{k+1}) - V(x(t_k), t_k). \qquad (7)$$

Substituting (3) into (7), ΔV becomes

$$\Delta V(x(t_k), t_k) = x(t_k)'[\Phi'P\Phi - P]x(t_k) + 2u(t_k)'\Delta'P\Phi x(t_k)$$
$$+ u(t_k)'\Delta'P\Delta u(t_k). \qquad (8)$$

The first term on the right-hand side of (8) is made negative definite by setting

$$\Phi'P\Phi - P = -Q \qquad (9)$$

where Q is a positive-definite matrix.

Now, let us consider the problem of choosing the control u in such a way that system disturbances are damped out as soon as possible. Then it is well known that an approximately optimal and practically useful design can be obtained by choosing $u(t_k)$ at each sampling instant t_k in such a way as to minimize ΔV [6]. However, for the sake of the constraints of the controls, u should be set as follows [6],

$$u_i^* = -c_i \text{ sat } [c_i^{-1}(\Delta'P\Delta)^{-1}\Delta'P\Phi x(t_k)]_i, \qquad i = 1, 2, \cdots, m$$

$$u^*(t) = u^*(t_k) \qquad t_k \le t < t_{k+1} \qquad (10)$$

where

$$\text{sat } x = \begin{cases} 1, & x > 1 \\ x, & |x| \le 1 \\ -1, & x < -1. \end{cases}$$

III. APPLICATION TO TWO-AREA LOAD FREQUENCY CONTROL SYSTEM

In order to test the utility of the proposed sampled-data control strategy, a two-area load frequency control system is considered (Fig. 1). The state variables and the controls are chosen as $x = (\Delta f_1, \Delta P_{g1}, \Delta X_{gv1}, \Delta P_{tie}, \Delta f_2, \Delta P_{g2}, \Delta X_{gv2})'$ and $u = (\Delta P_{c1}, \Delta P_{c2})'$, respectively, in (1).

As a numerical example, a symmetrical two-area load frequency control system is studied. The following representative values were used: $f^* = 60$ Hz, $H = 5$ s, $D = 8.33 \times 10^{-3}$ pu MW/Hz, $T_t = 0.3$ s, $T_{gv} = 0.08$ s, $R = 2.4$ pu MW/Hz, $T_{12}^* = 0.545$ pu MW/Hz, and $a_{12} = -1$. The constraints imposed on the control variables $c_i = 0.01$. A positive-definite matrix Q is chosen as unit matrix.

The simulation studies were carried out to examine the effectiveness of the proposed method. The initial condition corresponding to $\Delta P_{d1} = 0.01$ pu MW in area 1 is assumed as a load disturbance. The simulation result in the case of the sampling time $T = 0.1$ s is shown in Fig. 2. For comparison, the response using the conventional optimal control strategy [1] is shown in Fig. 3. From the simulation result in Fig. 2(a), the response of Δf_1, Δf_2 and ΔP_{tie} using the proposed method is fairly close to those of the conventional optimal control stragegy (Fig. 3(a)). In the proposed method, the behaviors of ΔP_{c1} and ΔP_{c2} as shown in Fig. 2(b) may be considered as a rectangular approximation of those of the conventional optimal control strategy (Fig. 3(b)).

IV. CONCLUSION

The sampled-data load frequency control strategy using the second method of Lyapunov was presented. The proposed method is simple and practically feasible for implementation. An added feature is that the constraints on the controllers are easily handed. The control law can be designed so as to reduce the number of load frequency control signals sent to power plants by adjusting the sampling times.

REFERENCES

[1] O. I. Elgerd and C. E. Fosha, "The megawatt-frequency control problem: a new approach via optimal control theory," *IEEE Trans. Power App. Syst.*, vol. PAS-89, pp. 563-577, Apr. 1970.
[2] R. K. Cavin, III, M. C. Budge, Jr., and P. Rasmussen, "An optimal linear systems approach to load frequency control," *IEEE Trans. Power App. Syst.*, vol. PAS-90, pp. 2472-2482, Nov./Dec. 1971.
[3] V. R. Moorthi and R. P. Aggarwal, "Suboptimal and near-optimal control of a load-frequency-control system," *Proc. Inst. Elec. Eng.*, vol. 119, pp. 1153-1660, Nov. 1972.
[4] E. V. Bohn and S. M. Miniesy, "Optimal load-frequency sampled-data control with randomly varying system disturbances," *IEEE Trans. Power App. Syst.*, vol. PAS-91, pp. 1916-1923, Sept./Oct. 1972.
[5] J. D. Glover and F. C. Schweppe, "Advanced load frequency control," *IEEE Trans. Power App. Syst.*, vol. PAS-91, pp. 2095-2103, Sept./Oct. 1972.
[6] R. E. Kalman and J. E. Bertram, "Control system analysis and design via the "Second method" of Lyapunov II discrete-time systems," *Trans. ASME, J. Basic Eng.*, pp. 394-400, June 1960.

A Device for Finding the Largest n-Bit Integer in an N-Bit String

C. K. YUEN

Abstract—This paper proposes a simple device for finding the maximum or minimum n-bit integer present in an N-bit string at high speed.

Given a string of N bits, $x_1 x_2 \cdots x_N$, one can identify within it $N - n + 1$ n-bit integers, namely, $x_1 x_2 \cdots x_n$, $x_2 x_3 \cdots x_{n+1}, \cdots, x_{N-n+1} \cdots x_N$. We wish to consider the problem of finding the maximum or minimum of these $N - n + 1$ values using specially constructed hardware. First we examine the following fairly obvious design. We have an n-bit register, which is initially cleared to 0. The content of this register is compared with the first n bits of the string, and if the latter is greater than the former, some control logic is activated to copy the latter into the register. Otherwise the register remains unchanged. We then compare the content of the register with a new portion of the string $x_2 x_3 \cdots x_{n+1}$, again copying the value into the register if it is greater. Continuing this, at the end of cycle $N - n + 1$ we have the largest n-bit integer in the string available for readout from the register.

The main weakness of this simple and inexpensive idea is its low speed. It takes some time to make an n-bit comparison; even if one employs carry lookahead type logic the compare time would still involve several gate delays. In addition, there is the need to activate the control logic and copying a greater value in the string into the register. Since the whole process takes $N - n + 1$ cycles to complete, the total time is quite significant.

In this paper, we propose an alternative design which is both simple and fast. It also requires $N - n + 1$ cycles to extract the maximum, but each cycle takes very little time. At the same time, the complexity of the design is no greater than the scheme considered before. While the new design requires a greater number of flip-flops, it employs fewer gates.

The design is based on a bit-sequential vector parallel method for extracting the maximum of a vector, proposed earlier by the present author [1]. The design is illustrated in Fig. 1. Here A, B, C, and D are input lines for elements of a vector of dimension 4. The device is operated by initializing the four flip-flops to 1 at the start, and sending the four integers to the inlets serially, most significant bit (MSB) first. After n cycles, n being the word length, we would have the maximum element, produced serially, MSB first, out of the serial output line. Explanation as to why the device works has been given in [1], and will not be repeated here.

Now consider what happens if we serially send the bits of an N-bit string across the four input points. That is, in cycle 1 we have x_1 at point D, x_2 at C, x_3 at B and x_4 at A. In cycle 2, D will receive x_2, C receives x_3, and so on. After four clock cycles, D would have received, serially, $x_1 x_2 x_3 x_4$, C received $x_2 x_3 x_4 x_5$, B received $x_3 x_4 x_5 x_6$ and A $x_4 x_5 x_6 x_7$. Since the whole circuit extracts the maximum, at the end of four clock cycles the maximum of these four integers would have been produced, serially, from the serial output line.

Generalizing the above to a device with n input lines, we know that if we send the bit string serially across the n inlets, after n clock cycles we would have produced the maximum n-bit integer present in the beginning portion of the N-bit string. But how do we extend the process to the whole string? The answer is to feed back the temporary maxi-
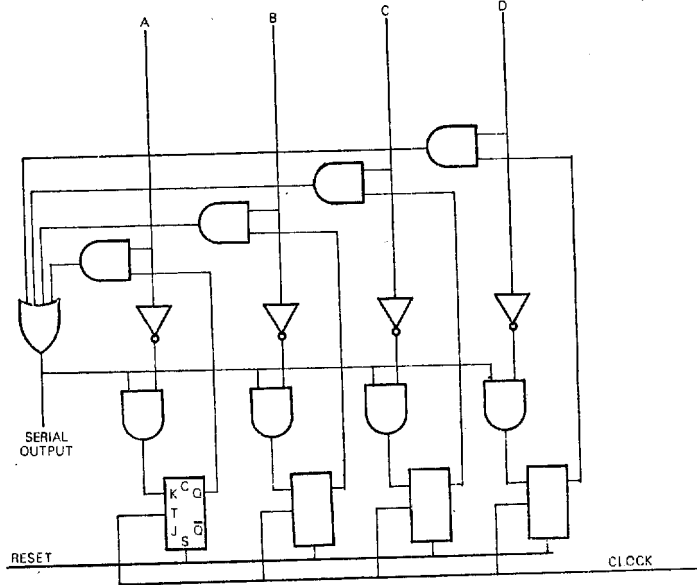
Fig. 1.
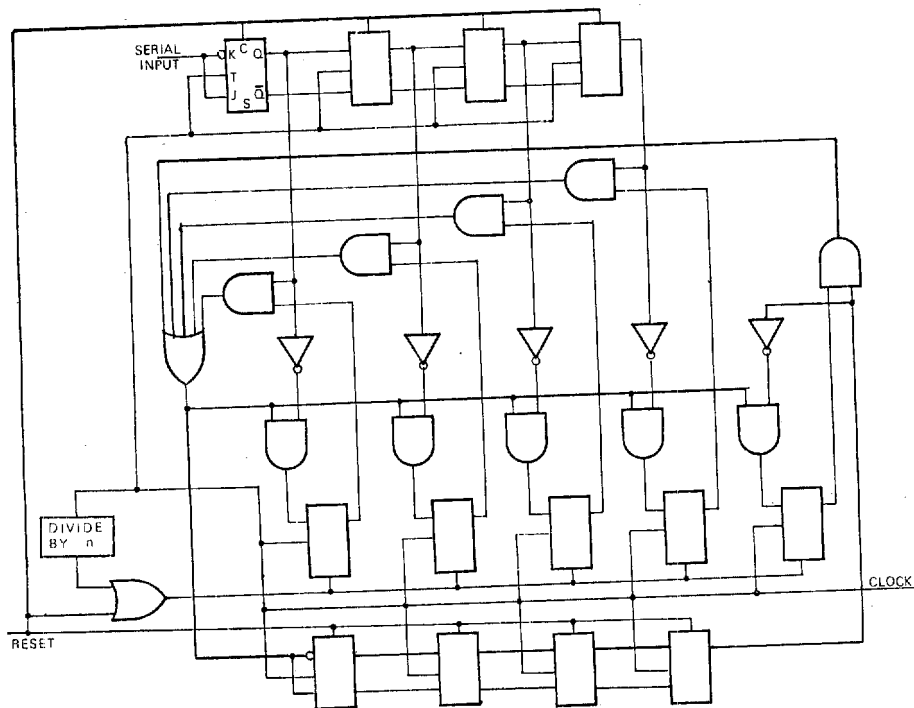
Fig. 2.

mum we have already produced into the maximum-extraction device at an additional inlet, and reinitializing the device. This will ensure that, after another n cycles we would have produced the maximum integer in the string x_1 to x_{2n}. Feeding the new temporary maximum back into the device again, we would then produce, successively, the maximum value in the string x_1 to x_{3n}, x_1 to x_{4n}, etc., until the whole string has been processed.

Fig. 2 shows the design for $n = 4$. At the top, the inlets ABCD are now fed from an n-bit register, in order that the string may be serially passed across the n inlets. At the bottom we have a second n-bit shift register for saving the temporary maximum and feeding it back into the extra inlet, provided on the right. We also have to add a divide-by-n device, which reinitializes the maximum extraction unit after every n cycles.

To illustrate the operation of the device, consider the example, bit string 10010111010. The master RESET pulse clears both the top

and the bottom registers. During the first four cycles the four inlets receive respectively the values 0000(D), 0001(C), 0010(B), 0100(A), while the fifth inlet receives just 0000. The maximum extraction unit would have produced 0100 and placed it into the bottom register. After cycle 4 the divide-by-n unit would reinitialize the extraction unit. In the next four cycles the four inlets would receive 1001(D), 1101(C), 0101(B), and 1011(A), while the extra inlet gets 0100 from the bottom register. The maximum extraction unit would then have produced 1101. During the next n cycles the five input values are 0111, 1110, 1101, 1010, and 1101, respectively. This would complete the whole process, leaving 1110 in the bottom register as the final result.[1]

We see that, to construct our device requires approximately $3n$ flip-flops and $3n$ gates, plus a divide-by-n unit. The cost should be com-

[1] Being a serial device, it has to search the whole string even after the maximum has been located.

parable to that of the earlier described register/comparator/control logic combination. The speed of the new design, however, is much greater, because each individual cycle involves only a few gate delays. When n is fairly large one would need to implement a multilevel OR to replace the single level OR in our diagram. But even if n is as large as 64 one could still manage with a two-level OR network, and the cycle time would still be quite low. In short, the design provides greater speed at very little cost.

REFERENCES

[1] C. K. Yuen, "A bit-serial device for maximization and sorting," *Proc. IEEE*, vol. 68, pp. 296–297, 1980.
[2] —, "A bit-serial device for extracting a vector velement of a specfied rank," *Digital Process.*, vol. 0, pp. 00–00, 1980.

Special Properties of Complement Codes for Redundant Residue Number Systems

W. K. JENKINS AND M. H. ETZEL

Abstract—Redundant residue number systems are of interest because they have properties that are useful for error control and failure recovery in digital processors. This letter shows how complement coding interferes with error detection in redundant residue systems. A technique is given to correct the difficulty computationally, and a modified coding scheme is presented for redundant residue systems.

It has been known for some time that redundant residue number systems have properties that are useful for error control and failure recovery in digital processors [1], [2]. Recently, these properties have been under investigation for the design of digital filters [3], [4]. A redundant residue number system (RRNS), is defined simply as a standard residue number system with r additional moduli. All the moduli $m_1, \cdots, m_L, m_{L+1}, \cdots, m_{L+r}$ must be relatively prime to ensure a unique representation for each state in the system. The moduli $m_1, \cdots, m_L$ are the nonredundant moduli; the additional r moduli $m_{L+1}, \cdots, m_{L+r}$ are the redundant moduli. In an RRNS a number is represented by $L + r$ residue digits $x_1, \cdots x_L, x_{L+1}, \cdots, x_{L+r}$ where the standard convention is the complement code given by (1), for $W = \frac{1}{2}M$.

$$X \in [0, W) \Rightarrow x_i = |X|_{m_i}, \qquad i = 1, \cdots, L + r$$
$$X \in [-W, 0) \Rightarrow x_i = m_i - |X|_{m_i}, \qquad i = 1, \cdots, L + r. \quad (1)$$

(Note that the subtraction is assumed to be a modular operation.)

The residue digits $x_1, \cdots, x_L$ are the nonredundant residue digits, and the digits $x_{L+1}, \cdots, x_{L+r}$ are the redundant residue digits. The total range of the RRNS, denoted $[0, M_T)$ spans the complete set of states represented by all of the $L + r$ residue digits, where $M_T = \Pi_{i=1}^{L+r} m_i$. The total range can be divided into adjacent intervals by considering the ranges defined by the nonredundant and redundant moduli. The interval $[0, M)$ is called the legitimate range, where $M = \Pi_{i=1}^{L} m_i$, and the interval $[M, M_T)$ is the illegitimate range.

To have redundancy, the operands and results of arithmetic operations carried out in the RRNS must be scaled so as to always fall in the legitimate range. This restriction defines the dynamic range of the system (computational range) to be $[-\frac{1}{2}(M - 1), \frac{1}{2}(M - 1)]$ if M is odd and $[-\frac{1}{2}M, \frac{1}{2}M - 1]$ if M is even. However, note that the common convention for complement coding defined in (1) represents the negative portion of the dynamic range with states at the upper extreme of the total range, which is part of the illegitimate range. Specifically, positive numbers of the dynamic range are mapped to the interval $[0, \frac{1}{2}(M + 1))$ if M is odd and to the interval $[0, \frac{1}{2}M)$ if M is even. Negative numbers are mapped to the interval $[M_T - \frac{1}{2}(M - 1), M_T)$ if M is odd and to the

interval $[M_T - \frac{1}{2}M, M_T)$ if M is even. Fig. 1 illustrates the mapping of the dynamic range onto corresponding intervals in the legitimate and illegitimate range.

Since the complement coding of (1) maps the negative states to the top of the illegitimate range, difficulties occur in error detection and correction because an error is detected by determining that a number falls into the illegitimate range. Since the negative numbers appear at the top of the illegitimate range, error detection, normally implemented by a mixed radix conversion, will identify all negative numbers to be erroneous.

One technique to correct this problem is to circularly rotate the residue ring into the position shown in Fig. 2, so that the dynamic range is mapped one-one onto the legitimate range. This circular rotation, referred to as a polarity shift, can be accomplished by adding the constant $C = \frac{1}{2}(M - 1)$ (M odd) or $C = \frac{1}{2}M$ (M even) to any $X \in [0, M_T)$ prior to executing the error detection. Note that there exists a one-one correspondence between the integers in the dynamic range and the states of the legitimate range for a nonredundant RNS. If $c_i = |C|_{m_i}$, the polarity shift within the RNS becomes a simple residue addition as described in (2), where x_{is} denotes the residue digits after the polarity shift

$$x_{is} = |x_i + c_i|_{m_i}. \quad (2)$$

Using this technique, it is possible to determine if a number contains an erroneous residue digit by checking for nonzero redundant mixed radix digits, providing the polarity shift is executed before the error check. The following theorem assures that the existence of a nonzero redundant mixed radix digit is both necessary and sufficient to identify an error condition. The mixed radix representation for a given state in an RRNS consists of $L + r$ mixed radix digits $a_{L+r}, \cdots, a_{L+1}, a_L, \cdots, a_1$. The relation between a number X and its mixed radix digits a_k is given by

$$X = \sum_{k=1}^{L+r} a_k \left\{ \prod_{i=1}^{k-1} m_i \right\} \quad (3)$$

where $0 \leqslant a_i < m_i$ for $i = i, \cdots, L + r$ and the product $\Pi_{i=1}^{0} m_i$ is understood to be 1. The digits $a_{L+r}, \cdots, a_{L+1}$ are the redundant mixed radix digits.

Theorem: Let $a_{L+r}, \cdots, a_1$ be the mixed radix digits representing a number X in a RRNS for which the moduli are ordered such that each redundant modulus is larger than each nonredundant modulus, i.e., $m_{L+j} > m_i$ for all $j = 1, \cdots, r$ and $i = 1, \cdots, L$. Then X lies in the legitimate range if and only if all redundant mixed radix digits are zero, i.e., $a_{L+j} = 0$ for all $j = 1, 2, \cdots, r$, providing a polarity shift is executed so that the conditions of Fig. 2 are satisfied.

Proof: From (3) if $a_{L+j} = 0$ for all $j = 1, \cdots, r$, then

$$X = \sum_{k=1}^{L} a_k \left\{ \prod_{i=1}^{k-1} m_i \right\}.$$

The largest value that X can take on occurs when $a_k = m_k - 1$ for each $k = 1, \cdots, L$. With these values of a_k the above becomes

$$X = \sum_{k=1}^{L} (m_k - 1) \left\{ \prod_{i=1}^{k-1} m_i \right\} = \sum_{k=1}^{L} \left\{ \prod_{i=1}^{k} m_i - \prod_{i=1}^{k-1} m_i \right\}$$
$$= m_1 + m_1 m_2 + \cdots + m_1 m_2 \cdots m_{L-1} + m_1 m_2 \cdots m_L$$
$$- 1 + m_1 - m_1 m_2 - \cdots - m_1 m_2 \cdots m_{L-1}$$
$$= m_1 m_2 \cdots m_L - 1 = M - 1.$$

Hence X must be in the legitimate range.

Now assume that for some $j = 1, 2, \cdots, r; a_{L+j} \neq 0$. The smallest value of X occurs for $j = 1$ and the corresponding expression for X is

$$X = \left[a_{L+j} M \prod_{i=1}^{j-1} m_{L+i} \right]_{j=1} = a_{L+1} M.$$

For $a_{L+1} = 1$ (smallest nonzero value) $\underline{X = M}$, and hence X falls in the illegitimate range.

The procedure of polarity shifting described above suggests a modified complement code that is obtained by adding the shifting constant C to the definitions given in (1)

$$x_{is} = |c_i + |X|_{m_i}|_{m_i}, \qquad X \in [0, W)$$
$$x_{is} = |c_i + m_i - |X|_{m_i}|_{m_i}, \qquad X \in [-W, 0). \qquad (4)$$

If the encoding is implemented by table look-up operations in ROM, (4) simply implies that a modified stored table can realize the proposed complement code with no additional hardware complexity. In this new code all calculations can be done as usual and the results can be directly checked for erroneous digits according to the theorem. The filter outputs must be decoded in a manner that is appropriate for the complement code. This could be accomplished quite easily by including a reverse polarity shift as part of the decoding algorithm.

REFERENCES

[1] D. Mandelbaum, "Error correction in residue arithmetic," *IEEE Trans. Comput.*, vol. C-21, pp. 538–545, June 1972.
[2] F. Barsi and P. Maestrini, "Error correcting properties of redundant residue number systems," *IEEE Trans. Comput.*, vol. C-22, pp. 307–315, Mar. 1973.
[3] M. H. Etzel and W. K. Jenkins, "Error correction and overflow suppression properties of RRNS digital filters," in *1980 IEEE Int. Circuits and Systems Proc.* (Houston, TX), pp. 1117–1120, Apr. 1980.
[4] ——, "Redundant residue number systems for error detection and correction in digital filters," *IEEE Trans. Acoust. Speech, and Signal Processing*, vol. ASSP-28, pp. 538–545, Oct. 1980.

An Adaptive Filter for Smoothing Noisy Radar Images

V. S. FROST, J. A. STILES, K. SAM SHANMUGAM, J. C. HOLTZMAN, AND S. A. SMITH

Abstract—Radar images are corrupted by multiplicative noise due to fading. This paper presents an algorithm for smoothing noisy radar images. The algorithm is easily implemented in the spatial domain and is computationally very efficient. By adapting the filter parameters to local statistics, it is shown that the filter preserves edges.

I. INTRODUCTION

Imaging radar systems are used to remotely sense terrain information. The radar attempts to measure the radar reflectivity by measuring received power. By displaying the power as a function of position (x, y) an image $I(x, y)$ is created where $I(x, y)$ is the tonal value that is proportional to the power. The analysis of radar images yields useful information about the nature of the terrain from which the image was produced.

A radar image can be viewed as being made up of many homogeneous areas. Each area belongs to one of many terrain categories. The reflectivity at each position within an area can be modeled by a stationary random process $r(x, y)$. Fading, due to the coherent nature of the illumination, introduces a multiplicative noise component in the image [1] and the point spread function of the system further degrades the image. Thus the recorded image $I(x, y)$ has the model

$$I(x, y) = [r(x, y) \cdot n(x, y)] * h(x, y) \qquad (1)$$

where $n(x, y)$ is the multiplicative noise due to fading, $h(x, y)$ is the point spread function of the imaging system, and $*$ denotes convolution. A common model for $n(x, y)$ is a stationary, white, non-Gaussian random process with χ^2 probability density function having $2N$ degrees of freedom where N is the number of independent radar returns that were averaged [1].

The problem addressed in this letter is one of processing the recorded image $I(x, y)$ to obtain an estimate of the reflectivity data $r(x, y)$. Several algorithms have been proposed for removing the effects of multiplicative noise. Commonly used techniques include inverse filtering followed by a linear operator (such as a Wiener filter) or a nonlinear filter

(such as a homomorphic filter). Linear filters [2] produce good estimates in the homogeneous areas of the image but they tend to blur the boundary between different areas. Homomorphic filtering [3] works reasonably well but it requires extensive computation in spite of fast implementation via the FFT algorithm. Furthermore, the homomorphic filter also tends to blur boundaries.

We present in this paper a spatial domain adaptive Wiener filter for smoothing radar (and other images) corrupted by multiplicative noise. The filter is optimum in a minimum mean squared error (MMSE) sense, is computationally efficient, and by its adaptive nature it preserves edges in the image better than other filters.

II. ADAPTIVE FILTER

The impulse response $m(t)$ and the transfer function $M(f)$ of the MMSE filter that provides an estimate of $r(t)$ from $I(t)$ is obtained by minimizing ϵ, where

$$\epsilon = E\{[r(t) - I(t)*m(t)]^2\} \qquad (2)$$

$E\{ \}$ denotes expection and $t = (x, y)$ is the spatial coordinate. The MMSE solution leads to a transfer function

$$M(f) = \begin{cases} \left[\dfrac{\bar{n}S_r(f)}{S_r(f)*S_n(f)}\right]\dfrac{1}{H^*(f)}, & \text{for } f \neq 0 \\[3mm] \dfrac{1}{\bar{n}}, & \text{at } f = 0 \end{cases} \qquad (3)$$

where $f = (f_x, f_y)$ is the spatial frequency coordinate and $\bar{n} = E\{n(t)\}$. $S_r(f)$ and $S_n(f)$ are the power spectral densities of the terrain reflectivity and the noise process, respectively. The filter given in (3) is valid for smoothing image data within areas inside of which $r(t)$ can be modeled as stationary. In (3), $H^*(f)$ is not data dependent and hence we will assume $H(f) = 1$ over some finite bandwidth for purposes of illustrating the properties of the data dependent part of the filter $M'(f)$,

$$M'(f) = \frac{\bar{n}S_r(f)}{S_r(f)*S_n(f)}. \qquad (4)$$

The standard model for $r(t)$ is an autoregressive process with an autocorrelation function [4]

$$R_r(\tau) = \sigma_r^2 e^{-a|\tau|} + \bar{r}^2 \qquad (5)$$

where the parameters σ_r^2, $\bar{r}^2$ and "a" have different values for different terrain categories. The model for the multiplicative white noise is

$$R_n(\tau) = \sigma_n^2 \delta(\tau) + \bar{n}^2 \qquad (6)$$

where the parameters σ_n^2 and $\bar{n}^2$ are sensor dependent but are not scene dependent. Substituting $S_r(f)$ and $S_n(f)$ in (4), it can be shown [5] that the impulse response of the filter is

$$m'(t) = K_1 \alpha e^{-\alpha|t|} \qquad (7)$$

with

$$\alpha = K_2\left(\frac{\sigma_I^2}{\bar{I}^2}\right) \qquad (8)$$

where K_1 and K_2 are normalizing constants, $\bar{I}$ and σ_I^2 are the mean and variance of the observed image $I(x, y)$. Thus the only data dependent parameters needed to implement the filter are $\bar{I}^2$ and σ_I^2 which can be easily estimated from the image data.

To smooth the image, $\bar{I}^2$ and σ_I^2 are estimated using data from a local neighborhood (say a 5 × 5 window) centered at (x_0, y_0) and the actual smoothing is done using the spatial domain version of the filter given in (7). The filter performs a weighted average of data in the neighborhood of (x_0, y_0) the weights being adaptively determined from local statistics of the data using (8).

To illustrate how the algorithm handles boundaries, consider two homogeneous areas A_1 and A_2 with $\bar{r}_1 = \bar{r}_2$, and $\sigma_{r_1}^2 > \sigma_{r_2}^2$. From (8), it can be seen that $\alpha_1 > \alpha_2$ and hence from (7) it follows that $m'(t)$ is narrower in region A_1 than in region A_2. However, $r(t)$ is the signal being estimated, so if $r(t)$ had a larger variance then a wide impulse response would excessively average the desired signal variations. Thus for areas with large σ_r^2, $m'(t)$ should be narrow and vice versa. Now, in the boundary region between A_1 and A_2, denoted by A_3, we have $\sigma_{r_3}^2 >$
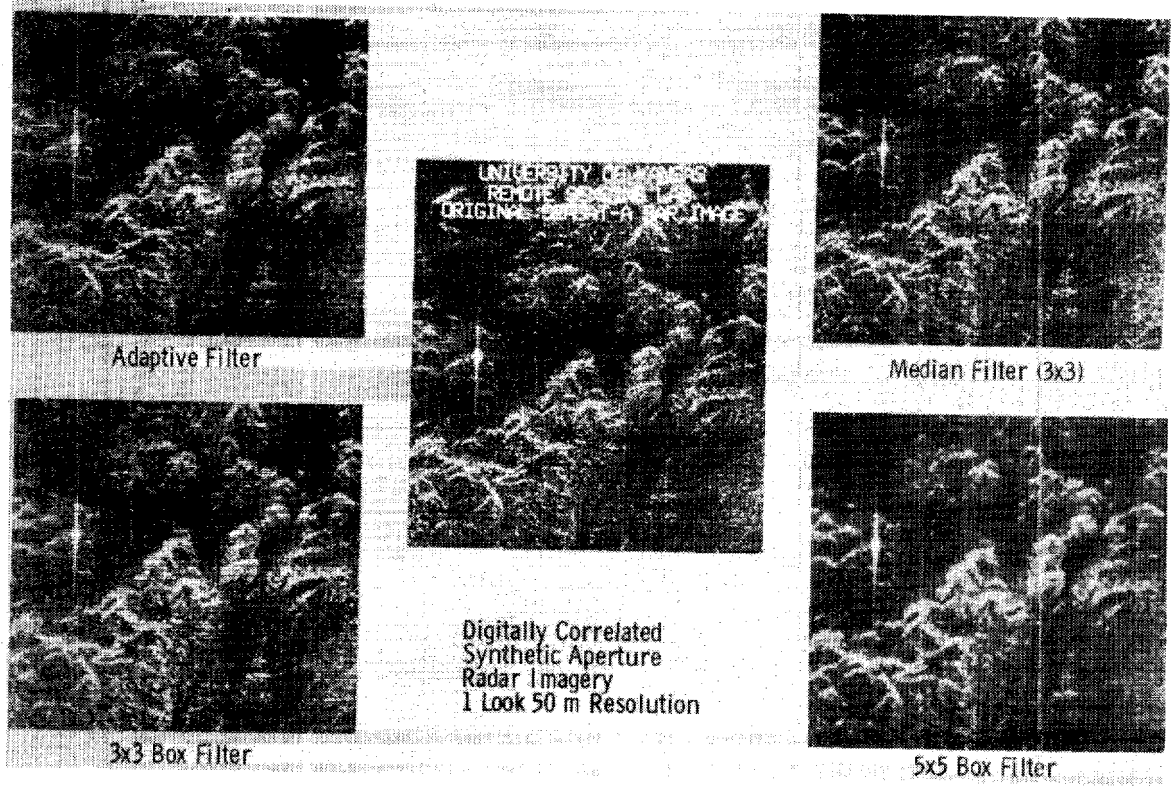
Fig. 1. Comparison of processing algorithm on radar imagery.
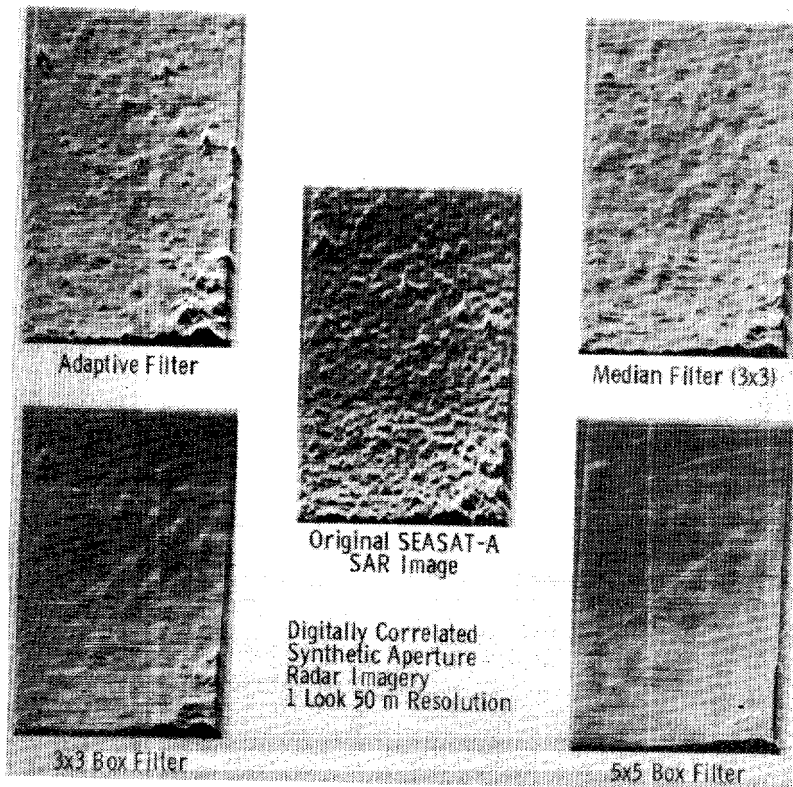
Fig. 2. Comparison of processing algorithm on radar imagery (isometric display).

$\sigma_{r_1}^2$ and $\sigma_{r_2}^2$, and hence $\alpha_3 > \alpha_1$ and α_2. This discussion shows that on a boundary $m'(t)$ has a very short duration and hence very little averaging is done on edges. The adaptive algorithm preserves boundaries, whereas a non-adaptive filter would have smeared the boundaries.

III. RESULTS AND CONCLUSIONS

The adaptive algorithm has been used to process a variety of radar imagery. A SEASAT-A SAR image of an area near Goldstone, CA is shown in Fig. 1. Two prominent point targets located in

the middle of the scene. The algorithm was applied to this image using a 5 × 5 window for both parameter estimation and smoothing. The output of the filter along with the outputs of several other operators are shown in Fig. 1. These results show that the adaptive algorithm smooths the effects of noise in homogeneous areas and preserves point targets and edges better than other filters. Fig. 2 shows an isometric display of the results in the vicinity of the point targets to illustrate the comparative performance of the adaptive filter.

In summary, we have presented an adaptive filter for removing the effects of multiplicative noise in radar imagery. This algorithm can also be used for processing optical images in which there are illumination variations that have a multiplicative effect. The filter is implemented in the spatial domain and is computationally very efficient. The adaptive nature of the filter allows it to preserve edges and point targets while smoothing the effects of noise in homogeneous areas.

REFERENCES

[1] J. W. Goodman "Some fundamental properties of speckle," *J. Opt. Soc. Amer.*, vol. 66, no. 11, pp. 1145–1150, Nov. 1976.
[2] K. Kondo, Y. Ichioka, and T. Suzuki, "Image restoration by Wiener filtering in the presence of signal dependent noise," *Applied Opt.*, vol. 16, no. 9, pp. 2554–2558, Sept. 1977.
[3] A. V. Oppenheim, R. W. Schafer, and T. G. Stockham, "Nonlinear filtering of multiplied and convolved signals," *Proc. IEEE*, vol. 56, pp. 1264–1291, Aug. 1968.
[4] A. Habibi, "Two-dimensional Bayesian estimates of images," *Proc. IEEE*, vol. 60, pp. 878–884, July 1972.
[5] V. S. Frost, J. A. Stiles, J. C. Holtzman, and D. N. Held, "Radar image preprocessing," in *Proc. 1980 Machine Processing of Remotely Sensed Data Symp.*, (Purdue University, Lafayette, IN), pp. 140–146, June 1980.

Fig. 1. A system for measuring the velocity of a flowing liquid, where $V_A = C - V \cos \theta$ and $V_B = C + V \cos \theta$.

Fig. 2. Schematic diagram of the circuit in the experiment, consisting of two zero crossing detectors, a phase comparator, a low-pass filter, a dc amplifier.

Liquid Velocity Measurement Using Interdigital Transducers

KOHJI TODA AND YOSHIAKI SHINODA

Abstract—A system for measuring the velocity of a flowing liquid is presented using three interdigital transducers, one of which is used for the radiation of the compressional wave into the liquid. The velocity is estimated from the measurement of the output voltage corresponding to the phase difference between two output signals detected at the output transducers, mounted on the same surface opposite to the surface with the input transducer.

A system for liquid velocity measurement has been developed. An interdigital transducer with uniformly spaced metallic fingers radiates the sound wave into a liquid from a liquid-solid boundary without focusing in both directions, and can be used as a receiving transducer as well as a transmitting transducer [1]. The principle and experimental data of a system for measuring the liquid velocity are given using the transducers described above.

Fig. 1 is a block diagram of the system. The sound beams radiated by the sending transducer (Tr_1) into the flowing liquid with the velocity V are received by the two output transducers (Tr_2 and Tr_3). The direction θ of the sound beam radiated from the liquid-solid boundary in the device with an interdigital periodicity of d is

$$\theta = \sin^{-1} C/df_0 \qquad (1)$$

at a frequency f_0, where C is the compressional wave velocity in the liquid [1].

The delay time difference Δt between two signals obtained at the output transducers is given as

$$\Delta t = L/(C - V \cos \theta) - L/(C + V \cos \theta)$$
$$\simeq 2LC^{-2} \cos \theta \cdot V \qquad (2)$$

where L is the propagation distance of the sound beam. The phase difference of two output signals $\Delta \phi$, therefore, is given as follows:

$$\Delta \phi = 2\pi f_0 \Delta t = 4\pi f_0 L C^{-2} \cos \theta \cdot V. \qquad (3)$$

Fig. 3. Liquid velocity versus dc output voltage, where the solid straight line is for theoretical and ● is for experimental.

This equation means that the relation between $\Delta \phi$ and V is linear and that it is possible to estimate the liquid velocity by measuring the phase difference between two output signals.

The substrate material of the device used in the experiment is a 91-A piezoelectric ceramic of the lead zirconate titanate (PZT) family produced by TDK Electronics Company, polarized preliminarily in the direction normal to the free surface. Its size is 50-mm long, 15 mm wide, and 5 mm thick. The periodic length of the interdigital electrodes with 40 finger pairs is 850 μm, corresponding to the center frequency of 2.40 MHz.

Using the circuit shown in Fig. 2, we have obtained a dc output voltage $\overline{E}$ corresponding to the phase difference $\Delta \phi$. In this case, the relation between $\overline{E}$ and V can be represented as follows:

$$\overline{E} = 2Ef_0 A \Delta t = 4Ef_0 ALC^{-2} \cos \theta \cdot V = KV \qquad (4)$$

where E is the amplitude of the output pulse at the section of the phase comparator, A is the amplification ratio of the dc amplifier. In the present experimental system, a typical value of K is 0.09 V/cm · s^{-1}, where $L = 13$ cm, $E = 3.9$ V, $f_0 = 2.40$ MHz, $A = 4.0$, $C = 1470$ m/s at 15°C, and $\theta = 45°$.

Fig. 3 shows the theoretical and the experimental relations between the liquid velocity and the dc output voltage. The theoretical curve is from (4) by substituting $K = 0.09$. The points in the figure represent experimental data obtained from the measurement of the dc output voltage corresponding to the reference liquid velocity known by another method. We can see from the figure that the agreement between the theoretical and the experimental data is excellent. The present system is available for measuring the average liquid velocity at any instant.

REFERENCE

[1] K. Toda and Y. Murata, "Acoustic focusing device with an interdigital transducer," *J. Acoust. Soc. Amer.*, vol. 62, pp. 1033–1036, 1977.

Book Reviews

The following reviews were selected from those recently published in various IEEE TRANSACTIONS *and Group/Society Magazines and News-letters. They are reprinted here to make them conveniently available to the many readers who otherwise might not have ready access to them. Each review is followed by an identification of its original source.*

Two-Dimensional Signal Processing–S. K. Mitra and M. P. Ekstrom. Eds. (Stroudsburg, PA: Dowden, Hutchison and Ross, 1978, 371 pp., $32.00). *Reviewed by Anil K. Jain, University of California, Davis, CA.*

This is volume twenty in the Benchmark papers series in electrical engineering and computer science. It is divided into three parts. Part I contains nineteen papers on deterministic, two-dimensional digital signal processing. Topics covered include: stability of two-dimensional systems, spectral factorization, and design of two-dimensional digital filters. A large number of these papers are either directly or indirectly concerned with the stability of two-dimensional IIR filters, thereby identifying it, and correctly so, as the major bottleneck in the development of algorithms for two-dimensional digital filters. The choice of papers included provide the basic results on these topics, which have led to the recent advances on stability theory, orthogonal polynomials, and spectral factorization [1]. This set of papers should be valuable in understand the basic problems in digital filter design and in knowing the first of the approaches to these problems.

Part II is devoted to statistical, two-dimensional digital signal processing and has nine papers. Basically, it contains papers addressed to the problems of recursive and nonrecursive Wiener filtering, with emphasis on state-variable recursive filtering of images. The papers represent several milestones in the development of image restoration algorithms (including an English translation of a Russian paper).

Part III contains the remaining fifteen papers on implementation aspects of two-dimensional filters. Several interesting topics, such as use of SVD expansion and projection operators in implementing two-dimensional filters as separable one-dimensional filters, FFT methods without matrix transposition, spectral transformations and error analysis of quantization effects, etc., are covered. The papers cover several diverse but well-connected topics.

A single volume in this area could never be complete. Topics such as orthogonal polynomials, two-dimensional transforms, fast algorithms (recursive and nonrecursive), signal extrapolation, spectral estimation etc., could not be covered and would require a separate volume. All the topics covered in this volume are important ones. It contains a large number of excellent papers which should be of interest to researchers in digital signal processing. Useful introductory comments have been made at various places by the editors to help a reader in understanding the problems discussed in subsequent papers. Although the state of the art in two-dimensional digital signal processing is advancing rapidly (see bibliography below), this volume offers a valuable introduction to several topics and basic problems in this area.

REFERENCES

[1] *Proc. IEEE* (Special Issue on Multidimensional Systems), vol. 66, 1978.
[2] *IEEE Trans. Automat. Contr.* (Mini Issue on Image Processing), vol. AC-23, Oct. 1978.
[3] *Proc. IEEE* (Special Issue on Pattern Recognition and Image Processing), vol. 67, May 1979.

Reprinted from IEEE Transactions on Acoustics, Speech, and Signal Processing, April 1980.

Elektrische Nachrichtentechnik–Eigenschaften und Darstellung von Signalen (Electrical Communication Technology–Characteristics and Representation of Signals)–H. Schroeder and G. Rommel (Munich/Heidelberg: Huthig & Pflaum Verlag, 1978, 412 pp.). *Reviewed by George M. Siouris, Aeronautical Systems Division (AFSC)/ENACA, Wright-Patterson AFB, OH 45433.*

This book is an attempt to treat the vast and extremely complex field of communication theory as analytically as possible, while at the same time treating the many practical aspects of the theory. Each of the authors is a recognized authority in the field, and this is the first volume of this serial publication, covering the gamut of electrical communication theory. Data communications deals with the conversion of signals to digital form, the transmission of digital data to remote locations, and the control of error rates in overall system operation. Specifically, the field of digital communications has been evolving rapidly in recent years and has revolutionized traditional signal processing. One can say with certainty that this is due to the availability of powerful and inexpensive digital processors, sensors, A/D and D/A converters, and programmable large-scale integration and switching devices. Moreover, recent advances in the techniques and hardware for data transmission via cable, fiber optics, microwave, and satellite links have provided communication systems designers with enhanced capability to design powerful systems resulting in superior performance, flexibility, and reduced cost.

At the present time, digital communication theory is an active and vital field of research. Analog processors, as well as digital processors of earlier design, are being replaced by modern digital processing techniques, which make optimal use of the new hardware and components and of new and improved algorithms. Applications extend far beyond transmission of computer data via general purpose computer communication systems.

The present book, which is part of a four-volume series on communication technology, contains three chapters, providing a useful and compact introduction to the fundamentals of communication theory. The book is divided into three chapters. Chapter 1 gives an overview of the subject matter and the various methods of signal transmission. A general digital information communication system consists of the information source, a transmitter, communication channel, receiver, and information sink. Chapter 2, entitled "Signals and their Description," contains three main sections: deterministic signals, stochastic signals, and signal conversion. In the section on deterministic signals, the authors treat periodic signals and their characteristic values in the frequency domain, determination of the characteristic values of periodic signals, measurement instruments and measurement methods, computational determination from measured data, signals in the time and frequency domains, the sampled-data theorem, the similarity theorem, acoustic, video, telegraphy, and test signals. The section on stochastic signals covers basic probability concepts, representation of stochastic signals, probability density and distribution, correlation functions and power spectral density, generation and measurement of stochastic signals, and measurement and characteristic values of stochastic signals. Section 3 on signal conversion covers the following topics: oscillatory modulation, amplitude modulation, phase modulation, pulse modulation, pulse modulation for discrete signals, and A/D conversion. Each section gives a summary of the most important results. Chapter 3 is devoted to information content of signals. The capacity of a channel is defined as the maximum information that can be transmitted through the channel by a suitable choice of source. The topics covered in this chapter include information content in which the information source is sign independent, code words, code trees, and information content with sign dependency. The book concludes with an extensive bibliography and a list of symbols.

The treatment of the material presented is essentially self-contained. Starting at an elementary level, the authors lead the reader gradually to the more advanced topics. The many practical examples in the book would be a useful supplement in a general course in communication theory, while at the same time making the volume ideal for self-study. This reviewer feels that the main strength of the book lies in the mathematical presentation of the theory. Furthermore, the book successfully combines simplicity, physical intuition, and the ability to perform concrete calculations. In conclusion, it can be said that this book gives an excellent review of the state-of-the-art of communication theory. It is a useful reference for the serious students and researchers of the field in general. The book is quite readable, and any reader with a basic knowledge of scientific German should have little difficulty in understanding it. Finally, the publishers have done an excellent job. The type is clear, figures are excellent, and typographical errors are rare.

Reprinted from IEEE Transactions on Systems, Man, and Cybernetics, March 1980.

A Guide to F.C.C. Equipment Authorization–William K. Roberts (New Smyrna Beach, FL: William K. Roberts, 1980, $24.50). *Reviewed by Sotirios J. Vahaviolos, Physical Acoustics Corporation, Princeton, NJ 08540.*

Practically every nonmilitary transmitter, receiver, or other electronic product which generates a frequency higher than 10 kHz for *any* pur-

pose must be authorized by the Federal Communications Commission (F.C.C.) before it may legally be marketed or used in the United States. The Commission's Equipment Authorization Program is the handle by which it controls pollution of the electromagnetic spectrum (radio interference). Designers, test engineers, manufacturers, and importers will find comprehensive information about F.C.C. Type Approval, Type Acceptance, Certification, and Registration in this new book, which was prepared by a former member of the F.C.C. staff.

The book identifies the categories of equipments which the Commission regulates. It shows how to obtain the regulations which apply to each class of equipment. It tells what kinds of equipment must be tested by the F.C.C. before authorization can be granted, and which kinds will be authorized if the applicant's own measurements are satisfactory. It identifies and explains test procedures which the Commission has prescribed, and those designed by others which it accepts. It advises how to apply for the necessary approvals, and indicates whom to contact in the Commission (and their phone numbers) if procedural or technical questions arise. It also deals with extensions of the equipment regulations to matters other than radio interference, including registration of telephone equipment and enforcement of comparable UHF–VHF capabilities of television receivers.

The book is the only one to cover so many diverse aspects of the F.C.C.'s regulation of electronic products. Other subjects include: list of F.C.C. publications on equipment authorizations; F.C.C.-recognized measurements standards published by professional societies and industry associations, and how to get them; application forms; F.C.C.-recognized antennas for field-strength measurements; dimensional drawings of special antennas used by the Commission; and, for most classes of equipments, specific references to the applicable regulations and measurement procedures. Also, as an aid to those who contemplate installing a test facility, suitable makes and models of equipment are listed, with names and addresses of their manufacturers.

Reprinted from *IEEE Transactions on Industrial Electronics and Control Instrumentation*, May 1980.

Introduction to Communications Engineering–Robert M. Gagliardi (New York: Wiley, 1978, 508 pp., $26.50). *Reviewed by Daniel F. DiFonzo, COMSAT Laboratories, Clarksburg, MD 20734.*

Professor Gagliardi's stated objective for this college engineering textbook is to present an introduction to the analysis and design of operating communications systems with emphasis on practical considerations. The book generally achieves this goal and it should serve very well for a course in modern communications at the upper undergraduate and beginning graduate levels.

The nine chapters and three appendices are laid out in a logical order, beginning with the broad definitions of communications system models and proceeding to describe in detail their various elements from beginning to end. The orientation of the book is clearly toward practical applications. The more theoretical and abstract topics in communications theory, such as detection and estimation theory, information and coding theory, and filter theory, are dealt with in an introductory manner to illustrate the terminology and to demonstrate their application. References are provided at the end of each chapter as are a number of problems. The exercises enhance the text, and problem results are referred to frequently throughout the book.

The book is classroom oriented, with many topics described in a way that requires supplemental information, e.g., classroom notes. An example is the author's view that "a previous course in probability would be advantageous to the student but is not necessary for one guided by an instructor." In my opinion a good deal of independent or supplementary exposure to the theory of random variables and processes is necessary to benefit from the book. Appendix B covers these subjects but the treatment is very condensed and is not presented in enough detail or depth to enable one who is encountering the material for the first time to gain an adequate understanding. However, for those who have seen the material before it is a good fast-paced review and summary of the more important concepts which form the basis for most of the developments in the text.

The book is somewhat less useful as a stand-alone reference for practicing engineers who are already specialists in communications theory. However, for those who have had some prior exposure to the requisite principles and yet are not specialists in these areas, it does provide very readable and up-to-date introductions to most of the topics in modern-day communications. Many of the examples and exercises relate to current communications satellite applications; the level of treatment is

appropriate for those working in other related aspects of this technology.

The first three chapters discuss basic communications system models, carrier transmission, and reception:

Chapter 1, "Communications System Models," (45 pp.) summarizes communications system models and discusses basic concepts of deterministic and random waveforms and signals, including the autocorrelation function and its Fourier transform, the spectral density. Definitions for bandwidth, filtering, waveform power, and energy are described and related. The basic forms for AM, PM and FM waves are described with reference to Appendix A. This appendix, "Fourier Transforms and Identities," is highly condensed and serves mainly as a quick reference for those already familiar with the subject.

Chapter 2, "Carrier Transmission," (45 pp.) describes in more detail the important properties of amplitude, phase, and frequency modulated carriers for deterministic, as well as stationary random processes waveforms. The power spectral density of a random AM carrier is obtained from the autocorrelation function and the conceptual progression to singlesideband AM is shown to follow naturally. The spectral properties of FM and PM carriers are explicitly described for several modulating waveforms, such as sine wave, sum of sine waves, and random modulation. The Carson's Rule bandwidth criterion is clearly explained in terms useful to understanding its practical application.

The carrier description for a PM binary waveform modulation and the basic properties of a PM wave modulated by a stationary random process are described by showing the simple relation between the autocorrelation function and the characteristic function of the modulating process; this relationship is used to derive the power spectrum for the special but important case of a Gaussian process. Several important topics are introduced and lucidly described in this chapter, such as amplifier linearity, backoff, efficiency, saturation, intermodulation, and impedance matching. Since this chapter concerns the sending end of a link, it provides a brief and rudimentary treatment of transmitting antennas which covers subjects such as gain, efficiency, field of view, and e.i.r.p. in just enough detail to enable one to see how the antenna performance affects the communications link.

Incidentally, the book contains a fair number of minor typographical errors and a few factual errors, which one hopes would be corrected in subsequent printings. For example, a factual error appears in Fig. 2.10, showing an antenna pattern having a $12°$ beamwidth which the author states "is just enough to cover the Earth when transmitting from a satellite at an altitude of 22 000 miles." Of course, the correct beamwidth for transmission from the geostationary altitude is $\approx 18°$, a fact which the author recognizes later in the book but which nevertheless contradicts the information in the figure. Chapter 2 concludes with a description of carrier propagation channels, briefly mentioning waveguides, but concentrating on propagation through the atmosphere and providing several useful curves of atmospheric and rainfall attenuation at microwave satellite communications frequencies.

Chapter 3, "Carrier Reception," (54 pp.), examines the receive side of a link. The basic properties of receiving antennas are described, the most important being the effective receiving antenna area, its relation to received power, and the effects of propagation. A very clear treatment of background noise and receiver front end analysis, including noise figure, bandwidth, antenna temperature, and line losses, culminates in the expression for the receive carrier-to-noise ratio (CNR). The effects of filtering on the carrier waveforms and receiver noise process are described. The receive chain description continues with frequency translation to an IF by mixing and concludes with a discussion of nonlinear processing and carrier limiting, illustrating the effects of hard limiting on the CNR.

Chapter 4, "Carrier Demodulation," (42 pp.) sets the stage for the remainder of the book by illustrating the various schemes for extracting the baseband information signal. Discussion is limited to carriers of the AM, FM, or PM type and demodulating systems are described for each. Functional block diagrams illustrate the basic components used in the demodulating process for those carriers. AM demodulation by envelope detection yields a relation between the baseband signal-to-noise ratio (SNR) and the IF CNR, introducing the SNR improvement and the notion of threshold. The SNR is also calculated for coherent AM demodulation and the importance of phase synchronization is illustrated. Frequency demodulation with feedback tracking and a feedback method for phase demodulation introduces the basic idea of the phase lock loop (PLL) and its important parameters. Table 4.2 is a useful summary of the basic SNR relations and baseband noise spectrum description for AM, FM, and PM, including FM and PM with modulation tracking.

Chapter 5, "Baseband Waveforms, Subcarriers, and Multiplexing," (40 pp.) deals with the entire analog baseband system from source to demodulated baseband waveform from the viewpoint of how well the

demodulated baseband reproduces the source content. The problem of selecting the "best" baseband filters to maximize the SNR or signal distortion ration (SDR) is treated and the notion of pre-emphasis introduced. Subcarrier modulation is shown to offer an additional degree of freedom in choosing the location of the baseband spectrum. Various methods for modulating the source waveform onto the subcarrier, such as AM/FM, FM/FM, FM/PM, are compared and source multiplexing, e.g., frequency division multiplexing (FDM) to combine a number of subcarriers, is briefly discussed.

The remaining chapters deal with digital signals. Chapter 5, "Digital Sources and Encoding," (46 pp.) begins appropriately with a section on analog to digital and digital to analog conversion schemes, quantization errors, sampling theorem, aliasing, and bit rate. A method is outlined for optimal quantization given the sample probability density, and the effects of transmission errors and noise on quantization are discussed. Source encoding is introduced and while information theory concepts such as entropy are only discussed briefly, there is sufficient material to provide an appreciation of the coding advantages obtainable. Concepts of block, binary, and convolutional encoding are presented in a very introductory fashion, but most of the important ideas are conveyed, with ample references at the end of the chapter.

Chapter 7, "Binary Digital Systems," (61 pp.) considers in some detail systems where the binary encoded bits are transmitted one at a time in sequence and uses as a performance measure the probability of recovering the bits in error. The baseband encoded signal spectrum of the binary waveform is derived. The decoder filter-sampler model leads to the process of maximum likelihood decoding and the probability of error follows from this analysis. The matched filter receiver is then defined for this type of decoding. In this and subsequent analyses, the measure of performance is the probability of error in received signals versus the energy-to-noise ratio per bit (E/N_b); curves relating these quantities are presented for various signal schemes. Antipodal signals are shown to yield the lowest E/N_b for a given PE. Orthogonal signals require twice the E/N_b to yield the same PE. With this background, the most common type of binary signal schemes, such as PCM, PSK, FSK, and minimum shift keying (MSK), are evaluated. Other concepts included in this chapter are effects of imperfect bit timing, non-coherent binary signaling, on-off keying, differential phase shift keying (DPSK), channel bandwidth, rate of data transmission, and intersymbol interference.

Chapter 8, "Block Encoded Digital Systems," (59 pp.) extends the work of the preceding chapter to systems where the source bits are grouped into "blocks" or binary words of k bits and transmitted. The receiver must then distinguish $M = 2^k$ waveforms and select the one received word that represents, with least error, the transmitted word. A decoder consisting of a parallel combination of matched filters, one for each word, followed by a "select maximum" decision, is a natural extension of binary decoding. Various signal sets used for block transmission and their corresponding waveforms are introduced, as is the idea of representing the signals as vectors in a multidimensional signal space. For orthogonal block signals, PE vs. E/N_b illustrates that, while k = 1 results in minimum E/N_b for a given PE, longer words are superior when the information rate is considered. Several types of signal sets are described such as biorthogonal signals and polyphase signals, the most notable of which is QPSK (M = 4, phase shift keying). An elementary discussion of convolutional coding mentions the Viterbi decoding algorithm but provides no details. Finally, the various coding alternatives are summarized and compared in terms of required bandwidth and bandwidth efficiency.

Chapter 9, "Frequency Acquisition, Phase Referencing, and Timing," (75 pp.) deals with the problems of maintaining frequency, phase, and/or timing references upon which the systems rely in order to function. This chapter describes a frequency acquisition scheme that uses a phase lock loop, as well as signal acquisition and locking, and the factors affecting acquisition time. Phase synchronization, in order to make the receiver phase coherent with the transmitter, had been shown to be important in preceding chapters; the influence of various factors such as tracking errors and receiver noise is described here. An important quantity affecting system performance in this regard is oscillator phase noise. This subject, which is extremely important to a satellite communications link, for example, is mentioned briefly in this chapter but it is supplemented by an excellent and thorough treatment in Appendix C, which discusses oscillator instability and phase noise. This appendix is self-contained and up-to-date, defining the important quantities and preparing the reader for the literature on the subject. Chapter 9 also describes methods for carrier extraction from a suppressed carrier system and concludes by discussing the effects of phase referencing and timing on the received signals.

In conclusion, this book does a good job of accomplishing what the author intended. It is to be commended for covering the important

practical aspects of communications principles at the introductory level in a language and style useful to those concerned with practical communications systems.

How to Write and Publish a Scientific Paper—Robert A. Day (Philadelphia, PA: ISI Press^{TM}, 1979, paperback. 160 pp., $8.95). *Reviewed by Herbert B. Michaelson, IBM Corporation, White Plains, NY 10601.*

It should be clear to graduate students and fledgling writers in all branches of science that they need to write about their work and to publish their results. The present book addresses this need and has some unique qualities—it is far more readable than most books of its kind and is liberally sprinkled with humorous but pithy observations.

Books on technical writing frequently are devoted to long-winded exposition on the virtues of good writing and effective communication. Such material tends to be heavily interspersed with illustrative examples of writing style and sound organization. Robert Day's book is somewhat different. Its 26 chapters, 21 of which have the words "how to" in the title, are brief and to the point. By constructing the chapters in such condensed form, Day shows by example how his readers can write short but powerful exposition.

The book is an outgrowth of an article published in 1975 by Day [1], which was later republished in this TRANSACTIONS. [2]. First, the book expounds a detailed philosophy on how to prepare the various sections of a paper: Abstract, Introduction, Materials and Methods, Results, Discussion, etc. Then it proceeds with several sections on where and how to submit a manuscript, how to deal with editors, the nature of the journal publishing process, and other information essential for authors that seldom appears in texts on writing. Day's treatment of these workaday topics is by no means dull and plodding, and so his book is to be highly recommended.

Even though the book is full of good insights about writing and publishing, it omits certain significant items that are important to any writer of scientific papers regardless of his experience or background.

Chapter 11, for example, entitled "How to Prepare the Literature Cited," is useful but includes little comment on the sins of ambiguity sometimes committed by authors when citing references *in the text*. One of these is the "handwaving reference," in which the reader is glibly referred to Smith's paper without any hint either of what Smith reported or how his results relate to the author's own contribution. An extended discussion of how references can be vaguely cited in the text and of why precise citation can be important would have been excellent because the problem is so widespread and so little recognized.

In the matter of references Day made some other omissions. His own list of 31 references on writing and publishing (pp. 153–154) could well have included articles pertinent to several of the more important chapters. For example, the chapter on how to design effective tables is fine as far as it goes but the interested reader could have been referred to an extensive treatment of the subject, for example, by C. K. Arnold [3].

Another example of omitted references is Day's brief discussion on pp. 15–16 of who should and who should not be coauthors of a given scientific paper. Here is a subject of concern to all scientific authors and their colleagues. Day might have referred the reader to sources of information on this tacky subject, e.g., a masterful treatise on the nagging question of proper authorship published by Sherrington and Orr [4].

One minor limitation of this book is the author's attempt to define and recommend a set of distinctive component parts of any scientific paper including, for example, Materials and Methods. The author's background is in biology and biochemistry and the book admittedly sets forth principles of scientific writing with examples in his own field. But the recommended rigid organization of a paper is parochial! Many disciplines of science are not concerned with materials nor even with experiments and experimental confirmation of theory. The disciplines include many branches of mathematics, language studies, computer programming, etc. Such papers can be scientific in every respect but may be devoted solely to theory, analysis, or simulation. The idealized structure of a manuscript needs to be a bit more flexible than is suggested in chapter 1.

Chpater 13, "How to Prepare Effective Illustrations," has some good, practical advice on the choice of material to be illustrated and on the visual clarity of graphs and photographs. It offers a more thorough treatment than do many books on scientific writing. It does, however, lack an adequate discussion of the crucial decision that all scientific authors must make: *How will the illustrations be related to the organization of the manuscript?* An ideal way for the author to decide is to choose his

illustrations before he writes the paper and to build the organization around those essential charts or photographs instead of treating them as an afterthought. The inevitable result of a prior choice of figures is to strengthen the manuscript with the proper emphasis as it is being written. This topic seldom appears in "how to" books on writing. But journal editors, scientific referees, and journal readers take delight in a paper constructed so that it clearly emphasizes its findings with carefully chosen figures. Any author must understand that a clearly labeled and nicely drawn chart on a peripheral subject is not nearly as powerful for his paper as one that illustrates his central point and supports his main claims.

Day's contribution, like all books on writing and publishing, could have pursued certain subtleties of these kinds at greater length. Overall, of course, it has much to offer—not only for the novice, but also for the mature writer. A fair sample of Day's choice bits of writing wisdom appears on p. 35:

> Seldom will you be able to illuminate the whole truth; more often, the best you can do is to shine a spotlight on one area of truth. ... The "whole truth" is a subject best left to the ignoramuses, who loudly proclaim its discovery every day.

A self-evident bit of philosophy. And by the same token, the "whole truth" about scientific writing and publishing will never be found in a single book.

REFERENCES

[1] R. A. Day, "How to write a scientific paper," *ASM News*, vol. 41, p. 486ff, 1975.
[2] ——, "How to write a scientific paper," *IEEE Trans. Prof. Commun.* vol. PC-20(1), pp. 32–37, June 1977.
[3] C. K. Arnold, "The Construction of Statistical Tables," *IRE Trans. Engineering Writing and Speech*, vol. EWS-5, pp. 9–14, Aug. 1962.
[4] A. W. Sherrington and R. H. Orr, "The ethic of personal responsibility for scientific publications: Problems of multiple authorship," in *STWP Conv. Proc.* (Society of Technical Writers and Publishers, now Society for Technical Communication), pp. 97–107, May 1965.

Communication for Managers—Paul Preston (Englewood Cliffs, NJ: Prentice-Hall, 1979, 307 pp., $14.95). *Reviewed by Della A. Whittaker, U.S. Army Harry Diamond Laboratories, Adelphi, MD 20783.*

For many years in many books, "communication" has been the key word taught to managers. It must not have been learned well or else those books must not have been read because the word is still a key one in titles of management textbooks. The repetition may succeed because every few years a new crop of managers bursts out of college classes or rises from the working ranks. It would not surprise me if Preston's *Communication for Managers* were pursued with enthusiasm today, tomorrow, and next year. It says what the older books say, it says so simply and firmly, and it allows instant transfer to the reader's setting.

Why shouldn't it? As an associate professor of management at the University of Texas at San Antonio, Preston must have read all those other useful, readable communication and management textbooks before writing eight himself. He understands management problems from working as a business consultant and has led seminars for big-name companies. He knows what he's writing about, he knows that his readers sort of know what they should be doing in communication as managers, and he charges them to communicate the way that they should.

The way he writes, no one should miss his meanings. With his examples, no one should feel left out. Anyone who has ever worked with or as a supervisor should be able to learn, to rethink, and to apply these standard techniques, these ever-present maxims made obviously practical by Preston: Be honest. Be open. Be kind. Be flexible. Be understanding. Be alert. Be positive. Be constructive. Be factual. Be current. Be objective. Be consistent. Be on time. Be careful.

Preston covers the topics expected in a basic book on communication for managers: hiring and firing employees and dehiring them (making life so uncomfortable that they quit), attending and running meetings, giving oral presentations, writing resumes, managing time, and managing subordinates. Managing subordinates is Preston's major emphasis. He tells how to listen to them, use space and body language so they'll listen, motivate them to increase productivity and quality of work, appraise their work, and persuade them to follow a new plan.

His style is definitely not stodgy. This textbook is not textbookish. Neither does Preston come across as "laid back." His writing reads as if a youthful, energetic pragmatist instructed the reader.

agement problem-solving session and leaped onto the lecture platform to convey to eager listeners how to figure out solutions to their similar problems. Confident because he bases his solutions on long-effective methods, he answers questions from all directions and hands out short bibliographies on topics that require more complex figuring, such as women's assertiveness or power politics. This book lets the reader attend such a lecture by Preston. The reader will be reminded of working principles, taught those principles that he hadn't caught in previous teachings, and helped to organize them all for application on the job.

The book's flaws are in its production. The print is tiny, the page numbers are placed inconsistently, the binding bends and peels, and misspellings average one in ten pages.

BOOK ALERT

The following descriptions of recent books were prepared by the staff of the Engineering Societies Library, 345 East 47 Street, New York, N.Y. 10017. These books are available in the Library for loan or reference use. The prospective buyer should contact the listed publishers or his local technical book store.

Microwave Devices and Circuits—Samuel Y. Liao (Englewood Cliffs, NJ: Prentice-Hall, 1980, 530 pp., bound, $27.95, ISBN 0-13-581207-0).

This book is intended as a text in a first course in microwave devices and circuits at the senior or beginning graduate level in electrical engineering. Its primary objectives are to provide the student with a clear understanding of the commonly used microwave devices, and with some techniques for analyzing microwave circuits and measurements. The content of the book is an outgrowth of lecture notes used for several years in a one-semester course taught by the author, and from his long industrial experience in microwave electronics. It is assumed that the student has had previous courses in electromagnetics and solid-state electronics. Because the book is, to a large extent, self-contained, it can also be used as a reference book by electronics engineers working the microwave area.

Educational Telecommunications Delivery Systems—John A. Curtis and Joseph Biedenbach, Eds. (Washington, DC: American Society for Engineering Education, 1979, 151 pp., paper, $7.00, ISBN 087823-105-6).

This publication is intended to guide educators in the use of the six major U.S. educational telecommunications methodologies: 1) Public Broadcasting (radio and TV); 2) Instructional Television Fixed Service (ITFS); 3) Teleconferencing-Telewriting (via standard telephone circuits); 4) FM-Broadcasting Station Multiplexing; 5) Community Antenna Television (CATV); 6) Satellite Circuitry. Each of the papers has been written by one or more experts from each field. Information on costs have been included.

Who's Who In Electronics: Data in Depth—(Twinsburg, OH: Harris Publishing Company, 1980, various pagings, paper, $59.95, ISBN 0-916512-66-5).

First section lists manufacturers alphabetically with their vital statistics including the SIC number. Second section lists companies geographically. The product director comprises the third section. Distributors are listed in the last 2 sections, alphabetically and geographically.

Formalization Of Natural Languages (Communications and Cybernetics, vol. 15)—Peter Kümmel (New York: Springer-Verlag, 1979, 223 pp., bound, $37.00, ISBN 0-540-08271-9).

Computer simulation of natural language communication functions necessitates the design of brainlike hybrid memories providing associative methods for answer searching. Research in this area has led to results exposing all redundancies in conventional human communication. The author compares phonographic functions with the properties of ideo-, logo-, and pictographic expressions. Analyses of isolated as well as agglutinated morphologies were carried out to gain insights into content phenomena. Evaluations of gesture systems, air-traffic control and children's languages served this purpose. Progressively complex morphology and syntax algorithms are introduced and six subcriteria of one meaning are defined, including significance and truth-values of new

Electro-Optics Handbook—R. Glenn Elion and Herbert A. Elion (New York: Marcel Dekker, 1979, 359 pp., bound, $39.75, ISBN 0-8247-6879-5).

This is the material that is fundamental to all electro-optics engineering, and to it has been added some specialized information pertaining to certain overlapping, developing fields. The present work is to be distinguished from product-oriented books put out by manufacturers for the application of their own products. Previously scattered data is integrated into one up-to-date source that includes fundamental definitions and symbols; radiometric and photometric quantities; sources of radiation; lasers; detectors; image and camera tubes; optical formulae, materials, and components; human-electro-optics interaction; atmospheric and underwater transmittance; displays and arrays; communication systems; specialized components; and computer design of components and systems.

Spatial Time Series: Analysis-Forecasting-Control—R. J. Bennett (New York: Academic Press, 1979, 674 pp., bound, $87.50, ISBN 0-85086-069-5).

This book is concerned with the analysis of sequences of observations of variables measured over a sample period of time or over a set of spatial regions for a set of sample time periods. The methods discussed are quite general but the most appropriate applications are likely to be environmental and socioeconomic systems. The latter include climatic, hydrological, ecological, biotic, and geomorphological process concerned with systems above, on, and within the earth's surface. It starts at the second year undergraduate level but much of the material is suitable for graduate students and research.

Laser Handbook, vol. 3—M. L. Stitch, Ed. (Amsterdam, The Netherlands and New York: North-Holland/Elsevier, 1979, 878 pp., bound, $122.00, ISBN 0-444-85271-9).

Laser Handbook is an authoritative and centralized source of information covering the entire laser field. Volume III continues the high standard set by the first two volumes. In this Volume, emphasis is placed on technology leading to improved mode characteristics and beam quality, increased efficiency, new wavelength regions, increased power and tunability. Applications addressed are either physical interactions which modify the laser's characteristics such as obtaining ultrashort pulses and high power second harmonic pulses, or scientific and engineering applications, such as laser induced chemical reactions and isotope separation, pulsed holography, inertial confinement fusion and picosecond spectroscopy. The topics covered in the articles account for a considerable amount of the activity in the laser field, and are of significance for workers in these subjects as well as for advanced students. Many references are included.

One-Dimensional Digital Signal Processing—Chi-Tsong Chen (New York: Marcel Dekker, 1979, 448 pp., bound, $24.75, ISBN 0-8247-6877-9).

Written and organized to provide relatively rapid access to digital signal processing for undergraduate and graduate student engineers and practicing engineers. Utilizing the method of examples to convey every concept and design technique, the book requires a knowledge of calculus but not of analog system theory, which is introduced only to fill out the presentation of digital techniques. The three parts cover, respectively, digital spectral analysis, design of filters, and statistical methods. The first part develops the discrete Fourier transform as a natural tool for computing the spectrum of signals. The basic idea of the fast Fourier transform is discussed, along with various problems encountered in its actual employment. The second part introduces the design of analog and digital filters and offers a superior new low-pass-to-band-stop frequency transformation. The final part discusses the design of Wiener FIR and IIR filters and delivers a precise formula for the design of Wiener IIR filters.

Mathematical Modeling With Computers—Samuel L. S. Jacoby and Janusz S. Kowalik (Englewood Cliffs, NJ: Prentice-Hall, 1980, 292 pp., bound, $21.50, ISBN 0-13-561555-0).

The book is a guide for builders and users of computer-implemented mathematical models. It is structured according to the stages of the mathematical model-building and modeling process which include: prototype identification and statement of the modeling problem; mathematical model definition and analysis; mathematical problem analysis; reformulation and solution development; computer program design and development; and model validation adjustment and use. It presents

brief surveys of types and purposes of models and of types and elements of mathematical models. In addition, necessary and sufficient conditions for mathematical model usefulness are proposed, explored, and related to the model-building stages. The book spans the whole process of mathematical model building and modeling, starting with the modeling objective and prototype definition and concluding with modeling and interpretion of results. Topics are discussed in the order in which the steps are normally carried out. However, the depth of coverage is not uniform because more emphasis and details are given for subjects not covered elsewhere. For the subjects not treated in great detail in this book, the reader is referred to articles and books from which he can get the information he will need. Thus this book, supplemented by the readily available reference material, is intended to be a study of and handbook or guide for mathematical model building and modeling with digital computers.

Soft Magnetic Materials: Fundamentals, Alloys, Properties, Products, Applications—Richard Boll (Philadelphia, PA: Heyden, 1979, 353 pp., bound, $28.00, ISBN 0-85501-263-3).

This handbook provides a review of the properties and applications of soft magnetic materials, laying particular emphasis on the requirements of the electrical and electronics industries. It is primarily aimed at practicing electrical engineers, metallurgists as well as advanced students. Part I is an introduction to the nature of magnetism and magnetic materials. The author discusses the magnetic circuit, summarizes the relevant formulas and provides an overview of measuring processes and conditions for magnetization. In part II he describes a wide variety of soft magnetic materials, their special characteristics and the resultant manufactured products. Guidelines are given on their uses, range of application and on the magnetic qualities of individual parts and components. Many graphs are included.

The Molecular Physics Of Liquid Crystals—G. R. Luckhurst and G. W. Gray, Eds. (New York: Academic Press, 1979, 494 pp., bound, $46.00, ISBN 0-12-458950-2).

Although the first liquid crystal was discovered almost a hundred years ago, our understanding of this unusual and important state of matter at the molecular level is still relatively sparse. The numerous techniques which are imployed to determine molecular properties vary widely and this makes it difficult to compare critically results using different methods. In addition, there is a bewildering array of molecular theories of the liquid crystalline states. This book has its origins in a NATO Advanced Study Institute whose primary aim as to clarify this situation by discussing both theoretical and experimental approaches used to study liquid crystals at the molecular level. The result is not only a unique reference work but, by virtue of the original research described, a stimulus for further investigation. Among the experimental techniques discussed are magnetic resonance spectroscopy, neutron, X-ray and light scattering, as well as thermodynamic measurements. The statistical mechanics necessary to understand the theory of liquid crystals are reviewed and then used to consider molecular-field and hard-particle theories of nematics and cholesterics. This book is not aimed exclusively at physicists and chemists, but contains much that is of value to engineers, applied physicists, electronic engineers and pure theoreticians. It will provide valuable reading and reference material for anyone commencing research in the area of liquid crystals.

Aepinus's Essay On the Theory Of Electricity and Magnetism—Introductory Monograph R. W. Home (Princeton, NJ: Princeton University Press, 1979, 514 pp., bound, $37.50).

First published in St. Petersburg in 1759, F. U. T. Aepinus's *Tentamen theoriae electricitatis et magnetismi* was one of the outstanding achievements of eighteenth-century physics. Its rigorous mathematical investigation of electricity and magnetism was an important and innovative departure from the primarily qualitative and non-mathematical treatments that preceded it. P. J. Connor's translation of the original Latin edition is the first to appear in any western European language, and the introductory monograph and notes by R. W. Home provide an account of Aepinus's life and work. Based on extensive archival research the monograph presents much new material about Aepinus's career, the influences upon him, the context of his research, and the contemporary and historical impact of his work and extends our knowledge of the scientific and intellectual life of eighteenth-century Germany and Russia. In addition to discussing the evolution of electrical and magnetic science during the 1700's, Professor Home also supplies a complete annotated bibliography of Aepinus's published writings.

Information for PROCEEDINGS Authors

The PROCEEDINGS OF THE IEEE welcomes for consideration (a) contributed tutorial and/or review papers in all areas of electrical science and technology, (b) contributed research papers on subjects of broad interest to IEEE members, and (c) technical letters. Research papers of narrow scope and on specialized subjects should be submitted to the appropriate IEEE TRANSACTIONS. The prospective author of a tutorial and/or review paper is encouraged to submit for review an advance proposal sketching the planned coverage, giving a brief explanation of why the subject is of current importance, and commenting on his relation to the subject.

Three copies of a manuscript, each complete with illustrations, should be submitted to the Managing Editor, PROCEEDINGS OF THE IEEE, 345 East 47th Street, New York, NY 10017. A signed copyright release form (see below) should accompany the manuscript. Detailed instructions for manuscript preparation are contained in "Information for IEEE Authors," available on request; some points of special interest to PROCEEDINGS authors are given in the following paragraphs.

Manuscript Preparation: The manuscript should be typewritten, using double spacing throughout, on one side of the paper. This includes the abstract, references, and figure captions. All pages should be numbered consecutively, including the references and figure captions. Good office-machine copies are acceptable.

Length and Presentation: There is no established length limit for papers, but they should deliver their message without verbosity. Since the PROCEEDINGS is read by people in various specialties but with broad interests, papers must be on subjects of general interest and must be written to make them accessible to the nonspecialist. They should always contain background and tutorial information necessary for this purpose. An author is urged to have his or her manuscript scrutinized by colleagues who are not experts in the field discussed so that their suggestions can lead to a manuscript more understandable to nonspecialists.

See the note published each month at the beginning of "Proceedings Letters" for special instructions for this section. In particular, authors should bear in mind that technical letters must be limited in length to five double-spaced pages, with each illustration counted as half a page.

Abstract: An abstract of not more than 200 words for papers and 50 words for technical letters is required. It should not only indicate the subject and scope of coverage but should also, in the case of research papers, give major results and conclusions.

Illustrations: Ordinary photocopies of figures and tables are usually adequate for review purposes. Upon acceptance of a paper, finished drawings in black ink on white paper or tracing cloth, or quality photographic prints of original drawings, and reproducible copies of tables must be provided. Illustrations should not exceed 22 cm by 28 cm ($8\frac{1}{2}$ in by 11 in) in size. Most are reduced to a 9 cm ($3\frac{1}{2}$ in) column width, so it is important that lettering be legible after reduction by as much as 4:1. Lettering should be in ink, not typewritten. Graphs should be drawn with no more than the main coordinates showing. All illustrations should have the figure number and author's name indicated on the back and, where necessary, a designation of which side is the top. Captions should be typed on a separate sheet, not included on the figures.

Mathematical Notation: All mathematical symbols, subscripts, superscripts, Greek letters, and unusual notations should be clearly identified for the typesetter. In particular, handwritten mathematical symbols should be written with extreme care so that there is no doubt about what is meant. Clearly distinguish between such symbols as zero and the letter "o," the small letter "l" and the numeral one and a prime sign, and the letters "k" and kappa, "u" and mu, "v" and nu, and "n" and eta.

Units: The International System of Units, which includes MKSA units, should be used. Where desirable, nonmetric equivalents can be included in parentheses. In certain few cases, where current practice in a given field is not to employ MKSA units, nonmetric units are acceptable.

References: References should be typed, using double spacing, in the IEEE style shown below. Note that the titles plus beginning and ending page numbers are included.

For an authored book:
[1] M. E. Van Valkenburg, *Prologemena on Network Theory*, vol. VI. Princeton, NJ: Fourier Press, 1977, ch. 2, pp. 966-968.

For an edited book:
[2] R. W. Lucky, "Communication with urceolate signals," in *Palimpsest on Communications*, N. C. Baskerville, Ed. Pleasantville, NY: Sunnyside Press, 1978, ch. 2, pp. 74-76.

For a journal:
[3] D. Slepian, "Information transfer at otiose bandwidth," *Proc. IEEE*, vol. 64, pp. 1969-1970, July 1976.

For a conference record:
[4] J. E. Rowe, "Methodology for optimizing maxima: An introduction," in *Proc. Joint Commun. Conf.*, 1971, pp. 71-73.

For an unpublished conference paper:
[5] G. Wade, "Ultrawide-Spectrum imaging using the Ogden model 7779 system," presented at the 1980 Southwestern IEEE Conf., Santa Barbara, CA, Mar. 19, 1980.

Review: All contributions are reviewed, as expeditiously as possible, in accordance with IEEE and PROCEEDINGS policy. Contributed papers are initially reviewed by the Managing Editor and an appropriate member of the Editorial Board; if they are judged suitable for PROCEEDINGS consideration, they are sent out for a full technical review, usually by three experts in the field. Proposals for papers are evaluated by the Editor and his advisers, after which submission of the paper for further consideration is either encouraged or discouraged. Technical letters are reviewed by at least one expert referee.

Photographs and Biographies: The authors of all papers, but not of technical letters, are requested to provide their photographs and short "technical" biographies for publication in the issue in which their papers appear. These can be provided, along with original illustrations, after a paper is accepted. See any recent issue for an example of the style for biographies.

Copyright: The PROCEEDINGS is copyrighted to protect the interests of the IEEE and its authors and their employers. To make this possible, authors must execute a copyright release form which maybe photocopied from the most recent January issue, before publication of their papers can proceed.

Proof: Before publication, galley proofs will be sent to the author, or to the coauthor who submitted the paper. Typographical errors should be marked according to the instructions accompanying the proof. This is not the time to revise the paper, and the cost of excessive changes will be billed to the author.

Voluntary Page Charges and Reprints: After a manuscript has been accepted for publication, the author's company or institution will be requested to pay a voluntary charge of $70 per printed page to cover part of the cost of publication. IEEE page charges, like those for journals of other professional societies, are not obligatory, and payment is not a prerequisite for publication. The author will receive 100 free reprints, if the charge is honored. Detailed instructions on page charges and on ordering reprints will accompany the galley proof.

> **Authors must enclose a signed copy of this form when submitting manuscripts to the Editor of this journal.**

IEEE COPYRIGHT FORM

Signed form, appropriately completed, MUST ACCOMPANY any paper to be published by IEEE.
PLEASE READ REVERSE OF THIS FORM FOR FURTHER DETAILS.

TITLE OF PAPER:

AUTHOR(S):

PUBLICATION TITLE: Proceedings of the IEEE
MONTH AND YEAR:

RETURN FORM TO:

Managing Editor
Proceedings of the IEEE
345 East 47 Street
New York, N.Y. 10017

PART A — COPYRIGHT TRANSFER FORM

(NOTE: Company or other forms may not be substituted for this form. U.S. Government employees whose work is not subject to copyright may so certify by signing Part B below.)

The undersigned, desiring to publish the above paper in a publication of the IEEE or cosponsored by the IEEE, hereby transfer their copyrights in the above paper to The Institute of Electrical and Electronics Engineers, Inc., known as the IEEE.

Returned Rights: In return for these rights, the IEEE hereby grants to the above authors, and the employers for whom the work was performed, royalty-free permission to:
  1. Retain all proprietary rights other than copyright, such as patent rights.
  2. Reuse all or portions of the above paper in other works.
  3. Reproduce, or have reproduced, the above paper for the author's personal use or for company use provided that (a) the source and IEEE copyright are indicated, (b) the copies are not used in a way that implies IEEE endorsement of a product or service of an employer, and (c) the copies per se are not offered for sale.
  4. Make limited distribution of all or portions of the above paper prior to publication.
  5. In the case of work performed under U.S. Government contract, the IEEE grants the U.S. Government royalty-free permission to reproduce all or portions of the above paper, and to authorize others to do so, for U.S. Government purposes.

IEEE Obligations: In exercising its rights under copyright, the IEEE will make all reasonable efforts to act in the interests of the authors and employers as well as in its own interest. In particular, the IEEE requires that:
  1. The consent of the first-named author be sought as a condition in granting republication permission to others.
  2. The consent of the undersigned employer be obtained as a condition in granting permission to others to reuse all or portions of the paper for promotion or marketing purposes.

In the event the above paper is not accepted and published by the IEEE or is withdrawn by the author(s) before acceptance by the IEEE, this agreement becomes null and void.

AUTHORIZED SIGNATURE

TITLE IF NOT AUTHOR

EMPLOYER FOR WHOM WORK WAS PERFORMED

DATE FORM SIGNED

PART B — U.S. GOVERNMENT EMPLOYEE CERTIFICATION

(NOTE: If your work was performed under Government contract but you are not a Government employee, sign transfer form above and see Item 5 under Returned Rights.)

This will certify that all authors of the above paper are employees of the U.S. Government and performed this work as part of their employment and that the paper is therefore not subject to U.S. copyright protection.

AUTHORIZED SIGNATURE

TITLE IF NOT AUTHOR

NAME OF GOVERNMENT ORGANIZATION

DATE FORM SIGNED

IEEE COPYRIGHT FORM
(continued)

Information to Authors

IEEE POLICY

Thank you for your interest in the IEEE. As you know, the IEEE distributes its technical publications throughout the world, and it is necessary to translate and abstract its publications, and articles contained therein, for inclusion in various compendiums and similar publications, etc. When an article is submitted for publication by the IEEE, the IEEE understands that its acceptance of the article implies that the IEEE has the rights to do all of the things it normally does with such an article.

In connection with its publishing activities, it is the policy of the IEEE to own the copyrights in its technical publications, and to the contributions contained therein, in order to protect the interests of the IEEE, its authors and their employers, and at the same time to facilitate the appropriate re-use of this material by others.

The new United States copyright law requires that the transfer of copyrights in each contribution from the author to the IEEE be confirmed in writing. It is therefore necessary that you execute either Part A–Copyright Transfer Form or Part B–U.S. Government Employee Certification on the reverse side of this sheet and return it to the Editor (or person who supplied this sheet) as promptly as possible.

AUTHOR/COMPANY RIGHTS

If you are employed and you prepared your paper as a part of your job, the rights to your paper initially rest with your employer. In that case, when you sign the copyright transfer form, we assume you are authorized to do so by your employer and that your employer has consented to all of the terms and conditions of this form. If not, it should be signed by someone so authorized.

> NOTE RE RETURNED RIGHTS: Just as the IEEE now requires a signed copyright transfer form in order to do "business as usual," it is the intent of this form to return rights to the author and employer so that they, too, may do "business as usual." If further clarification is required, please contact: Ms. Patricia Penick, Manager, Publication Administrative Services, IEEE, 345 E. 47th St., New York, NY 10017 (212) 644-7550.

JOINT AUTHORSHIP

For jointly authored papers, only one signature is required, but we assume all authors have been advised and have consented to the terms of this form.

U.S. GOVERNMENT EMPLOYEES

Authors who are U.S. Government employees are not required to sign the Copyright Transfer form (Part A), but any co-authors outside the Government are.

Part B of the form is to be used instead of Part A only if all authors are U.S. Government employees and prepared the paper as part of their job.

> NOTE RE GOVERNMENT CONTRACT WORK: Authors whose work was performed under a U.S. Government contract but who are not Government employees are required to sign Part A–Copyright Transfer Form. However, item 5 of the form returns reproduction rights to the U.S. Government when required even though the IEEE copyright policy is in effect with respect to the reuse of material by the general public.

Thank you for your prompt cooperation.

OCTOBER 1978

Our IEEE periodicals have only one competitor as an information source in electrotechnology.
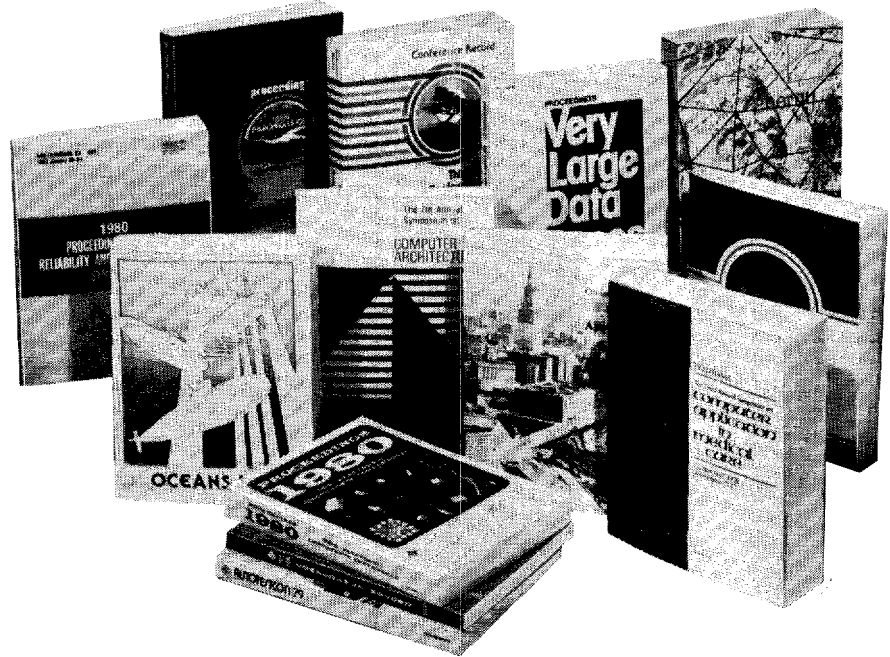
Electrooptics...bubble technology... image processing...large-scale integration...the microprocessor. With new electrical/electronics engineering breakthroughs on all fronts, keeping up to date is a formidable task for today's engineer.

Our 32 IEEE technically specialized Societies, Groups and Councils — and many of our geographical entities — help meet this problem head-on by regularly sponsoring local, regional, national, and international conferences where the state of the art in a special subject is covered in depth by experts from industry, government and academe.

In printed and microfiche editions.

Of the literally hundreds of such meetings yearly, we classify some 125 as "major", and generate a printed Conference Record or Digest of the proceedings. Each publication is also available in a space-saving microfiche edition — at a 50% discount when purchased along with the printed edition.

Our IEEE conference publications provide vital, first-hand information in a subject range as diverse as the names of our Societies, Groups and Councils.

From Acoustics to Vehicular Technology.

For example: *International Solid-State Circuits Conference...National Aerospace & Electronics Conference... National Telecommunications Conference... Oceans...International Electron Devices Meeting... COMPCON (Spring and Fall)...Annual Conference on Engineering in Medicine & Biology...*

In combination, our conference records and our massive periodicals program comprise the world's foremost source of original publishing in the burgeoning field of electrotechnology.

Special library purchase plans.

IEEE's Open Order Plan (OOP) permits libraries to place an advance order to

IEEE conference records
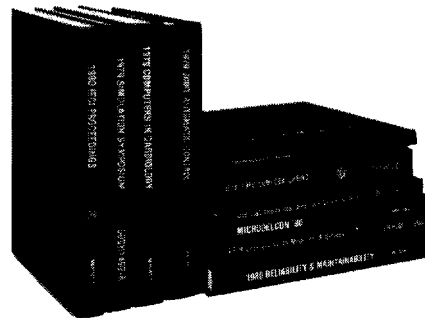
receive and be billed for every conference record as published, or only those titles falling within any of eight subject sub-groupings. And now libraries may enter a yearly subscription and receive *all* records (about 125) at a worthwhile saving. Normally paperbound, conference publications are specially clothbound for both subscribers and OOP customers.

Send for free catalog

If your library serves engineers or scientists involved in adapting electrical/ electronics engineering knowledge to problem-solving, then you should become familiar with the full extent of IEEE's resources. They are immense.

To obtain copies of our latest conference record listing, plus details on

our subscription offer and the IEEE Open Order Plan, call R. J. Jerril at IEEE ("I-Triple-E") headquarters: (212) 644-7596. Or mail the coupon below.

THE **I**NSTITUTE OF **E**LECTRICAL AND **E**LECTRONICS **E**NGINEERS, INC.

Serving 200,000 members and 14,000 libraries worldwide.

C

IEEE Technical Activities, Attn: R. J. Jerril 345 East 47th Street, New York, N.Y. 10017

Please send me _____ copy(ies) of your latest conference publications listing. Include details on purchase options.

Name _____

Organization _____

Address _____

City _____ State _____ Zip _____

IEEE. The world's leading source of new information in electrical and electronics science and engineering.

An essential reference book for those who need to keep abreast of electrotechnology.

IEEE Annual Combined Index

For engineers and scientists whose duties require detailed awareness of the state of the art in electrotechnology, there is no substitute for our annual Index.

In an easy-to-use single volume, the Index provides quick access to all IEEE-published papers, articles, and other communications covering every facet of electrical/electronics science and engineering. Information is accessible both by subject and by author.

Access 40,000 periodical pages.

Electrical/electronics applications are now so pervasive that there are IEEE periodicals specializing in fields of interest that might surprise you: biomedicine ... geoscience ... nuclear and plasma science ... pattern analysis ... oceanic engineering ... cybernetics.

These are the highly-cited, high-impact journals in their disciplines. There are now 45 such periodicals totaling over 40,000 pages annually.

Access 60,000 non-periodical pages.

The Index also cites all papers pre-sented at over 100 major IEEE-sponsored conferences covering every subject held worldwide during that year. In addition, the Index includes all new IEEE Standards, IEEE Press books, IEEE technical reports and miscellaneous IEEE publications. IEEE's massive book publishing program adds up to over 60,000 pages yearly.

Over 17,500 technical items. Over 120,000 entries.

The annual Index to IEEE Publications also contains several appendixes that provide useful bibliographic information on all indexed publications: periodicals ... special issues ... conference records and digests ... IEEE Standards and IEEE Press books. This is the information you will need in order to fully identify a complete publicaton or to order it from IEEE.

Our annual Index is the *only* index that covers the totality of IEEE publishing—the world's largest source of new information in electrotechnology.

How to order the IEEE Index.

The IEEE annual combined Index is available in the fall of the year following the publication year. These paperbound Indexes are now in stock:

Year	Pages	Product Number	IEEE/AIP Member	Non-member
1979 Index	800	JH53348	$45.00	$95.00
1978 Index	640	JH50088	$35.00	$75.00
1977 Index	622	JH46839	$25.00	$60.00
1976 Index	569	JH41905	$25.00	$60.00

To order, please enter full title, product number and price. Members of the IEEE and AIP must include member number to claim discounted price. Make check payable to IEEE. Orders on VISA, Master Charge or American Express credit cards are accepted. (Be sure to include card name, number and expiration date.) Add $2.00 handling charge if you wish to be billed direct. New Jersey residents please add 5% state sales tax. Mail your order to:

IEEE Service Center, Publication Sales - Dept. A 445 Hoes Lane, Piscataway, NJ 08854, U.S.A.

THE **I**NSTITUTE OF **E**LECTRICAL AND **E**LECTRONICS **E**NGINEERS, INC.

Serving 200,000 members and 14,000 libraries worldwide.

IEEE. The world's leading source of new information in electrical and electronics science and engineering.